Rotorcraft Terrain Awareness

Tau-based Approach to Helicopter Display Augmentation in Visual Degradation

D. L. da Silva Rosa

Master Thesis

TU Delft

Rotorcraft Terrain Awareness

Tau-based Approach to Helicopter Display Augmentation in Visual Degradation

by

D. L. da Silva Rosa

david@dasilvarosa.nl

a Master Thesis
to be presented on Thursday, 27 June 2019 at 14:00 PM
at the Delft University of Technology

Student number:	4047990	
Thesis committee:	Prof. dr. ir. M. Mulder,	TU Delft, Committee Chair
	Dr. ir. M. M. van Paassen,	TU Delft, Supervisor
	Dr. ir. C. Borst,	TU Delft, Daily Supervisor
	Dr. ir. W. J. C. Verhagen,	TU Delft, External Committee Member

Cover image adapted from Bundespolizei[‡], accessed December 12th, 2016.

Delft
University of
Technology

[‡] Retrieved from http://www.bundespolizei.de/Web/DE/Service/Presse/03Pressebilder/Imagebilder/bpol_phs-cockpit.jpg

Acknowledgments

Even though I am proud to present my Master's Thesis, I could not have accomplished this project on my own.

I'd like to thank all my daily supervisors for their involvement. Clark, thank you for your tireless positivism, academic creativity and jokes that kept me going. Your energy never failed to reach me through Skype, whether I was in Germany, Belgium or France.

Rene, thank you for the valuable feedback during the preliminary stage. And Max, thank you for putting your trust in me and organizing my stay with the DLR as well as your energy and helpful feedback. I can only admire the time and dedication given to all students at the C& O section.

Then, I would like to express my gratitude towards Johannes for making me feel so welcome in Braunschweig. Thank you for your involvement in the project and for helping me out with the simulator. I will also not forget the home-made pizza and Bavarian beer that contributed to this work.

A few words of gratitude towards Mary, Eduard and Nienke. Thank you for supporting me during my time in Delft. You were always there for me throughout the downs and to celebrate the ups.

Finally and most importantly, Rins. I can't thank you enough for supporting me throughout my studies. Thanks for your immense patience and understanding especially the last years. You have made my student life a bright one. It's finally time for our next adventure.

David
Limeyrat, 14 June 2019

Contents

Acknowledgments iii

List of Tables ix

List of Figures xi

1 Introduction 1

- 1.1 Problem Background 1
- 1.2 Problem Definition 2
- 1.3 Research Objective and Approach 4
- 1.4 Report Outline 4

I Paper 5

II Preliminary report 23

2 Visual Cues and Avoidance Manoeuvres 21

- 2.1 Visual Cues 22
  - 2.1.1 Compression, Splay & Edge Rate 22
  - 2.1.2 Optical Flow 23
  - 2.1.3 Time-to-Contact 26
- 2.2 Usable Cue Environment 27
- 2.3 Avoidance Manoeuvres 29
  - 2.3.1 Control of Avoidance Manoeuvres 29
  - 2.3.2 Mission Task Elements 31

3 Tau Theory in Rotorcraft Flight 33

- 3.1 Tau Guidance 33
  - 3.1.1 Tau Guiding a Quick Stop 33
  - 3.1.2 Tau Guiding Motion Variables 34
  - 3.1.3 Intrinsic Motion Guides 35
  - 3.1.4 Coupling Constant 36
- 3.2 Tau-coupling in Flight Manoeuvres 37
  - 3.2.1 Repositioning 37
  - 3.2.2 Hill Climb 37

4 Terrain Awareness in HMDs 43

4.1 Helicopter Terrain Awareness & Warning Systems . . . 43

4.2 Helmet Mounted Displays . . . 46

4.2.1 Human Factors Related to HMD Design . . . 46

4.2.2 Visual Attention Issues . . . 47

4.2.3 Conformal Symbology . . . 48

4.2.4 Colour in Head-Mounted Displays . . . 49

4.3 Terrain Awareness in HMDs . . . 49

4.3.1 Synthetic Terrain Imagery . . . 49

4.3.2 HMD Terrain Awareness Symbology . . . 50

5 Preliminary Concept 55

5.1 Gap Analysis . . . 55

5.2 Research Methodology . . . 56

6 Experiment Proposal 57

6.1 Research Question . . . 57

6.2 Experimental Set-up. . . . 58

6.2.1 Control Variables . . . 58

6.2.2 Independent Variables . . . 58

6.2.3 Dependent Variables . . . 59

6.2.4 Participants . . . 60

6.2.5 Experimental Procedures . . . 60

6.2.6 Apparatus . . . 60

6.3 Results, Outcome and Relevance. . . . 60

Bibliography 63

III Appendices 69

A Constant Acceleration Tau-Guide 71

B Heave Motion Constant Calculation 73

C UH-60 Z-Force Control & Stability 75

D Tau Analysis Plots 77

D.1 Flight path angle gap . . . 77

D.2 Maneuver duration. . . . 79

D.3 Coupling constant . . . 81

E Statistical Analysis 87
E.1 RMS of Altitude Error 87
E.2 Time fraction per performance boundary. 92
E.3 Control activity 101
E.4 Minimum time to contact 106
E.5 Manoeuvre duration 111
E.6 Flight path angle gap 116
E.7 Coupling constant 121

F Tau Motion Analysis 127
F.1 Manoeuvre selection 127
F.2 Fitting the tau guide 131
F.3 Rating the fit 133

G Optical variables analysis 137
G.1 Total depression angle rate 137
G.2 Splay rate 138

H Experiment Briefing 141

I Consent Form 143

List of Tables

2.1 System responses required for Level 1 handling qualities at all UCE levels. . . . 29

3.1 Average flight parameters for terrain following manoeuvre. 39
3.2 Hill climb manoeuvre coupling constant and correlation with constant acceleration guide. 40

6.1 Overview of experimental conditions. 59

B.1 Numerical properties of UH-60 for calculation of heave damping. 73

C.1 Numerical properties of UH-60 used in simulation control settings. 75

List of Figures

1.1 UH-60 Blackhawk landing in brownout 1
1.2 Sferion system, with 3D terrain and 2D flight symbology (left) and the dynamic safety line (right) 3
1.3 Schematic research project roadmap 4

2.1 Illustration of the three modes of near Earth flight. 21
2.2 Illustration of optical splay and compression 23
2.3 Visual cues of compression and splay represented by straight lines. 24
2.4 The optical flow of motion over flat terrain 24
2.5 Optical flow while approaching slanted surface. 25
2.6 Eye-height velocity while flying over flat terrain. 27
2.7 Optical flow while flying over flat terrain. 27
2.8 Usable Cue Environment chart including descriptions for each of the Visual Cue Ratings. 28
2.9 Optical flow and avoidance manoeuvres when flying towards an obstacle. 30
2.10 Quick stop manoeuvre 30
2.11 Climb manoeuvre 31
2.12 Rising ground Mission Task Element 32

3.1 Combined frames of bat catching a suspended prey. 35
3.2 Normalised distance, distance rate and tau of a constant acceleration motion. . 36
3.3 Effect of coupling constant on motion gap, gap closure rate and tau. 36
3.4 Optical flow in the rising ground Mission Task Elements (MTEs) before and after performing the pull up 38
3.5 Flight path angle used in hill climb tau analysis. 39
3.6 Progression of flight path angle and flight path angle rate for hill climb manoeuvre. 39
3.7 Tau of the flight path angle error 40
3.8 Taus of constant acceleration guide and flight path angle gap 40

4.1 Sandel HeliTAWS display 44
4.2 Garmin HTAWS on GNS 530W 45
4.3 Honeywell SmartView with HTAWS 45
4.4 Mesh (left) and points with ridgelines (right) STI that performed best in Honeywell experiment. 50

4.5 Mesh (left), contour (middle) and ridgelines (right) STIs tested in JAXA experiment. 50
4.6 Sferion obstacle pole and risk pixel symbology 51
4.7 SFERION terrain grid and ridge line symbology 51
4.8 TOAD display concepts. Left to right, top to bottom: Blinking Scene-Linked, Conformal (C), Guidance (G) and C+G 52
4.9 Standalone render and in-simulation photo of FGSA display concept 54

D.1 Run-averaged flight path angle gap γ_a. 78
D.2 Run-averaged maneuver duration T. 80
D.3 Run-averaged coupling constant k, all fits included. 82
D.4 Run-averaged coupling constant k, excluding fits rated below 2. 83
D.5 Run-averaged coupling constant k, excluding fits rated below 3. 84
D.6 Run-averaged coupling constant k, excluding fits rated below 4. 85
D.7 Run-averaged coupling constant k, excluding fits rated below 5. 86

E.1 Mixed-design Levene'e test of homogeneity of variance for RMSE. 87
E.2 Mixed-design Mauchly's test of sphericity for RMSE. 88
E.3 Mixed-design normality tests for RMSE. 88
E.4 Mixed-design ANOVA for RMSE. 88
E.5 Mauchly's test of sphericity for within-subjects RMSE. 89
E.6 Normality tests for within-subjects RMSE. 89
E.7 ANOVA for within-subjects RMSE. 90
E.8 Estimated marginal means and pairwise comparisons for Grid. 90
E.9 Estimated marginal means and pairwise comparisons for Dynamics. 91
E.10 Estimated marginal means of Grid - Dynamics interaction. 91
E.11 Profile plot for within-subjects ANOVA of RMSE. 92
E.12 Mixed-design Levene'e test of homogeneity of variance for time fraction per performance boundary. 93
E.13 Mixed-design Mauchly's test of sphericity for time fraction per performance boundary. 93
E.14 Mixed-design normality tests for time fraction per performance boundary. . . . 94
E.15 Mixed-design ANOVA for time fraction per performance boundary. 95
E.16 Mauchly's test of sphericity for the within-subjects time fraction per performance boundary. 95
E.17 Normality tests for within-subjects time fraction per performance boundary. . . 96
E.18 ANOVA for within-subjects RMSE. 97
E.19 Estimated marginal means and pairwise comparisons for Grid. 98
E.20 Estimated marginal means and pairwise comparisons for Dynamics. 99
E.21 Profile plot for within-subjects ANOVA of relative time spent within desired performance boundary. 99

E.22 Profile plot for within-subjects ANOVA of relative time spent within adequate performance boundary. 100
E.23 Profile plot for within-subjects ANOVA of relative time spent in inadequate performance zone. 100
E.24 Mixed-design Levene'e test of homogeneity of variance for control activity. . . . 101
E.25 Mixed-design Mauchly's test of sphericity for control activity. 102
E.26 Mixed-design normality tests for control activity. 102
E.27 Mixed-design ANOVA for control activity. 102
E.28 Mauchly's test of sphericity for within-subjects control activity. 103
E.29 Normality tests for within-subjects control activity. 103
E.30 ANOVA for within-subjects control activity. 104
E.31 Estimated marginal means and pairwise comparisons for Grid. 104
E.32 Estimated marginal means and pairwise comparisons for Dynamics. 105
E.33 Estimated marginal means of Grid - Dynamics interaction. 105
E.34 Profile plot for within-subjects ANOVA of control activity. 106
E.35 Mixed-design Levene'e test of homogeneity of variance for minimum tau. . . . 106
E.36 Mixed-design Mauchly's test of sphericity for minimum tau. 107
E.37 Mixed-design normality tests for minimum tau. 107
E.38 Mixed-design ANOVA for minimum tau. 107
E.39 Mauchly's test of sphericity for within-subjects minimum tau. 108
E.40 Normality tests for within-subjects minimum tau. 108
E.41 ANOVA for within-subjects minimum tau. 109
E.42 Estimated marginal means and pairwise comparisons for Grid. 109
E.43 Estimated marginal means and pairwise comparisons for Dynamics. 110
E.44 Estimated marginal means of Grid - Dynamics interaction. 110
E.45 Profile plot for within-subjects ANOVA of minimum tau. 111
E.46 Mixed-design Levene'e test of homogeneity of variance for manoeuvre duration. 111
E.47 Mixed-design Mauchly's test of sphericity for manoeuvre duration. 112
E.48 Mixed-design normality tests for manoeuvre duration. 112
E.49 Mixed-design ANOVA for manoeuvre duration. 112
E.50 Mauchly's test of sphericity for within-subjects manoeuvre duration. 113
E.51 Normality tests for within-subjects manoeuvre duration. 113
E.52 ANOVA for within-subjects manoeuvre duration. 114
E.53 Estimated marginal means and pairwise comparisons for Grid. 114
E.54 Estimated marginal means and pairwise comparisons for Dynamics. 115
E.55 Estimated marginal means of Grid - Dynamics interaction. 115
E.56 Profile plot for within-subjects ANOVA of manoeuvre duration. 116

E.57 Mixed-design Levene'e test of homogeneity of variance for flight path angle gap. 116
E.58 Mixed-design Mauchly's test of sphericity for flight path angle gap. 117
E.59 Mixed-design normality tests for flight path angle gap. 117
E.60 Mixed-design ANOVA for flight path angle gap. 117
E.61 Mauchly's test of sphericity for within-subjects flight path angle gap. 118
E.62 Normality tests for within-subjects flight path angle gap. 118
E.63 ANOVA for within-subjects flight path angle gap. 119
E.64 Estimated marginal means and pairwise comparisons for Grid. 119
E.65 Estimated marginal means and pairwise comparisons for Dynamics. 120
E.66 Estimated marginal means of Grid - Dynamics interaction. 120
E.67 Profile plot for within-subjects ANOVA of flight path angle gap. 121
E.68 Mixed-design Levene'e test of homogeneity of variance for coupling constant. . 121
E.69 Mixed-design Mauchly's test of sphericity for coupling constant. 122
E.70 Mixed-design normality tests for coupling constant. 122
E.71 Mixed-design ANOVA for coupling constant. 122
E.72 Mauchly's test of sphericity for within-subjects coupling constant. 123
E.73 Normality tests for within-subjects coupling constant. 123
E.74 Within-subjects ANOVA of coupling constant. 124
E.75 Estimated marginal means and pairwise comparisons for Grid. 124
E.76 Estimated marginal means and pairwise comparisons for Dynamics. 125
E.77 Estimated marginal means of Grid - Dynamics interaction. 125
E.78 Profile plot for within-subjects ANOVA of coupling constant. 126

F.1 Control input, vertical position, flight path angle and flight path angle rate are plotted against time. The selected maneuver is displayed in the bold, red curve. 128
F.2 Overview of various run data used during the analysis 130
F.3 Overview of plots used for the tau analysis, including flight path angle and its rate as a function of manoeuvre time, time to contact as a function of manoeuvre time and as a function of the time to contact of the motion guide, and the correlation. 133
F.4 Run rated 0 since the tau guide could not be fitted. 134
F.5 Run rated 1 since last half of manoeuvre is barely described by the tau guide. . 134
F.6 Run rated 2 since the tau guide could not be fitted. 135
F.7 Run rated 3 since the tau guide could not be fitted. 135
F.8 Run rated 4 since the tau guide could not be fitted. 136
F.9 Run rated 5 since the tau guide could not be fitted. 136

G.1 Compression and splay angle rates for nominal height across grid cell sizes and and starting positions (run 1 to 3) 139
G.2 Splay rate ratios comparing splay rates between the three grid cell sizes 140

1

Introduction

1.1. Problem Background

Degraded visual environment (DVE) is a major cause of helicopter incidents and accidents. Water, snow, sand or dust particles are thrown up by the rotor blades' downwash, blocking the crew's visual reference to the outside world as illustrated in Section 1.1. Pilots encountering these conditions suffer from spatial disorientation (SD), ultimately resulting in a significant amount of CFIT.

Various studies have shown the necessity to increase situation awareness (SA) and reduce pilot workload in DVE conditions for safer helicopter flight. Research by the Dutch National Aerospace Laboratory (NLR) on European helicopter accidents from 2000 through 2008 found that over half of the cases was related to DVE or CFIT [1]. Similarly, an analysis of U.S. Army helicopter accidents between 2002 and 2011 identified 100 cases linked to SD and concluded the phenomenon to be linked to significantly more fatalities [2].

Figure 1.1 – UH-60 Blackhawk landing in brownout (Source: Flickr[†])

Effective visual aid technologies such as helmet mounted displays (HMDs) provide a promising outlook towards increasing rotorcraft safety. They enable the integration of sensor and database information with the outside scene, allowing pilots to maintain situation awareness even without visual reference. State-of-the-art HMDs can display world-referenced symbologies including

---

[†] Retrieved from `https://www.flickr.com/photos/oregonmildep/25976543883`

terrain grids, obstacle icons and landing guidance using full-colour and a wide field of view (FOV) [3]. Combined with a Helicopter Terrain Awareness and Warning System (HTAWS), to become mandatory on helicopter emergency medical services (HEMS) [4], rotorcraft operations in all-weather, day-and-night conditions may soon become reality.

However, the implementation of HMD terrain awareness symbology to increase SA and decrease workload appears to be a balancing act between automation and human controller. Transparent displays are prone to clutter and attentional tunneling [5–7]. As a countermeasure some terrain awareness systems display a synthetic boundary, or safety line, to guide the flight path marker outside of terrain and obstacles [8, 9]. Despite a successful increase in safety and decrease in workload, the deeper structure of the task is hidden through automation. Pilots cannot grasp the functional principles and its constraints to find solutions to off-nominal situations. The automation logic is invisible to the pilot. As a result, the pilots' ability to quickly respond to unforeseen situations may be reduced [10, 11].

The control task at hand requires interfaces that integrate with the pilots' natural perception of the work domain in order to enhance their perception-action performance. Indeed, low level helicopter flight in DVE is highly dynamic in both visual conditions and kinematics. Therefore, visual aids need to seamlessly integrate with the pilots' ecological apprehension to have direct compatibility with the pilots' mental model. Designing such systems necessitates a thorough understanding of what visual information is used for terrain avoidance, how this information is mentally coupled for motion guidance and, finally, how visual aids affect this perception-action behaviour.

This thesis applies an ecological approach to terrain awareness in low level helicopter flight using an augmented reality display. The problem statement is introduced in Section 1.2. Consequently, the methodology for solving the problem is presented in Section 1.3. Finally, Section 1.4 guides the reader through the structure of this report.

1.2. Problem Definition

Strengthened requirements for flight procedures and the integration of advanced onboard equipment such as HTAWS' are set to improve helicopter safety during low flight and DVE [12]. Along with the expected adoption of HMDs, all-weather, day-and-night operations may eventually become a reality. Sferion is Airbus' implementation of a rotorcraft SA solution for all phases of flight including DVE[‡]. The system can display navigational and tactical guidance, a terrain grid and obstacle symbols on a HMD, as shown in Figure 1.2. Moreover, a dynamic safety line can be generated above which the flight path marker (FPM) should be kept to vertically clear obstacles with a preset margin as shown in Figure 1.2b [8].

The aforementioned display symbologies need to be evaluated for effectiveness and for potentially undesired side-effects on task performance and mitigating unexpected events. Ironically, the usage of an automated guidance line may negatively impact SA in DVE. First, its automatic calculation does not support pilot cognition. This is problematic when unanticipated conditions occur in which the pilot is expected to quickly make informed decisions. Second, an isolated symbol may stimulate over-reliance, especially when outside visual cues are absent. Without a visual reference the crew is likely to focus on the symbol that seems most safety-critical. As the safety line lacks contextual links to other factors used in the pilot's mental model (e.g. time to contact, rate of climb, energy levels, etc.), it is impossible to reflect on system integrity. Third, the specific format of a synthetic terrain visualisation may adversely affect the

---

[‡] Retrieved from `https://airbusdefenceandspace.com/sferion-situational-awareness-system/`

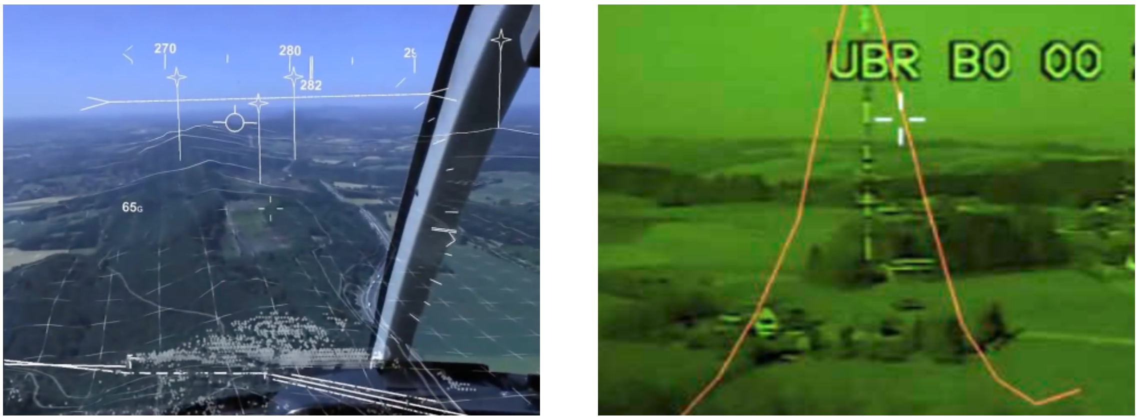

(a) enhanced vision on HMD **(b)** safety line on HDD

Figure 1.2 – Sferion system, with 3D terrain and 2D flight symbology (left) and the dynamic safety line (right). (Source: Airbus Defense and Space[‡])

ecological perception of the environment, potentially leading to pilots flying with suboptimal safety margins. To conclude, these factors can still lead to perilous situations.

The design of HMD symbology for helicopter terrain and obstacle avoidance in degraded visibility needs to bridge the gap between the pilots's perceptual and cognitive guidance functions. From a technological standpoint the perceptual functions of low rotorcraft flight can readily be shown. Task-relevant information based on fused sensor and database information can be presented within the natural perspective of the human controller. However the impact of such visual augmentation on the cognitive guidance functions remains unknown: how do they affect the control actions and their expected effects in relation to the system boundaries. The research question can now be formulated as follows:

Research question

*What **information** can support **helicopter terrain awareness** during **nap-of-the-Earth (NOE)** flight in **DVE** and how can this information be effectively **displayed on a colour HMD**?*

This research question will form the main theme of the thesis, it consists of two parts that are to be answered consecutively. The research project is considered to be succesful once this question can be answered. The following set of subquestions is formulated to aid the process:

- What **visual cues** and **avoidance manoeuvres** are used by helicopter pilots to evade obstacles and terrain in **low level DVE flight**?
- What is the state-of-the-art in **terrain awareness** and **avoidance systems**, **HMD technology** and **symbology**? How do these systems **support SA** in a DVE NOE task?
- How do pilots **coordinate** terrain avoidance **manoeuvres**? What **task-dependent information** can be displayed on a HMD to reinforce the **natural control strategy** in DVE?

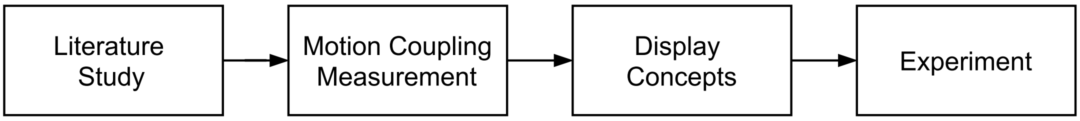

Figure 1.3 – Schematic research project roadmap

1.3. Research Objective and Approach

The thesis objective follows logically from the research question in Section 1.2. It is formulated as follows:

Research objective

Find and display relevant information in the work domain of rotorcraft NOE flight in DVE that supports pilot SA while using a colour HMD.

Given the extent of the research objective and the limited resources available for this thesis project, the problem is deliberately narrowed down to terrain avoidance using a climbing manoeuvre in the vertical plane.

An ecological approach will be used to solve the problem, more specifically general tau theory as introduced in Chapter 3. A roadmap of the approach is presented in Section 1.3. First, knowledge of the perceptual and cognitive functions that pilots use in NOE flight will be gathered through a literature survey. This will include visual cues and avoidance manoeuvres, terrain awareness and HMD display technologies as well as motion coupling through tau guides. Thereafter, a numerical tool will be developed to measure tau coupling in a climbing manoeuvre. Consequently, display concepts are to be developed that may support and enhance the natural perception-action system. Once it is hypothesized that the obtained interface design will lead to significant experimental results, its experimental evaluation will be undertaken.

1.4. Report Outline

This preliminary report documents the available knowledge in the domain of interest and includes experiment proposal. The report structure is as follows. **??** of this preliminary report consists of a literature survey. In Chapter 2 the literature on the visual cues and avoidance manoeuvres will be discussed, Chapter 3 deals with motion guide theory applied to helicopter flight and Chapter 4 covers the state-of-the-art in helicopter terrain awareness systems and HMDs. Chapter 5 presents a consolidated analysis of the discussed literature, including knowledge gaps that were identified. Then, Chapter 6 proposes a human factors experiment aimed at bridging those gaps.

Paper

Effects of Grid Cell Size in Altitude Control in an Augmented Reality Terrain Display

D. L. da Silva Rosa* (MSc Student), J. M. Ernst† (Doctoral Student),
Supervisors: dr. ir. C. Borst*, dr. ir. M. M. van Paassen*, Prof. dr. ir. M. Mulder*
*Delft University of Technology, Faculty of Aerospace Engineering, Department Control & Operations, Delft, The Netherlands
†German Aerospace Center (DLR), Institute of Flight Guidance, Braunschweig, Germany

Abstract—**Helicopter pilot performance in degraded visual conditions may be improved through sensor fusion and an augmented reality display. A simulator experiment with 12 participants was done to test the effect of synthetic terrain grid cell size and helicopter heave dynamics on task performance and control behaviour in a terrain-following hill-climb task. An increase in grid cell size lowered task performance and increased control activity due to reduced optical information. Slower heave dynamics decreased task performance and led to a more prospective control strategy. It was concluded that an effective AR terrain display for altitude control can be designed independently from the vehicle dynamics.**

ABBREVIATIONS

AGL	Above Ground Level
ANOVA	Analysis of Variance
AR	Augmented Reality
CFIT	Controlled Flight into Terrain
DVE	Degraded Visual Environment
GECO	Generic Cockpit
HMD	Helmet-Mounted Display
HD1/2	Heave Dynamics 1 or 2
MTE	Mission Task Element
NOE	Nap-of-the-Earth
RMSE	Root Mean Square Error
SA	Situation Awareness
SD	Standard Deviation
STI	Synthetic Terrain Imagery
UCE	Usable Cue Environment

I. INTRODUCTION

Low-level helicopter flight in a degraded visual environment (DVE) often leads to spatial disorientation and results in a significant amount of controlled flight into terrain (CFIT) incidents [1]–[4]. The out-of-the-window view of the surrounding terrain and obstacles can be degraded by unfavorable lighting conditions, as well as by dust particles (brown-out) or precipitation (white-out). As pilots rely on the visual cues present in the optical flow of the outside visual field, their degradation has adverse effects on situation awareness (SA) and workload, and eventually on flight safety.

An analysis of U.S. Army helicopter accidents between 2002 and 2011 identified 100 cases linked to spatial disorientation and concluded spatial disorientation to be related to significantly more fatalities [4]. Similarly, research on European helicopter accidents from 2000 through 2008 by the NLR, the Dutch National Aerospace Laboratory, found that more than half of the crashes was related to DVE or CFIT [3]. Both studies emphasise the necessity of effective visual aid technologies to increase situation awareness and reduce pilot workload in DVE conditions for safer helicopter flight.

To mitigate the risks of low-level helicopter flight in DVE, the information from board-mounted sensors and databases can be fused to reconstruct a virtual image of the surroundings. A virtual terrain grid can then be used to restore part of the degraded optic cues by means of an augmented reality (AR) display with semi-transparent visors and head-tracking capability, so the pilot can perceive the grid while preserving the out-of-the-window gaze [5]–[9]. This superimposing of symbology on the outside scene elements, to which sensory information is added, is known as conformal symbology [10].

However, designing safe and effective AR terrain symbology requires understanding how pilots use the optic flow in flight control, how they react to visual degradation and how a see-through display can help restore the essential optic cues. Extensive human factors studies on conformal symbology in optical see-through displays in DVE confirm benefits in divided attention and task performance but also pointed out the risks of clutter and attentional tunneling [11], [12]. Effective AR terrain symbology will need to mitigate these undesired side-effects.

Clark investigated the effect of various levels of visually degraded conditions on prospective guidance in low-level helicopter flight by analysing the time-to-contact in a terrain-following hill climb manoeuvre [13]. His analysis revealed that decreasing levels of visibility cause pilots to start their avoidance manoeuvre closer to the slope, and provided more evidence to suggest pilots use an implicit motion guide as a guidance strategy for the manoeuvre. A study by Flach et al. (2011) tasked participants to drive from an idle position to a stopped position just in front of an obstacle as quickly as possible while avoiding collision [14]. The method used by participants to determine the moment at which to release the accelerator to start braking corresponded to a constant time to contact strategy, that was being tuned ever more closely towards the optimal solution as the task was repeated. This led to the hypothesis that the optical time to contact variable expressed how participants were developing their internal model of the dynamical limits of the vehicle.

An AR terrain grid could partly replace the degraded visual cues in the optic flow by providing splay and depression angle cues. Flach et al. (1997) studied the relative effects of these optic cues on altitude control across various forward speeds [15]. They found that the visual system is not differentially tuned to either splay angle or depression angle for perceiving altitude change, but that splay angle provides a higher quality cue due to its increased visible range in the forward view, its insensitivity to forward motion and its symmetry properties.

Yet, the effects of AR terrain displays on altitude perception and control in DVE remain unclear. Clark's work on the hill climb begs the question whether visual augmentation would counteract the consequences of degraded optic cues on a pilot's control strategy [13]. Likewise, as the experiments of Flach et al. featured flat terrain, their work invites inquiry into the effects of relatively minor and major changes in terrain height on the optic cues of an AR terrain grid [15]. How do pilots react to the superimposing of an AR terrain grid on irregular, nonflat terrain? Does the terrain grid size change a pilot's perception of the terrain elevation profile? How does the AR terrain grid size affect the control strategy and is there an interaction effect with the vehicle dynamics?

This paper aims to investigate the effects of synthetic terrain grid size in head-worn displays on task performance and control behaviour in a realistic hill climb task throughout varying vehicle heave damping settings in DVE. The results are presented of an experiment conducted with 6 novices and 6 pilots in the generic cockpit (GECO) simulator of the DLR Institute of Flight Guidance in Braunschweig, Germany. The hill climb task in Clark's work is essentially modified into an altitude control task by adding terrain irregularity, reducing vehicle control complexity and adding a simulated AR terrain grid. The effects of terrain grid size, helicopter heave dynamics and experience on various measures for task performance are examined. Control behaviour is studied using a time to contact analysis.

The paper is structured as follows. First, section II introduces useful background concepts for time to contact analysis. Section III describes the experimental setup and methods. Experimental results are presented in Section IV, followed by a discussion in Section V. The paper ends with a conclusion.

II. BACKGROUND

A. Optic cues of a terrain grid

A nap-of-the-Earth flight course closely follows the terrain curvature, requiring accurate perception of the terrain geometry as well as the aircraft height and speed. Locomotion research has shown that pilots use the angles between the lines defining the textural gradients to determine their position and motion with respect to the terrain [16]. One of these angles is the optical splay angle S, defined as the angle at the vanishing point between an edge parallel to the direction of motion and a line on the ground along the direction of motion, perpendicular to the horizon line. It is calculated through:

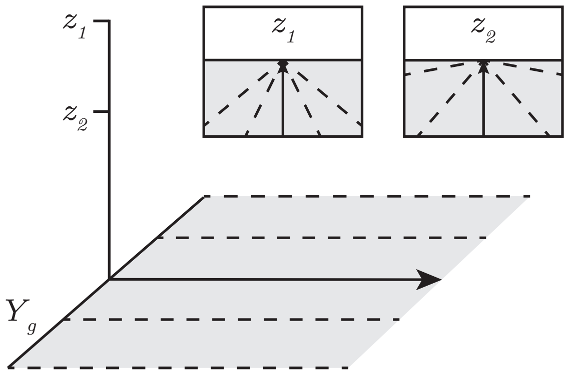

Fig. 1: Effect of altitude change on splay angle. As the altitude decreases from z_1 to z_2, the texture lines rotate away from the direction of motion toward the horizon, increasing the splay angle.

$$S = tan^{-1}\left(\frac{Y_g}{z}\right), \tag{1}$$

where S is the splay angle, Y_g is the lateral displacement from the ground track and z the altitude. This is illustrated in Figure 1.

The rate of change in splay angle with changing observer position can be calculated as :

$$\dot{S} = -\left(\frac{\dot{z}}{z}\right) cos(S) sin(S) + \left(\frac{\dot{Y}_g}{z}\right) cos^2(S) \tag{2}$$

In the case of symmetric forward flight, the rate of change in lateral position is zero and the second term in Equation (2) cancels out. We are left with the first term, which shows that changes in splay angle depend on the initial altitude since they are scaled by z. Moreover, increasing altitude leads to a decrease in splay angle and vice versa.

Another optical angle used to detect changes in altitude is optical depression. Any edge perpendicular to the direction of motion has an angular position with respect to the horizon as viewed by the observer, the optical depression angle [15]. By convention, this angle is calculated with respect to the observer taking the distance on the ground to the edge feature in the forward visual field and by scaling this distance by the height of the observer, as in Equation (3):

$$\delta = tan^{-1}\left(\frac{x_g}{z}\right), \tag{3}$$

with δ the depression angle, x_g the longitudinal distance on the ground to the texture element and z the altitude. Figure 2 illustrates the angular depression.

For rectilinear forward motion the rate of change in depression can be calculated as:

$$\dot{\delta} = -\left(\frac{\dot{z}}{z}\right) cos\ (\delta)\ sin(\delta) + \left(\frac{\dot{x}_g}{z}\right) cos^2(\delta) \tag{4}$$

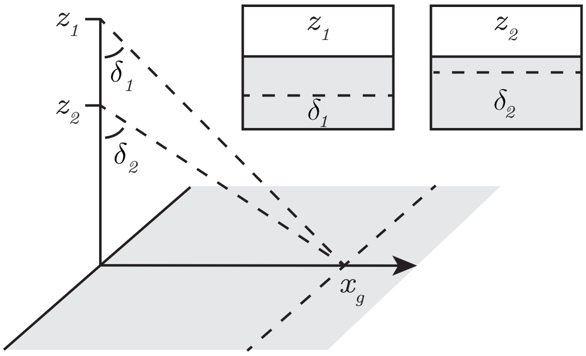

Fig. 2: Effect of altitude change on depression angle. As altitude decreases from z_1 to z_2, the depression angle increases, moving the texture lines perpendicular to the forward direction of motion upwards toward the horizon.

Similar to splay, the rate of change in depression angle depends on the eye-height scaled altitude and on on the initial optical position of a texture element. Texture elements that are low in the field of view will have a greater depression angle rate for constant forward speed.

Equations (2) and (4) show that altitude and forward speed have different effects on the splay and depression rate. Splay rate is a visual cue of higher quality for change in altitude as changes in speed do not affect edges parallel to the direction of motion. Depression angle rate, however, depends both on forward speed and on change in altitude. Through a series of experiments Flach et al. have demonstrated that both cues are used in altitude control [15]. The authors noted that splay angle is the preferred optical cue for altitude perception as a greater angular range is generally visible in the field of view, since it is decoupled of the natural forward motion and because it is symmetrically affected by altitude change as opposed to density angle.

Even if optical splay is preferred for altitude control, it may be infeasible to exclude the optical density angle from an AR terrain display for NOE flight. Such a display needs to support perception of irregular terrain elevations as well as speed, both of which benefit from the density angle cue. Adding optical density to optical splay naturally results in a grid texture, that may allow the geometry of rugged terrain to be perceived more easily. Corwin et al. had 12 military pilots compare different types of synthetic terrain imagery (STI) against a terrain background on a helmet-mounted display (HMD) in a full flight mission [17]. Among a variety of display formats, the one with an orthogonal mesh and the display with points and ridge lines were preferred.

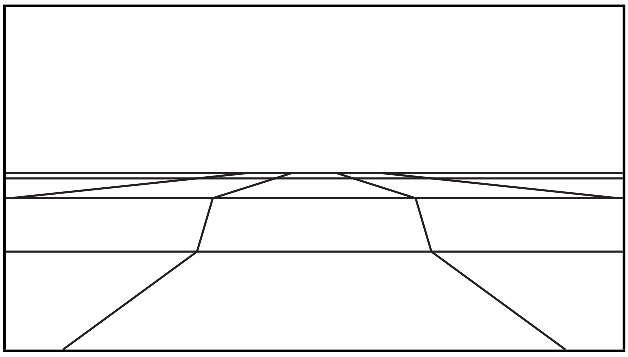

Fig. 3: Effect of forward increase in terrain elevation on synthetic terrain grid.

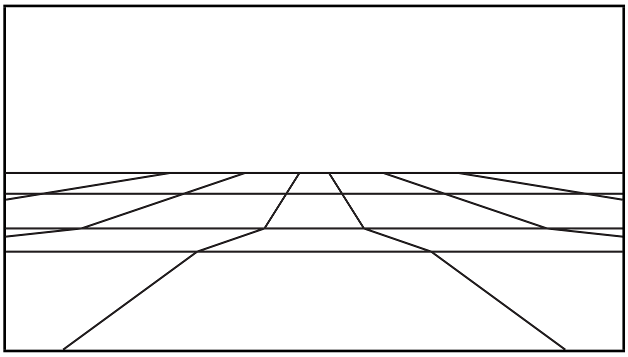

Fig. 4: Effect of forward decrease in terrain elevation on synthetic terrain grid.

Variations in terrain elevation change the geometry of a synthetic grid similarly to change in altitude, although the variations appear locally in the field of view. A square, synthetic grid orthogonally displayed to the direction of flight essentially replaces the optic cues of the splay and density angles, provided the terrain is flat. With flat terrain, texture lines parallel to the direction of motion run straight into the vanishing point at the horizon and the spacing between each horizontal texture line further ahead decreases, tending towards zero at the horizon line. When terrain elevation increases in the forward direction, the direction of the splay lines and the spacing between the density lines become distorted: the section of increasing elevation has a smaller splay angle than the flat area and the spacing between horizontal lines locally increases, as shown in Figure 3. On the contrary, a descending section leads to a larger local splay angle than the flat area and the spacing between horizontal lines locally decreases, as shown in Figure 4.

The grid cell size of a synthetic terrain grid determines the amount of grid lines in the field of view. This controls the magnitude of the optic flow used to perceive egomotion and the resolution of the terrain elevation available to the observer, consequently affecting flight control. The grid cell size of an AR terrain display should provide sufficient terrain detail while avoiding clutter. Let's consider an orthogonal terrain grid obtained by linear interpolation of perfectly accurate terrain elevation data. The accuracy of the terrain grid depends on the grid cell size. A smaller terrain grid leads to a more accurate terrain grid that's able to show finer variations in terrain elevation. Figure 5 illustrates the effect of doubling the cell size on the accuracy of a terrain grid.

Grid cell size in AR terrain displays turns out to be a

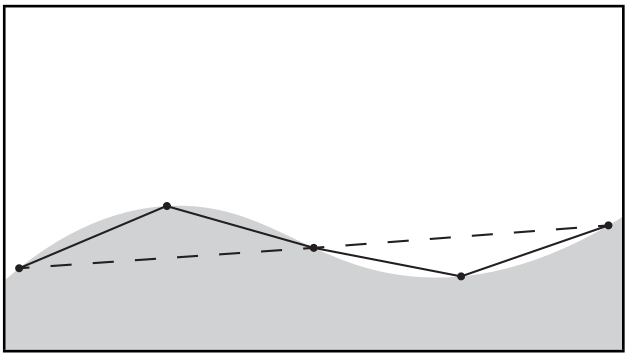

Fig. 5: A grid cell size twice as small shows more detail of a 2D terrain elevation profile. This effect is magnified in 3D.

key factor influencing the perception of altitude, speed and terrain geometry that can potentially cause human performance issues such as display clutter and attentional tunneling [11]. It affects the extent to which synthetic terrain imagery can show variations in terrain elevation, which in turn impact optic splay and density angles picked up as optic cues for altitude and speed. Yet, the direct effects of grid cell size remain largely undocumented. Their examination could benefit from an understanding of the coupling of perceptual information with the control strategy that pilots tend to use.

B. Optic Flow and Tau

Lee introduced an analytical form of Gibson's ecological optic flow theory that describes the fundamental relation between perceptual information and control coordination [18], [19]. This general tau theory hypothesises that targeted motion is not guided through the observation of its spatial form of displacement rate and remaining distance, but is rather directly perceived and controlled in its temporal form: the time-to-contact, tau (τ). The motion gap between a current and target state is effectively closed by keeping constant the rate of change of tau. Evidence for Lee's tau theory was found in a wide range of controlled motions including human and non-human animals, underpinning temporal motion control as a fundamental product of evolution [20]–[22].

Tau theory provides a unifying framework that encompasses a multitude of optic cues identified in studies of the perception of egomotion. As the invariants in the optic flow can be expressed as angles and angular rates, pilots infer tau to close gaps when moving from a current hovering position to an adjacent, desired one or when coupling an obstacle-bound trajectory onto one that safely evades the obstacle. For a given motion gap, the instantaneous time to contact τ is the ratio of the negative distance to the target $x(t)$ and the closure rate $\dot{x}(t)$:

$$\tau_x(t) = \frac{x(t)}{\dot{x}(t)} \tag{5}$$

τ is used to coordinate when to apply motion controls, but when combined with its derivative $\dot{\tau}$ there is sufficient perceptive information to tune the motion control. Differentiating and rearranging Equation (5) yields:

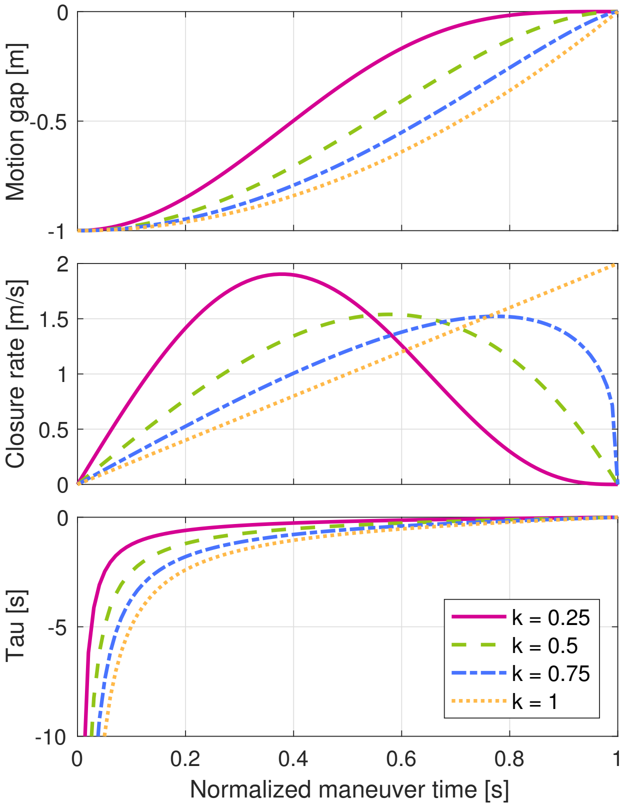

Fig. 6: Effect of coupling constant on motion gap, gap closure rate and tau for a normalised, constant acceleration motion.

$$1 - \dot{\tau_x} = \frac{x\ddot{x}}{\dot{x}^2} = \frac{\tau_x}{\tau_{\dot{x}}} \tag{6}$$

Tau theory hypothesises that τ and $\dot{\tau}$ are the fundamental inputs to the natural motion control system. If $\dot{\tau}$ is kept constant, the taus of the motion gap and of its closure rate remain in a fixed ratio while they are brought to zero. Equation (7) defines the coupling constant $k = 1 - \dot{\tau}$ for $0 \leqslant k \leqslant 1$:

$$\tau_x = k\tau_{\dot{x}} \tag{7}$$

The value of k in two tau-coupled motion gaps describes how one motion gap is closed in relation to the other. Using one tau motion to guide another is considered a natural control strategy. If the guiding tau motion is a mental model of the controller, it is referred to as an *intrinsic* motion guide. Evidence suggests that one such commonly used intrinsic tau-guide is the constant acceleration tau guide τ_g, presumably because the gravitational acceleration is ubiquitous. Figure 6 shows a distance and time-normalised, τ_g-guided motion gap, its closure rate and its tau for different values of k.

Figure 6 illustrates motions that follow a constant acceleration guide for different values of k:

- The motion directly starts with an acceleration, of which the intensity is higher for lower values of k. The point of maximum closure rate is therefore increasingly delayed for higher values of k.
- Increasing k from zero changes the deceleration at the end of the motion from gentle to aggressive. For $k = 0.5$ a finite deceleration can close the gap, higher k-values require infinite deceleration, e.g. a collision.
- For $k = 1$ the motion follows the guide exactly and constantly accelerates into the goal.

C. Tau guidance in hill-climb

Initiating a helicopter climb from steady horizontal flight requires raising the collective control θ_0 to move the flight path angle γ to the final flight path angle γ_f. The negative flight path gap γ_a is the difference between these angles ($\gamma_a = \gamma - \gamma_f$). The manoeuvre starts with θ_0 input and ends when the flight path rate goes from positive to negative ($\dot{\gamma}_a = 0$), defining the manoeuvre duration T.

The flight path gap tau τ_γ is calculated by applying Equation (5):

$$\tau_\gamma(t) = \frac{\gamma_a(t)}{\dot{\gamma}_a(t)} \tag{8}$$

Clark applied this method of analysis in an experiment with a single experienced pilot flying a hill-climb mission task element (MTE) across various levels of visibility in a UH60A Black Hawk simulator [13]. Starting from the initial hover point, the terrain had a flat run-in of 750 m, a 5 deg slope of 60 m high and a flat run-out of 2000 m to test the restabilization of the rotorcraft after the slope. Flight speed and altitude could be freely selected by the pilot. Visual conditions varied across usable cue environment UCE 1-3 [23], by blurring textures and decreasing the visible range. Instruments were disabled and trees were included for height reference. To relate the observed τ_γ to the constant acceleration tau-guide τ_g a least-squares fit was done, moving backwards from the end of the manoeuvre until the correlation coefficient R^2 went under a set threshold. The fit was then made using the resulting k. The tau analysis showed that decreasing visibility led to higher overshoots of the flight path angle and that the minimum time-to-contact τ_{min} decreased, both indicating an increased difficulty to perceive the slope angle. Significant correlations of the flight path gap tau τ_γ with the constant acceleration tau-guide τ_g were found. It appeared there was no link between the level of visibility and k.

One outcome of Clark's study was that the minimum tau decreased as the visibility deteriorated, so a setback in visual perception of the hill delayed the pull-up manoeuvre [13]. However, there was apparently no conflict yet with the pilot's mental model of the rotorcraft dynamics, which tolerated safely awaiting visual perception of the terrain before initiating the climb became necessary to avoid CFIT. Flach et al. (2011) showed that test subjects used a constant time-to-contact strategy to manoeuvre a car into standstill right before an obstacle while internalizing a mental model of the vehicle's dynamical limits [14].

This study attempts to start establishing the design trade-off for the appropriate grid cell size of an AR terrain for NOE flight. This flight task incorporates the interaction of pilots' visual perception of the environment and their awareness of the dynamical limits of the rotorcraft. As such, the influence of the vehicle dynamics on the control strategy will be investigated in combination with the variation of the grid cell size. Regarding the minimum distance to the slope, no effect of the grid cell size is expected as any synthetic terrain should provide sufficient information about the start of the slope regardless of its cell size. Pertaining to the vehicle dynamics, a slower flight-mechanical response of the controlled element should not lead to an effect on performance but instead to a more anticipating control strategy, e.g., higher minimum time-to-contact and a longer manoeuvre time.

III. EXPERIMENT DESIGN

To investigate how an augmented reality terrain grid affects task performance and control behaviour in DVE Nap-of-the-Earth (NOE) flight, a simulator-based experiment was conducted with a modified hill-climb Mission Task Element. Twelve participants were instructed to maintain constant altitude above ground level (AGL) in degraded visual conditions, the view out the window being their only source of visual information. A semi-transparent synthetic grid was overlaid on the outside visual to simulate an augmented reality terrain display. The experiment aimed to study the effect of *varying cell sizes in an augmented terrain grid* on altitude perception and control, and whether this phenomenon is affected by the *heave dynamics of the controlled rotorcraft*.

A. Participants & Instructions

A total of 12 right-handed men took part in the experiment, all with normal or corrected-to-normal vision. Participants were recruited within the DLR Institute of Flight Guidance. Two groups of equal size were formed. Six were non-pilots, six were licensed general aviation fixed-wing pilots with ratings ranging from glider pilot through to flight instructor. One held a commercial multi-engine pilot license with instrument rating. Half of the pilots had about 50 h of helicopter practice in simulators. Flight experience ranged from approximately 60 h to over 2000 h.

Average age of participants was 35.8 yrs ($\sigma = \pm 10.5$ yrs). A pre-experiment briefing was provided before the experiment to explain its purpose and the piloting task. Furthermore, the briefing explained the purpose and functioning of the peripheral display symbology used during training. The same briefing was repeated at the start of the experiment, to ensure the instructions were clear to all participants.

B. Control Variables

1) Apparatus: The experiment was conducted in the Generic Cockpit (GECO) simulator, shown in Figure 7. It

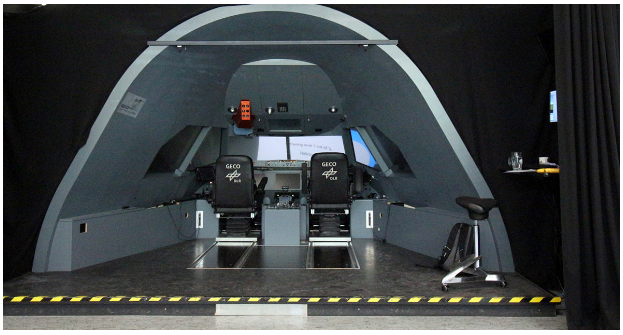

Fig. 7: The Generic Cockpit simulator of the DLR Institute of Flight Guidance in Braunschweig, Germany

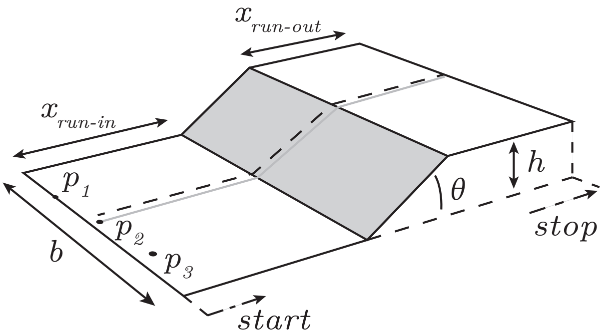

Fig. 8: Schematic representation of terrain geometry including starting positions and without Perlin noise

has a wooden A320 cockpit shell and a collimated visual system, providing depth perception of infinity, using three high resolution projectors (2160 × 1440 pixels) displaying an area of $180° \times 40°$. A spring-loaded, passive side-stick was used as manipulator, of which only the longitudinal axis was activated. Participants were seated in the same longitudinal position in the right seat. They were instructed to keep their gaze fixed forward to limit the slight advantage of looking at the edges of the display to infer altitude above terrain.

2) Control Task: Participants controlled the rotorcraft in the heave axis by manipulating the simulator sidestick using rate command. The dynamic model in the simulator had first-order linear dynamics in the heave axis as described by Equation (9), with w the vertical velocity (m/s), Z_{θ_0} the dimensionless collective control derivative in the Z-axis, and Z_w the heave damping coefficient (s^{-1}). A rotorcraft with relatively higher heave damping coefficient in absolute terms exhibits faster dynamical response in the heave axis.

$$\dot{w} = Z_{\theta_0}\theta_0 + Z_w w \tag{9}$$

Helicopter collective control θ_0 was replicated through the longitudinal axis of the manipulator, e.g., backward stick deflection increased altitude whereas forward stick deflection decreased it. Attitude remained constant at all times, so the simulated vehicle behaved more like a flying elevator than a helicopter, in order to control the amount of visible ground texture. The objective was to maintain a constant altitude of 70 ft above ground level (AGL) with varying terrain elevation, thus the terrain effectively acted as a disturbance signal.

3) Scene: Total terrain dimensions were 4000×4000 m, subdivided into a flat run-in length of 850 m, followed by a slope of 60 m height at an angle of 30°, which transitioned into a flat run-out section, as depicted in Figure 8. All runs started at the same initial condition of 70 ft AGL with an initial forward speed of 30 kts, corresponding to about 0.7 eye-heights/s. In order to reduce predictability, three starting positions introduced variation in longitudinal and lateral directions. One run was done from each starting position for every experimental condition.

The terrain simulation aimed to achieve a relatively high level of visual fidelity as to give participants some sense of realism. The simulation was built and rendered through the Unity3D gaming engine. Perlin noise was added to the three straight terrain sections to obtain an irregular ground surface. The generated terrain noise was configured such to keep the hill climb intact while providing enough visible relief. Its average was corrected to zero and its standard deviation was set at 0.85 m. The ground was rendered using multiple high-resolution textures to prevent artefacts, and covered with grass. Trees of 40-70 ft high were sparingly added along the flight trajectories which helped to estimate altitude. Unity's built-in wind simulation was used to animate the grass and trees. Linear density fog was simulated with a visible distance of 80 m, corresponding to UCE 3. Helicopter sound was played aloud during runtime.

The augmented reality terrain grid was displayed on the dome projection. A colour augmented reality headset with 90° field of view was originally planned to be used, but was unfortunately unavailable at the time of the experiment. The synthetic terrain display was rendered by vertically projecting an orthogonal grid on the ground and by connecting the adjacent intersection points with green, transparent lines, as shown in Figure 9.

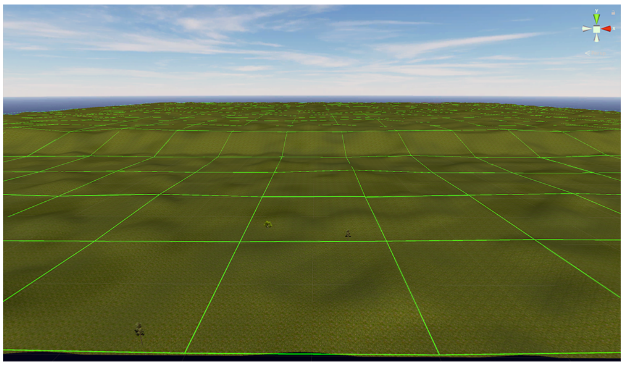

Fig. 9: Simulation scene overview including the augmented reality grid.

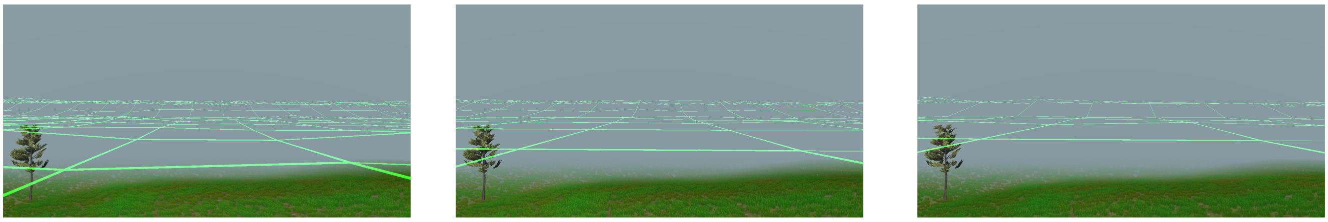

(a) S: 100 m (b) M: 150 m (c) L: 200 m

Fig. 10: The terrain display tested in the experiment for three different grid cell sizes. The terrain grid is superposed over the outside scene to simulate the augmented reality display.

C. Independent Variables

A 3 × 2 × 2 mixed design was used with terrain grid cell size at 100, 150 and 200 m (S, M and L, see Figure 9.) and helicopter dynamics with a heave damping coefficient Z_w of -0.56 s^{-1} (HD1) and -0.14 s^{-1} (HD2), both manipulated within-subjects. Piloting experience was a between-subjects factor (half the participants were novices, half were pilots). The within-subjects factors formed six experimental conditions, which were counterbalanced using the same Latin square design for both participant groups, as shown in Table I.

TABLE I: Experimental conditions with grid cell size (S, M and L) and heave dynamics (HD1 and HD2) for pilots and novices.

Subjects	**1**	**2**	**3**	**4**	**5**	**6**
N1 P1	S HD1	M HD1	L HD2	L HD1	M HD2	S HD2
N2 P2	M HD1	L HD1	S HD1	S HD2	L HD2	M HD2
N3 P3	L HD1	S HD2	M HD1	M HD2	S HD1	L HD2
N4 P4	S HD2	M HD2	L HD1	L HD2	M HD1	S HD1
N5 P5	M HD2	L HD2	S HD2	S HD1	L HD1	M HD1
N6 P6	L HD2	S HD1	M HD2	M HD1	S HD2	L HD1

D. Dependent Variables

Task performance was measured by the root-mean-square height error (RMSE) and fraction of runtime spent within performance boundaries around the desired flight path, e.g., desired and adequate within 25% and 50% of nominal height, respectively, or inadequate if over 50% of nominal height. Pilot control behaviour was measured by control activity (control signal variance), minimum time-to-contact to the slope and tau motion guide following (flight path angle gap γ_a, manoeuvre duration T and coupling constant k).

E. Procedures

The experiment consisted of two phases, training and measurement, combined taking a maximum of 3 h. During training participants got accustomed to the controls of both vehicle dynamics, the visual scene and the target altitude through three progressive training levels. The first level presented participants with maximum visual range and relatively simple ground height variation in the flight direction only. The second level additionally introduced ground height variation in the lateral direction and the same visual degradation as used in the measurement phase. During these first two levels, visual cues on the outermost edges of the visual field indicated whether participants were flying either within a 10% margin of the intended altitude, or above or below it. The peripheral cues provided the necessary information without obstructing the forward view. The third training level presented a more challenging terrain geometry and removed the peripheral height cues. This level pushed the participants' performance beyond the difficulty of the measurement runs, to ensure they were ready for the experiment. The synthetic terrain grid augmentation was not introduced during training to prevent pre-measurement adaptation to the terrain grid cell size factor. During training, the root mean square of the altitude error was tracked and reported to participants after each run to spur motivation. Each training level was practised until scores were approximately stable and with the same amount of runs for both vehicle dynamics.

During the measurement phase three runs were taken for each of the six experimental conditions to average out terrain geometry effects and to introduce some task variation. Throughout the three runs the starting position varied by 50 m longitudinally (obtaining effective run-in lengths of 850, 800 and 750 m, respectively) and laterally by 500 m (lateral starting positions of 1500, 2000 and 2500 m, respectively). Run order was unchanged between conditions and (groups of) participants. Runs ended once the longitudinal 1500 m mark was touched, between 90 and 100 s. 10-minute breaks were given after the training phase and after each pair of experimental conditions and micro-breaks could be taken between runs. Participants were informed of a new experimental condition being tested and of its vehicle dynamics (1 or 2), but not of the variations between runs of the same experimental condition.

F. Hypotheses

A smaller grid cell size enables perceiving a higher terrain resolution, it is therefore hypothesised that task performance will decrease with grid cell size, leading to a higher RMSE of the altitude error as well as higher fractions of runtime spent within the inadequate performance boundary. Clark's work has shown that minimum tau decreased as the visibility deteriorated and suggested that manoeuvre duration increases as well [13]. As an increasing grid cell size may lead to overestimaion of the distance to the slope, the minimum time-to-contact is expected to decrease. Manoeuvre duration is not expected to be affected by grid cell size. As less terrain detail is displayed, control activity is hypothesised to decrease and flight path angle gap is expected to increase with higher grid cell size. The coupling constant is expected to be unaffected by grid cell size in extension of the results of Clark's experiment, which showed no apparent effect of forward visibility on coupling constant [13].

A lower heave damping coefficient is analogous to having faster heave dynamics, e.g., a helicopter with a lower coefficient reacts quicker to collective control inputs along its heave axis. It is expected that slower heave dynamics leads to worse task performance, shown by an increase in mean RMS of the altitude error and an increased fraction of runtime spent outside of adequate performance boundary. Control activity is expected to decrease with rising heave damping in response to the filtering of higher frequency control inputs. The minimum time-to-contact is hypothesised to increase for HD2 compared to HD1 as pilots adapt to the slower vehicle response. The expectation is that slower heave dynamics with HD2 will lead to longer manoeuvre duration but will not impact flight path angle gap. The coupling constant is hypothesised not to be affected by the helicopter dynamics.

Piloting experience was assumed not to influence any of the dependent measures because of the simple dynamics and control task. Instead, this independent variable was included to verify that other results were not confounded by piloting skills.

IV. RESULTS

A. Tau analysis

For the tau analysis the start and end of the manoeuvre within the full run are selected by using the plots of control input, vertical position, flight path angle and flight path angle rate against time, as shown in Figures 11 to 14 respectively. The control input and vertical position signals indicate the approximate instant of climb initiation.

The start of the manoeuvre is the instant at which the pilot starts applying positive collective control input that sets the aircraft into a climb. At that moment the flight path angle rate crosses zero from negative to positive. The manoeuvre start is selected by means of the following criteria:

- Vertical flight position starts increasing with the intention of flying over the hill, as shown in Figure 12.
- Collective control input is positive and increasing, see Figure 11.
- Flight path angle is positive, as is the case in Figure 13.
- Flight path angle rate is positive after a zero-crossing, as in Figure 14.

The manoeuvre ends when the pilot has reached the target flight path angle. The moment of the last positive flight angle rate is automatically selected as the manoeuvre end. The manoeuvre time vector t_m is then calculated through Equation (10).

$$t_m = \{t_0 \leq t \leq t_f\} \tag{10}$$

with the starting instant of the tau manoeuvre t_0 and its end t_f, which are both used to calculate the manoeuvre duration T through:

$$T = t_f - t_0 \ , \tag{11}$$

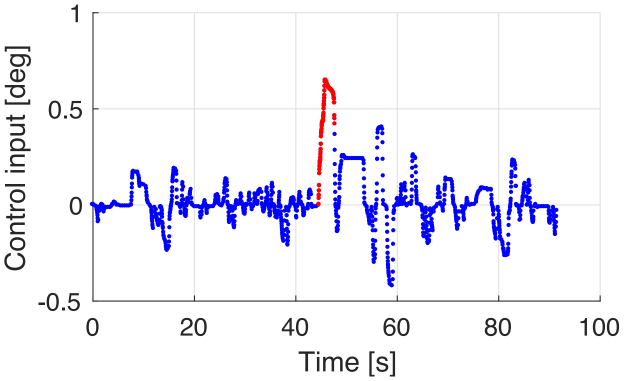

Fig. 11: Control input vs. time with selected manoeuvre

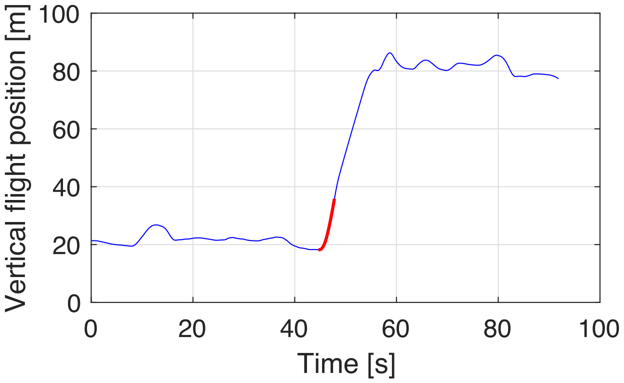

Fig. 12: Vertical position vs. time with selected manoeuvre

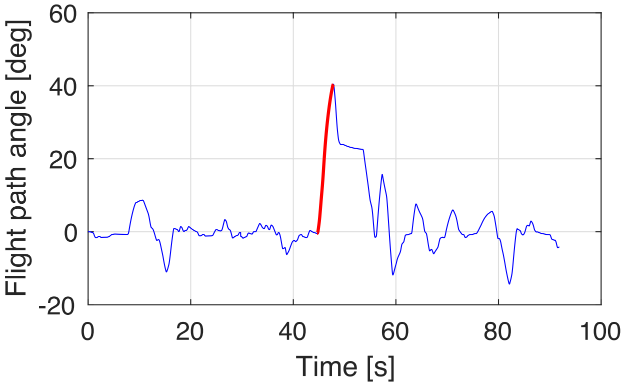

Fig. 13: Flight angle vs. time with selected manoeuvre

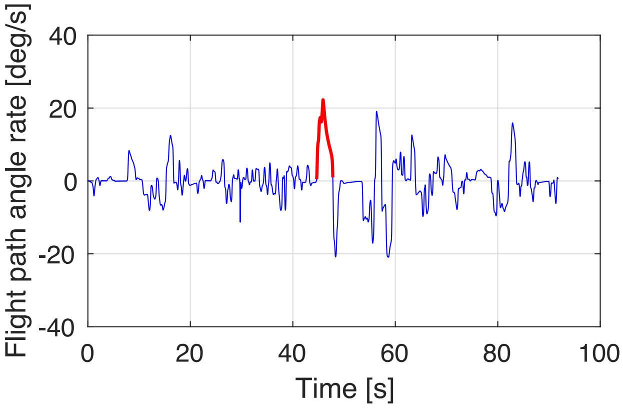

Fig. 14: Flight angle rate vs. time with selected manoeuvre

The instantaneous flight path error γ_a, also called gamma to go, is defined as the deviation from the goal flight path angle γ_f as:

$$\gamma_a = \gamma - \gamma_f \tag{12}$$

The angular motion gap γ_{gap} is calculated as the difference in flight path angle between the manoeuvre start and end:

$$\gamma_{\text{gap}} = \gamma_f - \gamma_0 \tag{13}$$

Everything is now set up for the actual tau analysis, which consists of finding a least-squares fit of the constant acceleration tau guide τ_g, linearly coupled by the coupling constant k, to the tau motion:

$$\tau_\gamma = k\ \tau_g\ , \quad 0 < k < 1 \tag{14}$$

From Equation (12) it is inferred that the instantaneous flight path error rate $\dot{\gamma}_a$ equals the flight path angle rate because γ_f is constant. The tau of the flight path angle error is calculated by:

$$\tau_\gamma = \frac{\gamma_a}{\dot{\gamma}_a} \tag{15}$$

The manoeuvre-scaled time vector $\bar{t}$ is set up by normalising the manoeuvre time vector t_m by means of the manoeuvre start t_0 and duration T as follows:

$$\bar{t} = \frac{t_m - t_0}{T} \tag{16}$$

The constant acceleration tau guide for the manoeuvre τ_g is calculated by:

$$\tau_g = -\frac{T}{2}\left(\frac{1}{\bar{t}} - \bar{t}\right) \tag{17}$$

Fitting the constant acceleration tau guide to the motion consists of selecting values of the linear coupling constant k and the number of data points used in the fit N_f for which the linear least-squares fit yields a sufficiently high coefficient of determination R^2. Figure 15 presents the flight path angle and its rate as functions of normalised manoeuvre time. As the flight path angle rate quantifies the variation of the motion variable the higher frequency content of the motion signal becomes more visible.

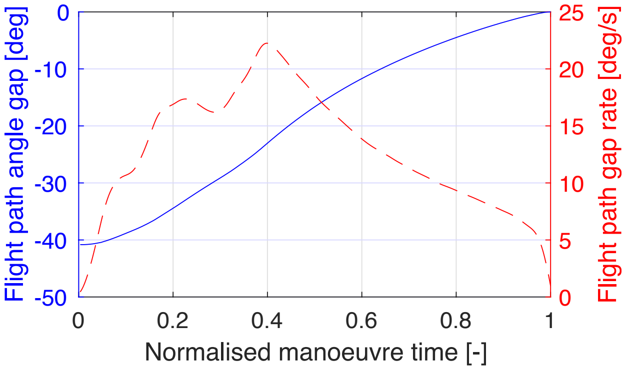

Fig. 15: Flight path angle and its rate vs. manoeuvre time

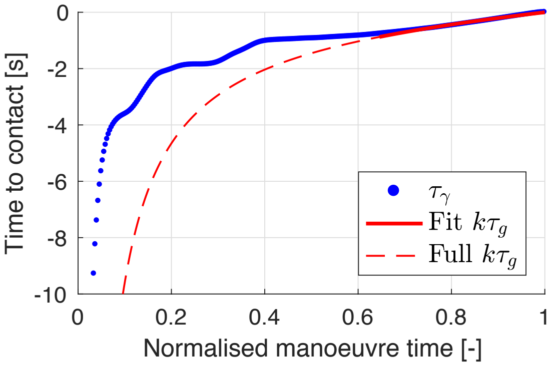

Fig. 16: time-to-contact and fitted guide vs. manoeuvre time

Applying Equation (15) yields tau, displayed as a function of normalised manoeuvre time in Figure 16 and as a function of the guide time-to-contact in Figure 17. The tau curve features the same high-variation signal content as the gamma rate. A decreasing tau differential is seen between adjacent data points on the graph towards the start of the manoeuvre, further extending to lower values of tau. This is due to the gamma rate tending to zero while the gamma gap is stable at its starting value.

Figure 18 displays the evolutions of R^2 and k as a function of N_f. This is the main plot used to determine the length of the recorded run the tau guide is fitted to. The coupling constant k and resulting R^2 are calculated for each fraction of the manoeuvre, moving back from the last two to all data points. Minimum satisfactory R^2 is set at 0.97 and k must be positive and inferior to 1.

Picking the manoeuvre length used in the fit is not as straightforward as selecting the maximum value of N_f that yields sufficient R^2. As data points with higher tau values at the start of the manoeuvre have a larger impact on R^2 then those at the end, R^2 meets the 0.97 threshold if (almost) all data points are included, i.e. $N_f = 314$ for the run shown in Figure 18. To summarise, the following criteria are used:

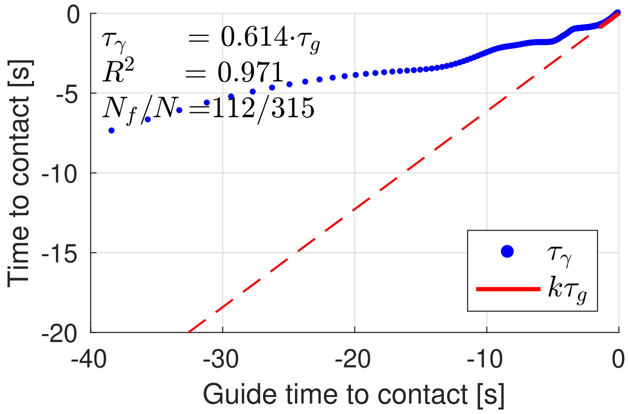

Fig. 17: time-to-contact vs. guide time-to-contact

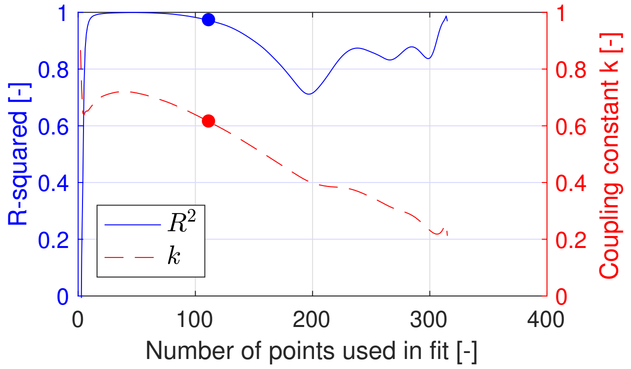

Fig. 18: Coefficient of determination and tau constant vs. number of points used in fit

- Coupling constant k from least-squares regression, not exceeding unity: $0 < k < 1$.
- Coefficient of determination $R^2 > 0.97$.
- Moving backwards from the end of the manoeuvre, N_f is selected as the last value before R^2 drops below its threshold.
- N_f values close to the maximum value that yield satisfactory R^2 are disregarded.

For the gamma gap, the manoeuvre duration and the coupling constant, the statistical analysis is applied to subsets of the data based on minimum subjective ratings. The results presented hereafter include all runs with minimum rating of 1. The ratings qualify the extent to which the fitted tau guide describes the last half of the manoeuvre on a scale of 0 to 5 with the following rating descriptions:

0) Does not meet fitting conditions
1) Barely describes last half of manoeuvre
2) Slightly good
3) Moderately good
4) Good
5) Very good

B. Statistical analysis

An example sideview of all three runs for a single experimental condition is displayed in Figure 19. Results were visually inspected by representing the run-averaged data in box plots. The sphericity assumption was tested using Mauchly's test for the grid cell size (Grid), as vehicle heave dynamics (Dynamics) had only two levels. Homogeneity of variance was tested using Levene's test and normality was graphically checked using Q-Q plots and numerically verified using a Shapiro-Wilk test.

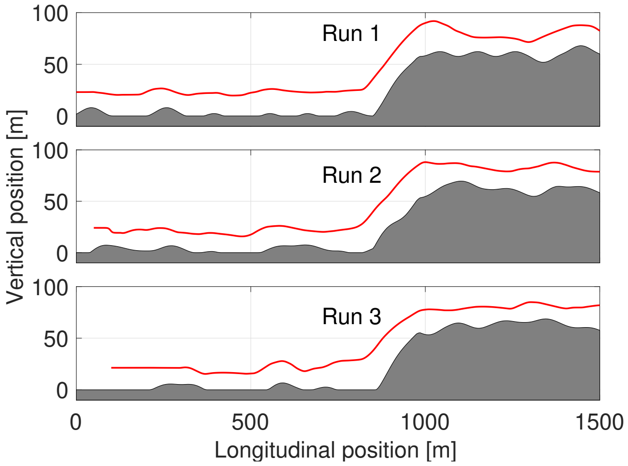

Fig. 19: Vertical position as a function of longitudinal psition for all three runs of a single experimental condition

A three-way repeated measures mixed-design Analysis of Variance (ANOVA) was performed with two within-subjects factors (Grid, Dynamics) and one within-subjects variable (Experience) to study whether Experience had an effect. If no significant effect of Experience was found, a two-way repeated measures ANOVA was done with the within-subjects factors Grid and Dynamics, thus increasing the sample size for each dataset.

The results show that Experience was not a significant factor for any tested variable. As hypothesised, mixed ANOVA did not reject the null hypothesis that Experience did not significantly affect any of the dependent variables, therefore a two-way repeated measures ANOVA was performed on the Experience-lumped data.

1) RMS of altitude error: An increase in grid cell size from S to L lead to higher RMSE, meaning worse task performance and confirming the hypothesis. Moreover, slower heave dynamics also decreased task performance in RMSE, opposing the hypothesis that pilots would adapt to the change in controlled element dynamics. The box plot for the Experience-lumped RMSE, shown in Figure 20, suggests that RMSE increases as Grid changes from small to medium and then to large. It also conveys that HD2 leads to higher RMSE than HD1. ANOVA showed main effects of Grid $F(2,22) = 5.64, p = .011$ and of Dynamics $F(1,11) = 12.22, p = .005$. Pairwise comparisons using the Bonferroni correction revealed that an increase in grid cell

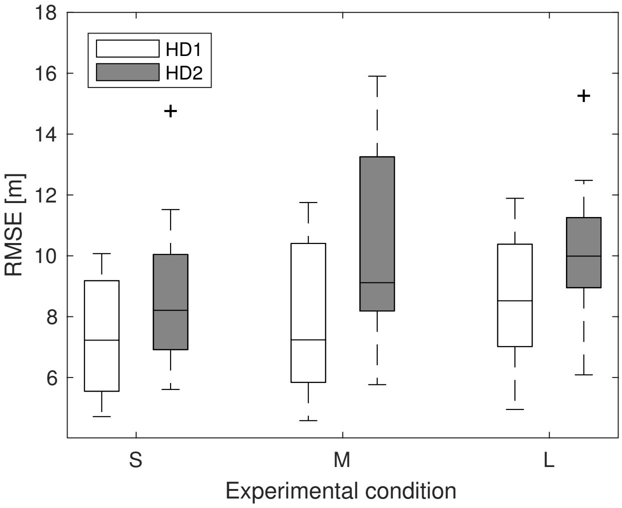

Fig. 20: Box plot of terrain error RMS

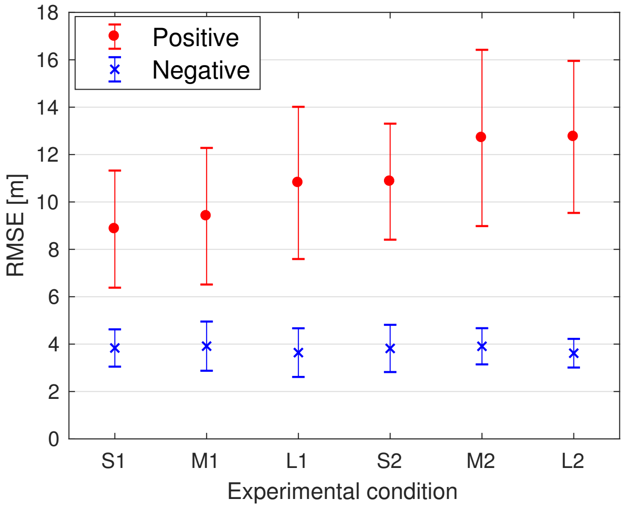

Fig. 21: Mean and standard deviation of the root mean square of positive and negative error.

size from small to medium elicited an insignificant increase in mean RMSE from $8.05(0.47)$ to $9.07(0.74)$ and an increase from medium to large increased mean RMSE to $9.34(0.62)$, also not statistically significant. However, a change from small to large Grid evoked a statistically significant increase in mean RMSE ($p = 0.011$). Switching Dynamics from HD1 to HD2 increased mean RMSE from $7.92(.59)$ to $9.73(.67)$. The Grid × Dynamics interaction turned out to have no significant effect on RMSE.

Positive and negative error contributions to the RMSE were determined to assess to which extent participants flew above or below the target signal. Figure 21 displays the mean and standard deviation (SD) of positive and negative error RMS for each condition. Mean and SD of the negative error RMS were significantly smaller than those of the positive error RMS across all conditions. Figure 22 shows the mean time fractions of the positive and negative error signals. Mean fraction of time spent below the target altitude varies between $3.3 - 7.6\%$.

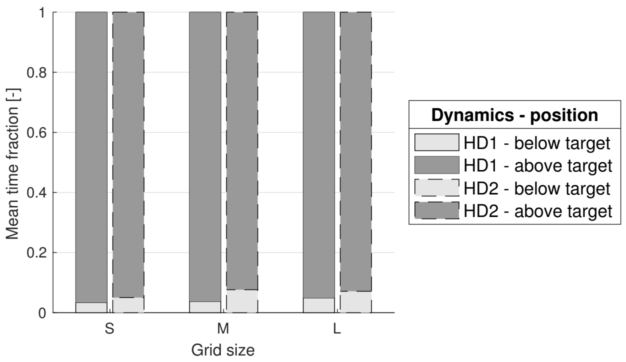

Fig. 22: Mean time fractions spent above and below target altitude.

2) Time fraction per performance boundary: Grid cell size did not affect the time fraction spent within performance zones, invalidating the hypothesis that it would increase T_{ina}. However, slower heave dynamics did negatively affect task performance measured by an increase in T_{ina}, disproving the hypothesis that pilots would adapt to changing vehicle dynamics to maintain consistent performance. Box plots of the Experience-lumped time fractions spent within desired, adequate and inadequate performance zones, shown in Figures 23 to 25, show no effect of Grid and only suggest that slower heave dynamics increased the relative amount of time spent in the inadequate region. ANOVA showed no main effect of Grid on either T_{des}, T_{adq} or T_{ina}. Dynamics had a main effect on T_{ina} only, $F(1, 11) = 6.665, p = .026$, with an increase in mean T_{ina} from $.122(.012)$ to $.173(.020)$ when switching from Dynamics 1 to 2. The Grid × Dynamics interaction effect was not not statistically significant. The participant-averaged, Experience-lumped time fractions spent within performance boundaries are represented by a barchart in Figure 26, summarizing the aforementioned effects.

3) Control activity: Control activity was significantly increased by a larger grid size, contrary to the hypothesis, yet the effect was only present between the medium and large grid cell size. Dynamics significantly lowered control activity, against the hypothesis as well. The box plot of the Experience-lumped ${\sigma_u}^2$, displayed in Figure 27, does not present a clear trend for the effect of Grid but does indicate that control activity increases with slower heave dynamics. ANOVA found a significant main effect of Grid on ${\sigma_u}^2$, $F(2, 22) = 4.737, p = .019$, with an insignificant decrease in mean ${\sigma_u}^2$ from $7.98 \times 10^{-3}(4.56 \times 10^{-3})$ for small to $7.11 \times 10^{-3}(3.86 \times 10^{-3})$ for medium, and a significant increase to a mean of $9.11 \times 10^{-3}(5.07 \times 10^{-3})$ for the large grid cell size ($p = .025$). A significant main effect of Dynamics on ${\sigma_u}^2$, $F(1, 11) = 30.062, p < .01$ was found too, with a decrease from $9.564 \times 10^{-3}(4.833 \times 10^{-3})$ for HD1 to $6.570 \times 10^{-3}(4.161 \times 10^{-3})$ for HD2. No statistically

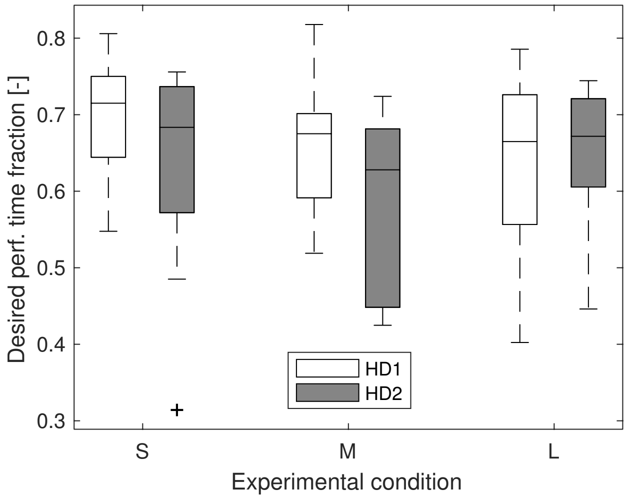

Fig. 23: Box plot of time fraction within desired performance boundary

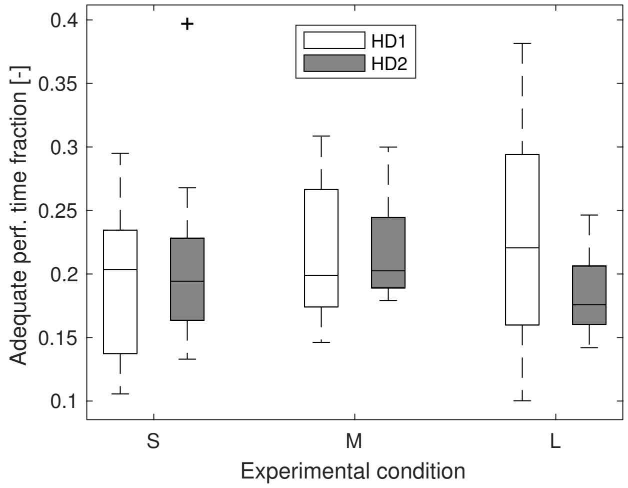

Fig. 24: Box plot of time fraction within adequate performance boundary

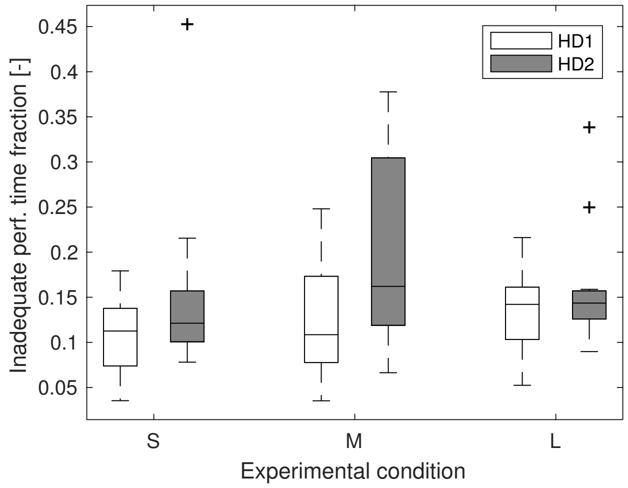

Fig. 25: Box plot of time fraction outside of adequate performance boundary

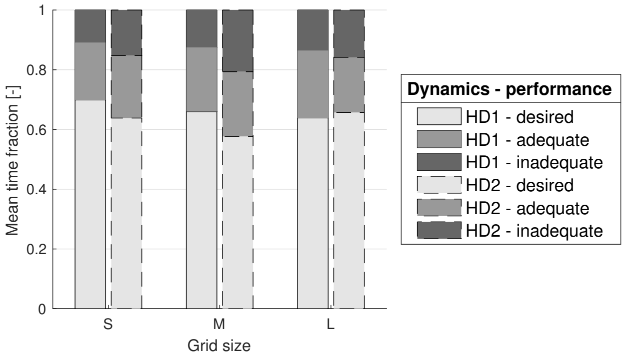

Fig. 26: Time fractions spent within performance boundaries.

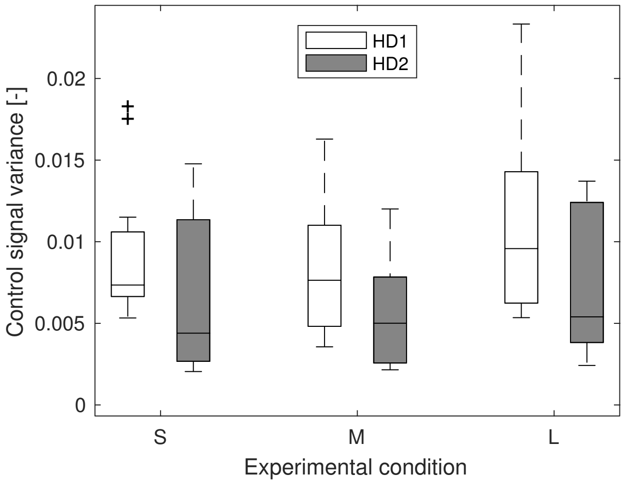

Fig. 27: Box plot of the control signal variance

significant interaction effect of Grid × Dynamics was found.

4) Minimum time-to-contact: Minimum time-to-contact was not affected by the grid cell size, though it had been hypothesised to decrease. As expected, an increase in heave damping raised the minimum time-to-contact. A box plot of the Experience-lumped τ_{min} is displayed in Figure 28, showing no discernible trend for Grid and an increase in τ_{min} for HD2. ANOVA indicated only a significant main effect of Dynamics on τ_{min} $F(1, 11) = 7.584, p = .019$, with an increase of mean τ_{min} from $6.026(.491)$ to $6.924(.521)$ when switching from HD1 to HD2. No statistically significant interaction effect of Grid × Dynamics was found.

5) Manoeuvre duration: As hypothesised, there was no effect of Grid on the duration of the tau manoeuvre. Dynamics did not have an effect either, against the expectation that manoeuvre duration would increase. The box plot of the Experience-lumped T, displayed in Figure 29, shows a lack of any apparent effect. ANOVA indicated no significant main effect of Grid or Dynamics, nor of their interaction of Grid × Dynamics.

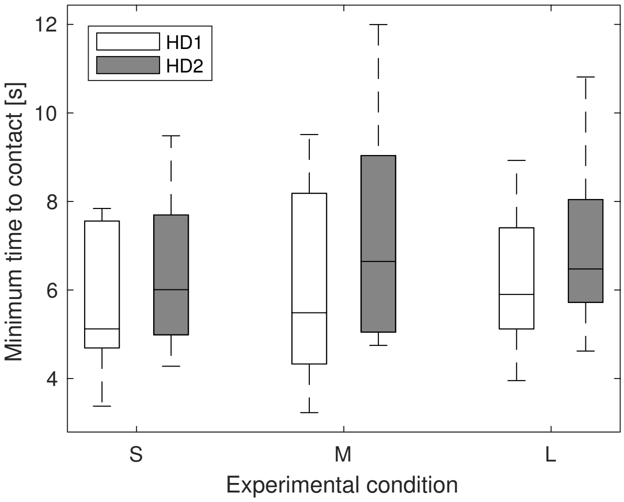

Fig. 28: Box plot of the minimum time-to-contact

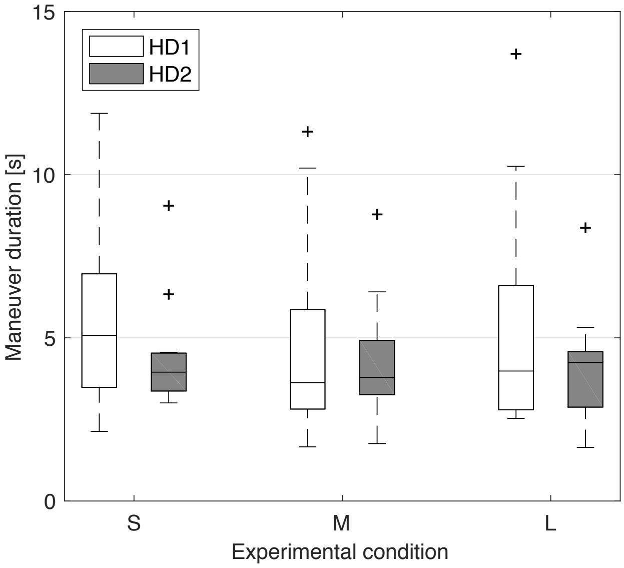

Fig. 29: Box plot of the manoeuvre duration

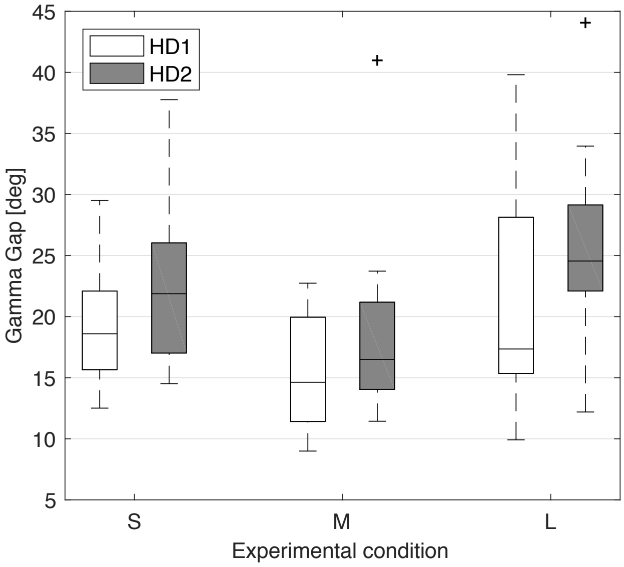

Fig. 30: Box plot of the gamma gap

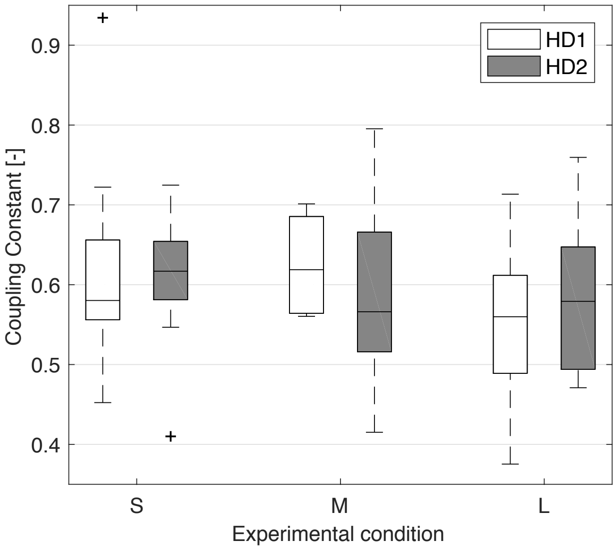

Fig. 31: Box plot of the coupling constant

6) Flight path angle gap: The hypothesis that the flight path angle gap would increase with an increase in grid cell size was partially confirmed. The hypothesis that Dynamics would have no effect is invalidated as γ_{gap} increased with the slower dynamics. The box plot of the Experience-lumped γ_{gap}, displayed in Figure 30, indicates that γ_{gap} goes down and then rises again as the grid cell size increases from small to medium to large. It also suggests that γ_{gap} is consistently higher for HD2 compared to HD1. ANOVA indicated a significant main effect of both Grid and Dynamics on γ_{gap}. An increase in Grid from small to medium elicited a statistically insignificant decrease in mean value from $20.82(5.75)$ deg to $17.19(6.50)$, whereas further enlarging to large significantly increased mean γ_{gap} to $23.33(8.29)$ deg ($p = .012$). Switching Dynamics from HD1 to HD2 showed a main effect by increasing mean γ_{gap} from $18.50(6.23)$ deg to $22.40(7.47)$ deg, $p = .006$. No interaction effect was found for Grid × Dynamics.

7) Coupling constant: Neither Grid nor Dynamics had an effect on the coupling constant, confirming the hypotheses. A box plot of the Experience-lumped k is displayed in Figure 31, showing no clear trend. ANOVA indicated neither a significant main effect of Dynamics or Grid on k, nor a significant interaction effect of Grid × Dynamics.

The statistical analysis has been repeated out by taking each rating between 1 to 5 as a minimum, omitting runs with a lower rating. No additional effects have been found by applying the statistical analysis to subsets of the data based on minimum ratings.

C. *Optical Analysis*

An optical variable analysis has been applied to the experiment scene, focusing on the effects of the terrain grid geometry on the splay and density angles and their rates in the experiment. To exclude potential pilot influences, point-mass simulations are done for each of the three starting positions in the experiment scene. During these simulations the nominal height of 70 ft above terrain is constantly maintained.

1) Total depression angle rate: As the terrain height in the experiment scene varies in the direction perpendicular to the direction of flight, the depression lines are slightly slanted. The grid height is therefore averaged between two laterally adjacent grid points to calculate the depression angle in the forward line of sight. The depression angle can then be calculated for each grid line perpendicular to the direction of flight by applying Equation (3).

As the AR terrain display has multiple grid lines, each visible at a certain depression angle varying across time, the combined depression angle rate cannot directly be expressed as a single value at each instant. The depression angle rate of each edge varies from naught when the edge is at the horizon to a maximum value when the edge is passing underneath the observer. If the depression angle rate of each edge visible in the forward field of view is summed, we get a total depression angle rate Δ as defined by Equation (18):

$$\Delta = \Sigma \begin{cases} \dot{\delta}, & \text{if } x_g \geq 0 \\ 0 & \text{if } x_g < 0. \end{cases} \tag{18}$$

Total depression angle rate for the first starting position across the three grid cell sizes is plotted against time in Figure 32. The passing of the lateral grid lines is displayed in the signal by the negative spikes. When the upcoming edge is relatively far away, total depression rate is near zero. Once the edge is approaching, the total depression angle rate decreases to a maximum negative value with an increasing rate. It quickly returns to about zero once the pilot has moved over the edge.

As the total number of edges increases as the grid cell size decreases, the total depression angle shows more peaks since the grid cell size is smaller. A smaller grid cell size will therefore provide more visual feedback, as confirmed by the total depression angle rate. Grid size does not have an effect on the absolute maximum depression angle rate, as witnessed by the coinciding edges of the small and large grid cells.

2) Splay rate: To calculate the splay angle in the experiment scene for the nominal height data, the average splay angle of the splay lines directly next to the pilot is determined through Equation (1). The splay rate is then computed by differentiating the splay angle against time.

Splay rate is plotted against time for starting position 1 for the different grid cell sizes in Figure 33. The time axis is broadly set around the moment of the climb. Comparing the effect of the different grid cell sizes, the splay rate appears to vary more when the grid size is smaller. In Figure 33 the small grid cell size shows the highest absolute splay ratios. To compare the magnitude of the splay rates between the grid cell sizes, splay rate ratios are shown in Figure 34. The plot does not seem to add additional insight.

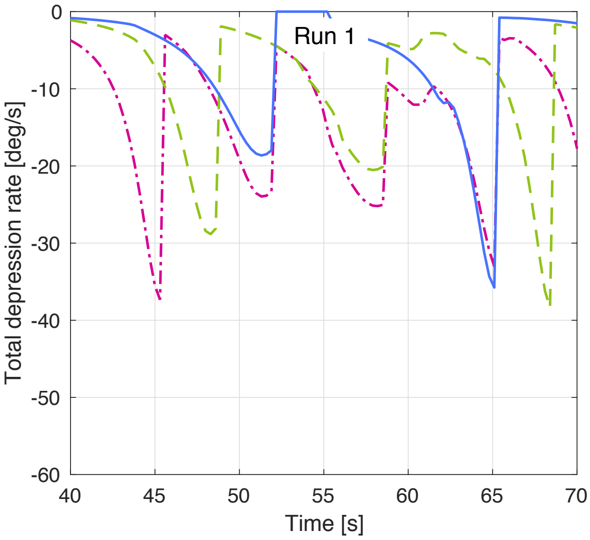

Fig. 32: Depression angle rate for nominal height across grid cell sizes for starting position 1

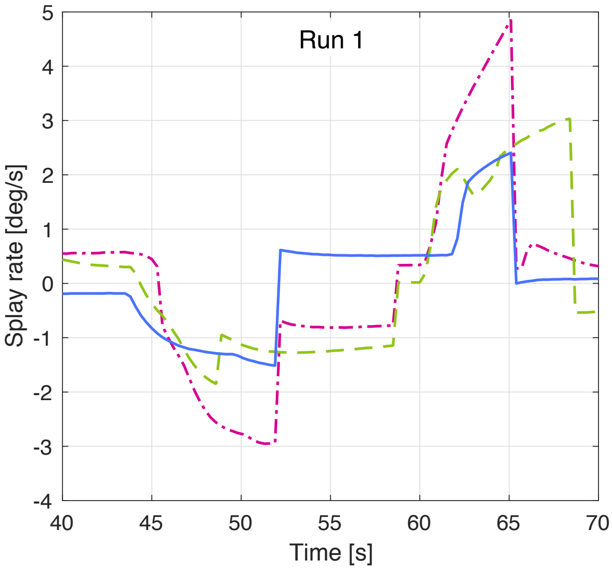

Fig. 33: Splay angle rate for nominal height across grid cell sizes for starting position 1

V. DISCUSSION

The results provide some insight on the implications of an AR terrain grid and the experiment design.

A. *Experience*

Following expectations, Experience did not affect any of the dependent variables, confirming that acquired piloting skills affected neither performance nor control behaviour. This suggests that the simplifications to the altitude control task

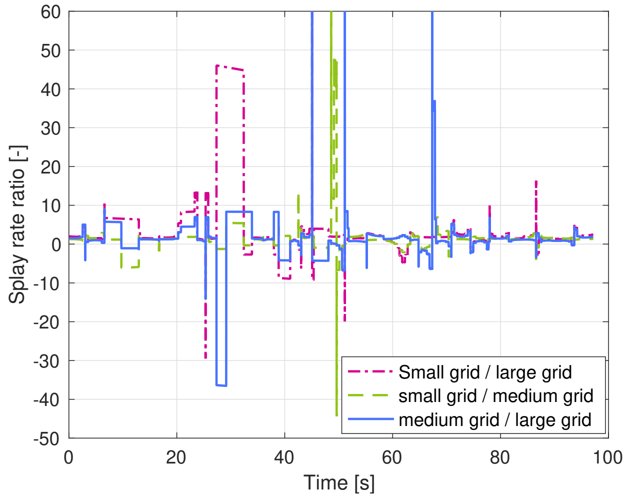

Fig. 34: Splay rate ratios comparing splay rates between the three grid cell sizes

were adequate for inclusion of participants of a lower skill level. Further, the pre-experiment training can be inferred to have provided sufficient familiarisation across varying experience levels. As Experience had no effect, the experiment could be reduced from a mixed design to a fully within-subjects design for Grid and Dynamics, doubling the group sample size for these factors. Based on this outcome it is recommended to assess the impact of Experience during preliminary testing for potential future experiments.

B. Grid cell size

The main outcome of this experiment is that an increase in grid cell size from small to large significantly decreased task performance measured in mean RMSE by 16%. This confirms the hypothesis that a larger grid cell size leads to a lower amount of perceivable detail in terrain geometry, in turn causing worse task performance in altitude control. Another outcome is the unexpected 28% increase in mean control activity for the large relative to the medium grid cell size. It suggests that pilots were controlling more actively because they had a higher degree of uncertainty due to less optical information. The large grid cell size also led to a 36% gain in mean flight path angle gap compared to the medium grid cell size, implying increasing the grid cell size incites pilots to close larger motion gaps.

The lack of significant differences in task performance and control behaviour between the small and medium grid cell sizes suggests that these sizes provided a similar perception of the terrain geometry. The decrease in task performance and the substantial increases in control activity and flight path angle gap for the larger grid cell size indicate adverse effects on terrain geometry perception. Each of the significant effects of Grid occurred between two levels: either between small and large or medium and large grid cell size. This suggests that the optic cues originating from the small and medium sizes grid cells were of similar quality for the pilots.

The absence of significant effects of Grid on the coupling constant is in agreement with previous findings [13], [24].

Point-mass simulations of the AR terrain grid in the experiment scene showed that a smaller grid cell size provides more visual feedback, but that grid cell size does not have an effect on the absolute maximum depression angle rate. Further, the splay rate has a higher amplitude when the grid size is smaller. The small grid cell size causes the highest absolute splay ratios.

C. Helicopter Dynamics

The performance effects of Dynamics were mostly in accordance with the expectations. Pilots had more difficulty controlling the altitude with slower heave dynamics in HD2 compared to HD1, as witnessed by a 23% increase in mean RMSE and a 42% rise in the mean relative time spent beyond the adequate performance boundary. The unexpected rise of 21% in mean γ_{gap} when switching from HD1 to HD2 reinforces that the slower heave dynamics were more difficult to control.

The results have substantiated the hypothesis that slower heave dynamics of the rotorcraft cause pilots to apply a more prospective control strategy. A 31% decrease in mean control activity was seen in HD2 compared to HD1 due to the damping of higher frequency inputs and a 15% increase in mean minimum time-to-contact to the slope to account for the slower pull-up.

D. Interaction of Grid with Dynamics

The results show that Grid and Dynamics have various effects on task performance and control behaviour, but that there is no interaction between the two factors. Not a single interaction effect of Grid × Dynamics was found, clearly answering the question whether grid cell size affects pilot behaviour differently for various heave dynamics: this is not the case. The lack of any interaction effect simplifies the design of an effective augmented reality terrain for altitude control since its grid cell size setting can be based on its main effects, independently from the rotorcraft heave dynamics.

E. Recommendations

The experiment setup was mainly built upon Clark's hill climb experiment, with the additions of a reduction in the complexity of the altitude control task, more realistic, irregular terrain and the simulated AR terrain display [13]. The simplification of the control task successfully prevented the potential influence of pilot experience on the results, but also means that the results cannot be assumed to be applicable to actual helicopter flight.

Another important limitation of the experiment was the simulation of the AR terrain display on the collimated dome projection. Negative side effects such as clutter and attentional tunneling related to head-worn displays could therefore not be considered. Subjects could focus their gaze both on the outside terrain visual as well as on the grid. The impact of this factor is arguably minor due to the extreme fog thickness.

The tau analysis led to a few insights. Both the manoeuvre duration and coupling constant were not affected by Grid or Dynamics. The lack of an effect in these parameters underline the difficulty in applying the tau analysis to realistic flight scenarios. The methodology of the tau analysis on experimental data is likely to benefit from improvements. First, it seems that the analysis can more easily be applied in strictly controlled conditions. For instance, the combination of the run-in length with irregular terrain before contact with the hill led to different starting conditions. Moreover, the analysis was indeed influenced by the manual work required to apply it. Applying a subjective rating to select the best fits over a large amount of runs did not prove fruitful either.

The effect of an AR terrain display with irregular terrain with variation in local height versus a flat one remains unclear. This could be further investigated by using the terrain geometry itself as an independent variable, rather than the geometry of the AR display. As the results between the small and medium grid cell sizes were statistically insignificant, this may be improved by testing sizes with larger differences. Finally, this study would greatly benefit from the addition of a baseline condition without any visual augmentation to see through the fog.

VI. CONCLUSION

The aim of this study was to research the effects of the grid cell size in an AR terrain display on task performance and control behaviour in a helicopter altitude control task with degraded visibility, and the potential impact of the controlled vehicle dynamics. Following a simulator experiment, analysis and discussion of the results several conclusions can be made.

First, a larger grid cell size negatively affects task performance and increases control activity, likely due to a worsened perception of the terrain geometry with the decrease in optic cues. This was further confirmed by an increase in the flight path angle gap when pilots had to pull up to climb over a hill. However, varying the vehicle dynamics by means of the heave damping coefficient had no interaction effect with the variation in grid cell size, meaning that this factor can likely be disregarded when designing an effective AR terrain display for altitude control.

It was recommended to investigate the effects of various terrain geometries, to test larger differences in grid cell size and to compare the effect of the AR terrain display with a baseline condition without visual aid.

REFERENCES

[1] S. Liewer, “Desert landings rattle pilots’ nerves,” *Stars and Stripes*, April 2003.

[2] L. Sabbagh, ““flying blind in iraq: U.S. Helicopters Navigate Real Desert Storms,” *Popular Mechanics*, October 2006.

[3] J. Vreeken, H. Haverdings, and M. Joosse, “Helicopter Flight in a Degraded Visual Environment,” Report NLR-CR-2013-229, National Aerospace Laboratory NLR, May 2013 2013.

[4] S. J. Gaydos, M. J. Harrigan, and A. J. R. Bushby, “Ten years of spatial disorientation in U.S. Army rotary-wing operations,” *Aviation Space and Environmental Medicine*, vol. 83, no. 8, pp. 739–745, 2012.

[5] K. Funabiki, H. Tsuda, T. Iijima, T. Nojima, K. Tawada, and T. Yoshida, “Flight experiment of pilot display for search-and-rescue helicopter,” vol. 7326, May 2009.

[6] T. Münsterer, T. Schafhitzel, M. Strobel, P. Völschow, S. Klasen, and F. Eisenkeil, “Sensor-enhanced 3D conformal cueing for safe and reliable HC operation in DVE in all flight phases,” vol. 9087, p. 90870I, 2014.

[7] P. Völschow, T. Münsterer, M. Strobel, and M. Kuhn, “Display of real-time 3d sensor data in a dve system,” in *Degraded Visual Environments: Enhanced, Synthetic, and External Vision Solutions*, vol. 9839 of *Proc. SPIE*, 2016.

[8] F. Viertler and M. Hajek, “Evaluation of visual augmentation methods for rotorcraft pilots in degraded visual environments,” *Journal of the American Helicopter Society*, vol. 62, pp. 1–11, 2017.

[9] Z. Szoboszlay, A. Kahana, and M. Rottem-Hovev, “Terrain and obstacle avoidance displays for low-level helicopter operations in degraded visual environments,” 2016.

[10] C. D. Wickens and J. Long, “Object versus space-based models of visual attention: Implications for the design of head-up displays,” *Journal of Experimental Psychology: Applied*, vol. 1, pp. 179–193, 1995.

[11] P. Knabl, *Towards reducing pilot workload during helicopter flight in degraded visual environment: An evaluation of helmet-mounted display symbology with special regard to attention allocation*. Thesis, TU Braunschweig, 2015.

[12] S. Schmerwitz, T. Lueken, H.-U. Doehler, N. Peinecke, J. M. Ernst, and D. L. da Silva Rosa, “Conformal displays: human factor analysis of innovative landing aids,” *Opt. Eng.*, vol. 56, 2017. doi: 10.1117/1.OE.56.5.051407.

[13] G. A. Clark, *Helicopter handling qualities in degraded visual environments*. PhD thesis, University of Liverpool, 2007.

[14] J. M. Flach, R. J. Jagacinski, M. R. Smith, and B. P. McKenna, “Coupling perception, action, intention and value: A control theoretic approach to driving performance,” in *Handbook of Driving Simulation for Engineering, Medicine and Psychology* (D. Fisher, M. Rizzo, J. Caird, and J. Lee, eds.), 2011.

[15] J. M. Flach, R. Warren, S. A. Garness, L. Kelly, and T. Stanard, “Perception and control of altitude: Splay and depression angles,” *Journal of Experimental Psychology: Human Perception and Performance*, vol. 23, p. 1764, 1997.

[16] C. D. Wickens and J. G. Hollands, *Engineering psychology and human performance*. Upper Saddle River, NJ: Prentice Hall, 2000.

[17] B. Corwin, R. Whillock, and J. Groat, “Synthetic terrain imagery for helmet-mounted display,” Tech. Rep. WL-TR-95-3025, Flight Dynamics Directorate, 1994.

[18] J. J. Gibson, “The perception of the visual world,” 1950.

[19] D. N. Lee, “A theory of visual control of braking based on information about time-to-collision,” *Perception*, vol. 5, pp. 437–459, 1976.

[20] D. N. Lee, M. N. Davies, and P. R. Green, “Visual control of velocity of approach by pigeons when landing,” *Journal of experimental biology*, vol. 180, pp. 85–104, 1993.

[21] D. N. Lee, J. A. Simmons, P. A. Saillant, and F. Bouffard, “Steering by echolocation: a paradigm of ecological acoustics,” *Journal of Comparative Physiology A*, vol. 176, pp. 347–354, 1995.

[22] A. L. van der Meer, F. R. van der Weel, and D. N. Lee, “Prospective control in catching by infants,” *Perception*, vol. 23, pp. 287–302, 1994.

[23] B. J. Baskett, “Aeronautical Design Standard performance specification Handling Qualities requirements for military rotorcraft,” Tech. Rep. No. ADS-33E-PRF, U.S. Army Aviation and Missile Command, 2000.

[24] G. D. Padfield and A. Taghizad, “How long do pilots look forward?,” in *31st European Rotorcraft Forum, Florence, Italy*, 2005.

II

Preliminary report

Graded in AE4020

2

Visual Cues and Avoidance Manoeuvres

Flying a helicopter in the near-Earth environment requires pilots to accurately perceive the external surroundings and to divert the flight trajectory towards one that clears terrain and obstacles. Three modes of low flight can be distinguished, as shown in Figure 2.1. In low-level flight, a direct heading towards the destination is flown while the height above ground level (AGL) clears the highest observable obstacle. Contour flight differs from low level flight in its AGL. The terrain contour is followed while clearing local obstacles. In NOE flight obstacles and terrain are used as a cover from enemy detection. The pilot flies as low as possible among obstacles, dynamically diverting the heading.

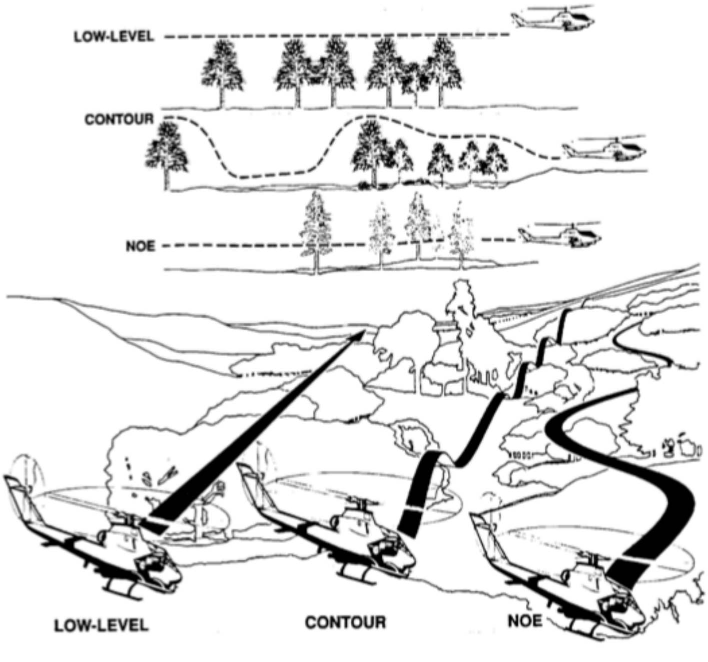

Figure 2.1 – Illustration of the three modes of near Earth flight (Source: [13]).

This chapter will lay the groundwork for the remainder of the literature study. It aims to form an understanding of the key factors involved in helicopter flight near the ground. Through an in-depth review of literature an answer to the following question will be answered: *How do helicopter pilots avoid obstacles and terrain while flying low?* First the visual cues will be introduced in Section 2.1. The effects of the visual degradation of these cues are then discussed in Section 2.2. Then the manoeuvres that pilots use to avoid obstacles are described in Section 2.3.

2.1. Visual Cues

This section will give an overview of a variety of optical cues that pilots can use to perceive ego-motion in low helicopter flight. Throughout several decades of research a significant body of knowledge has established the usage of optical variables in the optical flow-field, such as compression, splay and edge rate, in addition to optical flow and global optical flow, differential motion parallax and, finally, time to contact (TTC or τ). This section will introduce these variables and their role in the perception of ego-motion while flying low over terrain.

2.1.1. Compression, Splay & Edge Rate

Textural gradients can be used for navigation through a three-dimensional environment. The angle between lines defining the textural gradients, referred to as *optical depression* and *optical splay* respectfully, inform observers of their position with respect to these terrain features as illustrated in Figure 2.3 [14].

Optical Splay The optical splay angle is an optical invariant when moving forward with constant speed. Individual points along an edge parallel to the direction of motion move along a line that is inclined with respect to any reference line on the ground perpendicular to the horizon in the direction of motion [15]. The angle at the vanishing point between the reference line and the direction of motion is defined as the optical splay angle, calculated as in Equation (G.3):

$$S = tan^{-1} \frac{Y_g}{z} \tag{2.1}$$

Where S is the splay angle, y_g is the lateral displacement from the ground track and glsz the altitude of the observer. This is illustrated in Figure 2.2a.

The rate of change in splay angle with changing observer position can be calculated as in Equation (2.2).

$$\dot{S} = -\frac{\dot{z}}{z} cosSsinS + \frac{\dot{Y}_g}{z} cos^2 S \tag{2.2}$$

In the case of symmetric forward flight, the rate of change in lateral position is zero and the second term in Equation (2.2) cancels out. We are left with the first term, which shows that changes in splay angle depend on the initial altitude since they are scaled by z. Moreover, increasing altitude leads to a decrease in splay angle and vice versa.

Optical Depression Optical depression is another optical cue an observer can use to detect changes in altitude. Any edge perpendicular to the direction of motion has an angular position with respect to the horizon as viewed by the observer, the optical depression angle [15]. By convention, this angle is calculated with respect to the observer taking the distance on the

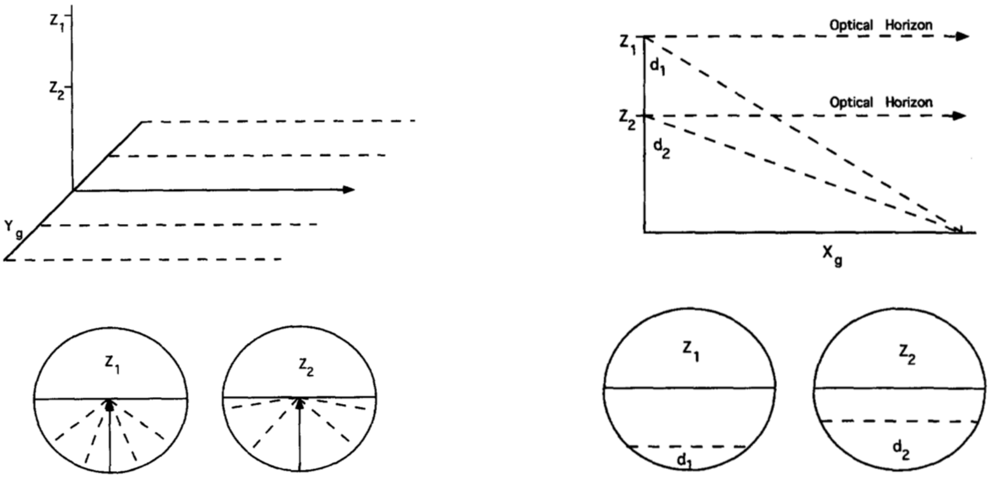

(a) Splay **(b)** Despression

Figure 2.2 – Illustration of optical splay (**a**) and compression (**b**) (Source: [15]).

ground to the edge feature in the forward visual field and by scaling this distance by the height of the observer, as in Equation (G.1):

$$\delta = tan^{-1}\frac{x_g}{z}\square \tag{2.3}$$

With δ the depression angle, x_g the longitudinal distance on the ground to the texture element and z the altitude. Figure 2.2b illustrates the angular depression.

For rectilinear forward motion the rate of change in depression can be calculated through Equation (2.4):

$$\dot{\delta} = -\frac{\dot{z}}{z}\square\, cos\delta sin\delta + \frac{\dot{x}_g}{z}\square\, cos^2\delta \tag{2.4}$$

Similar to splay, the rate of change in depression angle depends on the eye-height scaled altitude and on on the initial optical position of a texture element. Texture elements that are low in the field of view will have a greater depression angle rate for constant forward speed.

Edge Rate According to Wickens and Hollands, the total amount of discontinuities that crosses the observer's visual field per unit time defines the edge rate [14]. Trees are an example of vertical discontinuities that flow past when navigating through a natural environment. An estimate of the distance between discontinuities may help to determine one's moving speed. The texture density of the environment impacts the speed determination through through edge rate. An increase in distance between texture elements decreases the perceived speed. Similarly with more closely spaced texture elements the perceived speed through edge rate increases.

2.1.2. Optical Flow

In 1950 Gibson published a cornerstone theory on the perception of motion [16]. His famous theory on optical flow advanced how an observer uses motion patterns of the outside environment to determine its displacement in the world. The examples described by Gibson often include

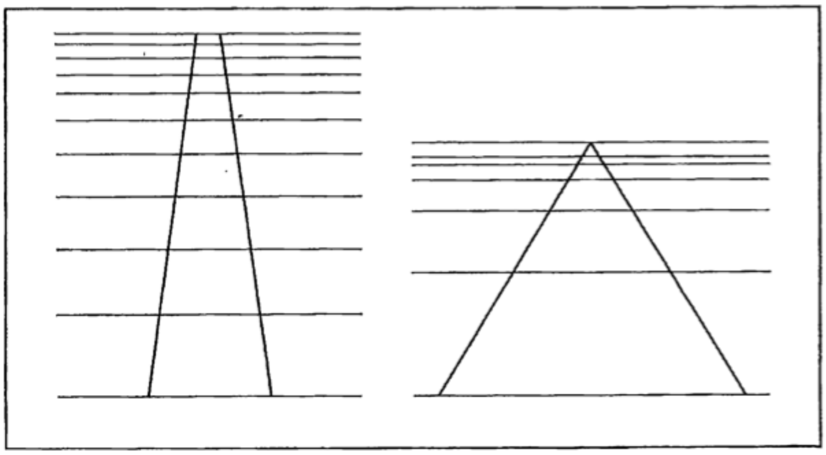

Figure 2.3 – Visual cues of compression and splay represented by straight lines. Note that increased compression and decreased splay angle give the impression of large height above terrain (left) whereas lower compression and increased splay angle are perceived as a low altitude (right). (Source: [14])

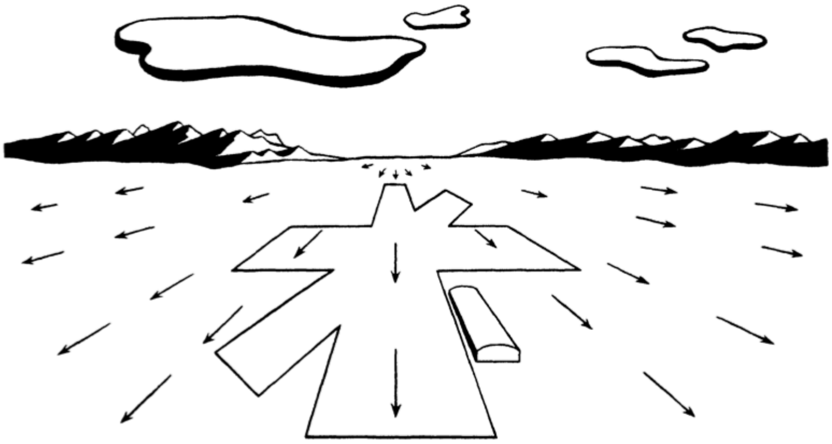

Figure 2.4 – The optical flow of motion over flat terrain (Source: [16])

aircraft flying through an environment. Figure 2.4 is one of these examples and neatly illustrates the case of an observer looking forward while steadily moving forward over a flat surface. The optical flow pattern radiates outward from the center of optical expansion, toward which the aircraft is moving. The magnitude of the optical flow vector is zero at the horizon, increases visually downward and attains its maximum directly beneath the aircraft.

When the aircraft accelerates, climbs or turns the optical flow changes. This allows the pilot to perceive and control the current and prospective state in terms of the direction and velocity of motion. Similarly, the optical flow varies with changes in surface shape as well as with the appearance of obstacles. The perception of the optical flow patterns enables pilots to navigate through their environment.

Global Optical Flow Global optical flow is the total rate of optical flow past the observer's visual field. It can be used by the pilot to determine the ground speed. Experiments by Johnson et al. let test subjects control the forward ground speed of an aircraft under tailwind disturbance [17]. Participants were presented with a simulated forward view of a flat terrain with a grid

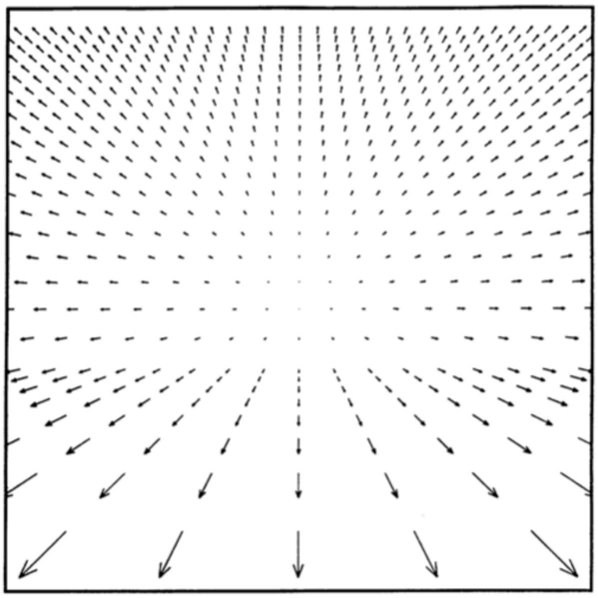

Figure 2.5 – Optical flow while approaching slanted surface (Source: [19]).

texture and a joystick to control a first-order airspeed controller in order to maintain constant ground speed. Optical flow rate and edge rate were manipulated throughout runs. The results showed that both edge rate as well as optical flow rate could be successfully used to main perceive and control ground speed.

A study by Warren, Morrish and Kalish has shown the usage of optical flow rate for determining heading changes [18]. The authors examined heading judgements of participants that were presented with translational visual cues parallel, perpendicular and at oblique angles to a random-dot plane. Observer speed and dot density of the random-dot plane were varied. Observers were asked to discriminate between changes in heading. It was found that the accuracy of heading estimation improved by an order of magnitude when the optical flow rate was presented.

Surface Slant Optical flow rate is also used as a cue for estimating surface slant. A paper by Perrone, however, draws attention towards the difficulties of perceiving a slanted terrain in front of an aircraft [19] using the optical flow rate. His analysis uses Equation (2.7) to show that the increasing height of points on a slanted terrain leads to a lowered angular velocity over a great portion of the visual field. This effect is illustrated in Figure 2.5. The small differences in angular velocity make detection of the surface layout quite difficult for observers. Fortunately, most terrains are not perfectly flat and other cues such as stereoscopic depth and texture are used as well.

Differential Motion Parallax According to Gibson's theory of optical flow, ego-motion is determined from the perception of radial patterns of optical flow that flow around the observer's fixation point. As eye movements confound the flow patterns, observers need to be capable of discriminating the direction in which they are moving from the direction in which they are looking. Otherwise, optical flow theory would not hold. In 1988, Warren and Hannon confirmed Gibson's theory that perception of self-motion while moving one's gaze is indeed possible from the optical flow patterns [20]. In a pair of experiments the researchers presented observers with generated optical flow patterns that simulated optical flow with and without eye movement.

The participants were asked to keep stationary eye fixation or to follow a moving target for half of the cases. The results showed that observers were able to accurately determine the direction in which they were moving independent of both real and simulated eye movement.

However, a mismatch between performance in simulated and real eye movement was found when observers were looking perpendicular to their direction of motion in a three-dimensional simulation. The simulated eye movement condition introduced a center of radial outflow in the plane of eye fixation, leading observers to believe they were moving towards that plane. On the contrary, using pursuit eye-movements the heading could successfully be determined, indicating the necessary use of differential motion between objects at different depths. This cue is known as differential motion parallax. The optical flow around a moving point of fixation is observed as a curling pattern around this point and can effectively be used to determine the direction of self-motion. This conclusion was confirmed in a a computational analysis as well [21].

2.1.3. Time-to-Contact

The application of optical flow theory to helicopter flight follows from several important developments of Gibson's work. First, in 1976 Lee proposed an analytical form of Gibson's theory, known as General Tau Theory, that explains the relation between perceptual information and control coordination [22]. According to Lee a controller estimates the TTC, or τ, to the intended target to determine when to apply control input. In the case of a flying helicopter decelerating in front of a tree, the TTC is defined by the ratio of the distance to the tree and the closing velocity as shown in the left hand side of Equation (2.5).

Essentially all pilot manoeuvres can be considered to be guided by τ. Pilots close gaps when moving from a current hovering position to an adjacent, desired one and when coupling an obstacle-bound trajectory onto one that safely evades the obstacle. The judgement of when to apply the control inputs to couple the current state onto a prospective one follows from the observation of the current displacement rate and the remaining distance. However, humans have been shown to inaccurately perceive monocular and binocular distance [23], as well as changes in their own velocity from the optical flow [24]. Therefore, rather than explicitly estimating distances and velocities, observers measure angles and angular rates in the optical flow to determine the TTC as shown in Equation (2.5). θ designates the optical flow angle and x designates the distance to an observed point on the ground.

$$\tau = \frac{x}{\dot{x}} = \frac{\theta}{\dot{\theta}} \tag{2.5}$$

Lee proposed the concept of action-scaling the TTC in 1980 [25]. It was posited that organisms that use sensors to control musculatory actions interpret the gap that they are trying to close according to the reach of the action. The application of this principle to helicopter flights is measuring the height above terrain z in eye-heights (eh). The concept of eye-height means that a pilot flying 50 kts at 30 ft experiences the same optical flow as a person that is jogging. The eye-height velocity $\dot{x}_e$ is then simply the forward velocity $\dot{x}$ scaled to the eye-height of the observer z according to Equation (2.6) and as illustrated in Figure 2.6.

$$\dot{x}_e = \frac{\dot{x}}{z} \tag{2.6}$$

Equation (2.6) shows that a change in flight velocity or in height results in a change in the perceived eye-height velocity. For instance, if z increases the perceived velocity decreases

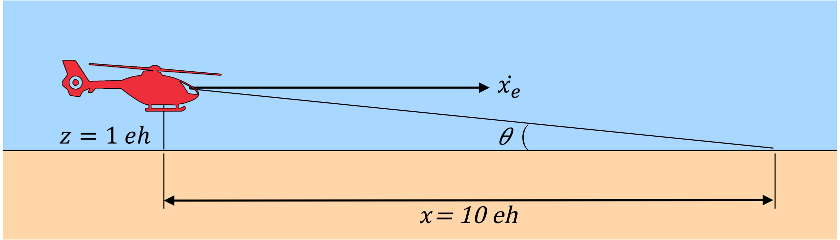

Figure 2.6 – Eye-height velocity while flying over flat terrain.

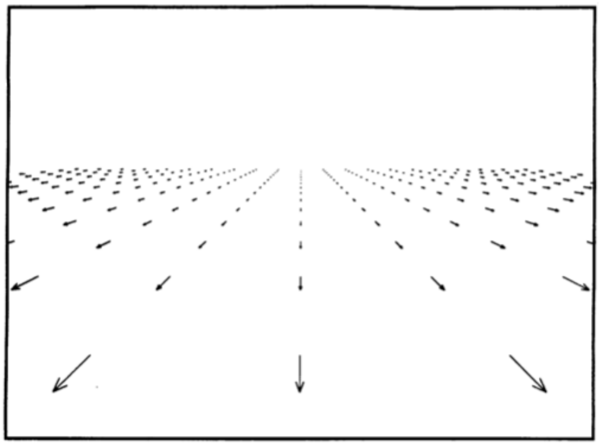

Figure 2.7 – Optical flow while flying over flat terrain (Source: [19])

and a decrease in z leads to an increase in perceived velocity. Figure 2.7 illustrates a theoretical flow field when flying at 3 eh/s above flat terrain. The motion field is displayed with a shutter time of 0.25 s while the vectors on the square grid are spaced 1 eye-height apart. This figure clearly shows how the velocity vectors quickly decrease in length in the distance. It turns out that the angular velocity in the median plane $\frac{d\theta}{dt}$ of a point at a distance x from the pilot falls off as the square of the distance from the observer as shown by Equation (2.7):

$$\frac{d\theta}{dt} = -\frac{dx}{dt}\frac{z}{x^2 + z^2} \tag{2.7}$$

According to Perrone [19], the threshold of velocity perception in practical applications is about 40 min.arc/s. Substituting in Equation (2.7), it appears that visual information further than 15-16 eye-heights away is not perceived. Similarly, flying at 3 eh/s would result in a look-ahead time of 5 seconds.

2.2. Usable Cue Environment

Helicopter pilots heavily depend on the visual cues described in Section 2.1 for stabilisation, guidance and navigation. However, throughout various terrain surfaces and weather conditions their clarity and reliability may decline. On the one hand particles such as dust, sand, water or snow are thrown into the air by the rotor downwash. On the other hand weather and lighting conditions such as night-time darkness or daytime solar flare may (partially) hinder visual perception.

Pilots should be able to perform the primary flight tasks of stabilisation (e.g. maintaining desired attitude) and guidance (e.g. controlling translational movement) while adversely affected

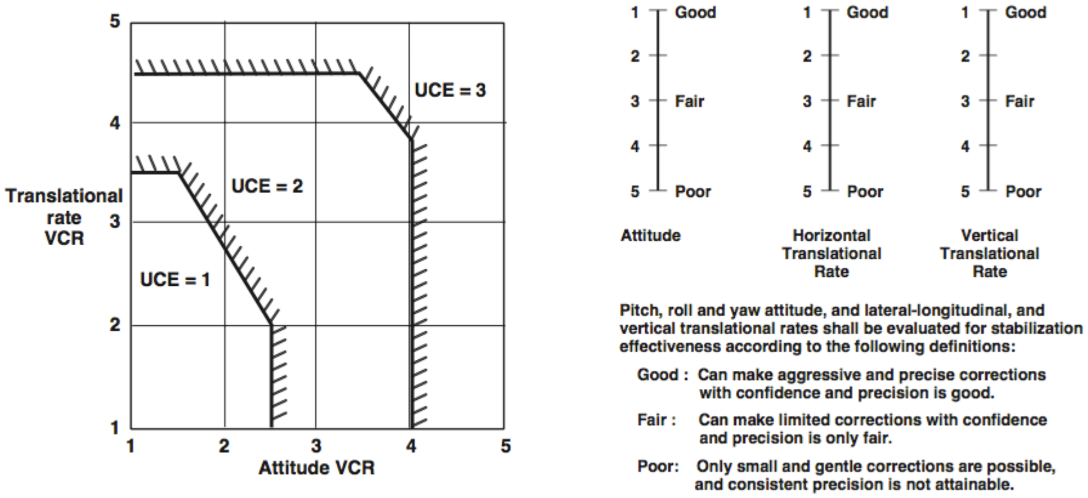

Pitch, roll and yaw attitude, and lateral-longitudinal, and vertical translational rates shall be evaluated for stabilization effectiveness according to the following definitions:

Good : Can make aggressive and precise corrections with confidence and precision is good.

Fair : Can make limited corrections with confidence and precision is only fair.

Poor: Only small and gentle corrections are possible, and consistent precision is not attainable.

(a) Usable Cue Environment chart

(b) Visual Cue Rating scales with cue descriptors

Figure 2.8 – Usable Cue Environment chart (**a**) including descriptions for each of the Visual Cue Ratings (**b**) (Source: [26]).

by the degradation of visual cues. Aeronautical Design Standard 33 (ADS-33) includes rating criteria for designing both the stability and control systems in addition to the display augmentation required to fly a rotorcraft in DVE [26]. Figure 2.8 shows the Usable Cue Environment (UCE) chart to match the visual cue rating (VCR) scores to the corresponding UCE levels. As stabilisation is prioritised over guidance, higher levels of translational rate VCR are tolerated before bumping up the UCE level.

ADS-33 requires a helicopter to respond with rate commands at each level. As visual cues deteriorate with higher levels, more automation is required to maintain adequate handling qualities. This is shown in Section 2.2. Moreover, a helicopter designed to provide rate command response in UCE1 will likely have level 2 handling qualities in UCE2 and level 2 handling qualities in UCE3. However, if the degraded outside visual cues can be sufficiently restored through display augmentation, the need for complex control automation is discharged. Display augmentation systems are in general more easily installed or retrofitted on a variety of aircraft types. By contrast, control augmentation systems are specifically tailored to the dynamics of the specific aircraft type.

Table 2.1 – System responses required for Level 1 handling qualities at all UCE levels (Source: [27]).

UCE	Required response types in hover/low speed flight
UCE 3	TRC + RCDH + RCHH + PH
UCE 2	ACAH + RCDH + RCHH + PH
UCE 1	RC

Response types

RC	rate command
TC	turn coordination (applies to yaw and pitch)
ACAH	attitude command, attitude hold (roll and pitch)
RCDH	rate command, direction hold (yaw)
RCHH	rate command, height hold (heave)
PH	position hold (horizontal plane)
TRC	translational rate command

2.3. Avoidance Manoeuvres

Let's consider the case of a helicopter that has been trimmed to fly with constant forward airspeed at a fixed height above terrain in good visual environment (GVE). A tree appears directly in the flight path, as shown in Figure 2.9a. In this case the pilot can decide to do one of three manoeuvres as depicted in Figure 2.9b: decelerate to a hover (quick stop), pull-up into a climb or make a turn. The three avoidance manoeuvres equally apply when approaching terrain, depending on the specific layout of the terrain.

2.3.1. Control of Avoidance Manoeuvres

This section provides a basic understanding of how pilots control avoidance manoeuvres.

Quick Stop Decelerating to a hover is called a quick stop, the manoeuvre is shown in Section 2.3.1. It consists of three components: the flare, the deceleration and the approach to a hover. The flare is initiated by pitching the nose up using aft cyclic while reducing the collective. The collective is lowered to decrease the main rotor lift in order to prevent climbing, as the flare would otherwise cause a rise in altitude. As the main rotor power is decreased counter-torque should be given through the right pedal. The flare causes the rotorcraft to decelerate and its aggressiveness determines the stopping distance. As energy is lost, the pitch angle can be increased or the collective can be raised to prevent the helicopter from settling and to maintain altitude and rotor thrust. The transition intro the hover is then done by using forward cyclic, maintaining a slight nose up attitude while the last forward speed bleeds out.

Climb When initiating a climb while maintaining airspeed, both the collective and throttle have to be increased while giving slight aft cyclic to maintain airspeed. The helicopter then climbs with the nose down, approximately keeping the same attitude as during the forward

---

[†] Retrieved from `http://www.danubewings.com/rapid-deceleration-or-quick-stop/`

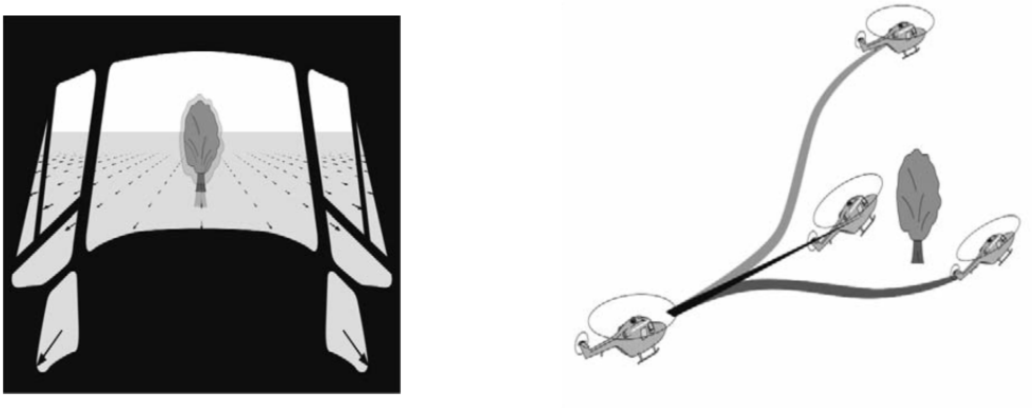

(a) Optical flow with approaching obstacle

(b) Avoidance manoeuvres: hover, stop and turn

Figure 2.9 – Optical flow (**a**) and avoidance manoeuvres (**b**) when flying towards an obstacle (**b**). (Source: [27]).

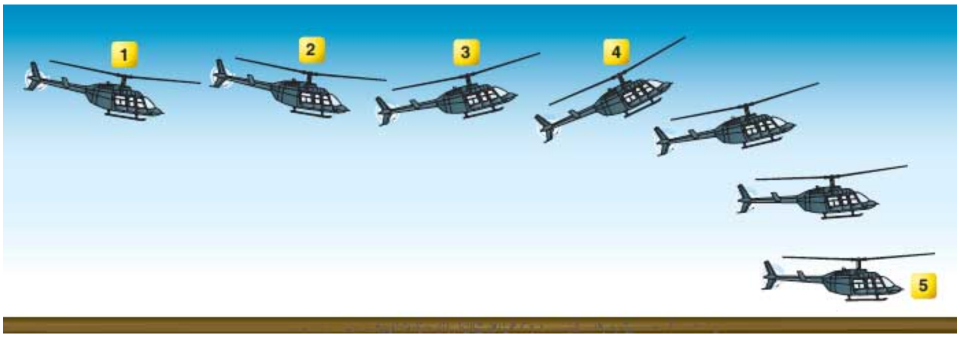

Figure 2.10 – Quick stop manoeuvre (Source: Danubewings†).

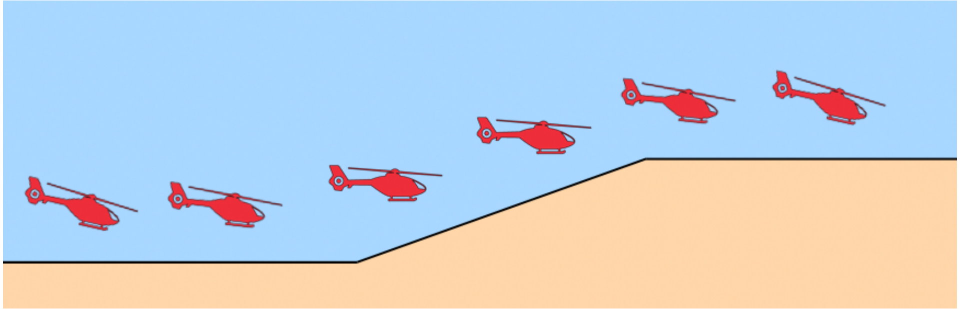

Figure 2.11 – Climb manoeuvre

level flight. To level-off, forward cyclic is applied to return to forward flight attitude. Then the collective and throttle are decreased to cruising power. Throughout the manoeuvre pedal inputs are required to prevent sideslip. Section 2.3.1 illustrates a climb over a terrain slope.

Turn When in forward flight a turn is commenced by applying sideward pressure on the cyclic in the turning direction. The pedals are then needed to compensate for torque in order to maintain trim around the vertical axis. Once the desired bank angle is reached, the cyclic is returned to its neutral position. Depending on the steepness of the bank some forward cyclic may be needed to maintain airspeed. Returning to straight level flight is similar to the entry, applying cyclic in the opposite direction.

2.3.2. Mission Task Elements

A flight mission can be separated into individual flight tasks referred to as MTE. Examples are displacement in vertical or lateral direction, hovering and landing. ADS-33 prescribes how helicopter handling qualities are awarded using the VCR scales. Test pilots fly the precisely defined MTEs and rank the quality of the control handling in that task. However, ADS-33 does not include specific MTEs for DVE conditions. To solve this problem, Gary Clark proposed a MTE for each of the previously explained avoidance manoeuvres.

For instance, the hill climb, or rising ground MTE, is meant to test the ability to detect changes in the ground slope in forward flight. A level run-in is followed by a faint slope of 5 degrees which switches to a flat run-out. Pilot guidance control is primarily tested in the heave axis during the climb and stabilisation control during the run-out. A small angle is chosen since it is more difficult to detect visually, especially in DVE, and therefore poses a higher risk level. The hill climb MTE is illustrated in Section 2.3.2.

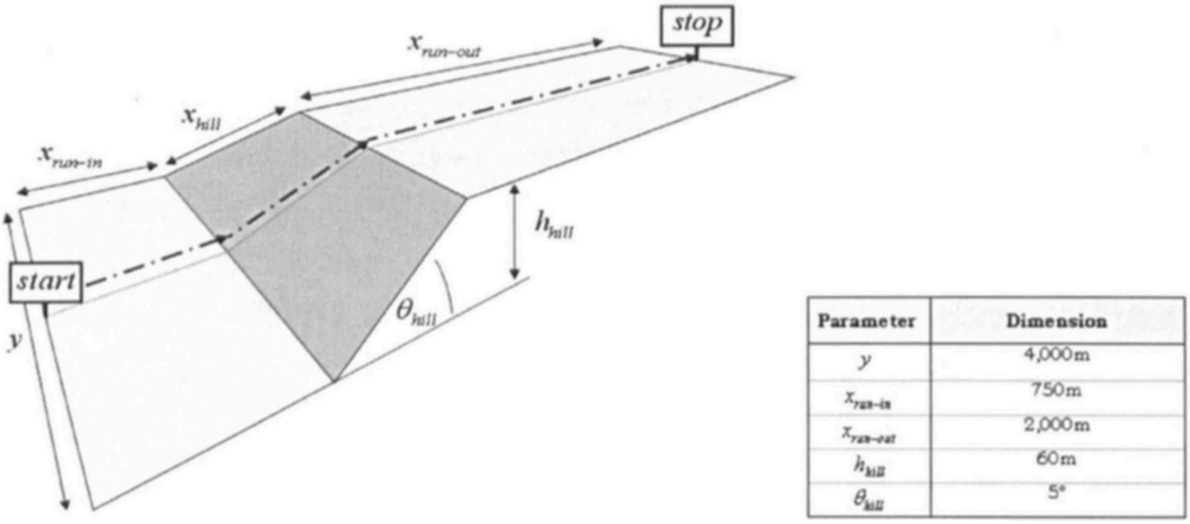

Parameter	Dimension
y	4,000m
x_{run-in}	750m
$x_{run-out}$	2,000m
h_{hill}	60m
θ_{hill}	5°

Figure 2.12 – Rising ground Mission Task Element (Source:[28])

3

Tau Theory in Rotorcraft Flight

The TTC is an important visual cue used to perceive ego-motion in relation to terrain and to coordinate control action. The theoretical foundation of the TTC has been discussed in Section 2.1.3. With respect to the research question it needs to be understood what strategy pilots use to couple the aircraft motion onto a desired trajectory such as to perform avoidance manoeuvres. Therefore this chapter presents a closer examination of τ and specifically its role in motion guide coupling.

Section 3.1 forms an introduction to tau guidance of motion. Consecutively, Section 3.2 discusses previous research on tau guidance in flight manoeuvres. Those manoeuvres that are relevant to this research project are symmetric manoeuvres such as a hover to hover reposition, described in Section 3.2.1, and the hill climb, extensively discussed in Section 3.2.1.

3.1. Tau Guidance

This section will build upon the concepts introduced in Chapter 2. Through the example of a quick stop, the concept of tau motion guides is first introduced in Section 3.1.1, after which Sections 3.1.2 to 3.1.4 cover the application of tau theory to motion variables, the modeling of intrinsic motion guides and the impact of the coupling constant k, respectively.

3.1.1. Tau Guiding a Quick Stop

In many control situations multiple motion gaps are simultaneously closed. In Section 2.3 the example was given of a helicopter approaching a tree. Let's suppose the pilot decides to come to a hover in front of the obstacle. A quick stop manoeuvre is initiated that involves decelerating to zero forward velocity, $\dot{x} = 0$, in addition to aiming the longitudinal position to stop in front of the obstacle to avoid a collision, $x = 0$. Simultaneously closing both motion gaps can be accomplished through a τ-guide.

As the tree approaches the helicopter its size grows in the visual field of the pilot. This so-called looming is an inherent feature of the optical flow and acts as a cue for τ to the pilot [25]. Knowing τ helps the pilot decide whether or not the aircraft will still be able to stop in front of the obstacle. However, perceiving how τ varies over time, defined as $\dot{\tau}$, is perhaps even more useful for motion control. The expression of $\dot{\tau}$ follows by deriving τ from Equation (2.5) as shown in Equation (3.1).

$$\dot{\tau} = 1 - \frac{x\ddot{x}}{\dot{x}^2} \tag{3.1}$$

The expression for τ of the gap τ_x and the inverse of the τ of the gap closure rate $\tau_{\dot{x}}$ can be substituted for on the right-hand side. After rearranging Equation (3.2) is obtained.

$$1 - \dot{\tau} = \frac{\tau x}{\dot{\tau}} \tag{3.2}$$

Keeping $\dot{\tau}$ constant during this manoeuvre comes down to applying a fixed coupling constant k to τ of the gap closure rate with respect to τ of the gap, as shown in Equation (3.3).

$$\tau_x = k\,\tau_{\dot{x}} \tag{3.3}$$

The value of $k = 1 - \dot{\tau}$ is this case can vary throughout a zero to unity range. It determines whether the helicopter will collide into the tree with constant velocity ($k = 0$), whether a constant deceleration is followed by a stop in front of the tree ($k = 0.5$) or whether the helicopter will follow an exponential deceleration that never attains the stopping point [27]. The effects of the coupling constant value are described in detail in Section 3.1.4.

3.1.2. Tau Guiding Motion Variables

The previous example of a helicopter decelerating in front of a tree involved τ-coupling the distance to the stopping point in front of the tree x and the distance closure rate $\dot{x}$. Both variables may be considered as a motion gap. Many control coordination tasks demand the concurrent closure of multiple motion gaps. Lee's General Tau Theory posits that any pair of motion variables x and y can be simultaneously brought to their respective target states by applying τ-coupling. The relation in Equation (3.4) is then to be followed:

$$\tau_x = k\,\tau_y \tag{3.4}$$

This equation simply states that the closure of gap x will get τ_x to zero while bringing τ_y to zero at the same time. Both variables will thus successfully reach their target states at the same instant. It is shown that two τ-coupled variables are related through a power law, which commonly describes natural phenomena of expansion and dilation in both space and time as per Equation (3.5) [29].

$$x = C\,y^{1/k} \tag{3.5}$$

Where $0 \leq k \leq 1$ and C is an arbitrary constant.

Lee and other authors have identified the τ-coupling strategy throughout a broad range of natural control tasks, including but not limited to object catching by infants [30], feet coordination in somersault landings [31], control of sucking pressure in newborns [32], step length control while running over irregular terrain [33] and coordinating singing and dancing in musical performance [34]. Two other examples are briefly touched upon hereafter.

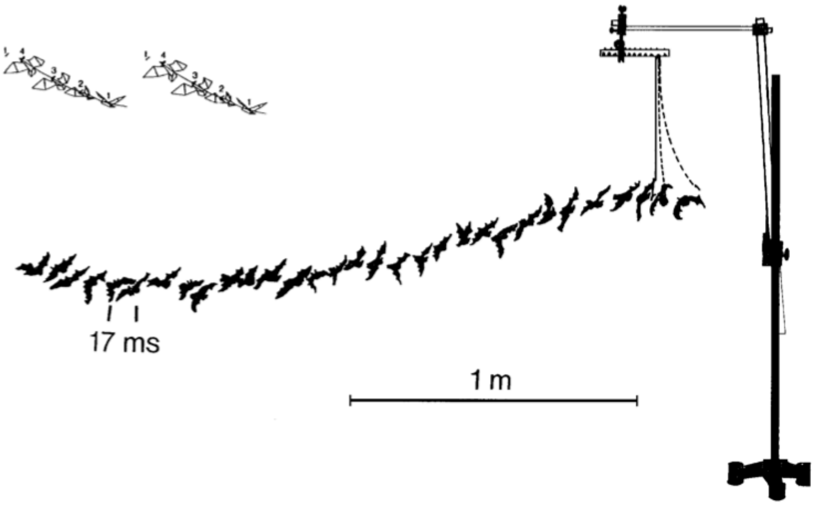

Figure 3.1 – Combined frames of bat catching a suspended prey (Source: [35]).

Echolocating Bats A study published in 1995 by Lee et al. analysed the movements of big brown bats in two different landing types [35]. Instead of visual perception, bats use echolocation for perceiving and controlling ego-motion. In one task the bats were filmed while landing on a hand. Another one had the bats catch a prey suspended on a string, as shown in Figure 3.1. Analysis of the footage of both tasks revealed that two motion variables were coupled through a τ-guide. These were the instantaneous distance to the target as well as the angle between the instantaneous direction to the target and the final approach direction. The individual bats maintained constant control parameters throughout trials and used different values between the two tasks.

Landing Pigeons A study by Lee et al. from 1993 researched what strategy pigeons used when coordinating feet extension before landing [36]. It turned out that the τ was maintained constant to control braking and that the extension of the feet was initiated at a precisely timed time value. By covering one eye it was shown that binocular depth perception did not play a role.

3.1.3. Intrinsic Motion Guides

In the previous examples of bats and pigeons the discussed motion gaps were visually perceived from the environment. These motion gaps are said to be extrinsic when they are directly observable. Contrary to the coordination of two motion gaps cases can be found where only a single extrinsic gap is closed. One such case is the control of sucking pressure by newborns, where the gap between the externally sensed intraoral pressure and an internally referenced target value is to be coordinated [32]. How can an observer-controller successfully time and execute this action in such case?

Lee theorised that the extrinsic τ of a motion gap is coupled onto an internally referenced τ-guide [37]. By definition this an intrinsic motion guide τ_g. It is thought that intrinsic motion guides are generated from learning experiences. They can be thought of as mental models that subconsciously guide the extrinsic motion gap according to a pre-planned strategy. Their

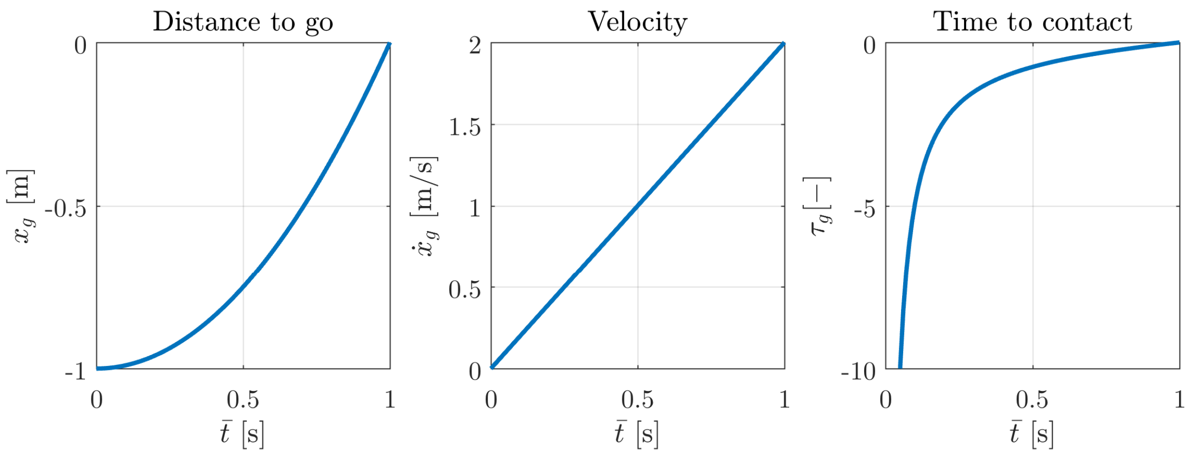

Figure 3.2 – Normalised distance, distance rate and tau of a constant acceleration motion.

coupling is similar to the coupling of extrinsic motion gaps as in Equation (3.6).

$$\tau_x = k\,\tau_g \tag{3.6}$$

Where τ_x relates to the sensed motion gap, k is the coupling constant, and τ_g is the intrinsic tau guide.

Lee hypothesised that learned experience of prevalently encountered motions could very well serve as an intrinsic motion guide [37]. One such motion is a constant acceleration, which occurs whenever an object is free-falling to the ground. If frictional forces are neglected, the object is purely subjected to the gravitational acceleration. Figure 3.2 depicts the tau-motion of an object falling towards the ground, with time and distance normalised to the total length and duration of the movement.

The constant acceleration intrinsic tau-guide can be expressed as a function of time $\bar{t}$ and the manoeuvre duration T according to Equation (3.7). The derivation of this equation is found in Appendix A.

$$\tau_g = \frac{1}{2}\,t - \frac{T^2}{t}\square \tag{3.7}$$

3.1.4. Coupling Constant

The coupling constant controls how the two taus are related while they are reduced to zero. In the case of an intrinsic motion guide, the value of k determines how the extrinsic motion gap is closed in relation to the intrinsic motion gap. Even though both motion gaps will be simultaneously closed, for the very same τ_g different values of the coupling constant lead to variations in the resulting motion. In essence the coupling constant may be considered as a measure on for aggressiveness in the τ_g-following. Figure 3.3 shows how the constant acceleration tau-guide is followed for different values of the coupling constant k. Plots are shown for the normalised motion gap distance, for its normalised closure rate and, lastly, for tau.

The plots shown in Figure 3.3 allow some general remarks to be made on the effects of the coupling constant k:

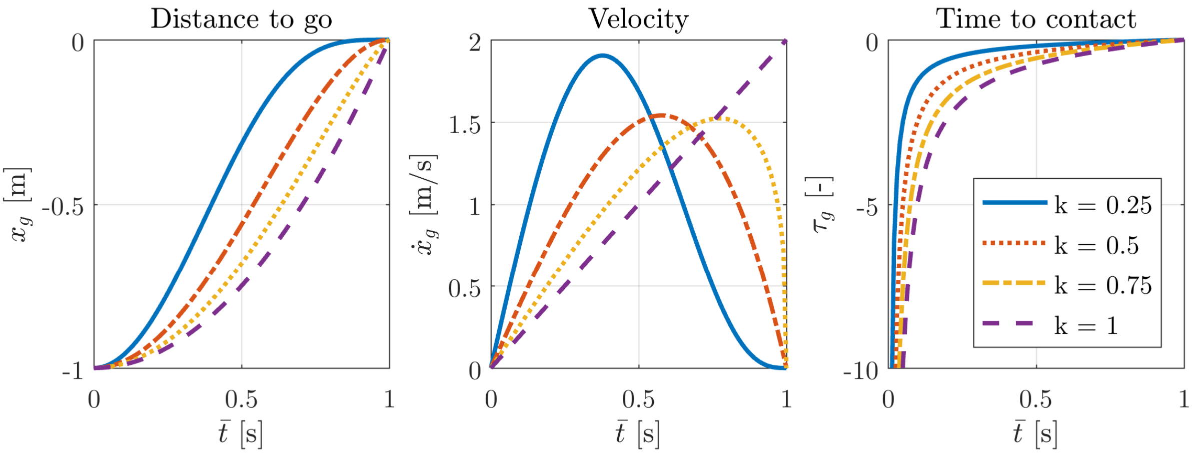

Figure 3.3 – Effect of coupling constant on motion gap, gap closure rate and tau.

- For $0 \leq k \leq 0.5$ the motion guide is aggressively followed through a hard acceleration which is followed by a deceleration until the motion gap is closed. The lower the value for k, the harder the initial acceleration and the sooner the maximum velocity value is reached. Conversely, increasing k results in the maximum velocity occurring later. This strategy has the advantage of closing the gap rather fast at the beginning, allowing for precise control at the end.

- For $k = 0.5$ the manoeuvre ends with a finite deceleration.

- For $0.5 \leq k \leq 1$ a full stop in front of the aiming point is not possible: in theory infinite deceleration is required at the stopping point. The acceleration at the beginning of the motion is rather gentle. Peak velocity is reached later in the motion and the motion is abruptly brought to a standstill.

- For $k = 1$ the constant acceleration motion guide is neatly followed. In other words, the movement is the same as shown in Section 3.1.3.

- For $k > 1$, the acceleration increases throughout the entire motion towards the goal. This case is not plotted in the figure.

3.2. Tau-coupling in Flight Manoeuvres

The previous sections have outlined the theoretical aspects of tau-guide following. The knowledge acquired will help in analysing the methods and results from earlier studies that dealt with terrain climb manoeuvres. This section will summarise those studies in an attempt to identify best practices in experimentation and to recognise opportunities in the application of the theory to visual augmentation.

3.2.1. Repositioning

The first study to take a tau-guidance approach to visual perception in helicopter flight was an exploratory analysis published by Padfield et al. in 2003 [38]. This paper was the first in a series in which the authors tried to find out how long forward in time pilots use information in the optic flow field, asuming that pilots use a temporal modal of the environment rather than a spatial one. They reasoned that an understanding of ecological prospective control would

Table 3.1 – Average flight parameters for terrain following manoeuvre (Source: [39]).

Distance to Fog [m]	Velocity [eh/s]	Time to 12 eh point [s]
720	2.25	5.30
480	2.70	4.40
240	2.24	5.36
80	1.78	6.74

benefit the design of visual aids, since it would reveal which cues are necessary for proper activation of the mental model in DVE.

Three pilots were asked to fly ‘accel-decels’ at different levels of aggressiveness in an advanced flight simulator simulating a Lynx helicopter model. The manoeuvre is a hover-to-hover displacement and only requires cyclic control input. It starts at a steady hover, followed by a forward acceleration up to an instructed maximum forward velocity is reached. Then the aircraft is decelerated and returned to a steady hover at a prescribed position. The pilots had to follow a straight flight-track, maintain altitude and come to a stop at 150 m from the starting point. Fitting the manoeuvres to a constant acceleration guide yielded mean values for k of 0.381, 0.324 and 0.317 for low, medium and high aggression respectively, thus following the expected trend. The correlation factor was above 0.98 for all recordings. These results confirmed that visual information from the optic flow indeed serves as input for tau-coupling the motion of the aircraft.

3.2.2. Hill Climb

The second work considered tau-coupling in a hill climb MTE. Experienced pilots started at hover at 750 m distance from a 5 deg terrain slope. They had to accelerate forward towards the terrain slope, climb over the 60 m high hill as they saw fit and fly another straight 2000 m over flat terrain. Visual conditions varied across UCE1-3, using blurred terrain textures and macrotextures obscured by fog at various forward distances. Instruments were disabled and trees were positioned along the otherwise flat terrain for height reference. The researchers looked for eye-height trends in the selection of airspeed and altitude to compare with Perrone’s perception threshold of 15-16 eye-heights as discussed in Section 2.1.2. Furthermore, they tried to identify if a tau-coupling strategy was used when aiming the flight path angle to fly over the hill.

Perception threshold Table 3.1 shows the eye-height velocity and time to the 12 eye-height point ahead of the aircraft for various fog distances. This point was shown to be the aiming point of the pilot’s gaze in the manoeuvre. The table shows that throughout different flight conditions the eye-height velocity remains near 2 eye-heights. The pilots picked up information at the 12 eye-height point. This corresponds to a look-ahead threshold of 6 seconds. As soon as the looming at the aiming point changed, as shown in Figure 3.4a, pilots waited approximately 3 seconds before initiating the climb manoeuvre. This means they were halfway above the hill before pulling up. The authors posited that during this time the pilot shifted his gaze upwards on the hill and aimed at this point in the climb manoeuvre. This behaviour is illustrated in Figure 3.4b.

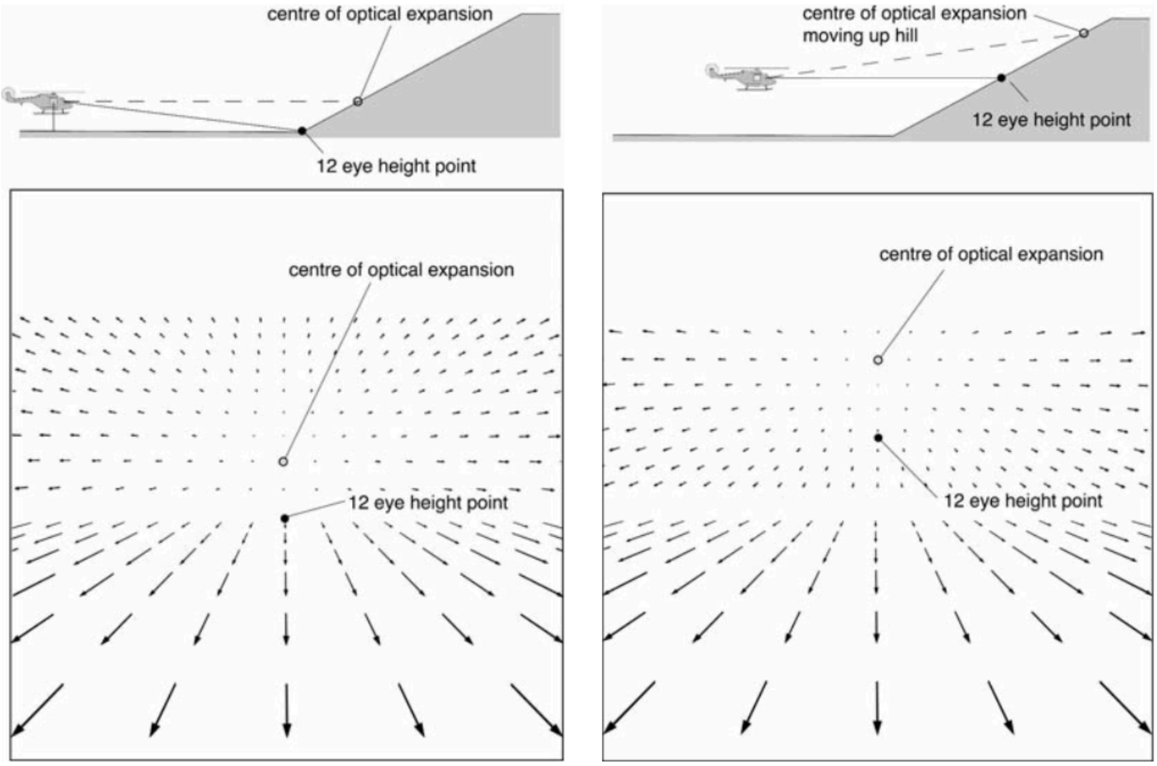

(a) Looming of aiming point

(b) Shifted aiming point after rotation

Figure 3.4 – Optical flow in the rising ground MTE before (**a**) and after performing the pull up (**b**). (Source: [28]).

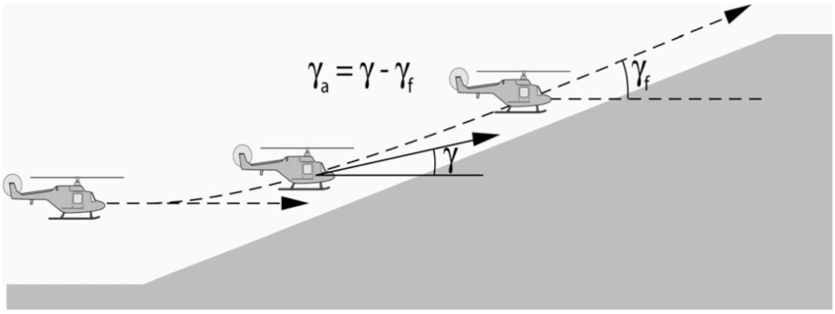

Figure 3.5 – Flight path angle used in hill climb tau analysis (Source: [39]).

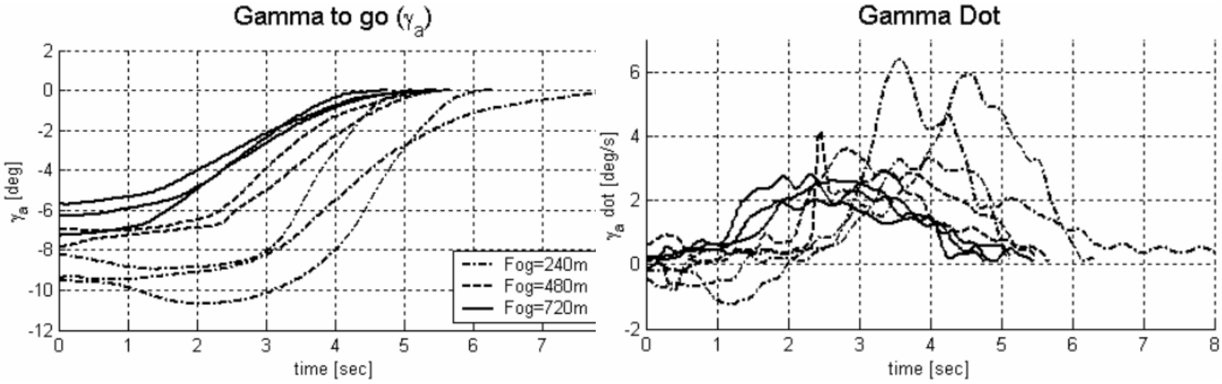

(a) Flight path angle gap γ_a **(b)** Flight path angle gap rate

Figure 3.6 – Progression of flight path angle (**a**) and flight path angle rate (**b**) for hill climb manoeuvre (Source: [39]).

Tau analysis For the hill climb manoeuvre the motion gap to be closed relates to the control of the flight path angle of the aircraft. The flight path error γ_a is defined as the deviation of the instantaneous flight path angle γ from the goal flight path angle γ_f as shown in Figure 3.5. The start and end of the manoeuvre were defined as the time of raising the collective control lever and the time $\dot{\gamma}$ first equals zero, respectively. The manoeuvre time T is consequently defined by the duration between these instants.

Figure 3.6 presents γ_a and $\dot{\gamma}$ as a function of manoeuvre time for the hill climb trials. It can be seen that pilots have more difficulty in judging the slope angle of the hill as visibility decreases. For the 240 m fog case γ_a at $t = 0$ s is nearly 10 deg, e.g. close to a 5 deg overshoot.

The tau of the motion was calculated using Equation (F.7). The resulting plots for the 240 m, 480 m and 720 m fog cases are shown in Figure 3.7.

$$\tau_\gamma = \frac{\gamma_a}{\dot{\gamma}_a} \tag{3.8}$$

The curves show a trend with high-frequency variations in the beginning of the manoeuvre that fade into a steady slope, suggesting a constant acceleration guide may be followed. The tau of the motion gap τ_γ and the constant acceleration tau-guide τ_g are compared for a single run of the 720 m fog case as a function of time in Figure 3.8, showing high correlation (R^2 factor of 0.981 for $k = 0.386$) over the entire manoeuvre. The average correlation with a constant acceleration tau-guide indicated significant coupling with an average $R^2 = 0.959$. However no significant effect was identified of fog distance on the value of the coupling constant k.

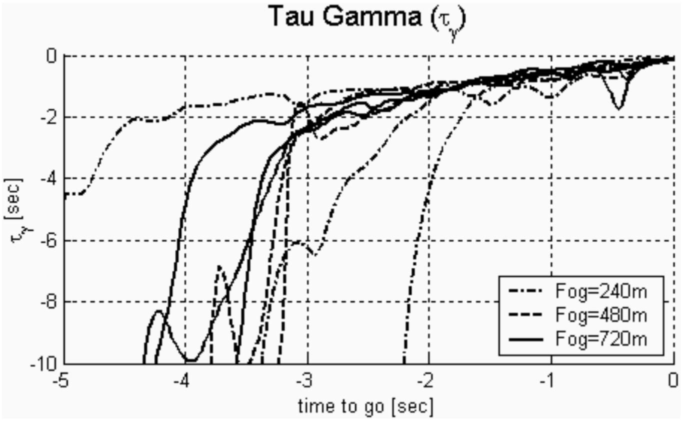

Figure 3.7 – Tau of the flight path angle error (Source: [39])

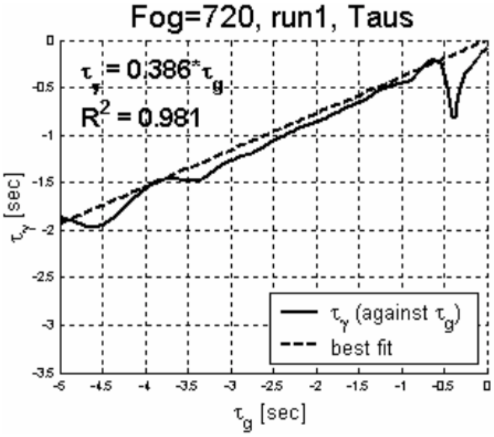

Figure 3.8 – Taus of constant acceleration guide and flight path angle gap (Source: [39])

Table 3.2 – Hill climb manoeuvre coupling constant and correlation with constant acceleration guide (Source: [28]).

Fog distance	Run	k	R^2
240 m	1	0.631	0.904
	2	0.384	0.908
	3	0.410	0.902
480 m	1	0.352	0.908
	2	0.352	0.908
	3	0.208	0.918
720 m	1	0.425	0.906
	2	0.326	0.921
	3	0.445	0.925

As part of his doctorate thesis on helicopter handling qualities in DVE Gary Clark investigated tau-guidance in a hill climb manoeuvre [28]. A single test pilot performed the same hill climb manoeuvre three times for each combination of fog distance (80 m, 240 m, 480 m and 720 m) and level of terrain surface microtexture (good, medium and poor). Discarding the UCE3 case due to high fluctuations in height and speed, the resulting tau-analysis was in agreement with the aforementioned results from Padfield et al. The closing of the flight path angle gap followed a constant acceleration motion guide with coupling constant and correlation values as shown in Table 3.2. For these 9 runs there was no significant effect of the visibility on the value of the coupling constant.

Concerning the perceived outside visual cues and the coordinated control actions, the rotary wing hill climb manoeuvre is comparable to a fixed wing landing flare, assuming symmetric flight. In both situations pilots are flying towards a plane that is inclined with respect to the direction of flight which requires an accurate control strategy. In the rotorcraft case the aircraft follows a level flight path and has to increase its flight path angle to match the angle of the inclined slope. Likewise, in the fixed wing case the aircraft flies a descending flight path that needs to be increased through the flare manoeuvre so the direction of flight matches the orientation of the terrain. In both cases pilots use the point of optical expansion to perceive the angle of the approached surface as well as the TTC, and they shift their gaze upwards in the flow field to pick up information on the motion gap that is closed.

Considering the aforementioned similarities between the two manoeuvres, it comes as little surprise that tau analysis of a landing flare showed comparable results. In a study by Jump and Padfield pilots flew approach and landing manoeuvres with fixed wing aircraft in GVE and DVE [40]. The tau of the height above the runway τ_h was coupled onto an intrinsic tau guide. Generally the rate of τ_h was maintained constant between 0.6 and 1.0 until touchdown, corresponding to a constant descent rate. Some runs in degraded visual conditions displayed a constant tau value being reached before touchdown. This means that the flare transitions into a level off right before touchdown.

4

Terrain Awareness in HMDs

As an increasing number of aircraft is equipped with a Helicopter Terrain Awareness and Warning System (HTAWS) the number of CFIT accidents that yield fatalities is likely to decrease. This equipment integrates several avionics systems to warn pilots of terrain, obstacles and wires using both head-down visual and aural warnings. HMDs provide the unique opportunity of presenting this information directly into the outside visual scene, potentially increasing operability in DVE.

However, displaying terrain awareness information in a using a visual conformal display requires knowledge of the state of the art in both terrain awareness systems and HMD technology. Therefore, this chapter will detail the capabilities of current HTAWS in Section 4.1. Then, Section 4.2 outlines HMDs and the relevant human factors that need to be considered. Lastly, existing HMD terrain awareness symbologies are described in Section 4.3.

4.1. Helicopter Terrain Awareness & Warning Systems

HTAWS use sensors and databases to analyse the environment and warn the pilots of obstacles and terrain in the projected flight path. Outboard mounted sensors may include forward looking infrared (FLIR), Light Detection And Ranging (LiDAR), millimetre wave (mmW) and TV. Their signals are filtered, fused and combined with navigation and mission information to obtain a synthetic representation of the vehicle surroundings. A detailed description of common filtering and fusion techniques is beyond the scope of this thesis, though the interested reader is referred to the extensive work of Liggins II et al. [41].

In 2014, the Federal Aviation Administation (FAA) increased the standards for commercial helicopter operators in Circular Advisory 29-2C [42]. Besides increased levels of training, HTAWS were now recommended to protect against CFIT, wire strikes and obstacles such as trees, buildings and towers. Three avionics manufacturers (Sandel, Garmin and Honeywell) have set out to develop solutions to the awareness and warning problem. These will be discussed in this section.

Sandel HeliTAWS is avionics manufacturer Sandel's line of HTAWS [43]. It warns when wires and towers appear in the direct flight path during low level flights. HeliTAWS uses radio altimeter and on-board GPS, i.e. all terrain and obstacle information comes from its 3-arc-second terrain database. The system features a 3 inch colour display, as shown in Section 4.1, and is packed in a standalone hardware unit. U.S. government and military helicopters have received upgrades to HeliTAWS. It also comes pre-installed with the new Sikorsky S70-I Black Hawks.

HeliTAWS allows the pilot to select the alert sensitivity mode in order to prevent nuisance warnings. The four selectable modes range from an obstacle only mode to 500 ft AGL. Detectable obstacles need to be higher than 50 ft above the ground and power lines at least 100 ft. A notable feature is the stressing of power lines by connected lines, as shown in Section 4.1. Where data is available, HeliTAWS renders synthetic displays of roads and waters to provide a reference for wire obstacle detection. Certainly, this functionality is only of use in visual flight rules (VFR).

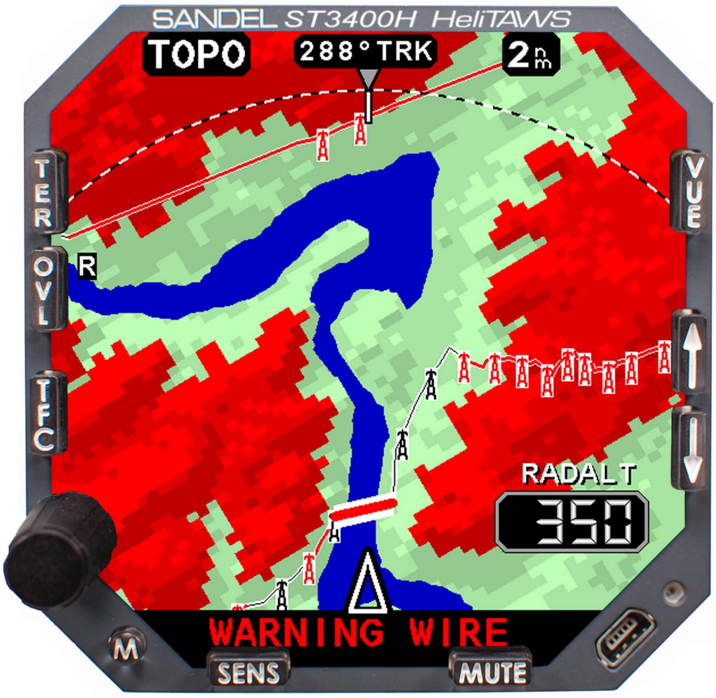

Figure 4.1 – Sandel HeliTAWS display (Source: Aviation Today†)

Sandel's system uses a top-down terrain visualization that colour codes the height of the surroundings. It lacks the use of real-time sensors, making it relatively inexpensive. The downside is that pilots have to rely on the accuracy of the database in degraded visibility. HeliTAWS uses the global positioning system (GPS) signal to project the flight path forward in time and compares this with its database. Caution alerts are given about 20 seconds ahead of a potential conflict. This turns into a warning alert 10 seconds ahead of the conflict. The system is explicitly not suitable for navigation purposes.

Garmin HTAWS is available as an add-on to existing Garmin navigators using wide area augmentation system (WAAS)-enabled GPS and, optionally, radio altimetry [43]. The supported devices have a top-down navigational display (ND), to which colour-coded terrain is added in five hues (red, orange, yellow, green and black). Conflict detection is based on a comparison of the predicted trajectory, and the terrain and obstacle database. The system features normal and reduced protection (RP) modes. Normal mode is default for takeoff, landing and instrument flight rules (IFR). RP mode is designed to protect specifically during low VFR flights. Obstacles

---

† Retrieved from http://www.aviationtoday.com/2012/02/13\/sikorsky-selects-sandels-helitaws-for-s-

are clearly displayed using large symbols. Pilots are visually and aurally notified of caution and warning alerts. Optional voice callouts inform pilots of the AGL when below 500 ft.

Figure 4.2 – Garmin HTAWS on GNS 530W (Source: Garmin ‡)

SmartView is avionics giant Honeywell's synthetic vision (SV)-based primary flight display (PFD) [43]. It incorporates a FLIR sensor into its SV PFD, a significant advantage compared to other systems. A special rotorcraft version sets itself apart from the competition by its built-in HTAWS functionality. This makes for an integrated system that combines terrain, wire and obstacle data with enhanced vision (EV) within the PFD and ND.

The system will include bridges, vertical city obstacles, radio towers and even animated wind turbines. Chosing to add HTAWS functionality to its PFD platform, Honeywell puts emphasis on the FPM as a visual support used for terrain avoidance. SmartView for rotorcraft has yet to be certified and released to the market at the time of writing.

Figure 4.3 – Honeywell SmartView with HTAWS (Source: [43])

---

‡Retrieved from https://buy.garmin.com/en-US/US/p/72799

When comparing the three HTAWS', it seems clear that Sandel aims for a system that works entirely isolated from other avionics. As a dedicated HTAWS unit it caters mostly to retrofitting aircraft as to meet updated regulations. Garmin makes use of its existing navigators, so that terrain awareness and warning becomes an additional feature and can easily be added to aircraft equipped with those devices. Both Garmin and Sandel systems are reliant on the accuracy of their database information. Moreover, the prediction of conflicts does not use a flight dynamics model, which necessitates increased safety margins for conflict warnings. Consequently, these systems could be more prone to nuisance. Besides, Honeywell's solution is the most advanced one, exploiting the latest technologies, such as FLIR, EV and SV, while integrating them on the PFD. When it comes to DVE operations, the Honeywell is the only commercial system suited for landing in unprepared landing sites thanks to its FLIR sensor.

4.2. Helmet Mounted Displays

From a human factors perspective, helmet-mounted displays offer multiple advantages. Helicopter pilots will generally fly head-up whenever possible, especially during a landing manoeuvre [44]. Awareness of the environment is maintained by visually scanning the landing zone and memorising the types and positions of potential obstacles. Moreover the environment provides visual cues for ego-motion such as compression, splay and optical flow as explained in Section 2.1. By flying head-up, the task-relevant features are directly perceived within the environment itself and the amount of cognitive processing required is thus substantially lower when compared to flying on head-down instruments.

However, during operations in DVE the outside cues are partly or wholly obscured. In the specific case of a helicopter landing, the visual reference is often gradually lost with decreasing altitude. As this phenomenon occurs the pilot will typically try to exploit the head-up visual cues for as long as possible, up until the point where these are no longer sufficiently reliable. Consequently the head-down instruments have to be used. This work flow results in a switching cost of physical sight and mental attention as both have to be refocused [45]. The effects of the induced time delay and the increased mental effort due to the switch in focus may prove to be crucial during the safety-critical landing phase.

HMDs may be a part of the solution to these problems. By overlaying symbology on the outside scene, the information of the environment becomes co-located with the sensory information provided by the on-board flight systems. This eliminates the need for a change in viewing direction, saving in information access cost. More interestingly though, instead of projecting the standard head-down display symbology onto the eyes-out display, the symbology can also be designed such that features in the visual interface add meaning to those present in the outside world. This is known as scene-linked or conformal symbology, and can be implemented using either 2D or 3D representations of symbols.

4.2.1. Human Factors Related to HMD Design

The capabilities and constraints of the human visual system should be carefully considered when designing a visual support system. After all, a visual human-machine interface that exceeds naturally present performance limits of the human user would be a waste of resources. Therefore the most relevant elements of the human visual system are recapitulated, after which their implications on HMD hardware design are given.

Foveal and Peripheral Vision The human visual system is limited in the amount of details it can resolve. The conversion of photons that reach the retina into nervous stimuli to be processed by the brain is done by two types of optical receptors, cones and rods. Cones are particularly adapted to resolve high detail and colour, although they require high luminance to do so. Contrarily rods are more suited for detecting large, moving objects with the advantage of a low luminance threshold [46].

The smallest distance between two elements that can be distinguished is called visual acuity. It is measured in minutes of arc, and it varies over the eye, due to the distribution of the cones on the retina. The fovea is the region on the retina with the highest concentration of cones and thus the largest visual acuity. It spreads about 1-2 minutes of arc in size [47]. The peripheral region of the retina contains mostly rods. Its visual acuity is therefore tenfold less than that of the fovea but it is most useful for perceiving self-motion thanks to optimised pattern recognition. In HMD design the peripheral vision could be used to present additional cues for self-motion or as an attention-grabber.

HMD Hardware Design The vertical and horizontal angles at which an HMD can show information to the eye define its field-of-view (FOV). Wider FOV improves user performance at various tasks since a pilot needs less head movement to obtain the same amount of information [47, 48]. Binocular displays feature a different image for each of the user's eyes. This enables stereoscopic depth cues, so the illusion of depth can be created within the interface [49]. The amount of detail that a display can show is defined as its resolution. It determines how small an interface element can be drawn. HMD designers should aim for the minimum human visual resolution of 1 minute of arc for an optimal viewing experience.

Luminance and contrast specifications of a see-through display primarily determine the legibility of its symbology. In order for an image to be visible even against bright backgrounds the display needs a high luminance capability. The maximum luminance ratio between adjacent areas is called contrast. High contrast ratio images are clearly visible whereas low contrast images appear to be washed-out [50]. The head-tracking system of an HMD measures changes in head orientation to realign the image such as to remain fixed with the outside environment. This leads to the optical illusion of a natural viewing condition. The head-tracking system needs to work accurately and feature a low latency to prevent disorientation, nausea and motion sickness [51]. Display collimation ensures the interface is shown to the user at optical infinity, so switching from far domain to symbology does not require reaccommodation of the eyes [52].

4.2.2. Visual Attention Issues

While our discussion concerns HMDs, it should be noted that these are often considered as the technological successors of head-up displays (HUDs). The main difference being that HMDs are displaced with head movements and feature head-tracking, whereas HUDs are fixed to the aircraft body axis. Certain advantages and disadvantages of HUD also apply to HMD [53]. The main issues in HUD that are transferable are clutter, attentional capture, and the use of nonconformal symbology.

Clutter Display clutter is one of the main problems with HMDs, providing an incentive for further research on lightweight visual interfaces. If an extensive amount and variety of display features is presented, focused attention and task performance may decline depending on the user's task proficiency [54]. The net result is a rise in both processing time and in mental effort required to interpret the visual interface [5]. Given that an HMD adds information to the outside environment, the amount of visual information increases by default. HMDs are therefore extremely susceptible to becoming cluttered, even more so as designers are tempted to project all head-down information on the eyes-out display.

A study of the effects of clutter on event detection in cruise flight found an increase in visual search time for near-domain events and a total disruption of far-domain event detection [45]. As the effects of clutter were found to be the same both head-up and head-down it was concluded that the total number of visual elements was responsible for the performance increase and not the overlapping on the outside scene itself. Overmore it is generally accepted that the gains in visual search time in HUD and in HMD outweigh the cost of clutter [55, 56]. Nevertheless clutter remains a key issue with the design of HMD interfaces and the usefulness of display elements needs to be carefully weighed before they are added.

Attentional Tunnelling In semi-transparent displays two sources of visual information are considered: the far domain and the near domain. The far domain contains the outside environment, including terrain, the landing site, obstacles and other aircraft. The near domain consists of the information projected by the eyes-out display and the head-down instrument panels. The principles of selective, focused and divided attention also apply to HMD. When searching and ranking visual elements for their usefulness in a specific task, this concerns selective attention. Focused attention is applied when an effort is made to perceive information from one domain while deliberately blocking elements from the other domain. When information of multiple sources needs to be integrated concurrently, we speak of divided attention. This is the case when information from the far domain needs to be interpreted along with information from the near domain [57].

A main concern with HMDs is attentional capture, and more specifically inattentional blindness (failing to see highly visible objects that are directly looked at when attention is elsewhere) and change blindness (failing to notice a change in an object due to absence of focused attention on that object). During helicopter landings, pilots need to respond to disturbing events as quickly as possible. For instance, a pilot can fail to detect an obstacle on the landing zone in the far domain because his/her attention is captured by the HMD instrumentation. Conversely, a critical system anomaly may remain unnoticed if attention is focused in the far domain. In HMD research these effects are usually quantified by event detection trials and eye tracking.

A review of research on HUDs has shown a negative effect on unexpected event detection [58]. This is attributed to attentional tunneling, the phenomenon during which too much focus is put on a single information channel leading to negligence of other channels [59]. Multiple studies have shown how different aspects of nonconformal symbology require an increased effort in mental integration. Contributing factors identified are differential motion between the two domains and head-up display location [60]. This can in turn lead to attentional tunnelling as the pilot excessively focuses on the near domain.

Superimposing information on the outside scene using a see-through display has the potential to take advantage of the proximity compatibility principle. This principle states that visual elements included in a task that are mentally of close proximity should also be perceptually grouped to support divided attention. This can be achieved by design features such as shape, colour, location, etc. Indeed, conformal symbology may be able to exploit the proximity compatibility principle by linking elements from the near domain to the far domain by their location.

4.2.3. Conformal Symbology

Conformal and scene-linked symbology may help counter the aforementioned clutter and attentional tunneling costs. The prime difference between nonconformal and conformal symbology being the frame of reference, where the location of the former is relative to the display and the location of the latter is relative to the outside scene. An example of conformal symbology is a marker that overlays an object, while a statically positioned sensor indicator is an example of nonconformal symbology. Lastly, symbology is scene-linked when its position is referenced within the outside scene, but is not tied to an object, like for example a projected landing aid that remains pointed towards the viewer [61].

Conformal symbology should benefit tasks that require divided attention. According to object-based perception theory, conformal symbology can be effective in fusing the representation of guidance symbology with its far domain counterpart to counter clutter and attentional costs [57]. When outside scene and superimposed symbology are fused into a single perceptual object attention allocation to the far domain is facilitated. This in turn helps in countering the negative consequences of expectancy and clutter on rare event detection. Conformal symbology decreases the amount of head and eye movements necessary to gather information from both domains. This advantage should be more pronounced in HMDs than in HUDs as they feature a larger field of regard thanks to their head-tracking capability [53].

4.2.4. Colour in Head-Mounted Displays

The onset of colour capable HMDs may contribute to mitigating problems in attention allocation and clutter. Most available HUD and HMD systems feature monochrome symbology in a green hue that is well perceivable against a wide variety of backgrounds. As an evolution from monochrome symbology, colour adds another way of encoding information and allows a more intuitive presentation of information. As technology for colour display in semi-transparent HMDs is becoming available to a larger market, several key problems remain to be solved.

Firstly minimum luminance contrast ratios need to be determined such that colors remain perceivable during all mission scenarios and visual flight conditions. As of writing there is controversy between experimentally obtained threshold values [62, 63]. Moreover the blending of outside scene colors with symbology colour remains to be modelled to be able to predict and possibly correct colour perception in optical see-through devices [64, 65].

Secondly design guidelines for effective and robust colour symbology design for use in semi-transparent displays need to be established. A survey of important variables in colored conformal displays found that perceptual problems make it difficult to find a suitable research method [66]. Colour is viewed as a perception and recognition of colour is affected by associations that originate from a person's memory. Since perception is difficult to measure in a practical setup, it is recommended to conduct human factors experiments with challenging pilot tasks to put various colour coding strategies to the test.

4.3. Terrain Awareness in HMDs

The previous sections have described the state-of-the-art in terrain awareness and warning systems, and HMDs. What symbologies allow the combining of these technologies with a view to obtaining a fully integrated visual interface for low flight in DVE? This section will attempt to answer this question. First of all, a visualisation of the terrain is required so pilots are aware of their surroundings. As such, Section 4.3.1 reviews research on synthetic terrain imagery (STI). Second, additional symbols may be added to increase situation awareness, to accentuate obstacles and to possibly to provide guidance through the environment. The state-of-the-art of HMD these additional terrain awareness symbologies are reviewed in Section 4.3.2.

4.3.1. Synthetic Terrain Imagery

In 1994 a study was done at Honeywell to investigate various STIs for viewing on a HMD against a terrain background [67]. A considerable amount of concepts were tested including, but not limited to, an optical expansion gradient, tiles, ridge lines, and an orthogonal mesh. Results of a simulator experiment with 12 U.S. Air Force (USAF) pilots showed that the mesh and points with ridge lines STIs, as depicted in Figure 4.4, were preferred. Moreover, it was recommended to show ridge lines regardless of terrain shape, to display emergent features at low altitudes and to prevent high densities of lines and points on the horizon.

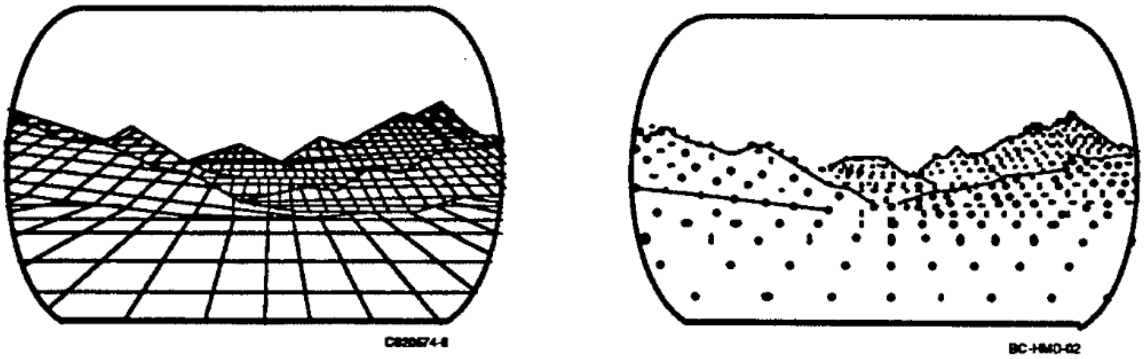

Figure 4.4 – Mesh (left) and points with ridgelines (right) STI that performed best in Honeywell experiment. (Source: [67])

In 2009 a flight test campaign was conducted by Japan Aerospace Exploration Agency (JAXA) using a research helicopter to put an integrated HMD and FLIR system to the test[68]. During the preliminary testing phase, three types of STI were shown on the HMD. They are illustrated in Figure 4.5. The mesh variation displayed an orthogonal grid with a 250 m pitch. The contour concept showed lines perpendicular to the flight path at 500 m pitch. Lastly, a skyline variant only rendered peaks and ridges in an uncluttered way. The mesh STI was rated the worst while the skyline one was most appreciated. This was due to their high and low amount of clutter, respectively.

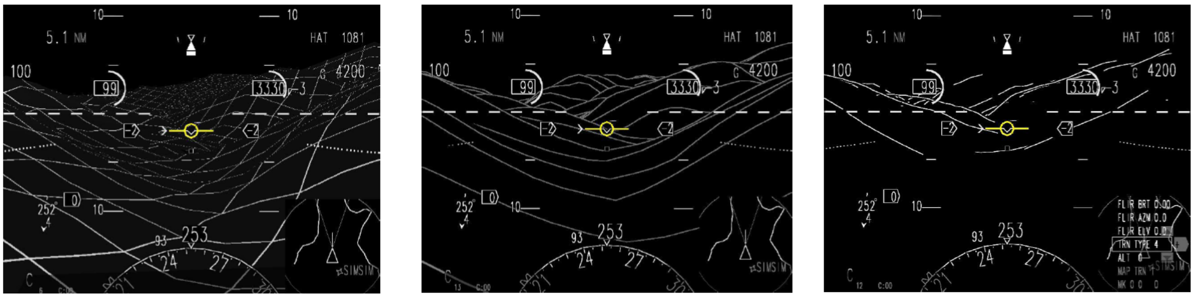

Figure 4.5 – Mesh (left), contour (middle) and ridgelines (right) STIs as tested in JAXA experiment. (Source: [68])

4.3.2. HMD Terrain Awareness Symbology

SFERION is Airbus Defence and Space's system for helicopter flight in DVE, specifically designed to be used with an HMD [69]. A 3D LiDAR sensor detects the layout and textural structure of the terrain, as well as obstacles such as trees, buildings and wires. This sensor is currently operated on the NH90 TTH. Data from the sensor is processed by a module that

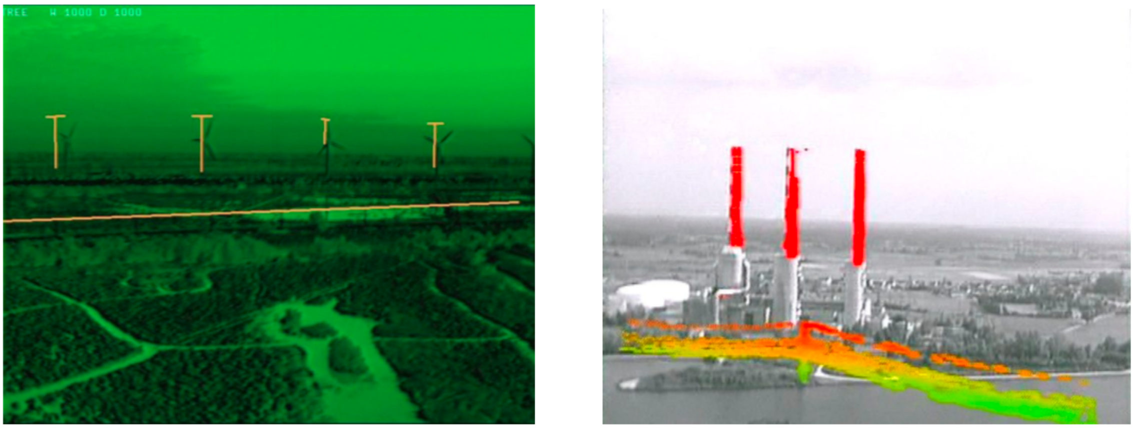

(a) T-shape poles

(b) Risk pixels

Figure 4.6 – Sferion obstacle pole (**a**) and risk pixel (**b**) symbology. (Source: [71])

categorises into terrain, ground details, obstacles and man-made objects. Another module fuses the sensor information with a database to obtain a live database of the surroundings.

SFERION generates 3D conformal symbology that can either be shown on an HMD, or used to generate a fully synthetic view on a HDD. An additional module can display tactical and navigational information within the same system. The conformal terrain markings consists of a grid, contour lines, and point-cloud markings of objects above the ground such as trees and buildings [8, 70]. The grid fades in the distance as a natural transition to the ridge lines as shown in Figure 4.6, is shown in a dark colour to be less obtrusiveness and can be culled to a set distance. Obstacles are marked by non-cluttering T-shaped symbols but can also be colour coded by 'risk pixels'. Furthermore, the system is designed to provide in-flight tactical support during all phases of flight. This includes 3D conformal symbology of the landing site and flight guidance like glide slope indication and approach path direction.

A flight test campaign of SFERION in 2014 included low level flights and brownout landings in a desert area [72]. One of the features tested included the so-called safety line, which provides guidance to clear obstacles at a preset margin. Pilots need to keep the FPM above the line to stay safe. The safety line takes into account the terrain and obstacle database, as well as a short-term prediction of the aircraft dynamics. The experiment series was to demonstrate the possibility of real-time sensor-enhanced helicopter flight using 3D conformal symbology. Unfortunately, results of the flight tests do not contain quantitative data with respect to human factors. The SFERION safety line is operational on German and Finnish NH90 helicopters.

TOAD was a joint U.S./Israel rotorcraft project, standing for Terrain and Obstacle Avoidance Display, that entailed the development of novel display symbology for low-level helicopter flight in DVE[9]. A key observation made in the analysis of existing displays was that a safety line as implemented in SFERION would, besides decreasing workload, be prone to promoting attentional tunneling and increasing reaction times to unexpected events. To mitigate these problems, improvements to the safety line were investigated, namely contour lines, that could allow pilots to make the connection between on the one hand the obstacles and terrain to avoid, and on the other hand the line being displayed.

Four display concepts were tested in a simulator compaign with 12 pilots. The simulated task comprised a low visibility terrain following flight as primary task and a target identification as secondary task. Six routes were constructed through valleys within in undulating terrain

Figure 4.7 – SFERION terrain grid and ridge line symbology (Source: [70])

with a range of slope angles. The terrain was scattered with trees and 12 obstacles such as poles, wires, antennas and trees were placed along each route such to enforce conflicts in the directed flight path. The simulated visibility through fog was about 400 m. Primary flight information was given in the form of 2D symbology (attitude indicater, 5-second preview FPM, ground speed, heading and altitude ladder) for situational awareness.

The blinking scene linked (BSL) concept consisted of lightweight 3D symbols placed within the environment that warned the pilot by blinking 5 seconds prior to a conflict. The second concept, conformal line (C), used a simulated LiDAR to display a filtered line that shows the maximum climb angles along azimuth to clear the terrain and obstacles in a range of 5 seconds forward, as shown on the upper left-hand side of Figure 4.8. Pilots were instructed not to let the FPM come below the line. The guidance (G) line concept is similar to C but has as distinct feature the addition of the commanded AGL of 50 ft as a margin. Moreover, the G line is smoothed more than C. Pilots were instructed to aim the FPM on the guidance line. The fourth concept simultaneously showed C and G (C+G) with no additional instruction given to the participants.

Objective results showed that, in obstacle-free conditions, the contour line displays were associated with higher flight levels, i.e. more flight time without cover, and more transitions between high and low flight regions when compared to BSL. When encountering obstacles, the C and G displays were associated with safer flight. Overall, BSL and C displays were unsafer than the G or C+G displays, with more time spent under 50 ft AGL and in close proximity of obstacles. Subjective ratings showed pilots preferred the contour displays over BSL, favouring the combined (C+G) condition. Variability in individual strategy of contour line usage made it difficult to conclude about their effectiveness. However, contour lines demanded more attention and lead to higher cognitive workload than BSL.

After analyis of the results, it was recommended to combine the BSL display with either the C or the G display. However, the usefulness of the displays was considered to be limited as they provided no predictive information beyond 5 seconds while visibility was still good enough to fly on visual information alone. Among the recommendations were a change of FPM colour when below the contour line and an expansion of the contour line along all directions.

The large amount of interindividual variability in both quantitative and qualitative data lead the authors to the main conclusion that HMD symbology should remain customisable among pilots and throughout flight phases. This suggests that there is no user-independent, task-centered

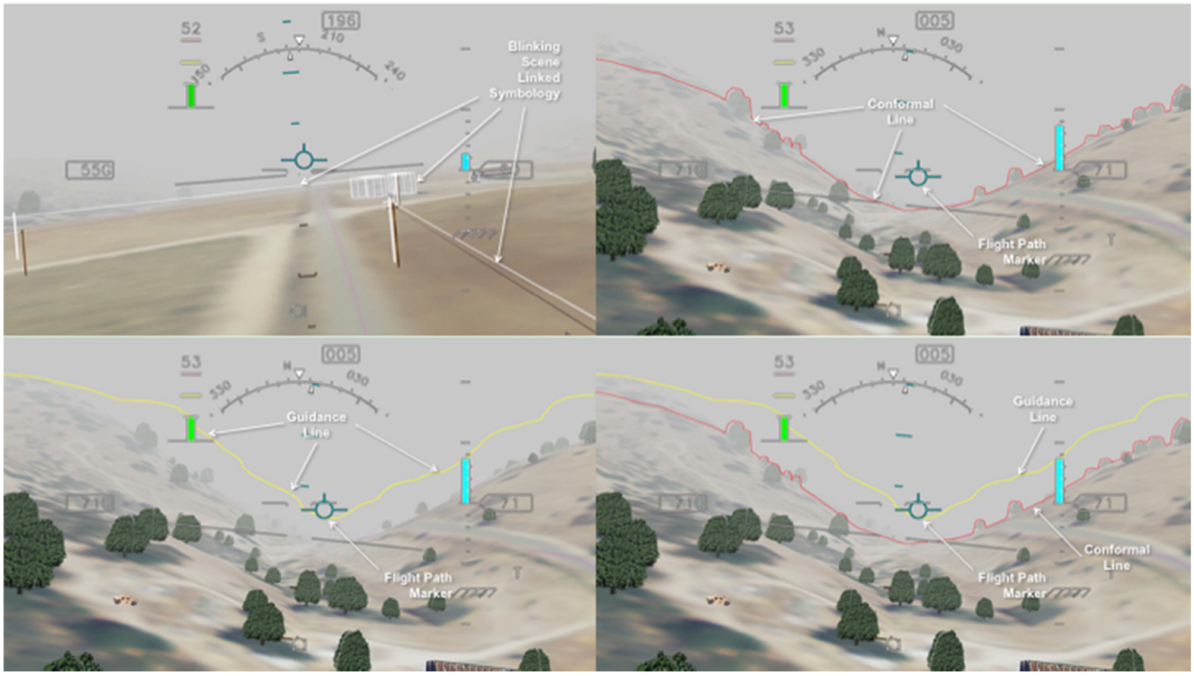

Figure 4.8 – TOAD display concepts. Left to right, top to bottom: Blinking Scene-Linked, Conformal (C), Guidance (G) and C+G. (Source: [9])

visual interface that is optimal for a specific task.

Viertler and Hajek have made a significant effort towards consolidating the results of the aforementioned works on terrain awareness symbology at the Institute of Helicopter Technology of the Technical University of München [73]. Using a sophisticated helicopter simulator they were able to test a fully integrated visual interface consisting of flight guidance and navigation, situational awareness, terrain and obstacle awareness on a full-colour HMD in simulated DVE conditions with visual ranges between 100 m and 800 m. Two displays were tested: The first version had only flight guidance (FG) while the second had flight guidance and sense and avoid (FGSA) symbology.

The full visual interface is shown in Figure 4.9. The FG format consisted of the primary aircraft states shown at the uoper side of the HMD in a T-pattern. The heading tape was shown on top where it interferes the least with the terrain in the visual field. The heading tape is fixed to the world-referenced coordinate system, while the attitude indicator remains fixed with the aircraft body-referenced coordinates system. Navigational markers on the ground show the flight route, causing less clutter compared to a tunnel-in-the-sky. The FGSA display adds STI and obstacle symbols to the FG one. The STI is a combination of an orthogonal grid close to the pilot with ridgelines in the distance to prevent clutter. Lastly, building and rooftop structures are marked by wireframes, obstacles are marked by an outline which, in addition to the state information, culls the STI. Pilots can select the st arting distance of the STI to blend the visible portion of the terrain with the augmentation. Lastly, colour coding is applied to group the various display elements.

16 pilots in total were asked to fly a low-level obstacle avoidance task at a reference height of 100 ft AGL with and without visual augmentation. The results showed that pilots were more effectively controlling airspeed and AGL using the visual aid when visibility decreased in comparison to flying without display augmentation. Workload was significantly reduced

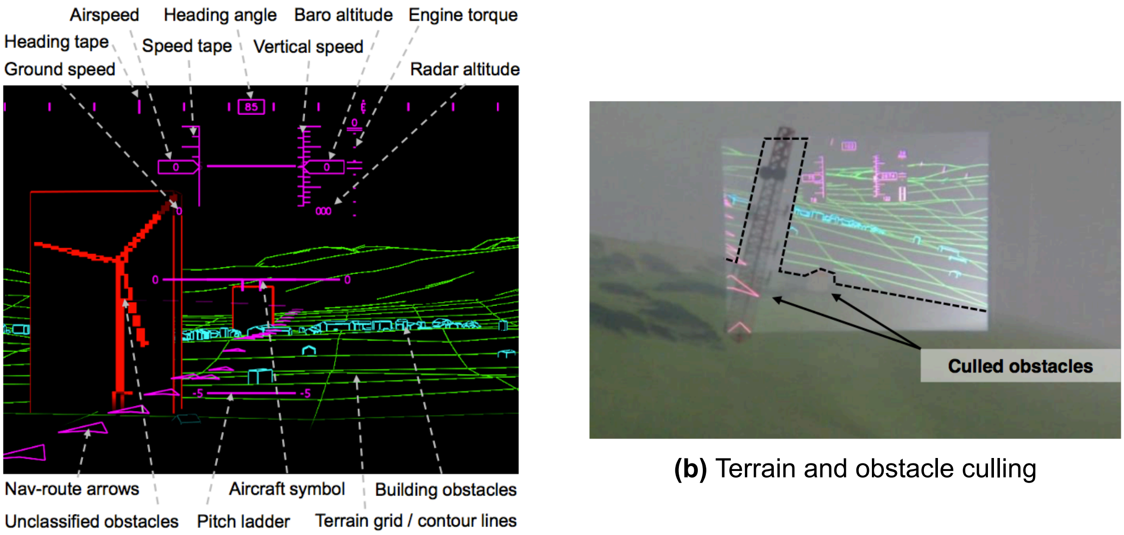

(b) Terrain and obstacle culling

(a) FGSA display

Figure 4.9 – Standalone render (**a**) and in-simulation photo (**b**) of FGSA display concept. (Source: [73])

thanks to the HMD symbology. Furthermore, the minimum allowed TTC before initiating an obstacle avoidance manoeuvre increased and a larger safety margin was maintained using the symbology set.

Regarding the TTC, Viertler and Hajek have limited their tau-analysis to the minimum time to contact before initiating an avoidance manoeuvre. The extent to which a motion guide is followed was beyond the scope of the study. Clark's findings that pilots maintain a τ_{min} of 5 to 8 seconds before initiating the avoidance manoeuvre throughout various visual conditions was confirmed. Moreover, the additional time margin τ_{margin} that pilots kept to manoeuvre in time decreased with higher UCE levels, but the FGSA succeeded in raising this margin by informing pilots of incoming obstacles earlier on.

5

Preliminary Concept

The literature review has established a broad overview of the elements involved in low-level helicopter flight in DVE, by means of an ecological analysis of the work domain, the introduction of tau as a relevant control-theoretical construct, and lastly the state-of-the-art in terrain awareness avionics. On the basis of this knowledge a scientific framework will be developed.

First, in Section 5.1 a research gap will be identified that offers an opportunity for answering the research question. Consecutively, in Section 5.2 a theoretical method is proposed.

5.1. Gap Analysis

First, the influence of some task-dependent features in a terrain avoidance task are unknown. Tau theory literature has shown that human controllers develop and use mental models of the controlled vehicle dynamics to couple onto temporally projected avoidance trajectories. HMD terrain avoidance symbologies such as the safety line visualise the limits of the vehicle dynamics in their automation without an explicit reference to primary flight information. At this point, it is unclear whether the costs of such hidden automation, attentional tunnelling and the lacking support for pilot cognition, are worth the benefits of a lower workload and a potential safety increase. Therefore, it is important first to understand whether the vehicle dynamics have an effect on the timing of an avoidance manoeuvre and the control strategy used. Both factors can be measured through tau theory.

Second, the effects of synthetic terrain imagery (STI) on intrinsic motion-guide following in degraded visual conditions are unknown. Clark has compared rotorcraft pilot control throughout three avoidance manoeuvres in DVE conditions without visual augmentation. The mission task elements he used, such as the hill climb, may be replicated in a more realistic scene and combined with STI. In turn, Jump and Padfield did study tau-guide following in the control strategy of the visually augmented, fixed-wing landing flare, but their symbology was aimed at specific task guidance instead of an increased terrain awareness through STI.

Third, the use of optical invariants such as splay and depression as provided by a visually augmented terrain grid in combination with a visually degraded environment is hardly understood. Flach et al. have shown that for altitude control splay cues are favoured over compression cues. However, the terrain type for which the optical cues were simulated was flat in all tested conditions. Moreover, in the case of visual terrain augmentation of non-flat terrain through a finite grid some discrepancy will occur. This is certainly an interesting topic for our research.

Finally, a lack of knowledge on the influence of terrain grid resolution on pilot control behaviour complicates finding the balance between display clutter and terrain awareness. A lower grid resolution decreases the amount of visible grid lines, so less clutter and attentional switching cost. Contrarily, this also decreases the total optical flow restored by the synthetic grid and the amount of terrain surface detail it reveals. This provides another research opportunity.

5.2. Research Methodology

Multiple theoretical concepts can be combined to attempt to bridge the knowledge gaps described in Section 5.1. This section explains what research methods are built upon and why they are appropriate for answering the research questions.

Tau theory describes the natural perception-action system that controllers use to time and coordinate aircraft motion. As the theory is able to describe the relationship between optical flow and control strategy, it provides a suitable metric system to study the effects of STI on task performance in low-level rotorcraft flight. By and large Clark's approach to tau-analysis of avoidance manoeuvres in DVE will be replicated. Specifically the hill-climb manoeuvre is chosen since it is more relevant to terrain awareness than the quick stop manoeuvre. Moreover, it is longitudinally symmetric, fitting the scope of this research project.

Part-task experimentation will be key to obtain generalisable conclusions. Results from the full terrain-following task in the TOAD study showed that display augmentation using contour and/or guidance lines significantly improves safety and workload. A negative side effect of the guidance (G) display may be a decrease in overall situation awareness and response time to unexpected events due to attentional capture. Moreover, pilot control behaviour showed significant spread, rendering solid understanding of the human-machine interaction more difficult. Therefore, in the present study a deliberate choice is made to limit a human-in-the-loop experiment to a part-task with significantly reduced control freedom for the participants. An additional benefit is that the tau-analysis can be applied with greater ease thanks to total control over the initial conditions before the climb manoeuvre.

Flying experience may be assumed to be irrelevant if the experiment is designed accordingly. First, the proposed part-task experiment will only attempt to offer a preliminary analysis of the effect of conformal STI. Second, the ecological perception-action system of the human controller is assumed to be naturally occurring behaviour, regardless of piloting experience. Third, through automation the control task can be reduced to a single degree of freedom. In order to study the effect of a display that visualises the limits of the aircraft across different helicopter types, it is best to use participants that are unbiased with respect to the vehicle dynamics. In the case of a hill-climb manoeuvre the most important parameter is the heave damping of the helicopter Z_w, which will therefore be an independent variable.

Simulation fidelity is mostly determined by the quality of the visual scene presented. A National Aeronautics and Space Administration (NASA) report on NOE simulation concludes that the visual channel is the primary source of information and that the motion channel provides finer maneuvering feedback [13]. The simulation should provide a very wide FOV and offer ample visual cues through fine scene textures and scattered objects. Moreover, a fixed-base simulator is preferred over a poorly-configured motion system. Display frame rate is of utmost importance.

An **Augmented Reality (AR) headset** was anticipated to be available at the onset of this study. Unfortunately, the display is finally not available due to logistical reasons. To cope with this change, display symbology will be overlaid on the outside visual display of the simulator. This method has been widely used for testing new head-up display (HUD) and HMD interfaces.

6

Experiment Proposal

Based on the literature review and the preliminary concept an experiment is proposed. This chapter describes the experiment in full detail: the research question, experimental set-up and the expected results and outcome.

6.1. Research Question

The goal of the human-in-the-loop experiment is to answer the main research question posed below:

Research question

*What are the effects of **synthetic terrain grid size** in head-worn displays on **task performance** and **control behaviour** in a realistic **hill-climb task** throughout varying **vehicle heave damping** settings in DVE?*

Flach et al. have demonstrated that both angular splay and compression are used to control altitude and that a bias exists towards splay [15]. The grid cell size of a synthetic grid determines the amount of grid lines in the full field of view and thus the amount of visual information available to the observer. More visual information through a smaller grid cell size should lead to a better perception of ego-motion and thus better task performance.

Clark has shown that pilots start their avoidance manoeuvre closer to the slope with decreasing levels of visibility [28]. Comparing the effect of different grid cell sizes on the minimum distance to the slope, no effect is expected as the grid does not affect the level of visibility. Any grid should provide sufficient information about the start of the slope, regardless of cell size.

According to general tau theory, controllers develop mental models of the controlled task that enable them to exert prospective control. Therefore a slower flight-mechanical responses of the controlled element should not lead to an effect on performance but instead to a more anticipating control strategy, e.g. higher minimum time-to-contact and a longer manoeuvre time.

The cross-effect of a low synthetic terrain grid size together with a slower heave response is difficult to predict: there is no prior work that combines these two independent variables.

A lower grid cell size could be a bigger advantage to slower vehicles, because the increased terrain resolution it provides the possibility to detect altitude changes with greater ease compared to a bigger grid size.

Therefore, we could hypothesise the following:

Hypotheses

- *Smaller grid cell size leads to a higher task performance.*
- *Grid cell sizes has no effect is on the minimum distance to the slope.*
- *Lower heave damping coefficient has no effect on performance and leads to a more prospective control strategy.*
- *A lower grid cell size leads to higher task performance in slow response aircraft compared to fast-response aircraft.*

6.2. Experimental Set-up

To evaluate how the visual cues of an augmented reality terrain grid affect pilot behaviour in terrain avoidance in a realistic scenario, a human-in-the-loop experiment will be conducted in the Generic Cockpit Simulator (GECO) at the DLR Institute of Flight Guidance in Braunschweig.

6.2.1. Control Variables

Control task The task is a hill climb MTE with first-order control dynamics on the vertical axis with fixed attitude to control the amount of visible ground texture . Participants are instructed to maintain the same altitude above terrain. A run-in length of 750 m is followed by a slope of 60 m height at an angle of 5 deg, which transitions into a run-out length of 750 m. All runs start at the same initial condition of 70 ft AGL with an initial forward speed of 30 kts, corresponding to about 0.7 eye-heights/s. In order to prevent predictability in the task, To introduce irregularity, the initial position of the vehicle is varied in longitudinal and lateral direction.

Visualisation The terrain simulation aims to achieve a relatively high level of visual fidelity as to give participants a some sense of realism. Therefore, Perlin noise is added to the three straight terrain sections to obtain an irregular ground surface. The average of the terrain noise is corrected to zero. The standard deviation of the terrain noise is set such to not disturb the hill climb task while providing enough visible relief. The ground is rendered using multiple high-resolution textures, to prevent artefacts, and covered with bill-boarded grass. Trees are sparingly added. Linear density fog is simulated with a visible distance of 80 m.

Display The display tested is a square terrain grid. The grid is shown on the outside visual of the simulator to simulate an optical see-through head-worn display (HWD). The mesh points of the grid are set at the same height as the terrain mesh and connected by green, semi-transparent lines with decreasing thickness to simulate depth in the grid. The grid visualisation is culled in the far distance to prevent clutter and always oriented in the direction of flight.

Table 6.1 – Overview of experimental conditions.

Condition	**Cell size**	**Heave time constant**
C1	100 m	1.8 s
C2	200 m	1.8 s
C3	300 m	1.8 s
C4	100 m	3.6 s
C5	200 m	3.6 s
C6	300 m	3.6 s

6.2.2. Independent Variables

Two independent variables are tested: grid cell size c and aircraft heave damping t_W.

Grid Cell Size The grid cell size affects the amount of optical flow restored by the display, the amount of display clutter and the resolution at which the terrain relief is restored by means of the grid. It is not clear how these three variables affect task performance in terms of altitude control, minimum time-to-contact before initiating the avoidance manoeuvre, and motion guide following.

Three grid cell sizes will be tested.

Heave Damping The heave damping time constant is introduced as a second independent variable to test whether changes in the mental model, that controllers develop of the task, affect the control strategy expressed in minimum time-to-contact and motion guide following. Moreover, the addition of this variable allows the identification of a cross-effect of grid cell size and aircraft flight mechanics on task performance.

The first value of the heave damping coefficient Z_W models the flight dynamics in the vertical axis of an UH-60A Blackhawk, leading to a heave time constant of t_{W_1} = 1.8 s. Its calculation is described in Appendix B. The second value of Z_W will have half the magnitude of the first one. Its response will therefore be twice as slow with t_{W_2} = 3.6 s.

This leads to a fully within-subjects experiment design, as shown in Table 6.1. The order of the conditions will be counterbalanced using a latin square design.

6.2.3. Dependent Variables

The following dependent variables will be included:

- root mean square error (RMSE) of the altitude
- Altitude AGL z
- Eye-height velocity $\dot{x}_e$
- Distance to slope in flight path direction d
- Minimum time to contact τ_{min}

- Variance of control input signal σ_{δ_c} as a measure for the control activity
- Flight path angle error γ_a for motion-guide analysis
- Subjective feedback through a questionnaire

6.2.4. Participants

A total of 18 participants will be recruited among the Institute's personnel. The experiment is designed as a part-task experiment so participants can be task-naive, e.g. no flight experience is required. Participant experience in flying and/or video games will be registered beforehand for later reference.

6.2.5. Experimental Procedures

Familiarisation phase Participants will be requested to read a briefing sent by email prior to the experiment. The briefing contains information about the research context, the task to perform (to maintain altitude), and a testing schedule. This briefing is verbally repeated to the participants at the start of the experiment. No reference will be made to the hill climb manoeuvre that is tested.

First, a training phase is started so participants can practice controlling the altitude in a special training scene with large, irregular hills in good visual conditions. It will be instructed to look maintain eye focus in the direction of flight. A score will be calculated and given to the participants for motivation and to indicate training progress. Through the familiarisation phase participants will get accustomed to both settings of the heave damping. Once task performance has converged, the degraded visual conditions of the experiment will be introduced to the training, without display augmentation.

Once the training phase is finished, a short 10-minute break will be given. The familiarisation phase should not take more than an hour, including briefing, training and break.

Measurement Phase The experimental conditions are tested next. Before each experimental condition, the vehicle type will be announced as vehicle 1 or 2 so pilots are able to anticipate the vehicle response to their inputs. Participants will be verbally encouraged after each run.

Each run will take approximately 120 seconds and will be repeated three times in order to measure average performance. Participants will be recommended to take micro-breaks after every run and will take mandatory breaks (max. 10 min) after each pair of experimental conditions. This means that each pair and its associated break will take up to 25 minutes and the whole measurement phase should take less than 1.5 hour.

A post-experiment questionnaire will be used to evaluate overall appreciation of the task, the grid display and the experiment as a whole.

6.2.6. Apparatus

The study will be conducted in the GECO simulator. The simulator has a wooden A320 cockpit shell and a collimated visual system, providing depth perception of infinity, using three high resolution projectors (2160x1440 pixels) displaying an area of 180° x 40°. A spring-loaded, passive side-stick will be used as manipulator, of which only the longitudinal axis will be measured. Care will be taken as to position all participants in the same longitudinal position in the right seat of the simulator.

6.3. Results, Outcome and Relevance

The expected results will include plots of the independent variables as a function of the dependent variables. Namely:

- Grid cell size c
- Heave damping time constant t_w

Vs.

- Task performance: RMS of altitude, eye-height velocity $\dot{x}_e$
- Safety: minimum time-to-contact τ_{min}
- Control activity: variance of control input signal σ_{δ_c}
- Motion-guide following: coupling constant k, manoeuvre time T, overshoot of goal flight path angle
- Subjective feedback of grid cell sizes

To ensure the repeated measures analysis of variance (ANOVA) test can be used, the data will first be tested on sphericity and normality [74]. Normality is tested using a Shapiro-Wilkes test, where a skewness of 0 and a Kurtosis of 3 should be found, or using a Kolmogorov-Smirnov test. Sphericity is tested using Mauchly's test since it is a fully within-subjects design. If the data is normally distributed and tested for sphericity, an ANOVA test can be applied, to compare the mean of the samples to a 'grand' mean. Note that the ANOVA is only used on interval and ratio data, since it works with a mean, which can not be taken from ordinal data. After the ANOVA test, post hoc tests will be used to trace the condition that causes any significant results. These can be Tukey's T-test, or a non-parametric Friedman test in case of non-normality. A non-parametric test transforms the data into ordinal data and looks for variability in the rank between experimental conditions. Wilcoxon Signed Rank test can be used if post-hoc tests are needed.

To summarise:

- Repeated measures ANOVA test
- Shapiro-wilkes test
- Kolmogorov-Smirnov test
- Non-Parameteric Friedman test (if necessary)
- Post hoc tests (if necessary)
  - Tukey's T-test after the ANOVA test
  - Wilcoxon Signed Rank test after the non-parametric Friedman test

This experiment will help understand how terrain awareness displays in HWDs are used in a terrain following task. More specifically, it will make clear whether the grid cell size has an impact on task performance and control behaviour. The unique characteristic of the experimental design is the application of tau theory to a visual conformal terrain symbology. A deliberate choice is made to study the effects of task-dependent variables on pilot control behaviour so that the resulting knowledge can be used to design visual interfaces that are user-independent.

In case cell grid size and flight-mechanical response exert a cross-effect on pilot control behaviour, this would bring about an important incentive for the industry. Namely, this would mean that a generic HWD symbology design can not be routinely applied to a range of different helicopters. Either the effect of various display settings would have to be tested for a range of flight-dynamic properties, or an extra selling point would be created for guidance symbology such as the safety line.

Bibliography

[1] J. Vreeken, H. Haverdings, and M. Joosse. *Helicopter flight in a Degraded Visual Environment*. Tech. rep. NLR-CR-2013-229. National Aerospace Laboratory NLR, 2013.

[2] S. J. Gaydos, M. J. Harrigan, and A. J. R. Bushby. “Ten years of spatial disorientation in U.S. Army rotary-wing operations”. In: *Aviation Space and Environmental Medicine* 83 (8 2012), pp. 739–745.

[3] Alex Cameron and Ross Hobson. “Head-up, eyes-out in day and at night: Striker HMD, evolution or revolution?” In: *Degraded Visual Environments: Enhanced, Synthetic, and External Vision Solutions 2016*. Ed. by Jack Sanders-Reed; Jarvis J. Arthur. Vol. 9839. 2016, 98390W–98390W–11.

[4] Stuart Lau. “HTAWS to be mandated on all EMS helicopters”. In: *Professional Pilot* 46 (6 2012).

[5] M. Yeh, C. D. Wickens, and F. J. Seagull. “Effects of frame of reference and viewing condition on attentional issues with helmet mounted displays”. In: *Effects of Frame of Reference and Viewing Condition on Attentional Issues with Helmet Mounted Displays* (1998).

[6] R. S. McCann, D. C. Foyle, and J. C. Johnston. “Attentional limitations with head-up displays”. In: *Proceedings of the 7th International Symposium on Aviation Psychology* (1993), pp. 70–75.

[7] Steven Fadden, Christopher D Wickens, and Patricia Ververs. “Costs and benefits of head-up displays: An attention perspective and a meta analysis”. In: *SAE transactions* 109 (1 2000), pp. 1112–1117.

[8] Thomas Münsterer et al. “Sensor-enhanced 3D conformal cueing for safe and reliable HC operation in DVE in all flight phases”. In: 9087 (2014), p. 90870I.

[9] Zoltan Szoboszlay, Allon Kahana, and M Rottem-Hovev. “Terrain and Obstacle Avoidance Displays for Low-Level Helicopter Operations in Degraded Visual environments”. In: (2016).

[10] Earl L Wiener and Renwick E Curry. “Flight-deck automation: Promises and problems”. In: *Ergonomics* 23 (10 1980), pp. 995–1011.

[11] Lisanne Bainbridge. “Ironies of automation”. In: *Automatica* 19 (6 1983), pp. 775–779.

[12] *Helicopter Air Ambulance, Commercial Helicopter, and Part 91 Helicopter Operations; Final Rule*. Tech. rep. 35. Federal Aviation Administration, 2014.

[13] Gregory W Condon. *Simulation of nap-of-the-Earth flight in helicopters*. Tech. rep. NASA-TM-102830. 1991.

[14] Christopher D. Wickens and Justin G. Hollands. *Engineering psychology and human performance*. Upper Saddle River, NJ: Prentice Hall, 2000.

[15] John M Flach et al. “Perception and control of altitude: Splay and depression angles”. In: *Journal of Experimental Psychology: Human Perception and Performance* 23 (6 1997), p. 1764.

[16] James J Gibson. “The perception of the visual world”. In: (1950).

[17] Walter W Johnson and Cynthia A Awe. “The selective use of functional optical variables in the control of forward speed”. In: (1994).

[18] William H Warren, Michael W Morris, and Michael Kalish. “Perception of translational heading from optical flow”. In: *Journal of Experimental Psychology: Human Perception and Performance* 14 (4 1988), p. 646.

[19] John A Perrone. *The perception of surface layout during low level flight*. Tech. rep. 1991.

[20] William H Warren and Daniel J Hannon. “Direction of self-motion is perceived from optical flow”. In: *Nature* 336 (6195 1988), pp. 162–163.

[21] J. H. Rieger and D. T. Lawton. “Processing differential image motion”. In: *Journal of the Optical Society of America A* 2 (2 1985), pp. 354–359.

[22] David N Lee. “A theory of visual control of braking based on information about time-to-collision”. In: *Perception* 5 (4 1976), pp. 437–459.

[23] John M. Foley. “Binocular distance perception”. In: *Psychological Review* 87 (5 1980), pp. 411–434.

[24] Jos Monen and Eli Brenner. “Detecting changes in one’s own velocity from the optic flow”. In: *Perception* 23 (6 1994), pp. 681–690.

[25] Denis N Lee and H Kalmus. “The optic flow field: The foundation of vision [and discussion]”. In: *Philosophical Transactions of the Royal Society B: Biological Sciences* 290 (1038 1980), pp. 169–179.

[26] Barry J Baskett. *Aeronautical Design Standard performance specification Handling Qualities requirements for military rotorcraft*. Tech. rep. No. ADS-33E-PRF. US Army Aviation and Missile Command, 2000.

[27] GD Padfield. “The tau of flight control”. In: *The Aeronautical Journal* 115 (1171 2011), pp. 521–556.

[28] Gary A Clark. “Helicopter handling qualities in degraded visual environments”. PhD thesis. University of Liverpool, 2007.

[29] David N Lee and David S Young. “Visual timing of interceptive action”. In: *Brain mechanisms and spatial vision*. Springer, 1985, pp. 1–30.

[30] Audrey LH van der Meer, FR Ruud van der Weel, and David N Lee. “Prospective control in catching by infants”. In: *Perception* 23 (3 1994), pp. 287–302.

[31] David N Lee, David S Young, and Dennis Rewt. “How do somersaulters land on their feet?” In: *Journal of Experimental Psychology: Human Perception and Performance* 18 (4 1992), p. 1195.

[32] Cathy M Craig and David N Lee. “Neonatal control of nutritive sucking pressure: evidence for an intrinsic tau-guide”. In: *Experimental Brain Research* 124 (3 1999), pp. 371–382.

[33] William H Warren Jr, David S Young, and David N Lee. “Visual control of step length during running over irregular terrain”. In: *Journal of Experimental Psychology: Human Perception and Performance* 12 (3 1986), p. 259.

[34] D. N. Lee and B. Schögler. “Music through movement”. In: *Communicative Musicality: Narratives of Expressive Gesture and Being Human*. Ed. by S. MALLOCH and C. TREVARTHEN. Oxford: Oxford University Press, 2007.

[35] D. N. Lee et al. “Steering by echolocation: a paradigm of ecological acoustics”. In: *Journal of Comparative Physiology A* 176 (3 1995), pp. 347–354.

[36] David N Lee, Mark NO Davies, and Patrick R Green. “Visual control of velocity of approach by pigeons when landing”. In: *Journal of experimental biology* 180 (1 1993), pp. 85–104.

[37] David N Lee. “Tau in action in development”. In: *Action As An Organizer of Learning and Development: Volume 33 in the Minnesota Symposium on Child Psychology Series*. Vol. 33. 2005, p. 1.

[38] Gareth D Padfield, David N Lee, and Roy Bradley. “How do helicopter pilots know when to stop, turn or pull up?(Developing guidelines for vision aids)”. In: *Journal of the American Helicopter Society* 48 (2 2003), pp. 108–119.

[39] Gareth D Padfield and A Taghizad. “How long do pilots look forward?” In: *31st European Rotorcraft Forum, Florence, Italy*. 2005.

[40] Michael Jump and Gareth Padfield. “Tau Flare or not Tau Flare: that is the question: Developing Guidelines for an Approach and Landing Sky Guide”. In: *AIAA Guidance, Navigation, and Control Conference and Exhibit*. American Institute of Aeronautics and Astronautics, 2005.

[41] Martin Liggins II, David Hall, and James Llinas. *Handbook of multisensor data fusion: theory and practice*. CRC press.

[42] anon. *Certification of Transport Category Aircraft*. Tech. rep. Federal Aviation Administration, 2014.

[43] Glenn Connor. “Sandel, Garmin and Honeywell develop new HTAWS to warn pilots about wires, cables and power lines”. In: *Professional Pilot* 48.6 (June 2014), pp. 48–52.

[44] Thorsten W. Eger. “Operational requirements for helicopter operations low level in degraded visual environment”. In: *Degraded Visual Environments: Enhanced, Synthetic, and External Vision Solutions*. Vol. 8737. Proc. SPIE. 2013.

[45] P. M. Ververs and C. D. Wickens. “Head-up displays: Effects of clutter, display intensity, and display location on pilot performance”. In: *International Journal of Aviation Psychology* 8 (4 1998), pp. 377–403.

[46] C. E. Rash et al. *Helmet-mounted displays: Sensation, perception and cognition issues*. Tech. rep. 2009.

[47] Richard L. Newman and Kevin W. Greeley. *Helmet-Mounted Display Design Guide*. Tech. rep. TR-97-11. Aeroflightdynamics Directorate, 1997.

[48] K. W. Arthur. “Effects of field of view on performance with head-mounted displays”. Diss. University of North Carolina at Chapel Hill, 2000.

[49] J. E. Melzer et al. “Guidelines for HMD Design”. In: *Helmet-Mounted Displays: Sensation, Perception and Cognition Issues*. Ed. by Michael B. Russo Clarence E. Rash. Fort Rucker, Alabama: U.S. Army Aeromedical Research Laboratory, 2009, pp. 805–848.

[50] C. E. Rash et al. *Design issues for Helmet-Mounted Display systems for rotary-wing aviation*. Tech. rep. USAARL Report No. 98-32. U.S. Army Aeromedical Research Laboratory, 1998.

[51] R. Patterson, M. D. Winterbottom, and B. J. Pierce. “Perceptual issues in the use of head-mounted visual displays”. In: *Human Factors* 48 (3 2006), pp. 555–573.

[52] I. Larish and C. D. Wickens. *Divided attention with superimposed and separated imagery: Implications for Head-Up Displays*. Tech. rep. ARL-91-4/NASA HUD-91-1. University of Illinois Institute of Aviation, 1991.

[53] III Arthur J. J. et al. “Synthetic Vision Enhanced Surface Operations with Head-Worn Display for Commercial Aircraft”. In: *The International Journal of Aviation Psychology* 19 (2 2009), pp. 158–181.

[54] Nadine Moacdieh and Nadine Sarter. “Clutter in Electronic Medical Records Examining Its Performance and Attentional Costs Using Eye Tracking”. In: *Human Factors* 57 (4 2015), pp. 591–606.

[55] C. D. Wickens. “Attentional issues in head-up displays”. In: *Engineering psychology and cognitive ergonomics: Transportation systems* 1 (1997), pp. 3–21.

[56] J. L. Merlo. “Effect of Reliability on Cue Effectiveness and Display Signaling”. Master’s thesis. University of Illinois at Urbana-Champaign, 1999.

[57] C. D. Wickens and J. Long. “Object Versus Space-Based Models of Visual Attention: Implications for the Design of Head-Up Displays”. In: *Journal of Experimental Psychology: Applied* 1 (3 1995), pp. 179–193.

[58] Steven Fadden, Patricia May Ververs, and Christopher D. Wickens. “Costs and benefits of head-up display use: A meta-analytic approach”. In: *Proceedings of the Human Factors and Ergonomics Society*. Vol. 1. 1998, pp. 16–20.

[59] C. D. Wickens. “Attentional tunneling and task management”. In: *International Symposium on Aviation Psychology*. Vol. 13. 2005, pp. 620–625.

[60] D. C. Foyle, R. S. McCann, and S. G. Shelden. “Attentional issues with superimposed symbology: Formats for scene-linked displays”. In: *International Symposium on Aviation Psychology*. Vol. 8. 1995, pp. 98–103.

[61] David C. Foyle, Mary K. Kaiser, and Walter W. Johnson. “Visual cues in low-level flight: Implications for pilotage, training, simulation, and enhanced/synthetic vision systems”. In: *Annual Forum Proceedings - American Helicopter Society*. Vol. 1. 1992, pp. 253–260.

[62] Gary L. Martinsen et al. “Luminance contrast requirements for colored symbols in helmet-mounted displays”. In: *Helmet- and Head-Mounted Displays VII*. Ed. by C. E. Reese C. E. Rash. Vol. 4711. Proc. SPIE. 2002, pp. 356–364.

[63] Thomas H. Harding, John S. Martin, and Clarence E. Rash. “The legibility of HMD symbology as a function of background local contrast”. In: *Head- and Helmet-Mounted Displays XII: Design and Applications*. Ed. by C. E. Reese R. W. Brown. Vol. 6557. Proc. SPIE. 2007.

[64] J. L. Gabbard et al. “More than meets the eye: An engineering study to empirically examine the blending of real and virtual color spaces”. In: *Virtual Reality Conference (VR)*. Proc. IEEE. 2010, pp. 79–86.

[65] J. L. Gabbard, J. E. Swan, and A. Zarger. “Color blending in outdoor optical see-through AR: The effect of real-world backgrounds on user interface color”. In: *Virtual Reality Conference (VR)*. Proc. IEEE. 2013, pp. 157–158.

[66] M. Fares and D. R. Jordan. “The impact of coloured symbology on cockpit eyes-out display effectiveness: A survey of key parameters”. In: *Display Technologies and Applications for Defense, Security, and Avionics IX; and Head- and Helmet-Mounted Displays XX*. Ed. by Peter L. Marasco D. D. Desjardins. Vol. 9470. Proc. SPIE. 2015.

[67] B Corwin, R Whillock, and J Groat. *Synthetic terrain imagery for helmet-mounted display*. Tech. rep. WL-TR-95-3025. Flight Dynamics Directorate, 1994.

[68] Kohei Funabiki et al. “Flight experiment of pilot display for search-and-rescue helicopter”. In: vol. 7326. 2009.

[69] Thomas Münsterer, Martin Kress, and Stephanus Klasen. “Sensor based 3D conformal cueing for safe and reliable HC operation specifically for landing in DVE”. In: *SPIE Defense, Security, and Sensing*. 2013.

[70] Philipp Völschow et al. “Display of real-time 3D sensor data in a DVE system”. In: *Degraded Visual Environments: Enhanced, Synthetic, and External Vision Solutions*. Vol. 9839. Proc. SPIE. 2016.

[71] Thomas Münsterer et al. “HMI aspects of the usage of ladar 3D data in pilot DVE support systems”. In: vol. 9471. 2015, 94710F–94710F–11.

[72] Thomas Münsterer et al. “DVE flight test results of a sensor enhanced 3D conformal pilot support system”. In: vol. 9471. 2015, pp. 947106–947106–7.

[73] Franz Viertler and Manfred Hajek. “Evaluation of visual augmentation methods for rotorcraft pilots in degraded visual environments”. In: *Journal of the American Helicopter Society* 62 (1 2017), pp. 1–11.

[74] Andy Field. *Discovering statistics using SPSS*. Sage publications.

[75] David N Lee. “Guiding movement by coupling taus”. In: *Ecological psychology* 10 (3-4 1998), pp. 221–250.

[76] Gareth D Padfield. *Helicopter flight dynamics*. John Wiley & Sons.

[77] Ki C Kim. *Analytical Calculations of Helicopter Torque Coefficient (CQ) and Thrust Coefficient (CT) Values for the Helicopter Performance (HELPE) Model*. Tech. rep. DTIC Document, 1999.

[78] Thomas R Norman et al. *Low-speed wind tunnel investigation of a full-scale UH-60 rotor system*. Tech. rep. DTIC Document, 2002.

[79] Patrick M Shinoda, Hyeonsoo Yeo, and Thomas R Norman. “Rotor Performance of a UH□60 Rotor System in the NASA Ames 80□by 120□Foot Wind Tunnel”. In: *Journal of the American Helicopter Society* 49 (4 2004), pp. 401–413.

III

Appendices

To be graded

A

Constant Acceleration Tau-Guide

The constant acceleration tau-guide is derived in this appendix [75].

For constant acceleration, the initial (t=0) remaining distance to close the motion gap depends on the amount of time to close that gap, as expressed through Equation (A.1).

$$x = \frac{1}{2}T^2\,\ddot{x} \tag{A.1}$$

At instant t, this distance is reduced by:

$$x = \frac{1}{2}t^2\,\ddot{x} \tag{A.2}$$

Therefore,

$$x(t) = \frac{1}{2}\ddot{x}\,T^2 - t^2\square \tag{A.3}$$

$$\dot{x}(t) = -\ddot{x}t \tag{A.4}$$

Introducing the expression for the tau of motion gap and substituting the expressions for x and $\dot{x}$:

$$\tau_{x(Const.Acc)} = \frac{x}{\dot{x}} = \frac{\frac{1}{2}\ddot{x}\,T^2 - t^2\square}{-\ddot{x}t} = \tau_g \tag{A.5}$$

This simplifies to Equation (F.9).

$$\tau_g = \frac{1}{2}\,t - \frac{T^2}{t}\square \tag{A.6}$$

B

Heave Motion Constant Calculation

The heave damping coefficient Z_w (s^{-1}) was calculated for the UH60 blackhawk using Equation (B.1) according to Padfield [76].

$$Z_w = -\frac{\rho a_0 V A_b}{2 M_a} \frac{4}{8\mu + a_0 s} \tag{B.1}$$

With ρ the air density (kg/m^3), a_0 the main rotor blade lift curve slope (rad^{-1}), A_b the main rotor blade area (m^3), M_a the aircraft mass (kg), s the rotor solidity and μ the unitless advance ratio as calculated using Equation (B.2).

$$\mu = \frac{V}{\Omega R} \tag{B.2}$$

V is the freestream velocity (m/s), Ω nominal rotor rotational speed (rad/s) and R the rotor radius (m).

Table B.1 contains the numerical values for both aircraft used in and resulting from the calculation of Z_w. The UH-60 data was collected across various NASA publications [77–79].

Table B.1 – Numerical properties of UH-60 for calculation of heave damping.

Property	unit	UH-60
a_0	rad^{-1}	5.73
V	kts	30
R	ft	26.83
A_b	ft^2	186.9
M_a	lb	16260
Ω	rad/s	32.88
μ	-	0.0574
s	-	0.08210
Z_w	s^{-1}	-0.5487

C

UH-60 Z-Force Control & Stability

The vertical stability and control properties of the UH-60 have been calculated. The dynamic model used in the simulator assumed first-order linear dynamics in the heave axis is described by Equation (C.1).

$$\dot{w} = Z_{\theta_0}\theta_0 + Z_w w \tag{C.1}$$

With w the vertical velocity (m/s), Z_{θ_0} the dimensionless collective control derivative in the Z-axis, and Z_w the heave damping coefficient (s^{-1}). However, as the value for Z_{θ_0} is unknown, a similar equation was used relating the collective stick input directly to the heave motion, as in Equation (C.2).

$$\dot{w} = Z_{\delta_c}\delta_c + Z_w w \tag{C.2}$$

With Z_{δ_c} the Z-force collective control sensitivity (ft/in./s^2) and δ_c the collective control input (in.). The excursion of the collective stick is measured in inches but its range is unknown. To solve this, the limits of the main rotor collective pitch angle θ_0 can be used in conjunction with the equation for the control gearing to calculate the maximum range of the collective stick in the UH-60.

$$\theta_0 = C_6\delta_c + C_5 \tag{C.3}$$

Where C_5 is the main rotor root collective pitch for zero collective stick (rad) and C_6 the main rotor collective control sensitivity (rad/in.). The resulting range is then mapped to the digital sidestick signal and used in the flight dynamic model. Table C.1 shows the control parameters used in the dynamic model for the UH60.

Table C.1 – Numerical properties of UH-60 used in simulation control settings.

Property	unit	UH-60
C_5	rad	0.2286
C_6	rad/in.	0.2792
$\theta_{0_{min,max}}$	deg	⍰9.9, 25.9⍰

D

Tau Analysis Plots

This appendix presents run-averaged dot plots that were made in the tau analysis. The runs included in each figure are selected based on the subjective rating of the second half of the fit as explained in Section F.3.

D.1. Flight path angle gap

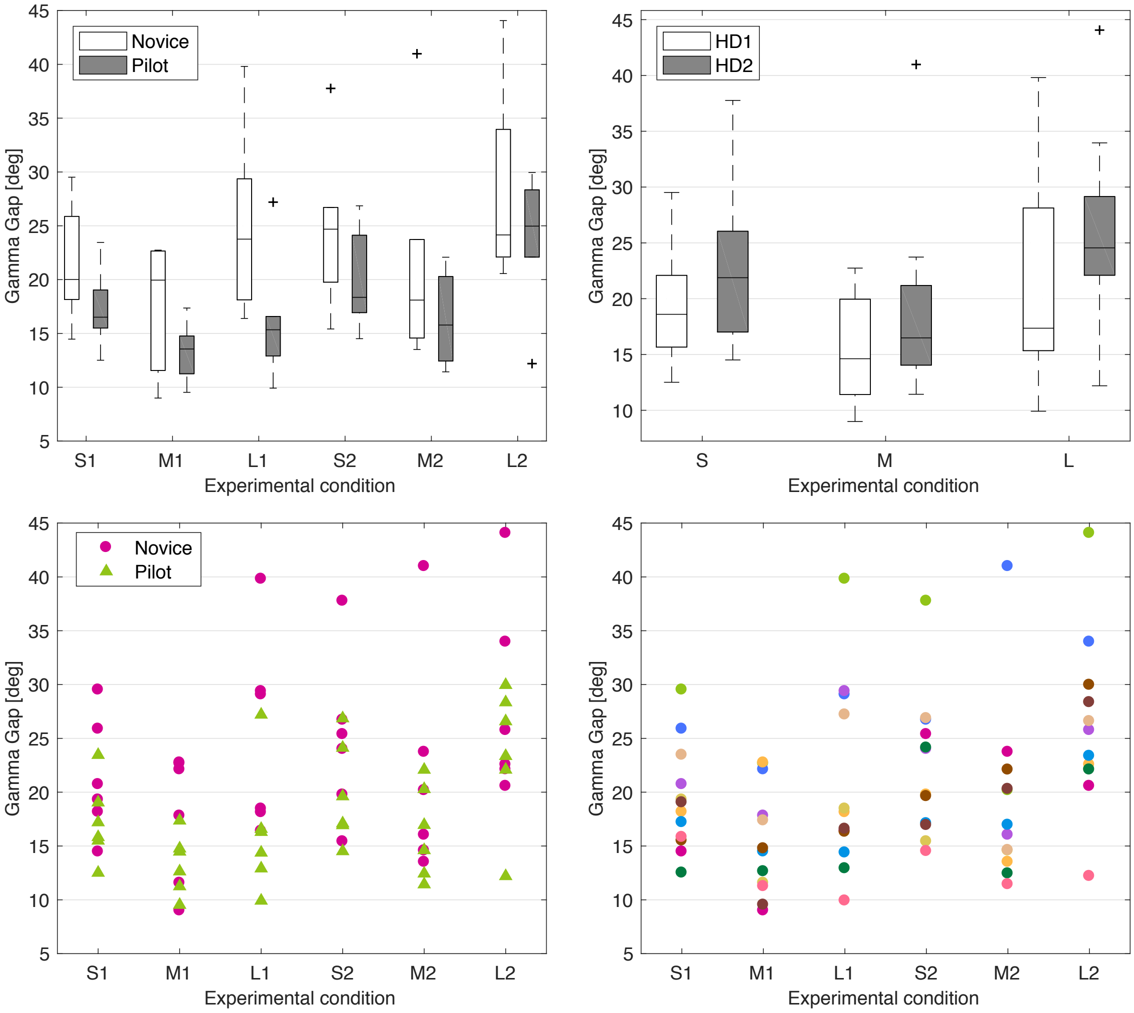

Figure D.1 – Run-averaged flight path angle gap γ_a.

D.2. Maneuver duration

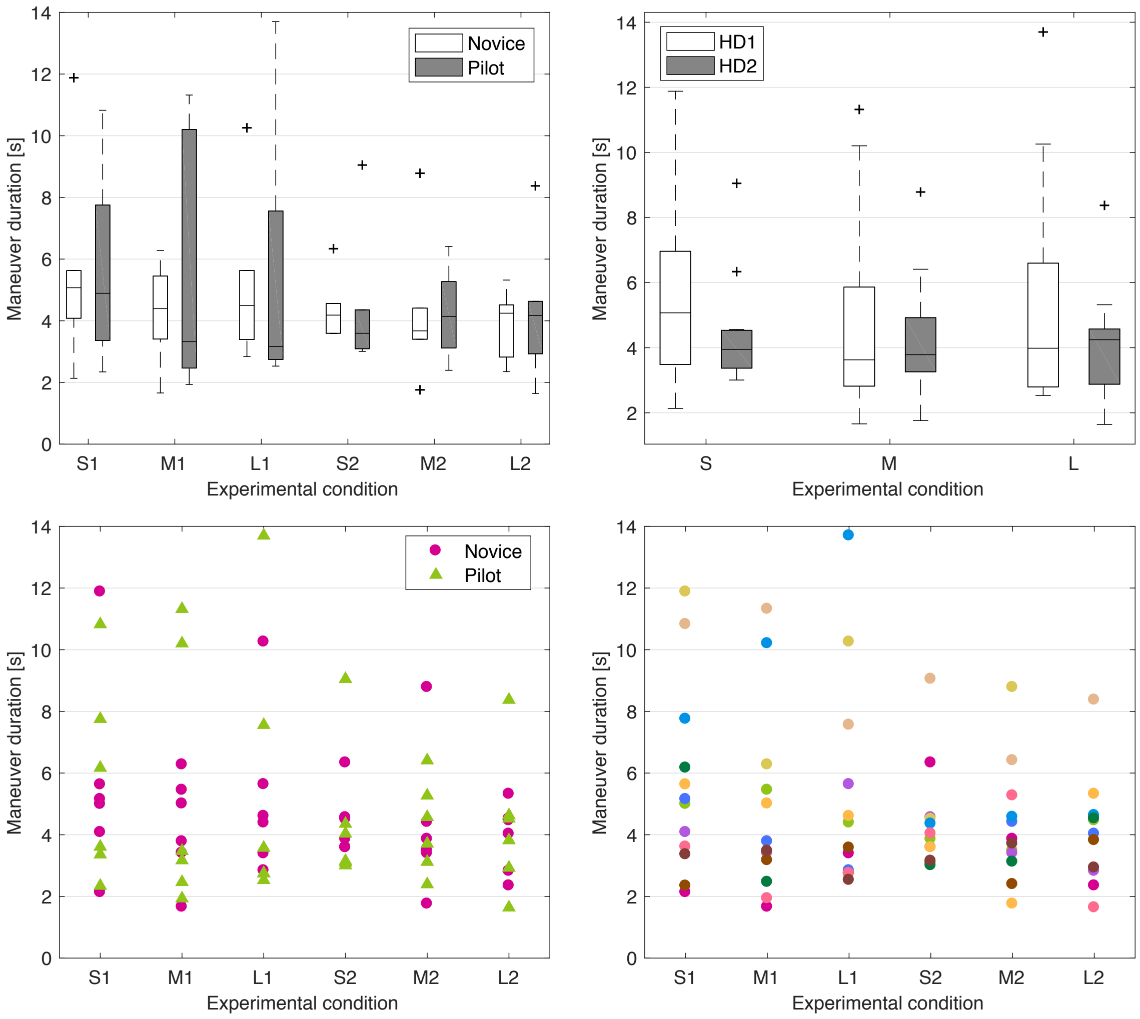

Figure D.2 – Run-averaged maneuver duration *T*.

D.3. Coupling constant

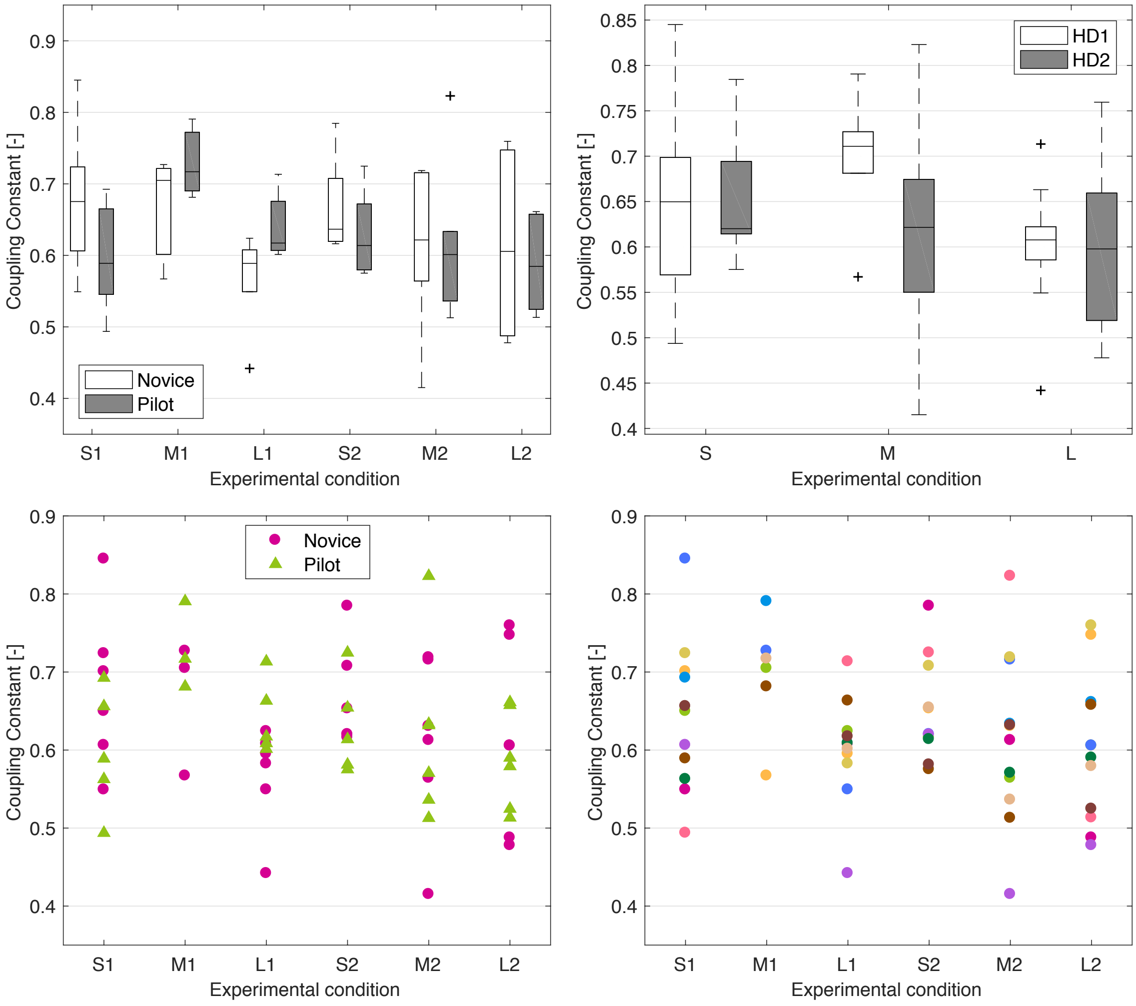

Figure D.3 – Run-averaged coupling constant *k*, all fits included.

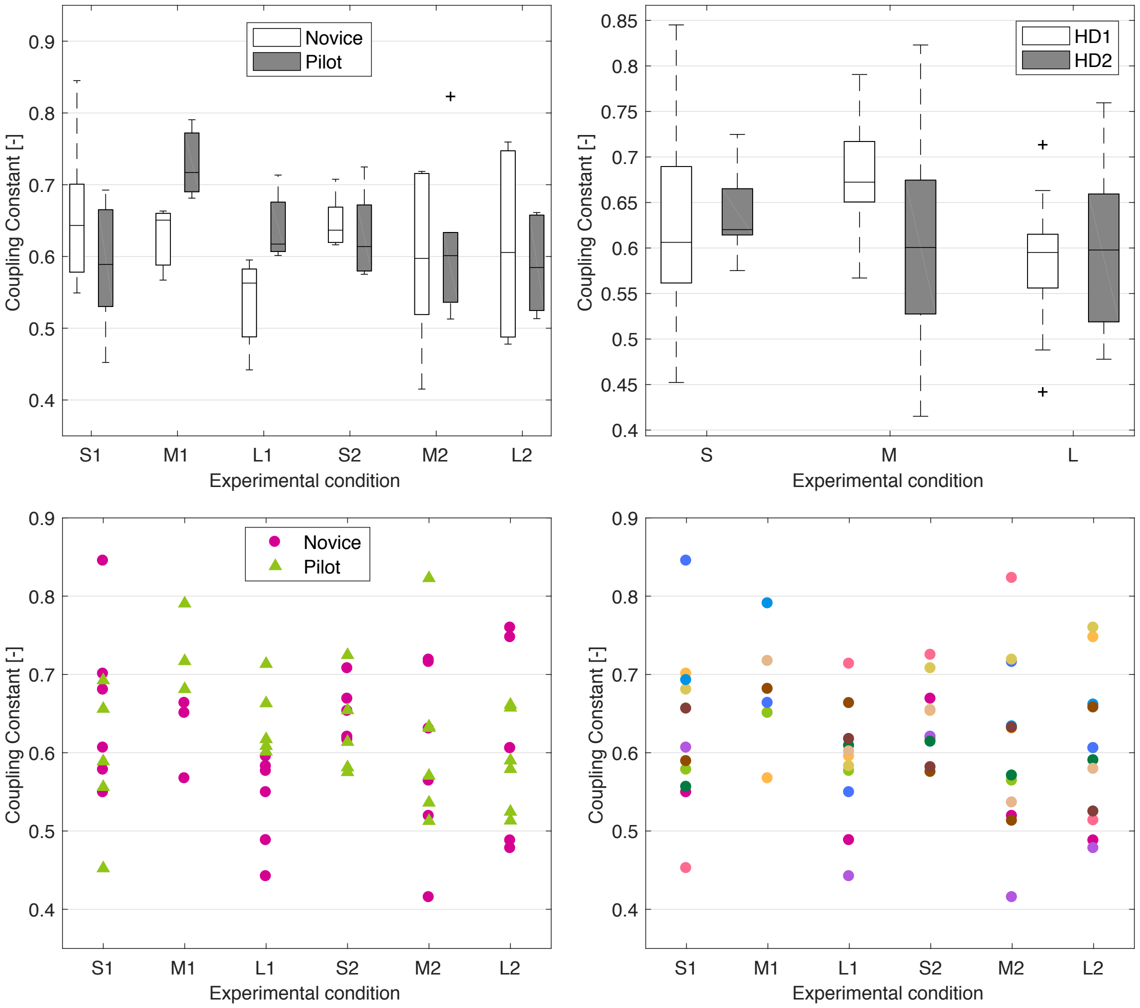

Figure D.4 – Run-averaged coupling constant *k*, excluding fits rated below 2.

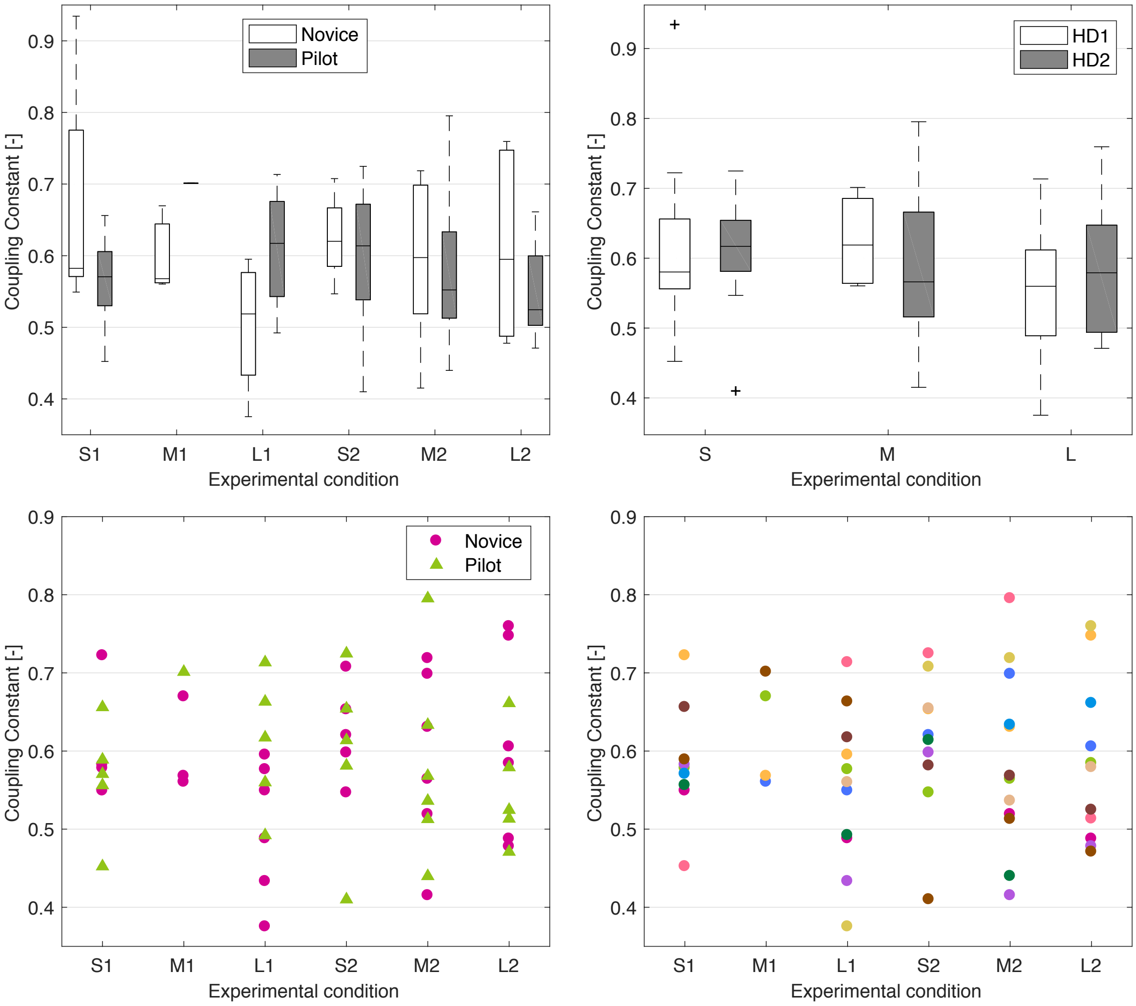

Figure D.5 – Run-averaged coupling constant *k*, excluding fits rated below 3.

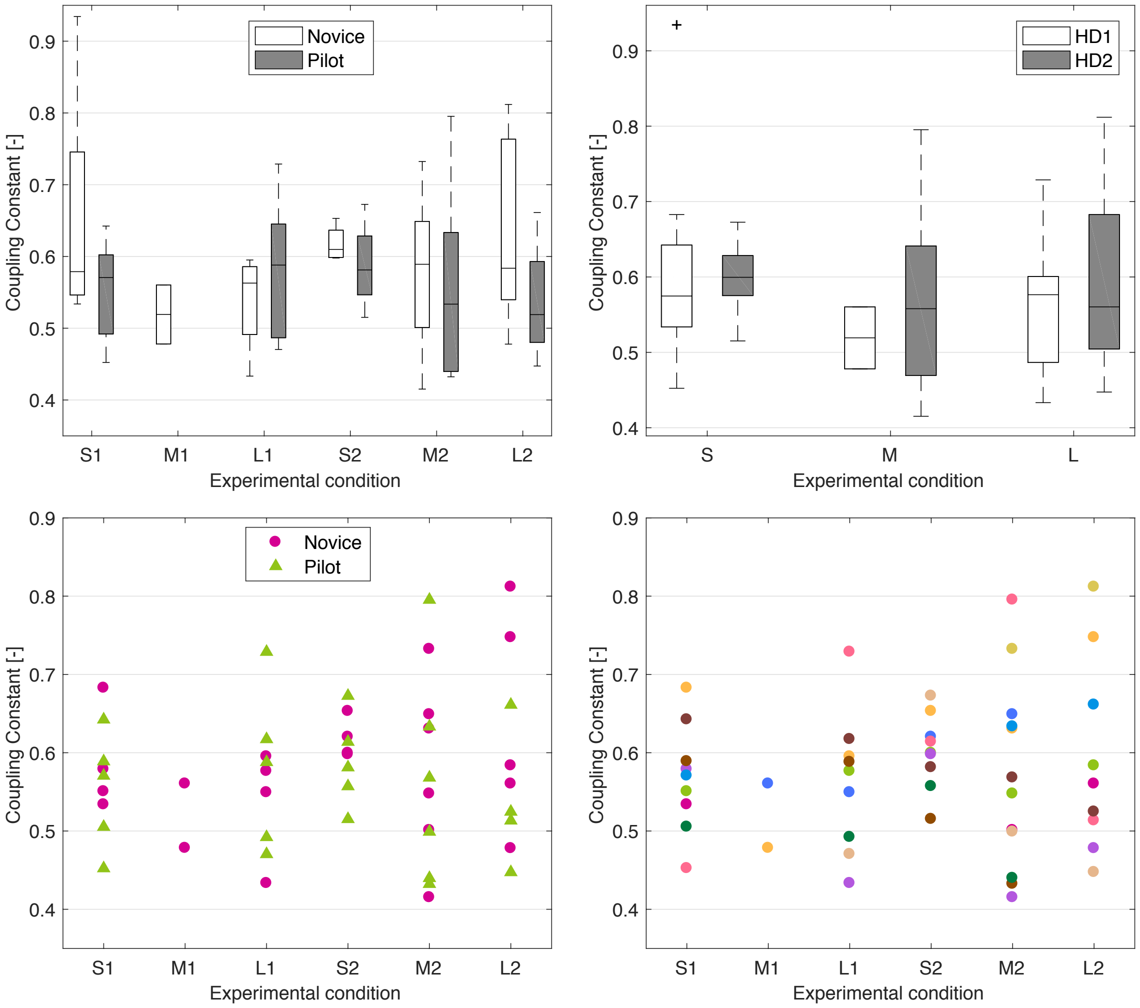

Figure D.6 – Run-averaged coupling constant *k*, excluding fits rated below 4.

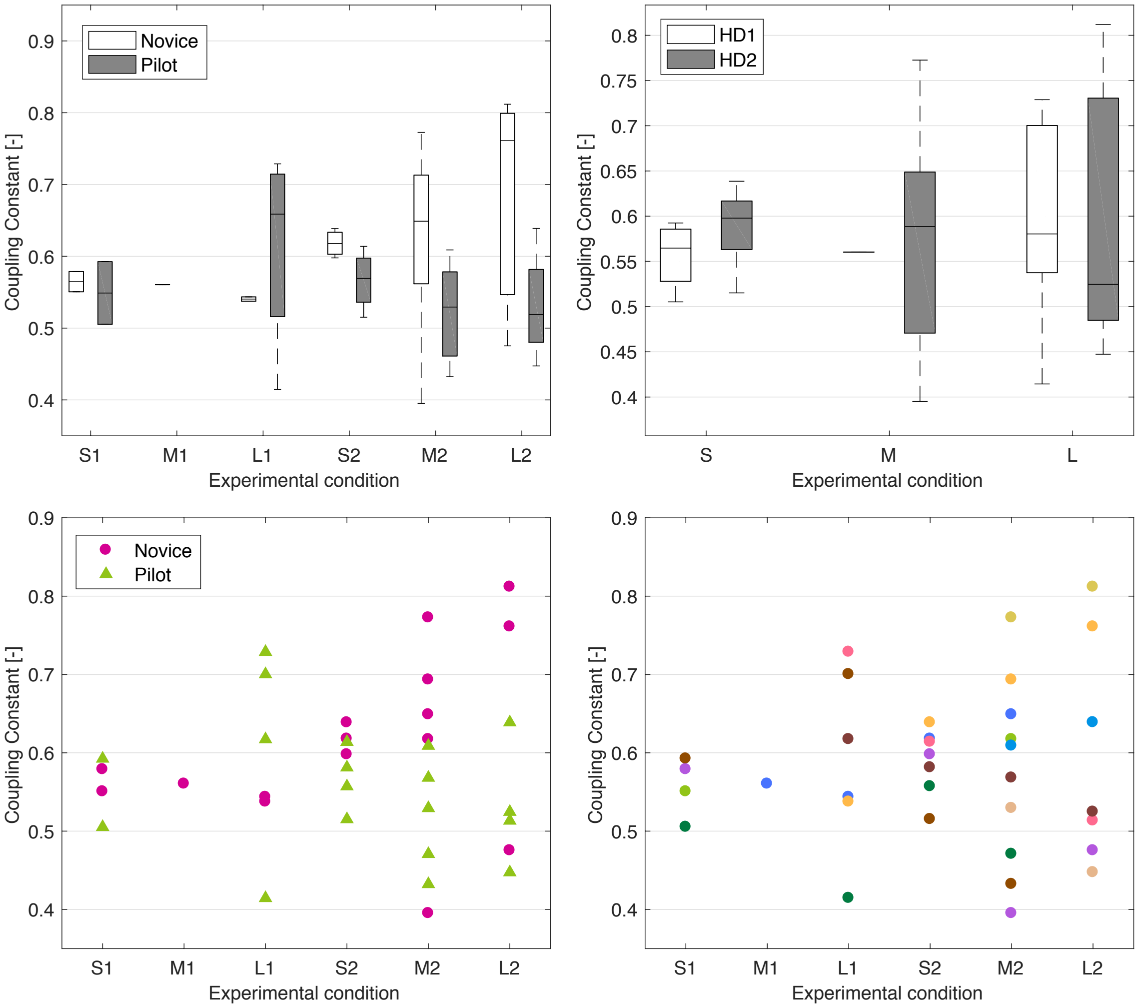

Figure D.7 – Run-averaged coupling constant *k*, excluding fits rated below 5.

E

Statistical Analysis

This Appendix presents the detailed statistical analysis of the experiment results. Statistical software package SPSS 24 was used. Initially a mixed three-way within- and between-subjects repeated measures Analysis of Variance (ANOVA) was done for all dependent variables. Then, as the between-subjects factor Experience turned out not to have any significant effect, a two-way within-subjects Analysis of Variance was done to increase the sample size in the groups.

E.1. RMS of Altitude Error

Mixed-Design ANOVA

The results show that Experience was not a significant factor for the root mean square of the altitude error with respect to the terrain (RMSE). Mauchly's test indicated that the assumption of sphericity had not been violated, $\chi^2(2)$ = 2.818, *p* = .244. Homogeneity of variance was assumed in spite of Levene's test indicating that one repeated measure out of six had unequal variance (*F* = 5.327, *p* = .044). The Shapiro-Wilk test did not reject the null hypothesis that the RMSE data came from a normally-distributed population. Mixed ANOVA did not reject the null hypothesis that Experience did not significantly affect RMSE.

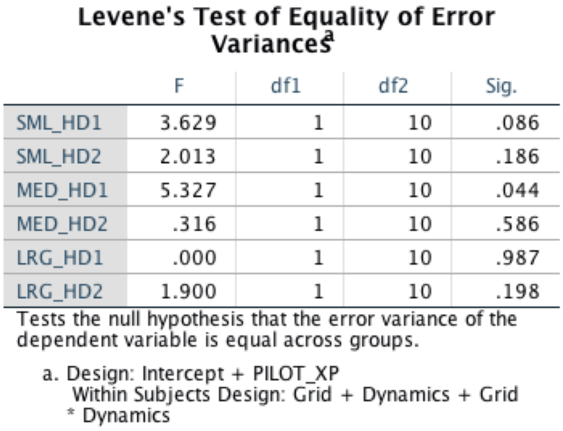

Levene's Test of Equality of Error Variances[a]

	F	df1	df2	Sig.
SML_HD1	3.629	1	10	.086
SML_HD2	2.013	1	10	.186
MED_HD1	5.327	1	10	.044
MED_HD2	.316	1	10	.586
LRG_HD1	.000	1	10	.987
LRG_HD2	1.900	1	10	.198

Tests the null hypothesis that the error variance of the dependent variable is equal across groups.

a. Design: Intercept + PILOT_XP
Within Subjects Design: Grid + Dynamics + Grid * Dynamics

Figure E.1 – Mixed-design Levene'e test of homogeneity of variance for RMSE.

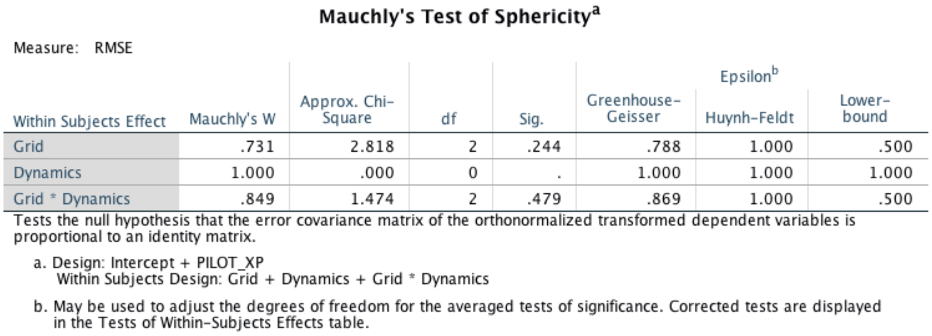

Mauchly's Test of Sphericity[a]

Measure: RMSE

					Epsilon[b]		
Within Subjects Effect	Mauchly's W	Approx. Chi-Square	df	Sig.	Greenhouse-Geisser	Huynh-Feldt	Lower-bound
Grid	.731	2.818	2	.244	.788	1.000	.500
Dynamics	1.000	.000	0	.	1.000	1.000	1.000
Grid * Dynamics	.849	1.474	2	.479	.869	1.000	.500

Tests the null hypothesis that the error covariance matrix of the orthonormalized transformed dependent variables is proportional to an identity matrix.

a. Design: Intercept + PILOT_XP
Within Subjects Design: Grid + Dynamics + Grid * Dynamics

b. May be used to adjust the degrees of freedom for the averaged tests of significance. Corrected tests are displayed in the Tests of Within-Subjects Effects table.

Figure E.2 – Mixed-design Mauchly’s test of sphericity for RMSE.

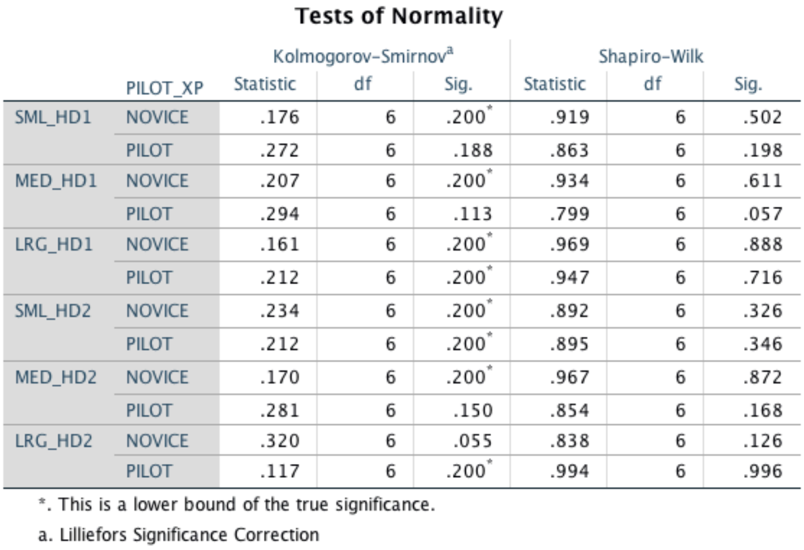

Tests of Normality

		Kolmogorov-Smirnov[a]			Shapiro-Wilk		
	PILOT_XP	Statistic	df	Sig.	Statistic	df	Sig.
SML_HD1	NOVICE	.176	6	.200*	.919	6	.502
	PILOT	.272	6	.188	.863	6	.198
MED_HD1	NOVICE	.207	6	.200*	.934	6	.611
	PILOT	.294	6	.113	.799	6	.057
LRG_HD1	NOVICE	.161	6	.200*	.969	6	.888
	PILOT	.212	6	.200*	.947	6	.716
SML_HD2	NOVICE	.234	6	.200*	.892	6	.326
	PILOT	.212	6	.200*	.895	6	.346
MED_HD2	NOVICE	.170	6	.200*	.967	6	.872
	PILOT	.281	6	.150	.854	6	.168
LRG_HD2	NOVICE	.320	6	.055	.838	6	.126
	PILOT	.117	6	.200*	.994	6	.996

*. This is a lower bound of the true significance.

a. Lilliefors Significance Correction

Figure E.3 – Mixed-design normality tests for RMSE.

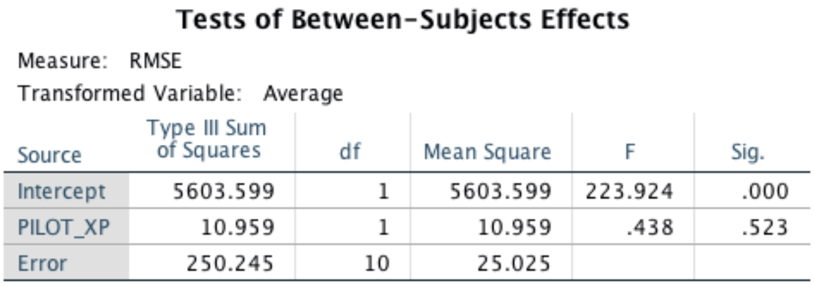

Tests of Between-Subjects Effects

Measure: RMSE
Transformed Variable: Average

Source	Type III Sum of Squares	df	Mean Square	F	Sig.
Intercept	5603.599	1	5603.599	223.924	.000
PILOT_XP	10.959	1	10.959	.438	.523
Error	250.245	10	25.025		

Figure E.4 – Mixed-design ANOVA for RMSE.

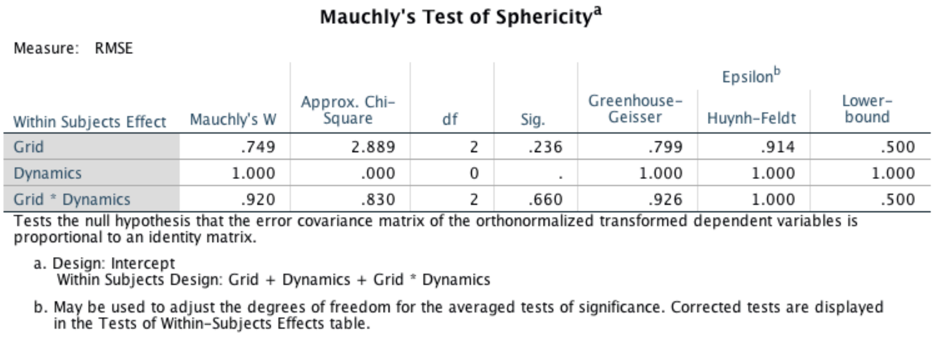

Mauchly's Test of Sphericity[a]

Measure: RMSE

					Epsilon[b]		
Within Subjects Effect	Mauchly's W	Approx. Chi-Square	df	Sig.	Greenhouse-Geisser	Huynh-Feldt	Lower-bound
Grid	.749	2.889	2	.236	.799	.914	.500
Dynamics	1.000	.000	0	.	1.000	1.000	1.000
Grid * Dynamics	.920	.830	2	.660	.926	1.000	.500

Tests the null hypothesis that the error covariance matrix of the orthonormalized transformed dependent variables is proportional to an identity matrix.

a. Design: Intercept
Within Subjects Design: Grid + Dynamics + Grid * Dynamics

b. May be used to adjust the degrees of freedom for the averaged tests of significance. Corrected tests are displayed in the Tests of Within-Subjects Effects table.

Figure E.5 – Mauchly's test of sphericity for within-subjects RMSE.

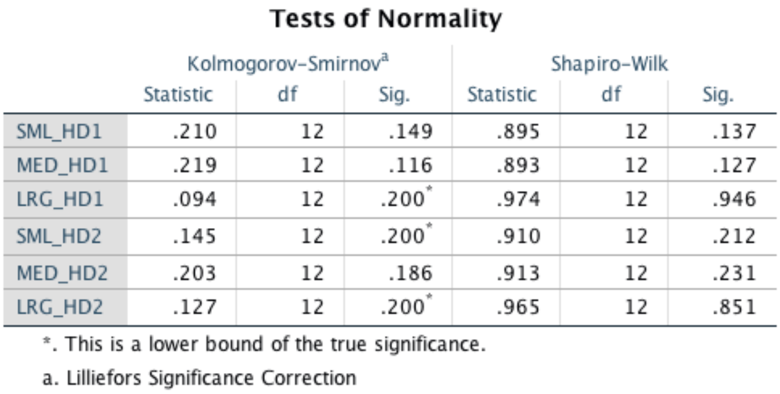

Tests of Normality

	Kolmogorov-Smirnov[a]			Shapiro-Wilk		
	Statistic	df	Sig.	Statistic	df	Sig.
SML_HD1	.210	12	.149	.895	12	.137
MED_HD1	.219	12	.116	.893	12	.127
LRG_HD1	.094	12	.200*	.974	12	.946
SML_HD2	.145	12	.200*	.910	12	.212
MED_HD2	.203	12	.186	.913	12	.231
LRG_HD2	.127	12	.200*	.965	12	.851

*. This is a lower bound of the true significance.

a. Lilliefors Significance Correction

Figure E.6 – Normality tests for within-subjects RMSE.

Within-Subjects ANOVA

Mauchly's test failed to reject the sphericity assumption for Grid and for the Grid × Dynamics interaction, $\chi^2(2) = 2.889$, $p = .236$ and $\chi^2(2) = .830$, $p = .660$, respectively. The Shapiro-Wilk test confirmed the hypothesis that the RMSE data came from a normally-distributed population. ANOVA showed main effects of Grid $F(2, 22) = 5.64, p = .011$ and of Dynamics $F(1, 11) = 12.22, p = .005$.

Pairwise comparisons using the Bonferroni correction revealed that an increase in grid cell size from small to medium elicited an increase in mean RMSE from 8.05(0.47) to 9.07(0.74) which was not statistically significant ($p = .193$). An increase in Grid from medium to large increased mean RMSE to 9.34(0.62), also not statistically significant ($p = 1.00$). However, a change from small to large Grid evoked a statistically significant increase in mean RMSE ($p = 0.011$). Switching from Dynamics 1 to 2 increased mean RMSE from 7.92(.59) to 9.73(.67). The Grid × Dynamics interaction turned out not to have a significant effect on RMSE.

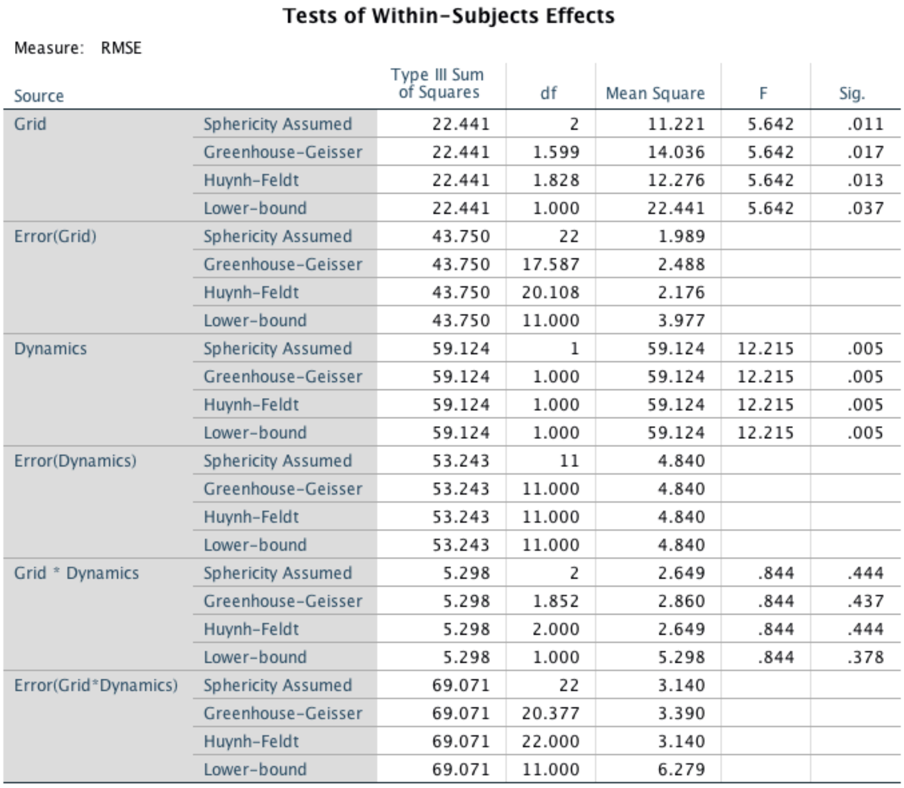

Tests of Within-Subjects Effects

Measure: RMSE

Source		Type III Sum of Squares	df	Mean Square	F	Sig.
Grid	Sphericity Assumed	22.441	2	11.221	5.642	.011
	Greenhouse-Geisser	22.441	1.599	14.036	5.642	.017
	Huynh-Feldt	22.441	1.828	12.276	5.642	.013
	Lower-bound	22.441	1.000	22.441	5.642	.037
Error(Grid)	Sphericity Assumed	43.750	22	1.989		
	Greenhouse-Geisser	43.750	17.587	2.488		
	Huynh-Feldt	43.750	20.108	2.176		
	Lower-bound	43.750	11.000	3.977		
Dynamics	Sphericity Assumed	59.124	1	59.124	12.215	.005
	Greenhouse-Geisser	59.124	1.000	59.124	12.215	.005
	Huynh-Feldt	59.124	1.000	59.124	12.215	.005
	Lower-bound	59.124	1.000	59.124	12.215	.005
Error(Dynamics)	Sphericity Assumed	53.243	11	4.840		
	Greenhouse-Geisser	53.243	11.000	4.840		
	Huynh-Feldt	53.243	11.000	4.840		
	Lower-bound	53.243	11.000	4.840		
Grid * Dynamics	Sphericity Assumed	5.298	2	2.649	.844	.444
	Greenhouse-Geisser	5.298	1.852	2.860	.844	.437
	Huynh-Feldt	5.298	2.000	2.649	.844	.444
	Lower-bound	5.298	1.000	5.298	.844	.378
Error(Grid*Dynamics)	Sphericity Assumed	69.071	22	3.140		
	Greenhouse-Geisser	69.071	20.377	3.390		
	Huynh-Feldt	69.071	22.000	3.140		
	Lower-bound	69.071	11.000	6.279		

Figure E.7 – ANOVA for within-subjects RMSE.

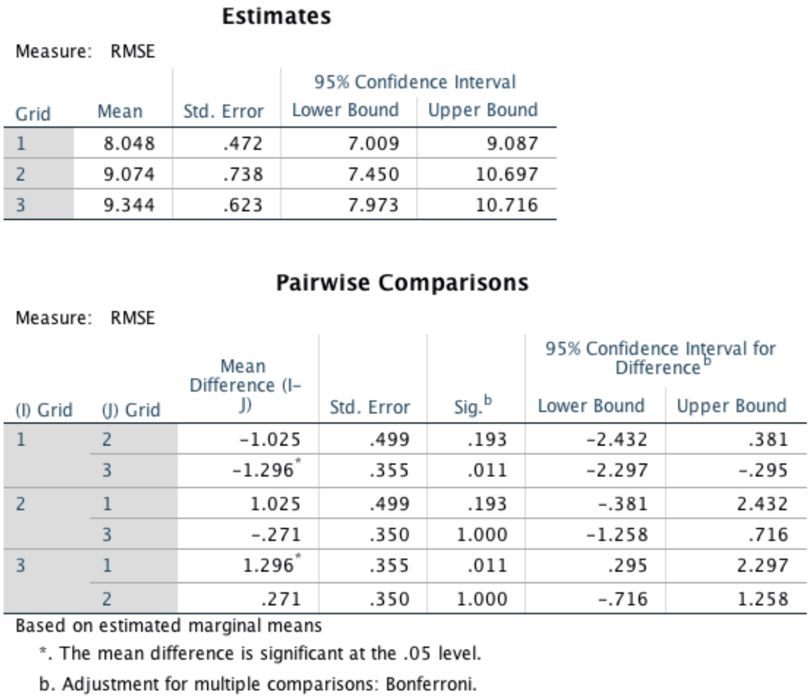

Estimates

Measure: RMSE

Grid	Mean	Std. Error	95% Confidence Interval	
			Lower Bound	Upper Bound
1	8.048	.472	7.009	9.087
2	9.074	.738	7.450	10.697
3	9.344	.623	7.973	10.716

Pairwise Comparisons

Measure: RMSE

(I) Grid	(J) Grid	Mean Difference (I-J)	Std. Error	Sig.[b]	95% Confidence Interval for Difference[b]	
					Lower Bound	Upper Bound
1	2	-1.025	.499	.193	-2.432	.381
	3	-1.296*	.355	.011	-2.297	-.295
2	1	1.025	.499	.193	-.381	2.432
	3	-.271	.350	1.000	-1.258	.716
3	1	1.296*	.355	.011	.295	2.297
	2	.271	.350	1.000	-.716	1.258

Based on estimated marginal means

*. The mean difference is significant at the .05 level.

b. Adjustment for multiple comparisons: Bonferroni.

Figure E.8 – Estimated marginal means and pairwise comparisons for Grid.

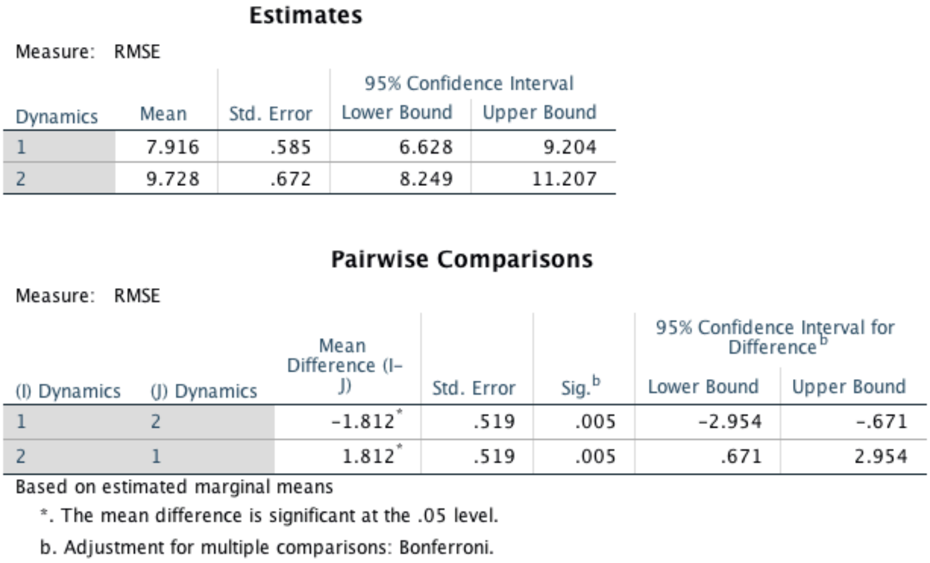

Estimates

Measure: RMSE

Dynamics	Mean	Std. Error	95% Confidence Interval Lower Bound	 Upper Bound
1	7.916	.585	6.628	9.204
2	9.728	.672	8.249	11.207

Pairwise Comparisons

Measure: RMSE

(I) Dynamics	(J) Dynamics	Mean Difference (I−J)	Std. Error	Sig.[b]	95% Confidence Interval for Difference[b] Lower Bound	 Upper Bound
1	2	-1.812*	.519	.005	-2.954	-.671
2	1	1.812*	.519	.005	.671	2.954

Based on estimated marginal means

*. The mean difference is significant at the .05 level.

b. Adjustment for multiple comparisons: Bonferroni.

Figure E.9 – Estimated marginal means and pairwise comparisons for Dynamics.

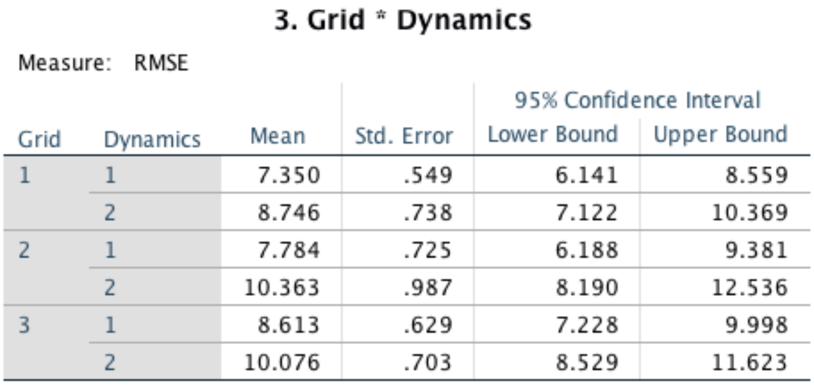

3. Grid * Dynamics

Measure: RMSE

Grid	Dynamics	Mean	Std. Error	95% Confidence Interval Lower Bound	 Upper Bound
1	1	7.350	.549	6.141	8.559
	2	8.746	.738	7.122	10.369
2	1	7.784	.725	6.188	9.381
	2	10.363	.987	8.190	12.536
3	1	8.613	.629	7.228	9.998
	2	10.076	.703	8.529	11.623

Figure E.10 – Estimated marginal means of Grid - Dynamics interaction.

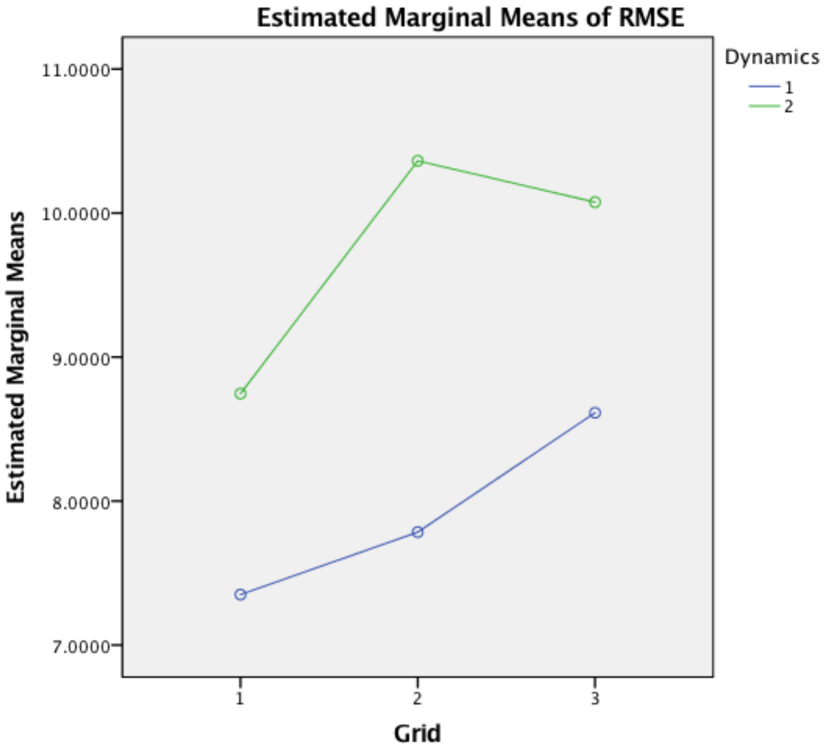

Figure E.11 – Profile plot for within-subjects ANOVA of RMSE.

E.2. Time fraction per performance boundary

Mixed-Design ANOVA

Experience had no significant effect on the fractions of time spent within handling qualities performance boundaries. Mauchly's test indicated that the assumption of sphericity had not been violated for relative time flown within desired, adequate and inadequate performance boundaries, for T_{des} $\chi^2(2) = .887$, $p = .642$; for T_{adq} $\chi^2(2) = .768$, $p = .681$ and T_{ina} $\chi^2(2) = 2.828$, $p = .243$. Shapiro-Wilk's test suggested 6 out of 36 samples did not come from a normal distribution. Levene's test was unable to reject equal error variance across groups. Mixed ANOVA did not reject the null hypothesis that the means of T_{des}, T_{adq} and T_{ina} are the same for both levels of Experience. So, ANOVA was done on the Experience-lumped performance boundary data.

Within-Subjects ANOVA

Box plots of the Experience-lumped time fractions spent within desired, adequate and inadequate performance boundaries are shown in **??????**. According to Mauchly's test the assumption of homogeneity of variance had not been violated for the fractions of time spent within the three performance boundaries, for T_{des} $\chi^2(2) = .828$, $p = .661$; for T_{adq} $\chi^2(2) = 1.137$, $p = .566$ and T_{ina} $\chi^2(2) = 3.829$, $p = .147$. Shapiro-Wilk's test indicated 5 out of 18 samples were not drawn from a normal distribution. ANOVA showed no main effect of Grid on either T_{des}, T_{adq} or T_{ina}. Dynamics had a main effect on T_{ina} only, $F(1, 11) = 6.665, p = .026$, with an increase in mean T_{ina} from .122(.012) to .173(.020) when switching from Dynamics 1 to 2. The Grid × Dynamics interaction effect was not not statistically significant. The participant-averaged, Experience-lumped time fractions spent within performance boundaries are represented by a barchart in the research paper, summarizing the aforementioned effects.

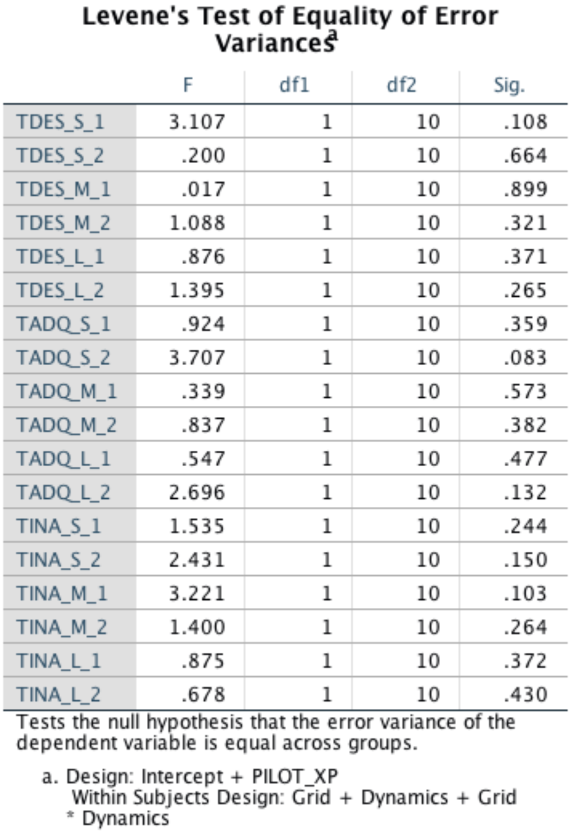

Levene's Test of Equality of Error Variances[a]

	F	df1	df2	Sig.
TDES_S_1	3.107	1	10	.108
TDES_S_2	.200	1	10	.664
TDES_M_1	.017	1	10	.899
TDES_M_2	1.088	1	10	.321
TDES_L_1	.876	1	10	.371
TDES_L_2	1.395	1	10	.265
TADQ_S_1	.924	1	10	.359
TADQ_S_2	3.707	1	10	.083
TADQ_M_1	.339	1	10	.573
TADQ_M_2	.837	1	10	.382
TADQ_L_1	.547	1	10	.477
TADQ_L_2	2.696	1	10	.132
TINA_S_1	1.535	1	10	.244
TINA_S_2	2.431	1	10	.150
TINA_M_1	3.221	1	10	.103
TINA_M_2	1.400	1	10	.264
TINA_L_1	.875	1	10	.372
TINA_L_2	.678	1	10	.430

Tests the null hypothesis that the error variance of the dependent variable is equal across groups.

a. Design: Intercept + PILOT_XP
Within Subjects Design: Grid + Dynamics + Grid * Dynamics

Figure E.12 – Mixed-design Levene'e test of homogeneity of variance for time fraction per performance boundary.

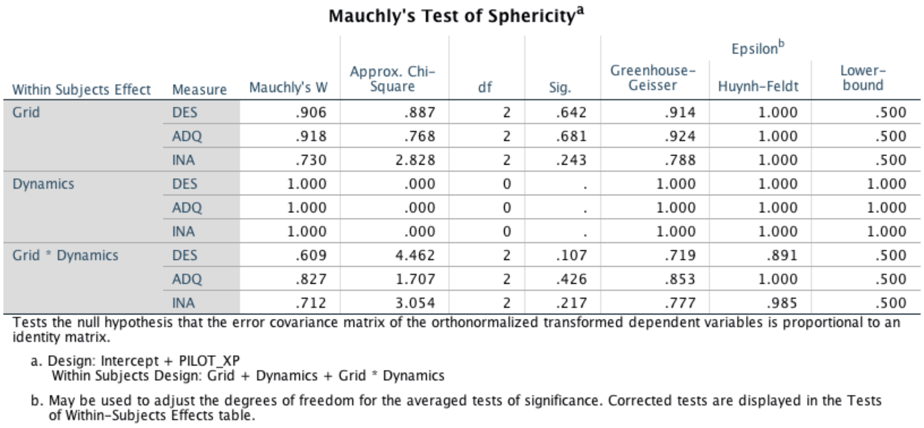

Mauchly's Test of Sphericity[a]

						Epsilon[b]		
Within Subjects Effect	Measure	Mauchly's W	Approx. Chi-Square	df	Sig.	Greenhouse-Geisser	Huynh-Feldt	Lower-bound
Grid	DES	.906	.887	2	.642	.914	1.000	.500
	ADQ	.918	.768	2	.681	.924	1.000	.500
	INA	.730	2.828	2	.243	.788	1.000	.500
Dynamics	DES	1.000	.000	0	.	1.000	1.000	1.000
	ADQ	1.000	.000	0	.	1.000	1.000	1.000
	INA	1.000	.000	0	.	1.000	1.000	1.000
Grid * Dynamics	DES	.609	4.462	2	.107	.719	.891	.500
	ADQ	.827	1.707	2	.426	.853	1.000	.500
	INA	.712	3.054	2	.217	.777	.985	.500

Tests the null hypothesis that the error covariance matrix of the orthonormalized transformed dependent variables is proportional to an identity matrix.

a. Design: Intercept + PILOT_XP
Within Subjects Design: Grid + Dynamics + Grid * Dynamics

b. May be used to adjust the degrees of freedom for the averaged tests of significance. Corrected tests are displayed in the Tests of Within-Subjects Effects table.

Figure E.13 – Mixed-design Mauchly's test of sphericity for time fraction per performance boundary.

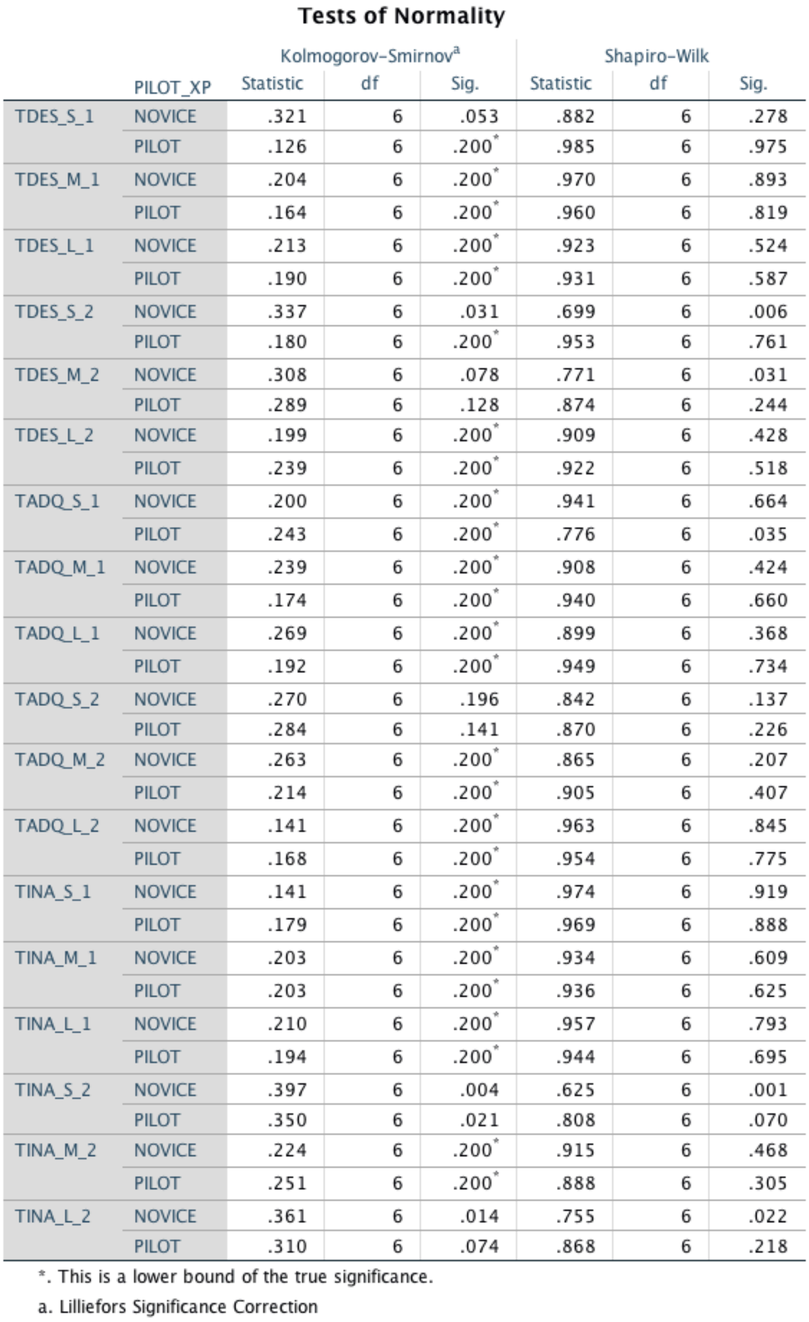

Tests of Normality

		Kolmogorov-Smirnov[a]			Shapiro-Wilk		
	PILOT_XP	Statistic	df	Sig.	Statistic	df	Sig.
TDES_S_1	NOVICE	.321	6	.053	.882	6	.278
	PILOT	.126	6	.200*	.985	6	.975
TDES_M_1	NOVICE	.204	6	.200*	.970	6	.893
	PILOT	.164	6	.200*	.960	6	.819
TDES_L_1	NOVICE	.213	6	.200*	.923	6	.524
	PILOT	.190	6	.200*	.931	6	.587
TDES_S_2	NOVICE	.337	6	.031	.699	6	.006
	PILOT	.180	6	.200*	.953	6	.761
TDES_M_2	NOVICE	.308	6	.078	.771	6	.031
	PILOT	.289	6	.128	.874	6	.244
TDES_L_2	NOVICE	.199	6	.200*	.909	6	.428
	PILOT	.239	6	.200*	.922	6	.518
TADQ_S_1	NOVICE	.200	6	.200*	.941	6	.664
	PILOT	.243	6	.200*	.776	6	.035
TADQ_M_1	NOVICE	.239	6	.200*	.908	6	.424
	PILOT	.174	6	.200*	.940	6	.660
TADQ_L_1	NOVICE	.269	6	.200*	.899	6	.368
	PILOT	.192	6	.200*	.949	6	.734
TADQ_S_2	NOVICE	.270	6	.196	.842	6	.137
	PILOT	.284	6	.141	.870	6	.226
TADQ_M_2	NOVICE	.263	6	.200*	.865	6	.207
	PILOT	.214	6	.200*	.905	6	.407
TADQ_L_2	NOVICE	.141	6	.200*	.963	6	.845
	PILOT	.168	6	.200*	.954	6	.775
TINA_S_1	NOVICE	.141	6	.200*	.974	6	.919
	PILOT	.179	6	.200*	.969	6	.888
TINA_M_1	NOVICE	.203	6	.200*	.934	6	.609
	PILOT	.203	6	.200*	.936	6	.625
TINA_L_1	NOVICE	.210	6	.200*	.957	6	.793
	PILOT	.194	6	.200*	.944	6	.695
TINA_S_2	NOVICE	.397	6	.004	.625	6	.001
	PILOT	.350	6	.021	.808	6	.070
TINA_M_2	NOVICE	.224	6	.200*	.915	6	.468
	PILOT	.251	6	.200*	.888	6	.305
TINA_L_2	NOVICE	.361	6	.014	.755	6	.022
	PILOT	.310	6	.074	.868	6	.218

*. This is a lower bound of the true significance.

a. Lilliefors Significance Correction

Figure E.14 – Mixed-design normality tests for time fraction per performance boundary.

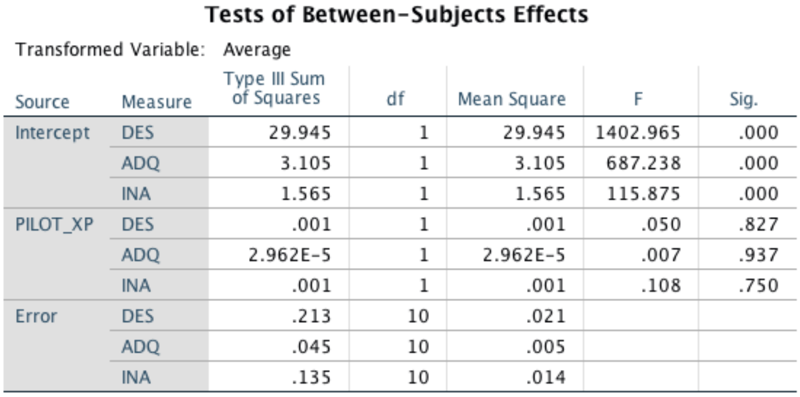

Tests of Between-Subjects Effects

Transformed Variable: Average

Source	Measure	Type III Sum of Squares	df	Mean Square	F	Sig.
Intercept	DES	29.945	1	29.945	1402.965	.000
	ADQ	3.105	1	3.105	687.238	.000
	INA	1.565	1	1.565	115.875	.000
PILOT_XP	DES	.001	1	.001	.050	.827
	ADQ	2.962E-5	1	2.962E-5	.007	.937
	INA	.001	1	.001	.108	.750
Error	DES	.213	10	.021		
	ADQ	.045	10	.005		
	INA	.135	10	.014		

Figure E.15 – Mixed-design ANOVA for time fraction per performance boundary.

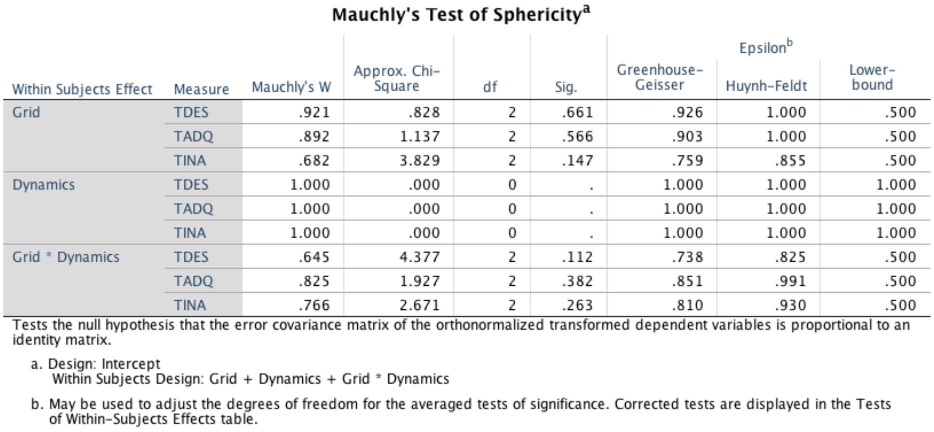

Mauchly's Test of Sphericity[a]

						Epsilon[b]		
Within Subjects Effect	Measure	Mauchly's W	Approx. Chi-Square	df	Sig.	Greenhouse-Geisser	Huynh-Feldt	Lower-bound
Grid	TDES	.921	.828	2	.661	.926	1.000	.500
	TADQ	.892	1.137	2	.566	.903	1.000	.500
	TINA	.682	3.829	2	.147	.759	.855	.500
Dynamics	TDES	1.000	.000	0	.	1.000	1.000	1.000
	TADQ	1.000	.000	0	.	1.000	1.000	1.000
	TINA	1.000	.000	0	.	1.000	1.000	1.000
Grid * Dynamics	TDES	.645	4.377	2	.112	.738	.825	.500
	TADQ	.825	1.927	2	.382	.851	.991	.500
	TINA	.766	2.671	2	.263	.810	.930	.500

Tests the null hypothesis that the error covariance matrix of the orthonormalized transformed dependent variables is proportional to an identity matrix.

a. Design: Intercept
Within Subjects Design: Grid + Dynamics + Grid * Dynamics

b. May be used to adjust the degrees of freedom for the averaged tests of significance. Corrected tests are displayed in the Tests of Within-Subjects Effects table.

Figure E.16 – Mauchly's test of sphericity for the within-subjects time fraction per performance boundary.

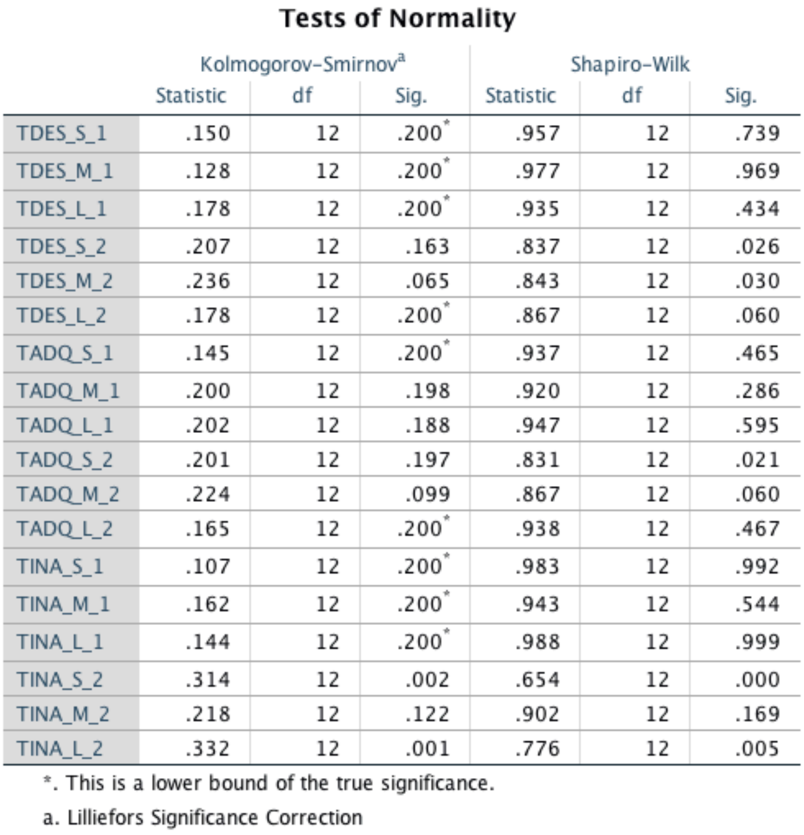

Tests of Normality

	Kolmogorov-Smirnov[a]			Shapiro-Wilk		
	Statistic	df	Sig.	Statistic	df	Sig.
TDES_S_1	.150	12	.200*	.957	12	.739
TDES_M_1	.128	12	.200*	.977	12	.969
TDES_L_1	.178	12	.200*	.935	12	.434
TDES_S_2	.207	12	.163	.837	12	.026
TDES_M_2	.236	12	.065	.843	12	.030
TDES_L_2	.178	12	.200*	.867	12	.060
TADQ_S_1	.145	12	.200*	.937	12	.465
TADQ_M_1	.200	12	.198	.920	12	.286
TADQ_L_1	.202	12	.188	.947	12	.595
TADQ_S_2	.201	12	.197	.831	12	.021
TADQ_M_2	.224	12	.099	.867	12	.060
TADQ_L_2	.165	12	.200*	.938	12	.467
TINA_S_1	.107	12	.200*	.983	12	.992
TINA_M_1	.162	12	.200*	.943	12	.544
TINA_L_1	.144	12	.200*	.988	12	.999
TINA_S_2	.314	12	.002	.654	12	.000
TINA_M_2	.218	12	.122	.902	12	.169
TINA_L_2	.332	12	.001	.776	12	.005

*. This is a lower bound of the true significance.

a. Lilliefors Significance Correction

Figure E.17 – Normality tests for within-subjects time fraction per performance boundary.

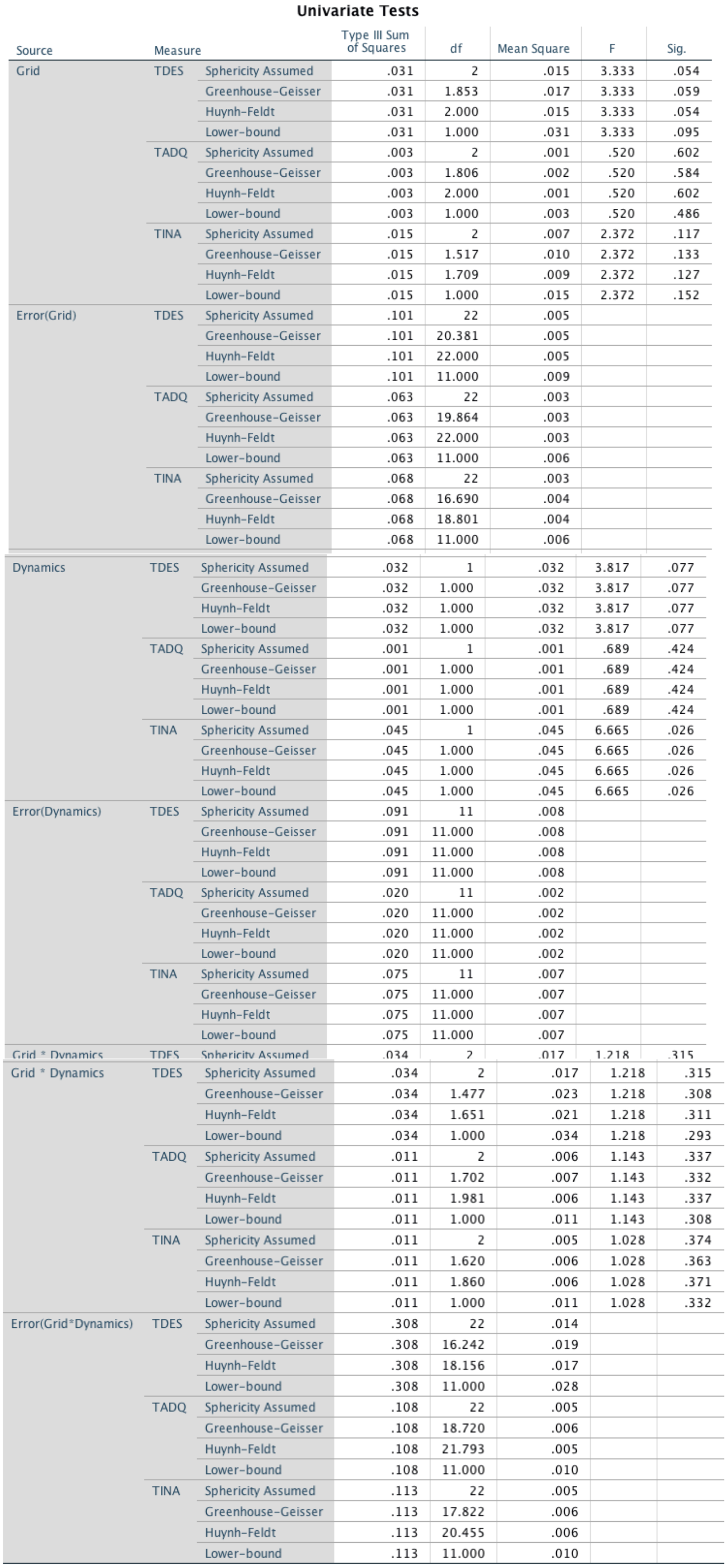

Univariate Tests

Source	Measure		Type III Sum of Squares	df	Mean Square	F	Sig.
Grid	TDES	Sphericity Assumed	.031	2	.015	3.333	.054
		Greenhouse-Geisser	.031	1.853	.017	3.333	.059
		Huynh-Feldt	.031	2.000	.015	3.333	.054
		Lower-bound	.031	1.000	.031	3.333	.095
	TADQ	Sphericity Assumed	.003	2	.001	.520	.602
		Greenhouse-Geisser	.003	1.806	.002	.520	.584
		Huynh-Feldt	.003	2.000	.001	.520	.602
		Lower-bound	.003	1.000	.003	.520	.486
	TINA	Sphericity Assumed	.015	2	.007	2.372	.117
		Greenhouse-Geisser	.015	1.517	.010	2.372	.133
		Huynh-Feldt	.015	1.709	.009	2.372	.127
		Lower-bound	.015	1.000	.015	2.372	.152
Error(Grid)	TDES	Sphericity Assumed	.101	22	.005		
		Greenhouse-Geisser	.101	20.381	.005		
		Huynh-Feldt	.101	22.000	.005		
		Lower-bound	.101	11.000	.009		
	TADQ	Sphericity Assumed	.063	22	.003		
		Greenhouse-Geisser	.063	19.864	.003		
		Huynh-Feldt	.063	22.000	.003		
		Lower-bound	.063	11.000	.006		
	TINA	Sphericity Assumed	.068	22	.003		
		Greenhouse-Geisser	.068	16.690	.004		
		Huynh-Feldt	.068	18.801	.004		
		Lower-bound	.068	11.000	.006		
Dynamics	TDES	Sphericity Assumed	.032	1	.032	3.817	.077
		Greenhouse-Geisser	.032	1.000	.032	3.817	.077
		Huynh-Feldt	.032	1.000	.032	3.817	.077
		Lower-bound	.032	1.000	.032	3.817	.077
	TADQ	Sphericity Assumed	.001	1	.001	.689	.424
		Greenhouse-Geisser	.001	1.000	.001	.689	.424
		Huynh-Feldt	.001	1.000	.001	.689	.424
		Lower-bound	.001	1.000	.001	.689	.424
	TINA	Sphericity Assumed	.045	1	.045	6.665	.026
		Greenhouse-Geisser	.045	1.000	.045	6.665	.026
		Huynh-Feldt	.045	1.000	.045	6.665	.026
		Lower-bound	.045	1.000	.045	6.665	.026
Error(Dynamics)	TDES	Sphericity Assumed	.091	11	.008		
		Greenhouse-Geisser	.091	11.000	.008		
		Huynh-Feldt	.091	11.000	.008		
		Lower-bound	.091	11.000	.008		
	TADQ	Sphericity Assumed	.020	11	.002		
		Greenhouse-Geisser	.020	11.000	.002		
		Huynh-Feldt	.020	11.000	.002		
		Lower-bound	.020	11.000	.002		
	TINA	Sphericity Assumed	.075	11	.007		
		Greenhouse-Geisser	.075	11.000	.007		
		Huynh-Feldt	.075	11.000	.007		
		Lower-bound	.075	11.000	.007		
Grid * Dynamics	TDES	Sphericity Assumed	.034	2	.017	1.218	.315
		Greenhouse-Geisser	.034	1.477	.023	1.218	.308
		Huynh-Feldt	.034	1.651	.021	1.218	.311
		Lower-bound	.034	1.000	.034	1.218	.293
	TADQ	Sphericity Assumed	.011	2	.006	1.143	.337
		Greenhouse-Geisser	.011	1.702	.007	1.143	.332
		Huynh-Feldt	.011	1.981	.006	1.143	.337
		Lower-bound	.011	1.000	.011	1.143	.308
	TINA	Sphericity Assumed	.011	2	.005	1.028	.374
		Greenhouse-Geisser	.011	1.620	.006	1.028	.363
		Huynh-Feldt	.011	1.860	.006	1.028	.371
		Lower-bound	.011	1.000	.011	1.028	.332
Error(Grid*Dynamics)	TDES	Sphericity Assumed	.308	22	.014		
		Greenhouse-Geisser	.308	16.242	.019		
		Huynh-Feldt	.308	18.156	.017		
		Lower-bound	.308	11.000	.028		
	TADQ	Sphericity Assumed	.108	22	.005		
		Greenhouse-Geisser	.108	18.720	.006		
		Huynh-Feldt	.108	21.793	.005		
		Lower-bound	.108	11.000	.010		
	TINA	Sphericity Assumed	.113	22	.005		
		Greenhouse-Geisser	.113	17.822	.006		
		Huynh-Feldt	.113	20.455	.006		
		Lower-bound	.113	11.000	.010		

Figure E.18 – ANOVA for within-subjects RMSE.

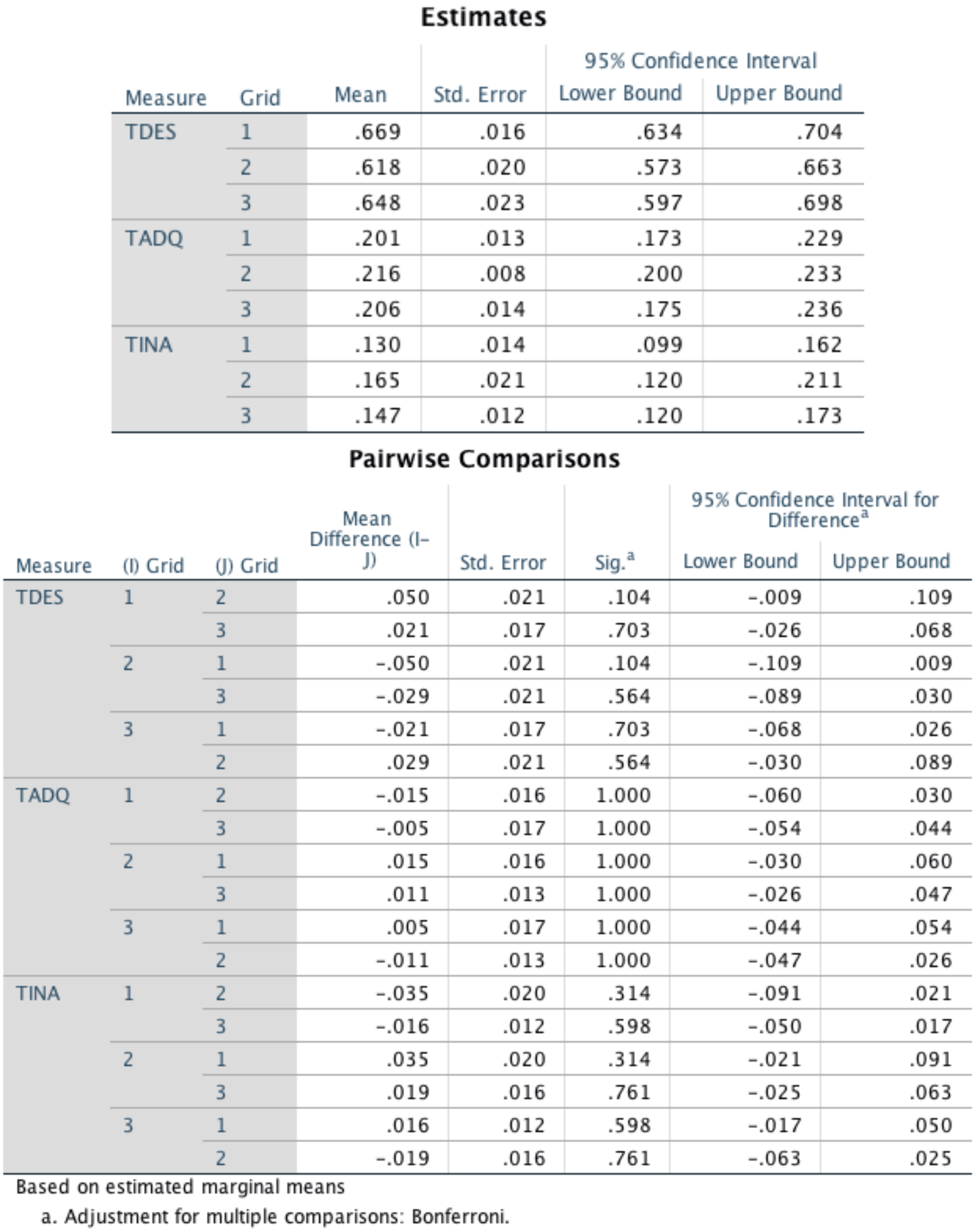

Estimates

Measure	Grid	Mean	Std. Error	95% Confidence Interval Lower Bound	95% Confidence Interval Upper Bound
TDES	1	.669	.016	.634	.704
	2	.618	.020	.573	.663
	3	.648	.023	.597	.698
TADQ	1	.201	.013	.173	.229
	2	.216	.008	.200	.233
	3	.206	.014	.175	.236
TINA	1	.130	.014	.099	.162
	2	.165	.021	.120	.211
	3	.147	.012	.120	.173

Pairwise Comparisons

Measure	(I) Grid	(J) Grid	Mean Difference (I-J)	Std. Error	Sig.[a]	95% Confidence Interval for Difference[a] Lower Bound	95% Confidence Interval for Difference[a] Upper Bound
TDES	1	2	.050	.021	.104	-.009	.109
		3	.021	.017	.703	-.026	.068
	2	1	-.050	.021	.104	-.109	.009
		3	-.029	.021	.564	-.089	.030
	3	1	-.021	.017	.703	-.068	.026
		2	.029	.021	.564	-.030	.089
TADQ	1	2	-.015	.016	1.000	-.060	.030
		3	-.005	.017	1.000	-.054	.044
	2	1	.015	.016	1.000	-.030	.060
		3	.011	.013	1.000	-.026	.047
	3	1	.005	.017	1.000	-.044	.054
		2	-.011	.013	1.000	-.047	.026
TINA	1	2	-.035	.020	.314	-.091	.021
		3	-.016	.012	.598	-.050	.017
	2	1	.035	.020	.314	-.021	.091
		3	.019	.016	.761	-.025	.063
	3	1	.016	.012	.598	-.017	.050
		2	-.019	.016	.761	-.063	.025

Based on estimated marginal means

[a] Adjustment for multiple comparisons: Bonferroni.

Figure E.19 – Estimated marginal means and pairwise comparisons for Grid.

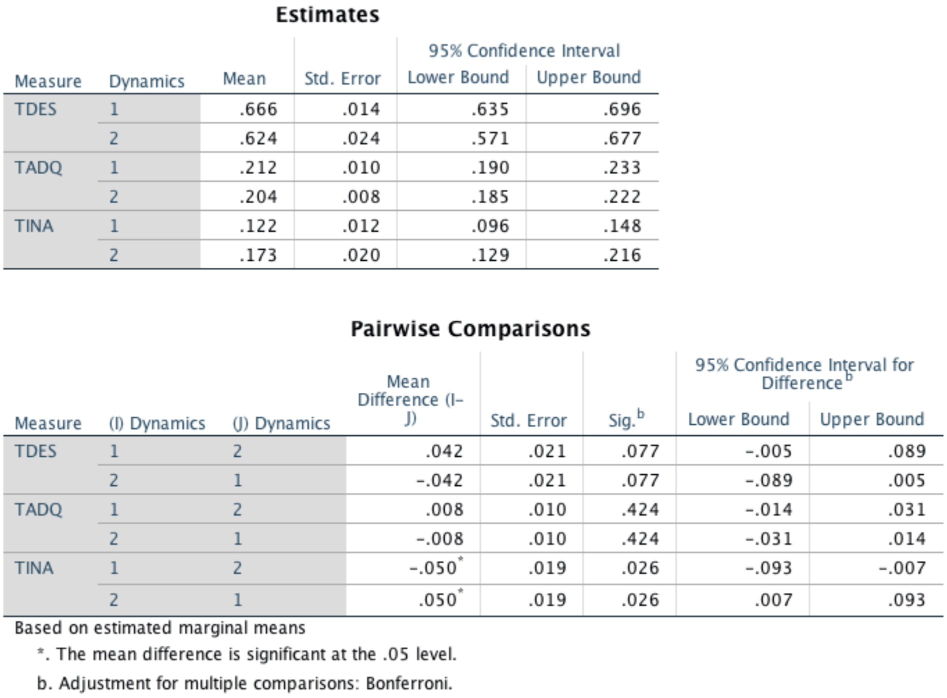

Estimates

Measure	Dynamics	Mean	Std. Error	95% Confidence Interval Lower Bound	95% Confidence Interval Upper Bound
TDES	1	.666	.014	.635	.696
	2	.624	.024	.571	.677
TADQ	1	.212	.010	.190	.233
	2	.204	.008	.185	.222
TINA	1	.122	.012	.096	.148
	2	.173	.020	.129	.216

Pairwise Comparisons

Measure	(I) Dynamics	(J) Dynamics	Mean Difference (I–J)	Std. Error	Sig.[b]	95% Confidence Interval for Difference[b] Lower Bound	95% Confidence Interval for Difference[b] Upper Bound
TDES	1	2	.042	.021	.077	−.005	.089
	2	1	−.042	.021	.077	−.089	.005
TADQ	1	2	.008	.010	.424	−.014	.031
	2	1	−.008	.010	.424	−.031	.014
TINA	1	2	−.050*	.019	.026	−.093	−.007
	2	1	.050*	.019	.026	.007	.093

Based on estimated marginal means

*. The mean difference is significant at the .05 level.

b. Adjustment for multiple comparisons: Bonferroni.

Figure E.20 – Estimated marginal means and pairwise comparisons for Dynamics.

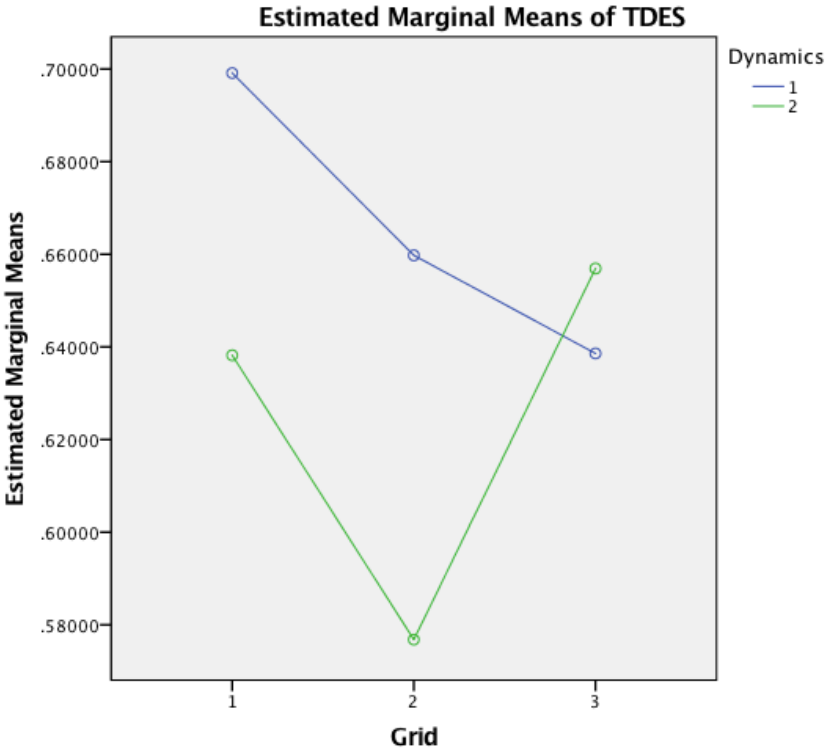

Figure E.21 – Profile plot for within-subjects ANOVA of relative time spent within desired performance boundary.

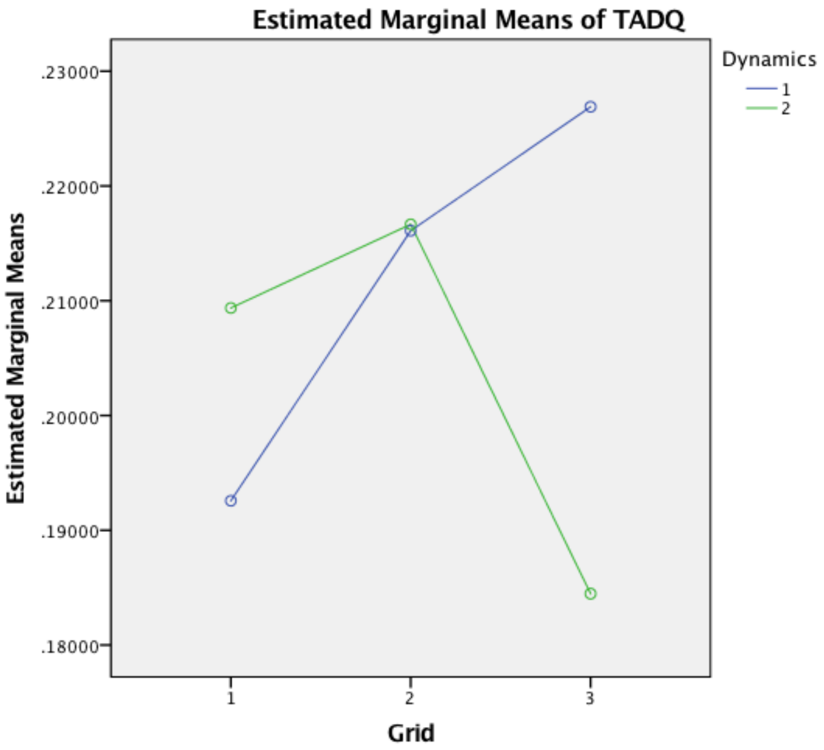

Figure E.22 – Profile plot for within-subjects ANOVA of relative time spent within adequate performance boundary.

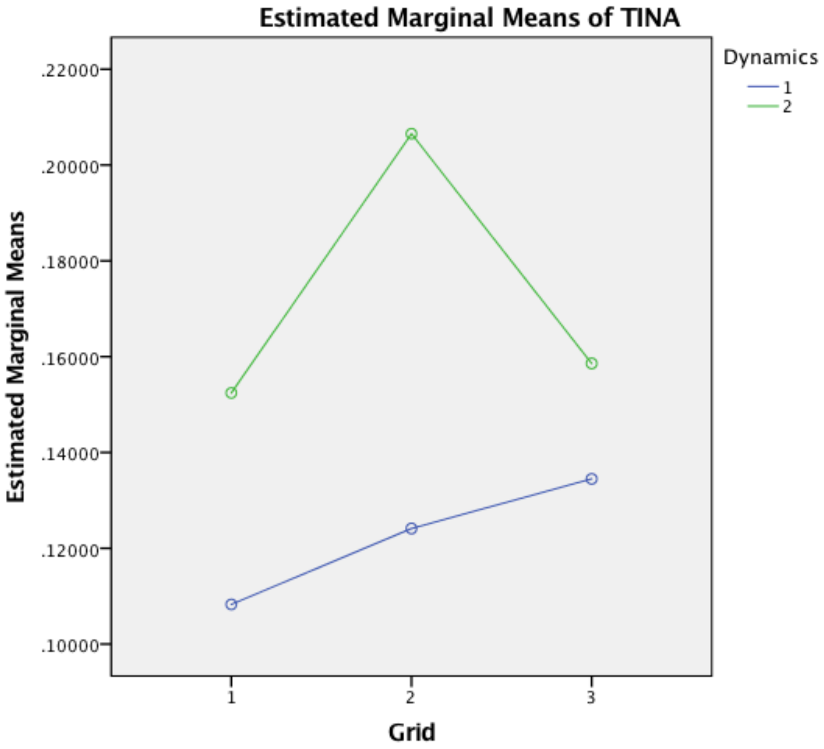

Figure E.23 – Profile plot for within-subjects ANOVA of relative time spent in inadequate performance zone.

E.3. Control activity

Mixed Design ANOVA

Experience was an insignificant factor for the variance of the input signal σ_u^2, as a measure of control activity. Mauchly's test indicated that the assumption of sphericity had not been violated, $\chi^2(2) = .892$, $p = .640$. Homogeneity of variance was assumed, though Levene's test rejected the assumption for one out of six repeated measures, ($F = 11.03, p = .008$). The null hypothesis that the σ_u^2 data came from a normally-distributed population was rejected by Shapiro-Wilk's test for one repeated measure, $W = .736$, $p = .014$. Mixed ANOVA did not reject the null hypothesis that the means of σ_u^2 are the same for both Experience levels, therefore ANOVA was done on the Experience-lumped data.

Within-Subjects ANOVA

A box plot of the Experience-lumped σ_u^2 is displayed in **??**. Mauchly's test could not reject the assumption of sphericity for either Grid or the Grid × Dynamics interaction, $\chi^2(2) = 0.479$, $p = .787$ and $\chi^2(2) = 1.351$, $p = .509$, respectively. The assumption of normality was made, even though a Shapiro-Wilk test rejected it for four out of six repeated measures. ANOVA found a significant main effect of Dynamics on σ_u^2, $F(1, 11) = 30.062$, $p = .000$, with a decrease in σ_u^2 from $9.564 \times 10^{-3}(4.833 \times 10^{-3})$ for Dynamics 1 to $6.570 \times 10^{-3}(4.161 \times 10^{-3})$ for Dynamics 2. Grid had a significant main effect on σ_u^2 too, $F(2, 22) = 4.737, p = .019$, while mean σ_u^2 of $7.98 \times 10^{-3}(4.56 \times 10^{-3})$ for the small grid insignificantly decreased to a mean of $7.11 \times 10^{-3}(3.86 \times 10^{-3})$ for the medium grid ($p = .762$), and significantly increased from the medium grid to a mean of $9.11 \times 10^{-3}(5.07 \times 10^{-3})$ for the large grid ($p = .025$). No statistically significant interaction effect of Grid × Dynamics was found.

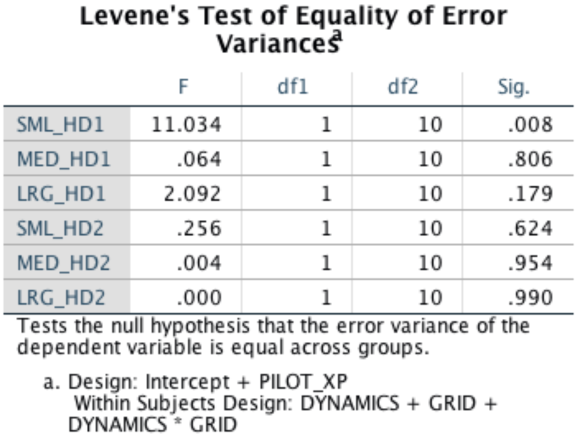

Levene's Test of Equality of Error Variances[a]

	F	df1	df2	Sig.
SML_HD1	11.034	1	10	.008
MED_HD1	.064	1	10	.806
LRG_HD1	2.092	1	10	.179
SML_HD2	.256	1	10	.624
MED_HD2	.004	1	10	.954
LRG_HD2	.000	1	10	.990

Tests the null hypothesis that the error variance of the dependent variable is equal across groups.

a. Design: Intercept + PILOT_XP
Within Subjects Design: DYNAMICS + GRID + DYNAMICS * GRID

Figure E.24 – Mixed-design Levene'e test of homogeneity of variance for control activity.

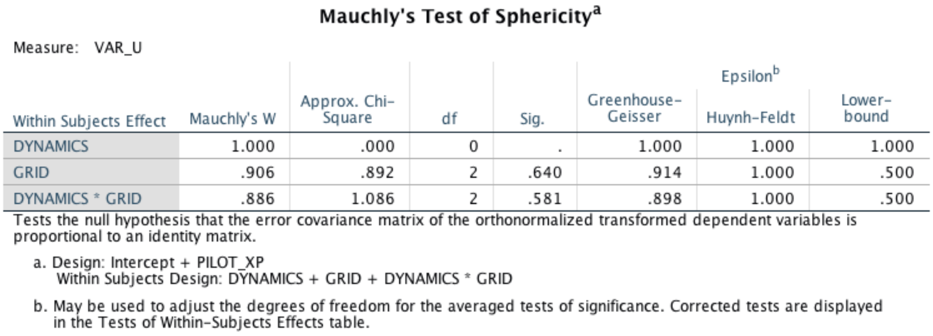

Mauchly's Test of Sphericity[a]

Measure: VAR_U

Within Subjects Effect	Mauchly's W	Approx. Chi-Square	df	Sig.	Epsilon[b] Greenhouse-Geisser	Huynh-Feldt	Lower-bound
DYNAMICS	1.000	.000	0	.	1.000	1.000	1.000
GRID	.906	.892	2	.640	.914	1.000	.500
DYNAMICS * GRID	.886	1.086	2	.581	.898	1.000	.500

Tests the null hypothesis that the error covariance matrix of the orthonormalized transformed dependent variables is proportional to an identity matrix.

a. Design: Intercept + PILOT_XP
Within Subjects Design: DYNAMICS + GRID + DYNAMICS * GRID

b. May be used to adjust the degrees of freedom for the averaged tests of significance. Corrected tests are displayed in the Tests of Within-Subjects Effects table.

Figure E.25 – Mixed-design Mauchly's test of sphericity for control activity.

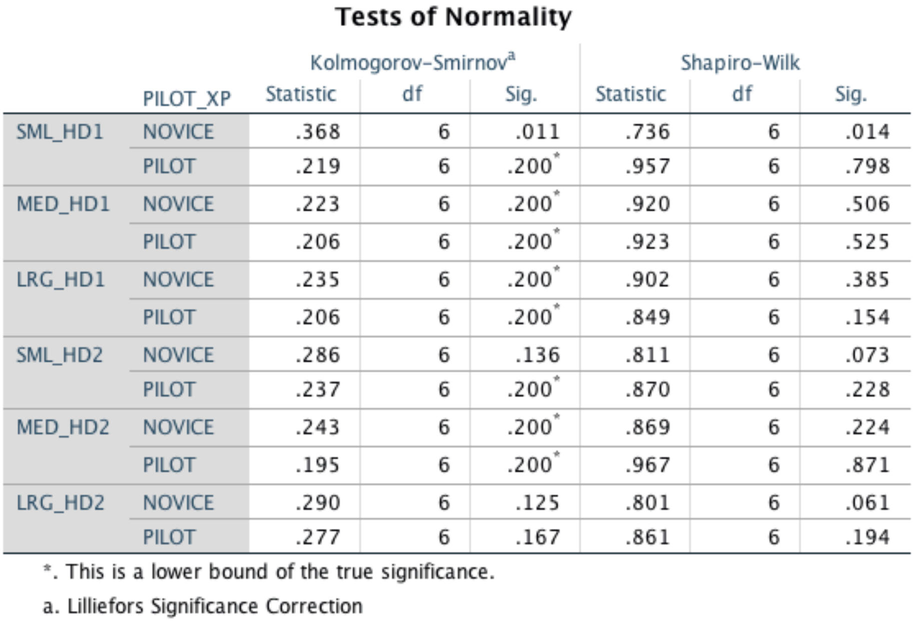

Tests of Normality

	PILOT_XP	Kolmogorov-Smirnov[a] Statistic	df	Sig.	Shapiro-Wilk Statistic	df	Sig.
SML_HD1	NOVICE	.368	6	.011	.736	6	.014
	PILOT	.219	6	.200*	.957	6	.798
MED_HD1	NOVICE	.223	6	.200*	.920	6	.506
	PILOT	.206	6	.200*	.923	6	.525
LRG_HD1	NOVICE	.235	6	.200*	.902	6	.385
	PILOT	.206	6	.200*	.849	6	.154
SML_HD2	NOVICE	.286	6	.136	.811	6	.073
	PILOT	.237	6	.200*	.870	6	.228
MED_HD2	NOVICE	.243	6	.200*	.869	6	.224
	PILOT	.195	6	.200*	.967	6	.871
LRG_HD2	NOVICE	.290	6	.125	.801	6	.061
	PILOT	.277	6	.167	.861	6	.194

*. This is a lower bound of the true significance.

a. Lilliefors Significance Correction

Figure E.26 – Mixed-design normality tests for control activity.

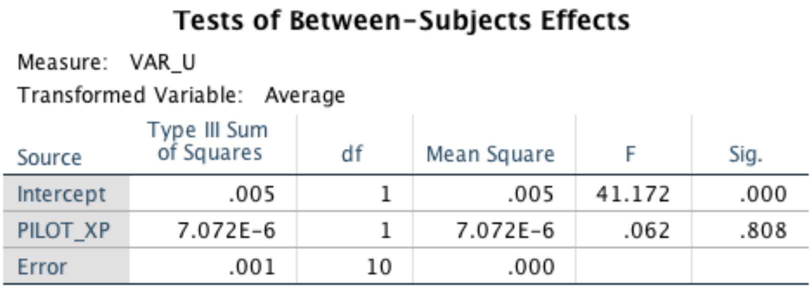

Tests of Between-Subjects Effects

Measure: VAR_U
Transformed Variable: Average

Source	Type III Sum of Squares	df	Mean Square	F	Sig.
Intercept	.005	1	.005	41.172	.000
PILOT_XP	7.072E-6	1	7.072E-6	.062	.808
Error	.001	10	.000		

Figure E.27 – Mixed-design ANOVA for control activity.

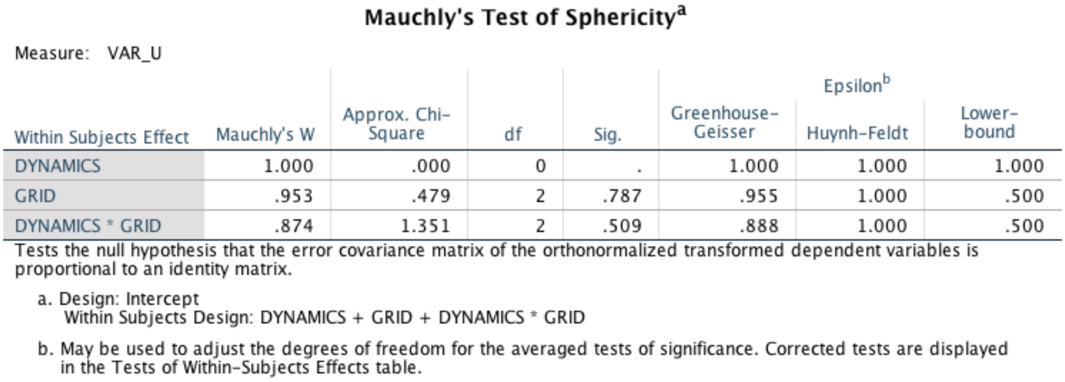

Mauchly's Test of Sphericity[a]

Measure: VAR_U

					Epsilon[b]		
Within Subjects Effect	Mauchly's W	Approx. Chi-Square	df	Sig.	Greenhouse-Geisser	Huynh-Feldt	Lower-bound
DYNAMICS	1.000	.000	0	.	1.000	1.000	1.000
GRID	.953	.479	2	.787	.955	1.000	.500
DYNAMICS * GRID	.874	1.351	2	.509	.888	1.000	.500

Tests the null hypothesis that the error covariance matrix of the orthonormalized transformed dependent variables is proportional to an identity matrix.

a. Design: Intercept
Within Subjects Design: DYNAMICS + GRID + DYNAMICS * GRID

b. May be used to adjust the degrees of freedom for the averaged tests of significance. Corrected tests are displayed in the Tests of Within-Subjects Effects table.

Figure E.28 – Mauchly's test of sphericity for within-subjects control activity.

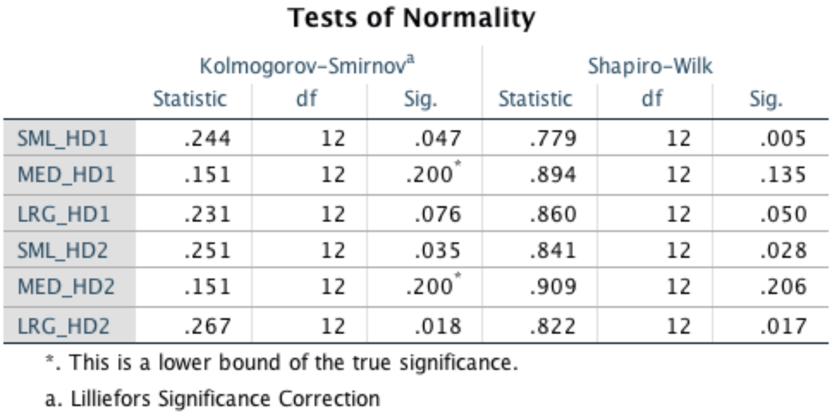

Tests of Normality

	Kolmogorov-Smirnov[a]			Shapiro-Wilk		
	Statistic	df	Sig.	Statistic	df	Sig.
SML_HD1	.244	12	.047	.779	12	.005
MED_HD1	.151	12	.200*	.894	12	.135
LRG_HD1	.231	12	.076	.860	12	.050
SML_HD2	.251	12	.035	.841	12	.028
MED_HD2	.151	12	.200*	.909	12	.206
LRG_HD2	.267	12	.018	.822	12	.017

*. This is a lower bound of the true significance.

a. Lilliefors Significance Correction

Figure E.29 – Normality tests for within-subjects control activity.

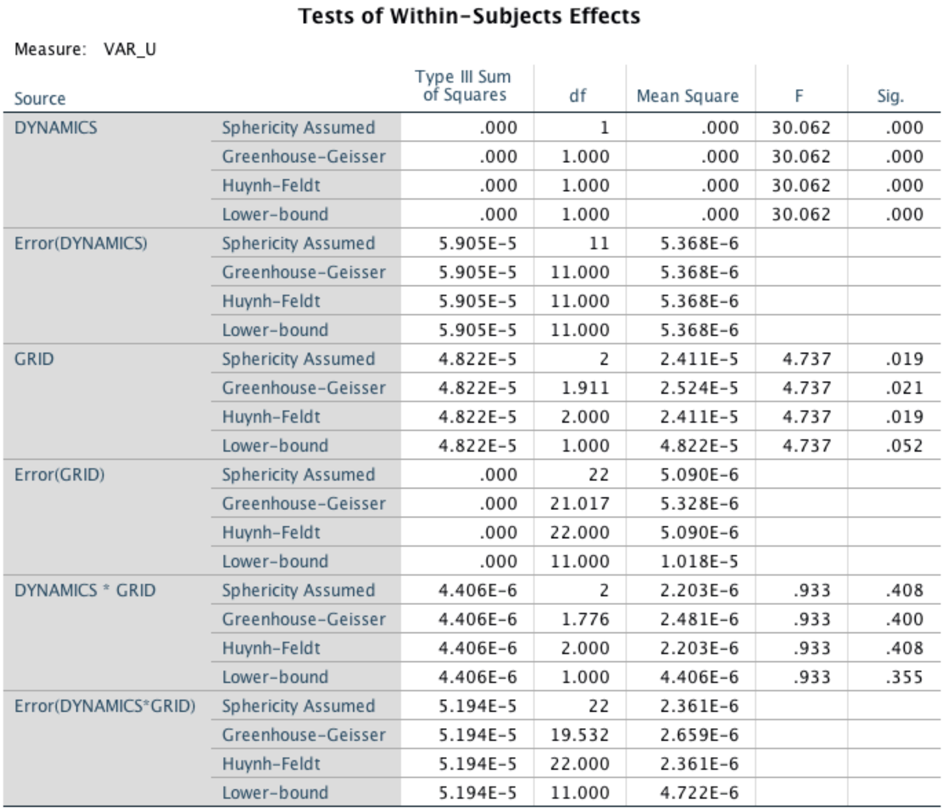

Tests of Within-Subjects Effects

Measure: VAR_U

Source		Type III Sum of Squares	df	Mean Square	F	Sig.
DYNAMICS	Sphericity Assumed	.000	1	.000	30.062	.000
	Greenhouse-Geisser	.000	1.000	.000	30.062	.000
	Huynh-Feldt	.000	1.000	.000	30.062	.000
	Lower-bound	.000	1.000	.000	30.062	.000
Error(DYNAMICS)	Sphericity Assumed	5.905E-5	11	5.368E-6		
	Greenhouse-Geisser	5.905E-5	11.000	5.368E-6		
	Huynh-Feldt	5.905E-5	11.000	5.368E-6		
	Lower-bound	5.905E-5	11.000	5.368E-6		
GRID	Sphericity Assumed	4.822E-5	2	2.411E-5	4.737	.019
	Greenhouse-Geisser	4.822E-5	1.911	2.524E-5	4.737	.021
	Huynh-Feldt	4.822E-5	2.000	2.411E-5	4.737	.019
	Lower-bound	4.822E-5	1.000	4.822E-5	4.737	.052
Error(GRID)	Sphericity Assumed	.000	22	5.090E-6		
	Greenhouse-Geisser	.000	21.017	5.328E-6		
	Huynh-Feldt	.000	22.000	5.090E-6		
	Lower-bound	.000	11.000	1.018E-5		
DYNAMICS * GRID	Sphericity Assumed	4.406E-6	2	2.203E-6	.933	.408
	Greenhouse-Geisser	4.406E-6	1.776	2.481E-6	.933	.400
	Huynh-Feldt	4.406E-6	2.000	2.203E-6	.933	.408
	Lower-bound	4.406E-6	1.000	4.406E-6	.933	.355
Error(DYNAMICS*GRID)	Sphericity Assumed	5.194E-5	22	2.361E-6		
	Greenhouse-Geisser	5.194E-5	19.532	2.659E-6		
	Huynh-Feldt	5.194E-5	22.000	2.361E-6		
	Lower-bound	5.194E-5	11.000	4.722E-6		

Figure E.30 – ANOVA for within-subjects control activity.

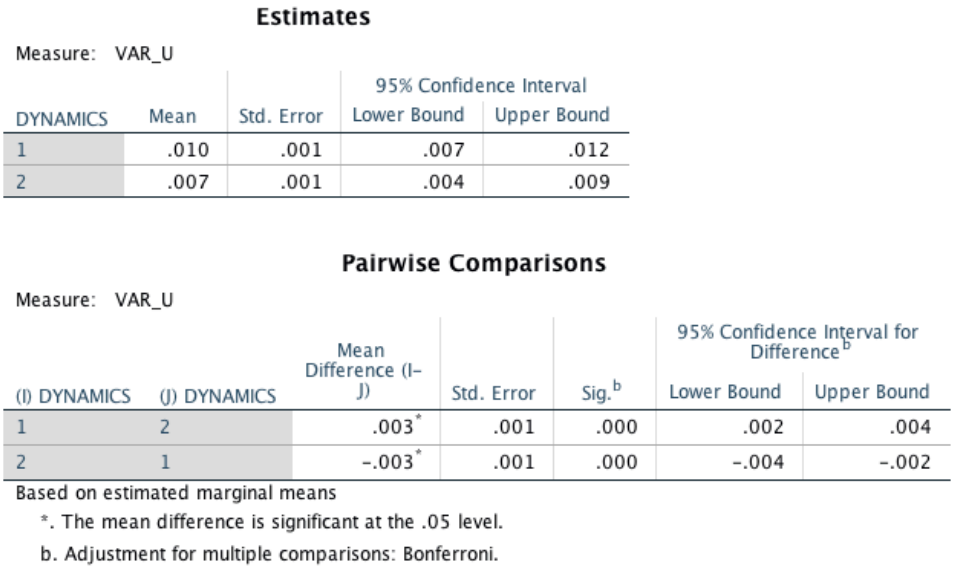

Estimates

Measure: VAR_U

DYNAMICS	Mean	Std. Error	95% Confidence Interval Lower Bound	95% Confidence Interval Upper Bound
1	.010	.001	.007	.012
2	.007	.001	.004	.009

Pairwise Comparisons

Measure: VAR_U

(I) DYNAMICS	(J) DYNAMICS	Mean Difference (I-J)	Std. Error	Sig.[b]	95% Confidence Interval for Difference[b] Lower Bound	95% Confidence Interval for Difference[b] Upper Bound
1	2	.003*	.001	.000	.002	.004
2	1	-.003*	.001	.000	-.004	-.002

Based on estimated marginal means

*. The mean difference is significant at the .05 level.

b. Adjustment for multiple comparisons: Bonferroni.

Figure E.31 – Estimated marginal means and pairwise comparisons for Grid.

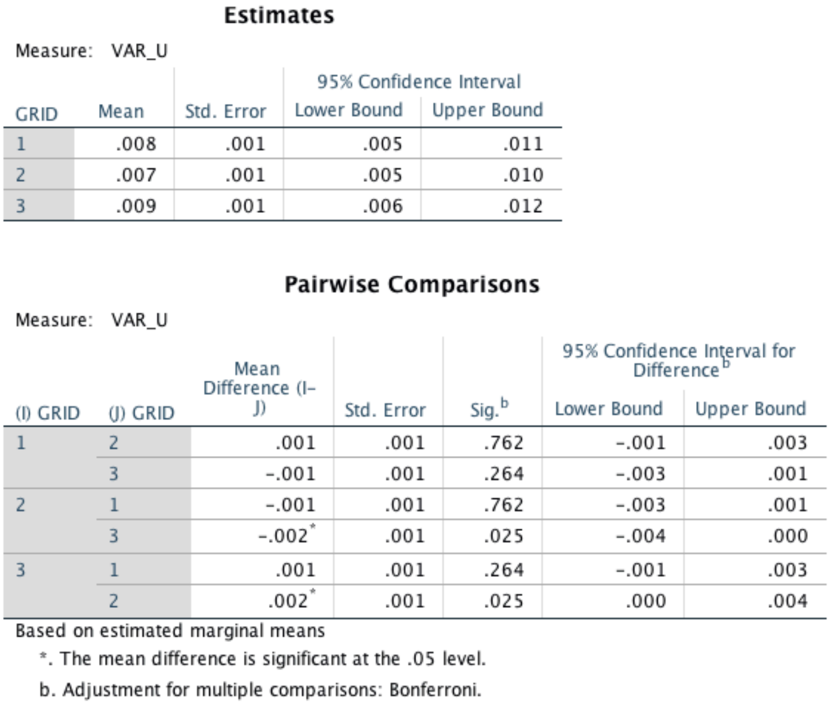

Estimates

Measure: VAR_U

GRID	Mean	Std. Error	95% Confidence Interval Lower Bound	95% Confidence Interval Upper Bound
1	.008	.001	.005	.011
2	.007	.001	.005	.010
3	.009	.001	.006	.012

Pairwise Comparisons

Measure: VAR_U

(I) GRID	(J) GRID	Mean Difference (I-J)	Std. Error	Sig.^{b}	95% Confidence Interval for Difference^b Lower Bound	95% Confidence Interval for Difference^b Upper Bound
1	2	.001	.001	.762	-.001	.003
	3	-.001	.001	.264	-.003	.001
2	1	-.001	.001	.762	-.003	.001
	3	-.002*	.001	.025	-.004	.000
3	1	.001	.001	.264	-.001	.003
	2	.002*	.001	.025	.000	.004

Based on estimated marginal means

*. The mean difference is significant at the .05 level.

b. Adjustment for multiple comparisons: Bonferroni.

Figure E.32 – Estimated marginal means and pairwise comparisons for Dynamics.

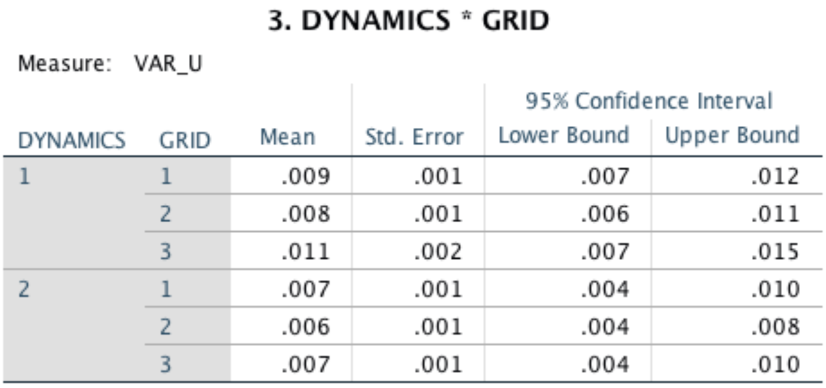

3. DYNAMICS * GRID

Measure: VAR_U

DYNAMICS	GRID	Mean	Std. Error	95% Confidence Interval Lower Bound	95% Confidence Interval Upper Bound
1	1	.009	.001	.007	.012
	2	.008	.001	.006	.011
	3	.011	.002	.007	.015
2	1	.007	.001	.004	.010
	2	.006	.001	.004	.008
	3	.007	.001	.004	.010

Figure E.33 – Estimated marginal means of Grid - Dynamics interaction.

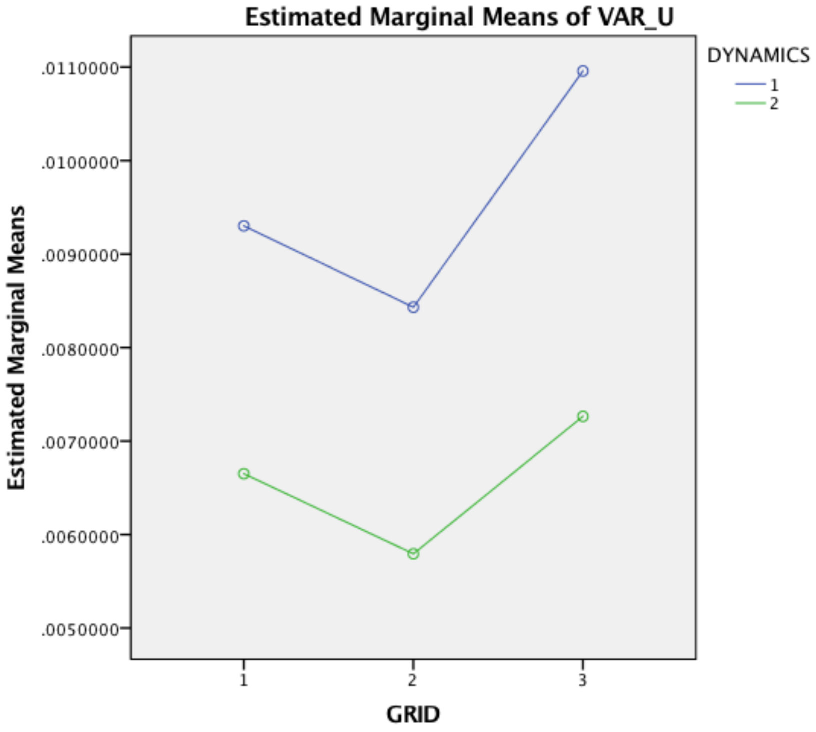

Figure E.34 – Profile plot for within-subjects ANOVA of control activity.

E.4. Minimum time to contact

Mixed-Design ANOVA

Experience turned out not to be a significant factor for the minimum time to contact (τ_{min}). Mauchly's test indicated that the assumption of sphericity had not been violated, $\chi^2(2) = 2.533$, $p = .282$. The assumption of homogeneity of variance was not rejected by Levene's test. The null hypothesis that the τ_{min} data came from a normally-distributed population was confirmed by Shapiro-Wilk's test. Mixed ANOVA did not reject the null hypothesis that the means of τ_{min} are the same for both Experience levels, therefore ANOVA was done on the Experience-lumped τ_{min} data.

Within-Subjects ANOVA

A box plot of the Experience-lumped τ_{min} is displayed in **??**. The assumption of sphericity

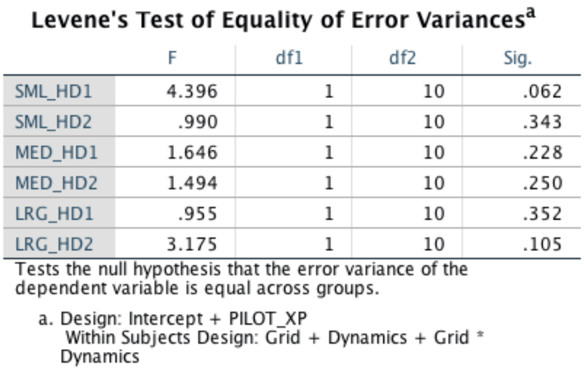

Levene's Test of Equality of Error Variances[a]

	F	df1	df2	Sig.
SML_HD1	4.396	1	10	.062
SML_HD2	.990	1	10	.343
MED_HD1	1.646	1	10	.228
MED_HD2	1.494	1	10	.250
LRG_HD1	.955	1	10	.352
LRG_HD2	3.175	1	10	.105

Tests the null hypothesis that the error variance of the dependent variable is equal across groups.

a. Design: Intercept + PILOT_XP
Within Subjects Design: Grid + Dynamics + Grid * Dynamics

Figure E.35 – Mixed-design Levene'e test of homogeneity of variance for minimum tau.

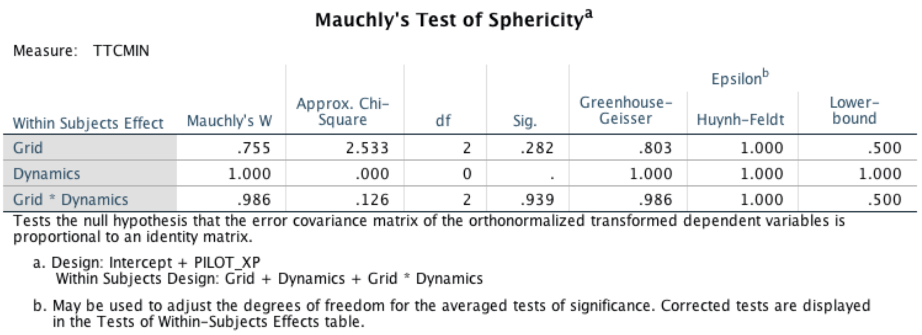

Mauchly's Test of Sphericity[a]

Measure: TTCMIN

Within Subjects Effect	Mauchly's W	Approx. Chi-Square	df	Sig.	Epsilon[b] Greenhouse-Geisser	Huynh-Feldt	Lower-bound
Grid	.755	2.533	2	.282	.803	1.000	.500
Dynamics	1.000	.000	0	.	1.000	1.000	1.000
Grid * Dynamics	.986	.126	2	.939	.986	1.000	.500

Tests the null hypothesis that the error covariance matrix of the orthonormalized transformed dependent variables is proportional to an identity matrix.

a. Design: Intercept + PILOT_XP
Within Subjects Design: Grid + Dynamics + Grid * Dynamics

b. May be used to adjust the degrees of freedom for the averaged tests of significance. Corrected tests are displayed in the Tests of Within-Subjects Effects table.

Figure E.36 – Mixed-design Mauchly's test of sphericity for minimum tau.

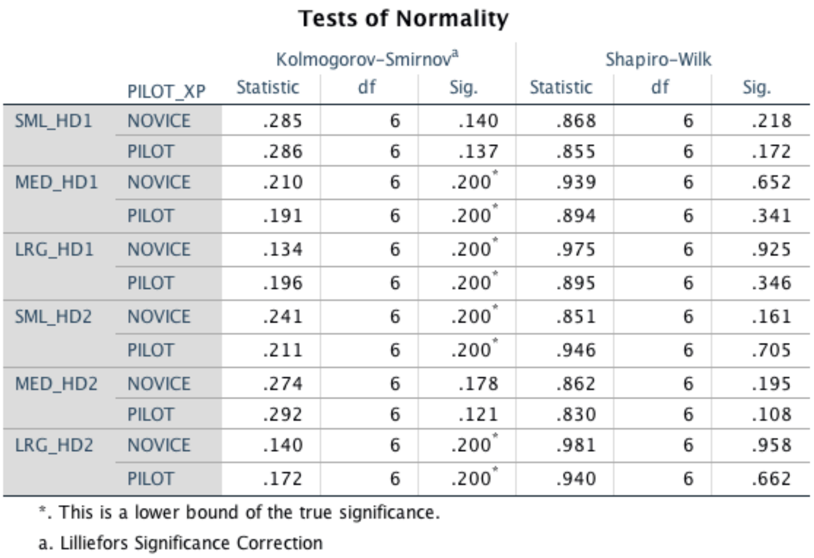

Tests of Normality

	PILOT_XP	Kolmogorov-Smirnov[a] Statistic	df	Sig.	Shapiro-Wilk Statistic	df	Sig.
SML_HD1	NOVICE	.285	6	.140	.868	6	.218
	PILOT	.286	6	.137	.855	6	.172
MED_HD1	NOVICE	.210	6	.200*	.939	6	.652
	PILOT	.191	6	.200*	.894	6	.341
LRG_HD1	NOVICE	.134	6	.200*	.975	6	.925
	PILOT	.196	6	.200*	.895	6	.346
SML_HD2	NOVICE	.241	6	.200*	.851	6	.161
	PILOT	.211	6	.200*	.946	6	.705
MED_HD2	NOVICE	.274	6	.178	.862	6	.195
	PILOT	.292	6	.121	.830	6	.108
LRG_HD2	NOVICE	.140	6	.200*	.981	6	.958
	PILOT	.172	6	.200*	.940	6	.662

*. This is a lower bound of the true significance.

a. Lilliefors Significance Correction

Figure E.37 – Mixed-design normality tests for minimum tau.

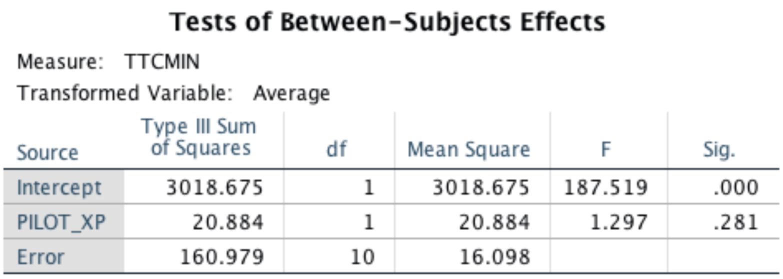

Tests of Between-Subjects Effects

Measure: TTCMIN
Transformed Variable: Average

Source	Type III Sum of Squares	df	Mean Square	F	Sig.
Intercept	3018.675	1	3018.675	187.519	.000
PILOT_XP	20.884	1	20.884	1.297	.281
Error	160.979	10	16.098		

Figure E.38 – Mixed-design ANOVA for minimum tau.

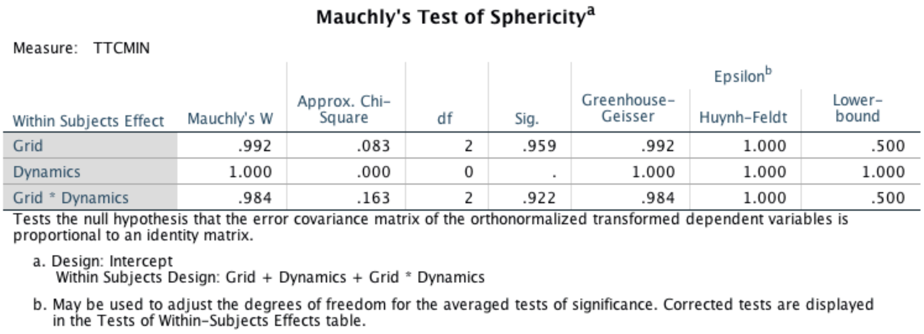

Mauchly's Test of Sphericity[a]

Measure: TTCMIN

Within Subjects Effect	Mauchly's W	Approx. Chi-Square	df	Sig.	Epsilon[b] Greenhouse-Geisser	Huynh-Feldt	Lower-bound
Grid	.992	.083	2	.959	.992	1.000	.500
Dynamics	1.000	.000	0	.	1.000	1.000	1.000
Grid * Dynamics	.984	.163	2	.922	.984	1.000	.500

Tests the null hypothesis that the error covariance matrix of the orthonormalized transformed dependent variables is proportional to an identity matrix.

a. Design: Intercept
Within Subjects Design: Grid + Dynamics + Grid * Dynamics

b. May be used to adjust the degrees of freedom for the averaged tests of significance. Corrected tests are displayed in the Tests of Within-Subjects Effects table.

Figure E.39 – Mauchly's test of sphericity for within-subjects minimum tau.

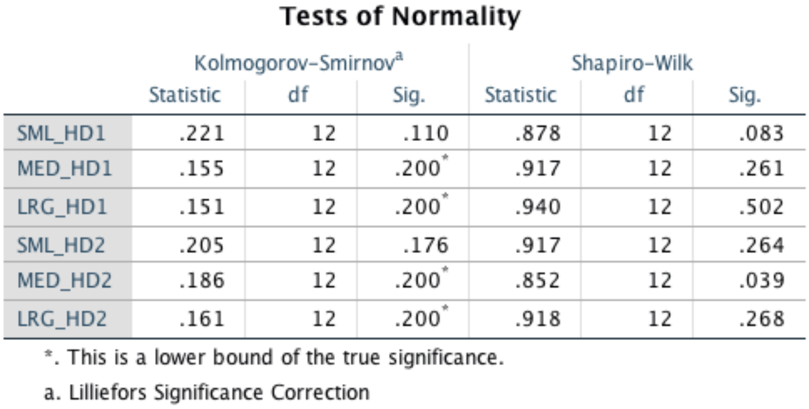

Tests of Normality

	Kolmogorov-Smirnov[a]			Shapiro-Wilk		
	Statistic	df	Sig.	Statistic	df	Sig.
SML_HD1	.221	12	.110	.878	12	.083
MED_HD1	.155	12	.200*	.917	12	.261
LRG_HD1	.151	12	.200*	.940	12	.502
SML_HD2	.205	12	.176	.917	12	.264
MED_HD2	.186	12	.200*	.852	12	.039
LRG_HD2	.161	12	.200*	.918	12	.268

*. This is a lower bound of the true significance.

a. Lilliefors Significance Correction

Figure E.40 – Normality tests for within-subjects minimum tau.

could not be rejected for Grid and for the Grid × Dynamics interaction by Mauchly's test, $\chi^2(2) = 0.083$, $p = .959$ and $\chi^2(2) = .163$, $p = .922$, respectively. The assumption of normality of the τ_{min} data was made, despite a Shapiro-Wilk test rejecting it for one repeated measure, $W = .852, p = .039$. ANOVA indicated only a significant main effect of Dynamics on τ_{min} $F(1, 11) = 7.584, p = .019$, with an increase of mean τ_{min} from 6.026(.491) to 6.924(.521) when switching from Dynamics 1 to 2. No statistically significant interaction effect of Grid × Dynamics was found.

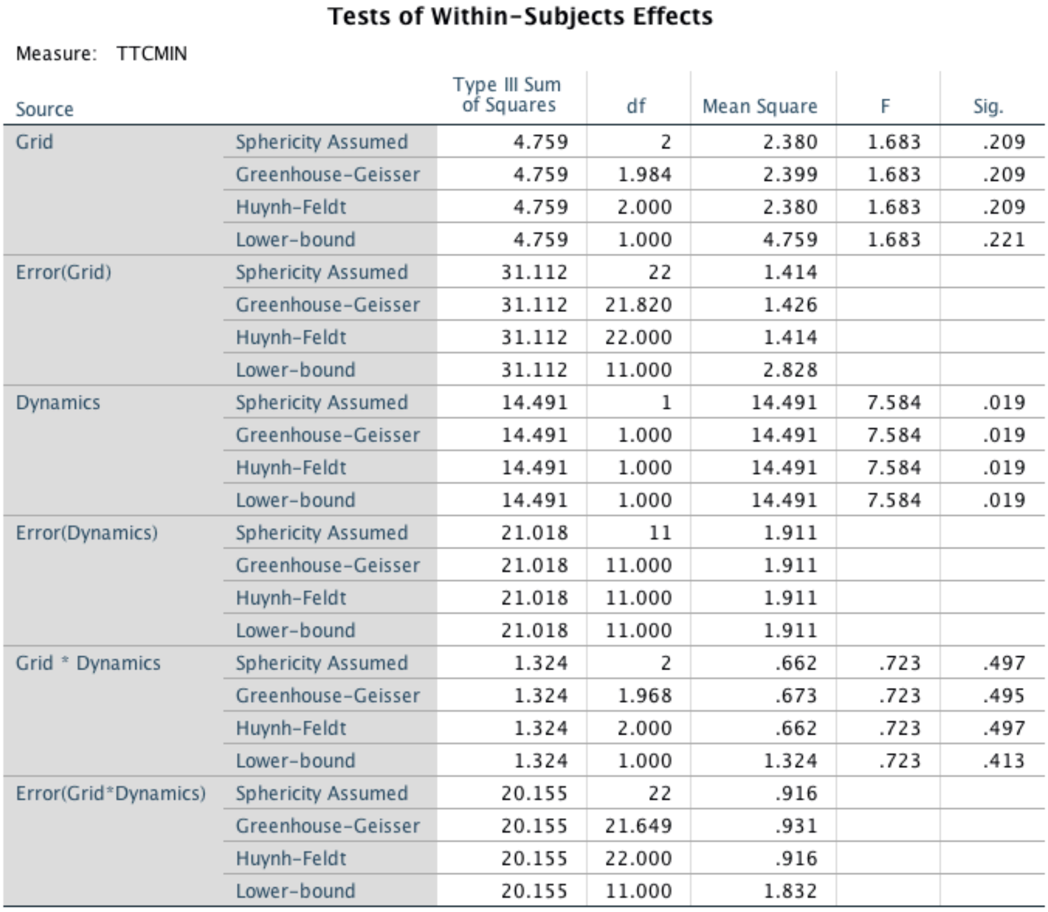

Tests of Within-Subjects Effects

Measure: TTCMIN

Source		Type III Sum of Squares	df	Mean Square	F	Sig.
Grid	Sphericity Assumed	4.759	2	2.380	1.683	.209
	Greenhouse-Geisser	4.759	1.984	2.399	1.683	.209
	Huynh-Feldt	4.759	2.000	2.380	1.683	.209
	Lower-bound	4.759	1.000	4.759	1.683	.221
Error(Grid)	Sphericity Assumed	31.112	22	1.414		
	Greenhouse-Geisser	31.112	21.820	1.426		
	Huynh-Feldt	31.112	22.000	1.414		
	Lower-bound	31.112	11.000	2.828		
Dynamics	Sphericity Assumed	14.491	1	14.491	7.584	.019
	Greenhouse-Geisser	14.491	1.000	14.491	7.584	.019
	Huynh-Feldt	14.491	1.000	14.491	7.584	.019
	Lower-bound	14.491	1.000	14.491	7.584	.019
Error(Dynamics)	Sphericity Assumed	21.018	11	1.911		
	Greenhouse-Geisser	21.018	11.000	1.911		
	Huynh-Feldt	21.018	11.000	1.911		
	Lower-bound	21.018	11.000	1.911		
Grid * Dynamics	Sphericity Assumed	1.324	2	.662	.723	.497
	Greenhouse-Geisser	1.324	1.968	.673	.723	.495
	Huynh-Feldt	1.324	2.000	.662	.723	.497
	Lower-bound	1.324	1.000	1.324	.723	.413
Error(Grid*Dynamics)	Sphericity Assumed	20.155	22	.916		
	Greenhouse-Geisser	20.155	21.649	.931		
	Huynh-Feldt	20.155	22.000	.916		
	Lower-bound	20.155	11.000	1.832		

Figure E.41 – ANOVA for within-subjects minimum tau.

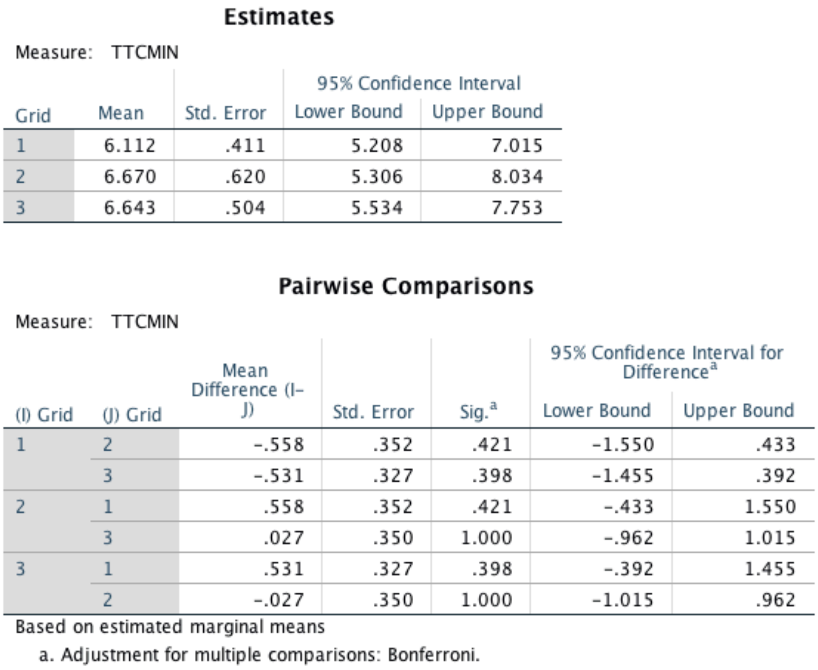

Estimates

Measure: TTCMIN

Grid	Mean	Std. Error	95% Confidence Interval Lower Bound	95% Confidence Interval Upper Bound
1	6.112	.411	5.208	7.015
2	6.670	.620	5.306	8.034
3	6.643	.504	5.534	7.753

Pairwise Comparisons

Measure: TTCMIN

(I) Grid	(J) Grid	Mean Difference (I-J)	Std. Error	Sig.[a]	95% Confidence Interval for Difference[a] Lower Bound	95% Confidence Interval for Difference[a] Upper Bound
1	2	-.558	.352	.421	-1.550	.433
	3	-.531	.327	.398	-1.455	.392
2	1	.558	.352	.421	-.433	1.550
	3	.027	.350	1.000	-.962	1.015
3	1	.531	.327	.398	-.392	1.455
	2	-.027	.350	1.000	-1.015	.962

Based on estimated marginal means

a. Adjustment for multiple comparisons: Bonferroni.

Figure E.42 – Estimated marginal means and pairwise comparisons for Grid.

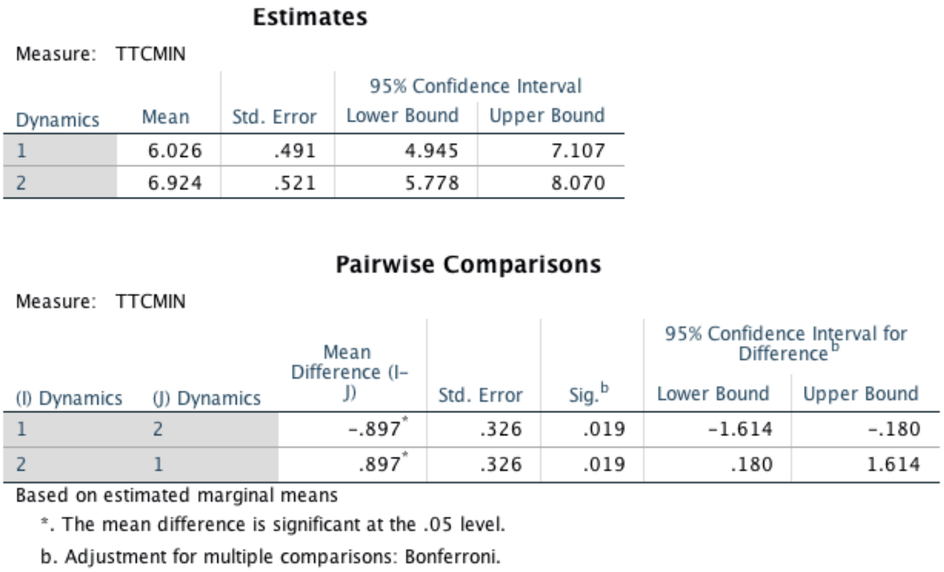

Estimates

Measure: TTCMIN

Dynamics	Mean	Std. Error	95% Confidence Interval	
			Lower Bound	Upper Bound
1	6.026	.491	4.945	7.107
2	6.924	.521	5.778	8.070

Pairwise Comparisons

Measure: TTCMIN

(I) Dynamics	(J) Dynamics	Mean Difference (I-J)	Std. Error	Sig.[b]	95% Confidence Interval for Difference[b]	
					Lower Bound	Upper Bound
1	2	-.897*	.326	.019	-1.614	-.180
2	1	.897*	.326	.019	.180	1.614

Based on estimated marginal means

*. The mean difference is significant at the .05 level.

b. Adjustment for multiple comparisons: Bonferroni.

Figure E.43 – Estimated marginal means and pairwise comparisons for Dynamics.

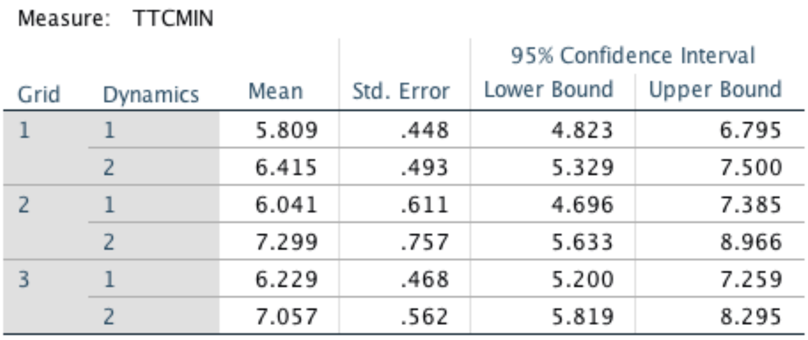

Measure: TTCMIN

Grid	Dynamics	Mean	Std. Error	95% Confidence Interval	
				Lower Bound	Upper Bound
1	1	5.809	.448	4.823	6.795
	2	6.415	.493	5.329	7.500
2	1	6.041	.611	4.696	7.385
	2	7.299	.757	5.633	8.966
3	1	6.229	.468	5.200	7.259
	2	7.057	.562	5.819	8.295

Figure E.44 – Estimated marginal means of Grid - Dynamics interaction.

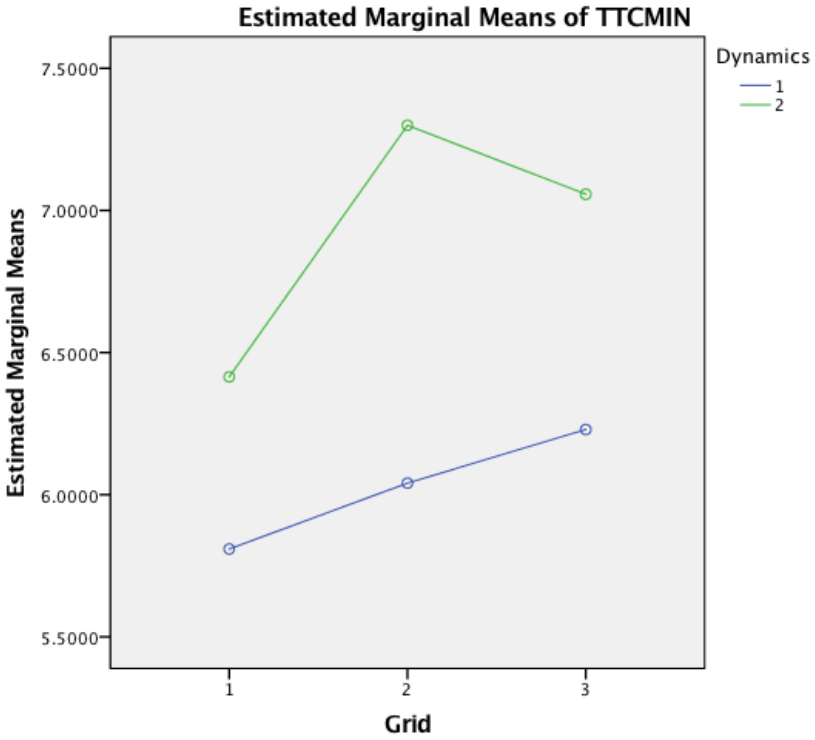

Figure E.45 – Profile plot for within-subjects ANOVA of minimum tau.

E.5. Manoeuvre duration

Mixed-Design ANOVA

No significant effect of Experience on manoeuvre duration (*T*) was found. Mauchly's test indicated that the assumption of sphericity had not been violated, $\chi^2(2) = 3.604$, $p = .165$. The assumption of homogeneity of variance was rejected by Levene's test for one repeated measure ($F = 10.090, p = .010$). Shapiro-Wilk's test rejected the null hypothesis that the *T* data came from a normally-distributed population for 3 repeated measures. Mixed ANOVA did not reject the null hypothesis that the means for *T* are the same across both levels of Experience, therefore ANOVA was done on the Experience-lumped *T* data.

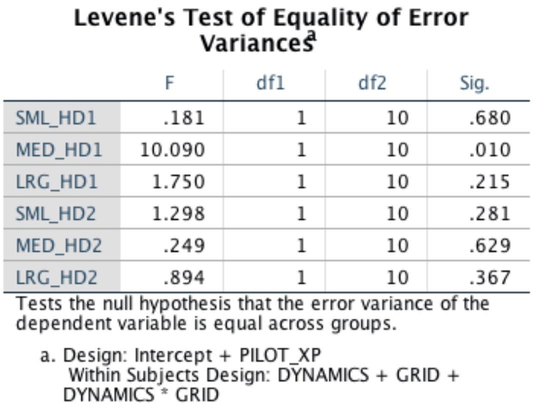

Levene's Test of Equality of Error Variances[a]

	F	df1	df2	Sig.
SML_HD1	.181	1	10	.680
MED_HD1	10.090	1	10	.010
LRG_HD1	1.750	1	10	.215
SML_HD2	1.298	1	10	.281
MED_HD2	.249	1	10	.629
LRG_HD2	.894	1	10	.367

Tests the null hypothesis that the error variance of the dependent variable is equal across groups.

a. Design: Intercept + PILOT_XP
Within Subjects Design: DYNAMICS + GRID + DYNAMICS * GRID

Figure E.46 – Mixed-design Levene’e test of homogeneity of variance for manoeuvre duration.

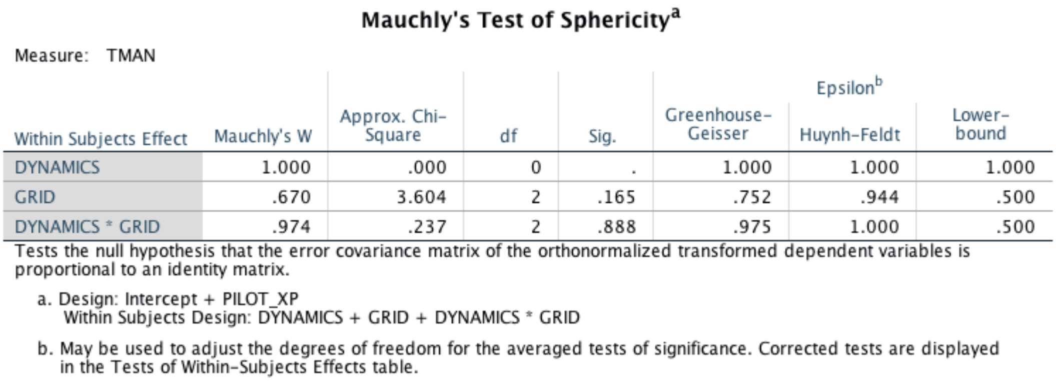

Mauchly's Test of Sphericity[a]

Measure: TMAN

Within Subjects Effect	Mauchly's W	Approx. Chi-Square	df	Sig.	Epsilon[b] Greenhouse-Geisser	Huynh-Feldt	Lower-bound
DYNAMICS	1.000	.000	0	.	1.000	1.000	1.000
GRID	.670	3.604	2	.165	.752	.944	.500
DYNAMICS * GRID	.974	.237	2	.888	.975	1.000	.500

Tests the null hypothesis that the error covariance matrix of the orthonormalized transformed dependent variables is proportional to an identity matrix.

a. Design: Intercept + PILOT_XP
Within Subjects Design: DYNAMICS + GRID + DYNAMICS * GRID

b. May be used to adjust the degrees of freedom for the averaged tests of significance. Corrected tests are displayed in the Tests of Within-Subjects Effects table.

Figure E.47 – Mixed-design Mauchly's test of sphericity for manoeuvre duration.

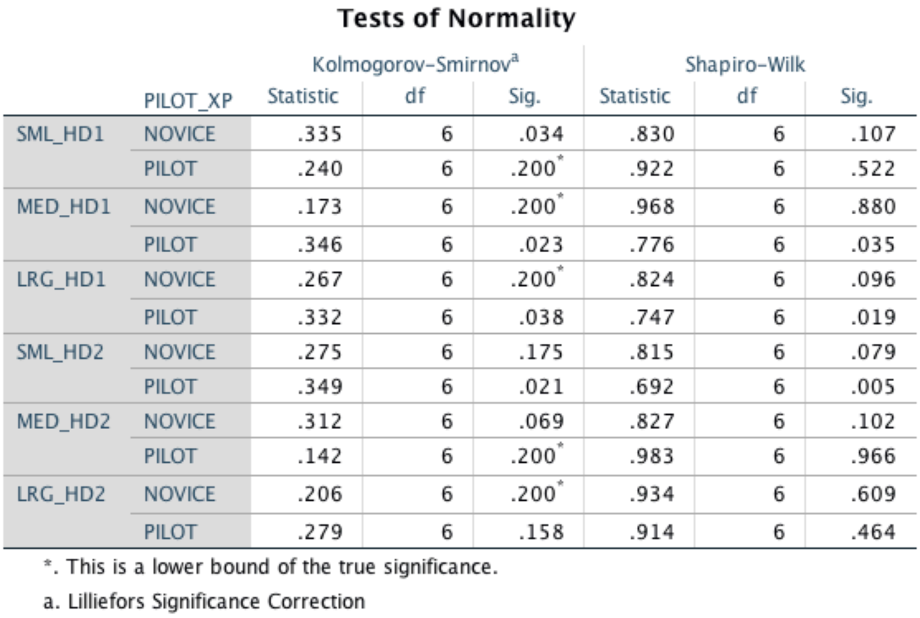

Tests of Normality

		Kolmogorov-Smirnov[a]			Shapiro-Wilk		
	PILOT_XP	Statistic	df	Sig.	Statistic	df	Sig.
SML_HD1	NOVICE	.335	6	.034	.830	6	.107
	PILOT	.240	6	.200*	.922	6	.522
MED_HD1	NOVICE	.173	6	.200*	.968	6	.880
	PILOT	.346	6	.023	.776	6	.035
LRG_HD1	NOVICE	.267	6	.200*	.824	6	.096
	PILOT	.332	6	.038	.747	6	.019
SML_HD2	NOVICE	.275	6	.175	.815	6	.079
	PILOT	.349	6	.021	.692	6	.005
MED_HD2	NOVICE	.312	6	.069	.827	6	.102
	PILOT	.142	6	.200*	.983	6	.966
LRG_HD2	NOVICE	.206	6	.200*	.934	6	.609
	PILOT	.279	6	.158	.914	6	.464

*. This is a lower bound of the true significance.

a. Lilliefors Significance Correction

Figure E.48 – Mixed-design normality tests for manoeuvre duration.

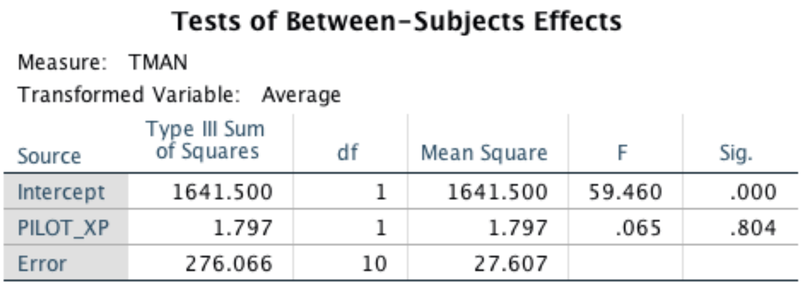

Tests of Between-Subjects Effects

Measure: TMAN
Transformed Variable: Average

Source	Type III Sum of Squares	df	Mean Square	F	Sig.
Intercept	1641.500	1	1641.500	59.460	.000
PILOT_XP	1.797	1	1.797	.065	.804
Error	276.066	10	27.607		

Figure E.49 – Mixed-design ANOVA for manoeuvre duration.

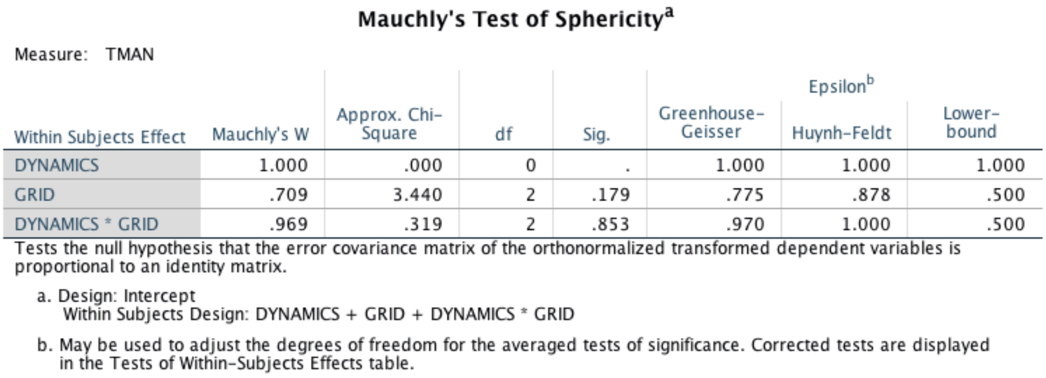

Mauchly's Test of Sphericity[a]

Measure: TMAN

Within Subjects Effect	Mauchly's W	Approx. Chi-Square	df	Sig.	Epsilon[b] Greenhouse-Geisser	Huynh-Feldt	Lower-bound
DYNAMICS	1.000	.000	0	.	1.000	1.000	1.000
GRID	.709	3.440	2	.179	.775	.878	.500
DYNAMICS * GRID	.969	.319	2	.853	.970	1.000	.500

Tests the null hypothesis that the error covariance matrix of the orthonormalized transformed dependent variables is proportional to an identity matrix.

a. Design: Intercept
Within Subjects Design: DYNAMICS + GRID + DYNAMICS * GRID

b. May be used to adjust the degrees of freedom for the averaged tests of significance. Corrected tests are displayed in the Tests of Within-Subjects Effects table.

Figure E.50 – Mauchly's test of sphericity for within-subjects manoeuvre duration.

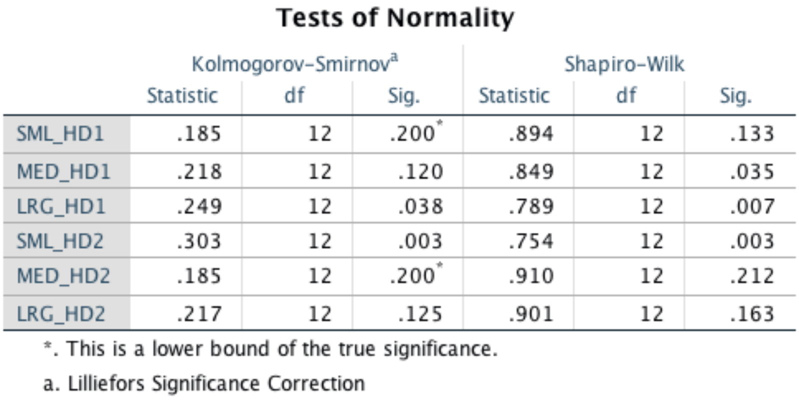

Tests of Normality

	Kolmogorov-Smirnov[a]			Shapiro-Wilk		
	Statistic	df	Sig.	Statistic	df	Sig.
SML_HD1	.185	12	.200*	.894	12	.133
MED_HD1	.218	12	.120	.849	12	.035
LRG_HD1	.249	12	.038	.789	12	.007
SML_HD2	.303	12	.003	.754	12	.003
MED_HD2	.185	12	.200*	.910	12	.212
LRG_HD2	.217	12	.125	.901	12	.163

*. This is a lower bound of the true significance.

a. Lilliefors Significance Correction

Figure E.51 – Normality tests for within-subjects manoeuvre duration.

Within-Subjects ANOVA

A box plot of the Experience-lumped *T* is displayed in **??**. Mauchly's test could not reject the assumption of sphericity for Grid and for the Grid × Dynamics interaction $\chi^2(2) = 3.440$, $p = .179$ and $\chi^2(2) = .319$, $p = .853$, respectively. Normality was assumed even though a Shapiro-Wilk test rejected it for three out of six of the repeated measures. ANOVA indicated no significant main effect of Grid or Dynamics, nor of their interaction of Grid × Dynamics.

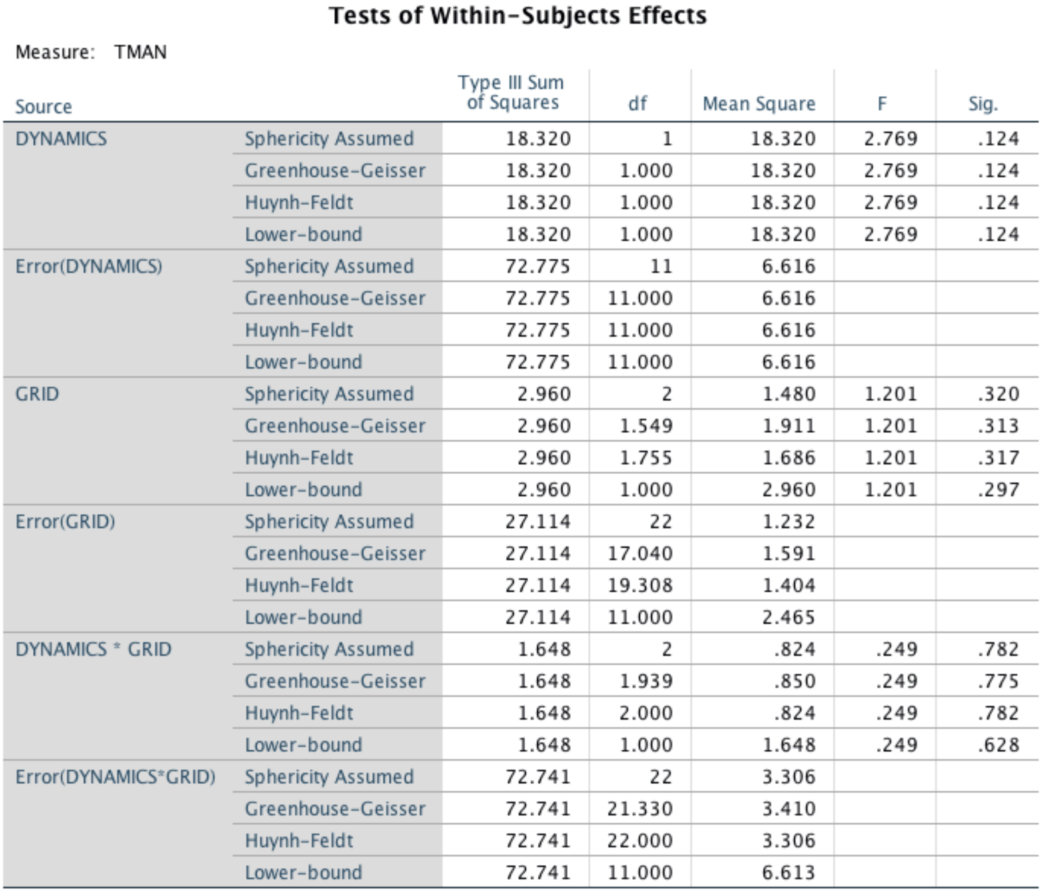

Tests of Within-Subjects Effects

Measure: TMAN

Source		Type III Sum of Squares	df	Mean Square	F	Sig.
DYNAMICS	Sphericity Assumed	18.320	1	18.320	2.769	.124
	Greenhouse-Geisser	18.320	1.000	18.320	2.769	.124
	Huynh-Feldt	18.320	1.000	18.320	2.769	.124
	Lower-bound	18.320	1.000	18.320	2.769	.124
Error(DYNAMICS)	Sphericity Assumed	72.775	11	6.616		
	Greenhouse-Geisser	72.775	11.000	6.616		
	Huynh-Feldt	72.775	11.000	6.616		
	Lower-bound	72.775	11.000	6.616		
GRID	Sphericity Assumed	2.960	2	1.480	1.201	.320
	Greenhouse-Geisser	2.960	1.549	1.911	1.201	.313
	Huynh-Feldt	2.960	1.755	1.686	1.201	.317
	Lower-bound	2.960	1.000	2.960	1.201	.297
Error(GRID)	Sphericity Assumed	27.114	22	1.232		
	Greenhouse-Geisser	27.114	17.040	1.591		
	Huynh-Feldt	27.114	19.308	1.404		
	Lower-bound	27.114	11.000	2.465		
DYNAMICS * GRID	Sphericity Assumed	1.648	2	.824	.249	.782
	Greenhouse-Geisser	1.648	1.939	.850	.249	.775
	Huynh-Feldt	1.648	2.000	.824	.249	.782
	Lower-bound	1.648	1.000	1.648	.249	.628
Error(DYNAMICS*GRID)	Sphericity Assumed	72.741	22	3.306		
	Greenhouse-Geisser	72.741	21.330	3.410		
	Huynh-Feldt	72.741	22.000	3.306		
	Lower-bound	72.741	11.000	6.613		

Figure E.52 – ANOVA for within-subjects manoeuvre duration.

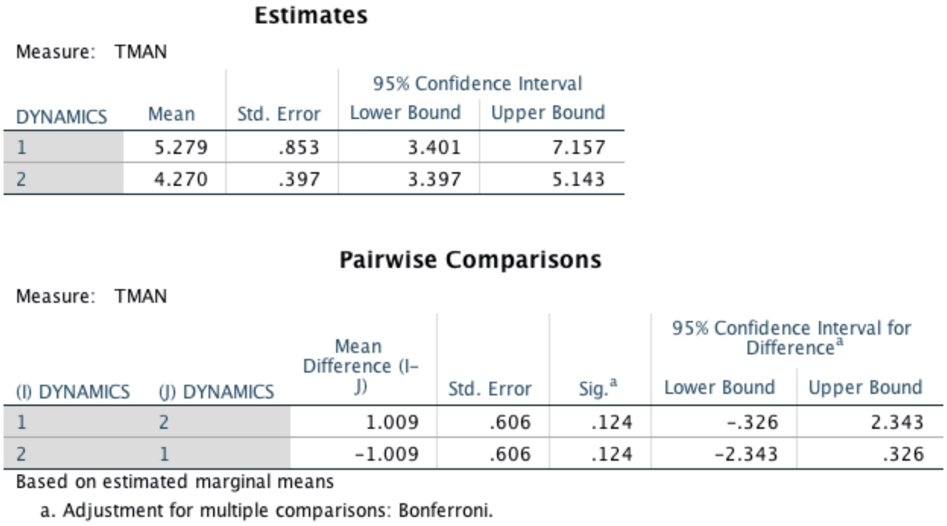

Estimates

Measure: TMAN

DYNAMICS	Mean	Std. Error	95% Confidence Interval	
			Lower Bound	Upper Bound
1	5.279	.853	3.401	7.157
2	4.270	.397	3.397	5.143

Pairwise Comparisons

Measure: TMAN

(I) DYNAMICS	(J) DYNAMICS	Mean Difference (I-J)	Std. Error	Sig.[a]	95% Confidence Interval for Difference[a]	
					Lower Bound	Upper Bound
1	2	1.009	.606	.124	-.326	2.343
2	1	-1.009	.606	.124	-2.343	.326

Based on estimated marginal means

a. Adjustment for multiple comparisons: Bonferroni.

Figure E.53 – Estimated marginal means and pairwise comparisons for Grid.

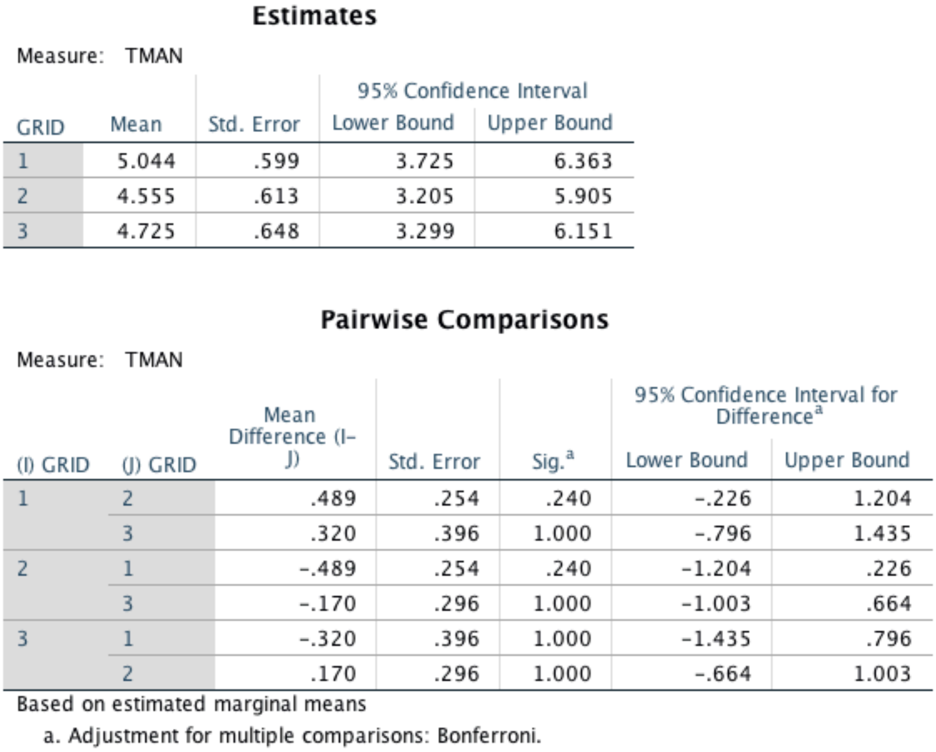

Estimates

Measure: TMAN

GRID	Mean	Std. Error	95% Confidence Interval Lower Bound	95% Confidence Interval Upper Bound
1	5.044	.599	3.725	6.363
2	4.555	.613	3.205	5.905
3	4.725	.648	3.299	6.151

Pairwise Comparisons

Measure: TMAN

(I) GRID	(J) GRID	Mean Difference (I–J)	Std. Error	Sig.[a]	95% Confidence Interval for Difference[a] Lower Bound	95% Confidence Interval for Difference[a] Upper Bound
1	2	.489	.254	.240	-.226	1.204
	3	.320	.396	1.000	-.796	1.435
2	1	-.489	.254	.240	-1.204	.226
	3	-.170	.296	1.000	-1.003	.664
3	1	-.320	.396	1.000	-1.435	.796
	2	.170	.296	1.000	-.664	1.003

Based on estimated marginal means

a. Adjustment for multiple comparisons: Bonferroni.

Figure E.54 – Estimated marginal means and pairwise comparisons for Dynamics.

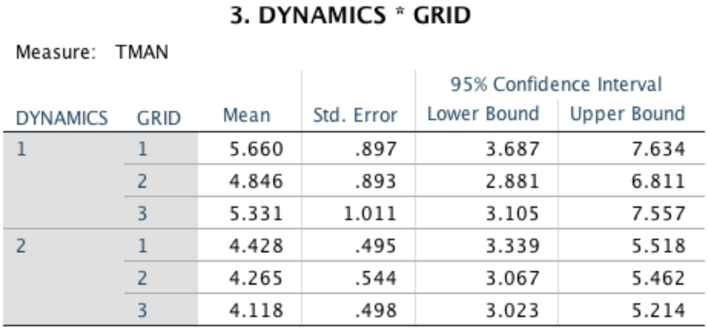

3. DYNAMICS * GRID

Measure: TMAN

DYNAMICS	GRID	Mean	Std. Error	95% Confidence Interval Lower Bound	95% Confidence Interval Upper Bound
1	1	5.660	.897	3.687	7.634
	2	4.846	.893	2.881	6.811
	3	5.331	1.011	3.105	7.557
2	1	4.428	.495	3.339	5.518
	2	4.265	.544	3.067	5.462
	3	4.118	.498	3.023	5.214

Figure E.55 – Estimated marginal means of Grid - Dynamics interaction.

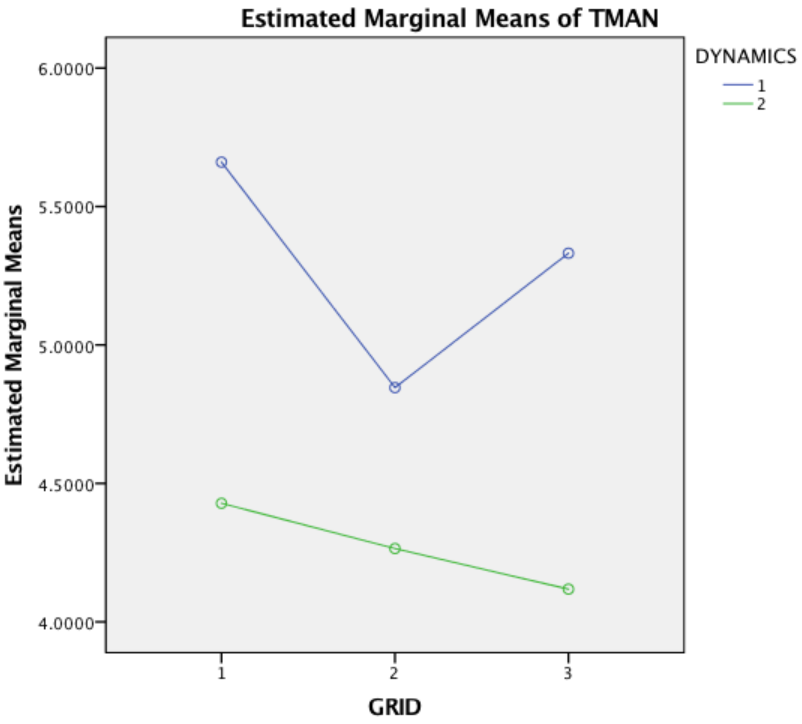

Figure E.56 – Profile plot for within-subjects ANOVA of manoeuvre duration.

E.6. Flight path angle gap

Mixed-Design ANOVA

Experience was not a significant factor for the manoeuvre gap γ_{gap}. Mauchly's test indicated that the assumption of sphericity had not been violated, $\chi^2(2) = 3.988$, $p = .136$. The assumption of homogeneity of variance could not be rejected by Levene's test. Shapiro-Wilk's test could not reject the null hypothesis that the γ_{gap} data came from a normally-distributed population. Mixed ANOVA did not reject the null hypothesis that the means for γ_{gap} are the same across both levels of Experience, therefore ANOVA was done on the Experience-lumped γ_{gap} data.

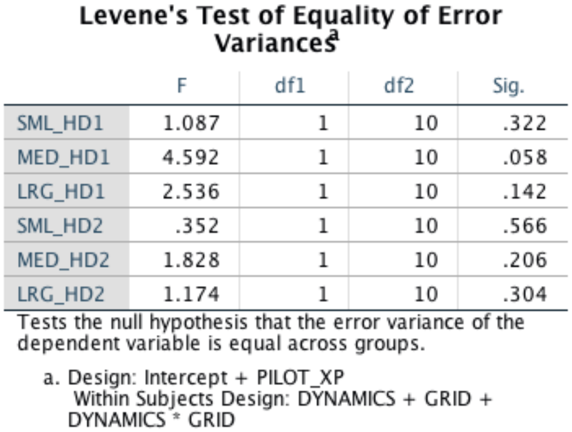

Levene's Test of Equality of Error Variances[a]

	F	df1	df2	Sig.
SML_HD1	1.087	1	10	.322
MED_HD1	4.592	1	10	.058
LRG_HD1	2.536	1	10	.142
SML_HD2	.352	1	10	.566
MED_HD2	1.828	1	10	.206
LRG_HD2	1.174	1	10	.304

Tests the null hypothesis that the error variance of the dependent variable is equal across groups.

a. Design: Intercept + PILOT_XP
Within Subjects Design: DYNAMICS + GRID + DYNAMICS * GRID

Figure E.57 – Mixed-design Levene'e test of homogeneity of variance for flight path angle gap.

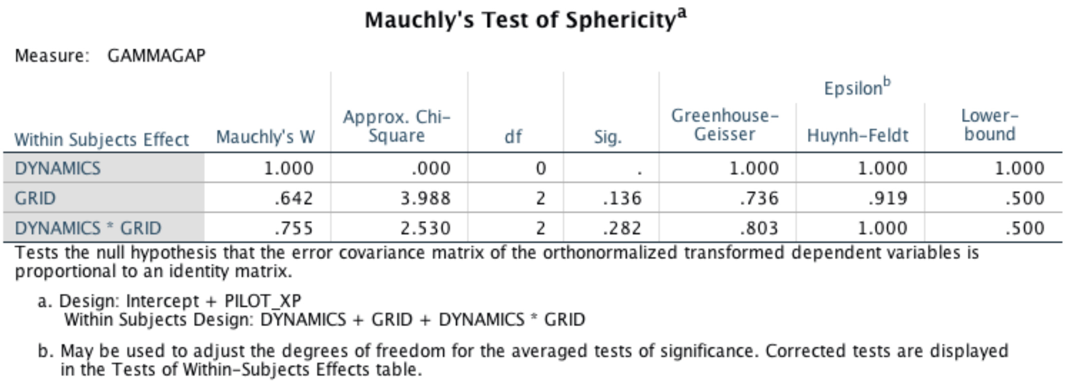

Mauchly's Test of Sphericity[a]

Measure: GAMMAGAP

Within Subjects Effect	Mauchly's W	Approx. Chi-Square	df	Sig.	Epsilon[b] Greenhouse-Geisser	Huynh-Feldt	Lower-bound
DYNAMICS	1.000	.000	0	.	1.000	1.000	1.000
GRID	.642	3.988	2	.136	.736	.919	.500
DYNAMICS * GRID	.755	2.530	2	.282	.803	1.000	.500

Tests the null hypothesis that the error covariance matrix of the orthonormalized transformed dependent variables is proportional to an identity matrix.

a. Design: Intercept + PILOT_XP
Within Subjects Design: DYNAMICS + GRID + DYNAMICS * GRID

b. May be used to adjust the degrees of freedom for the averaged tests of significance. Corrected tests are displayed in the Tests of Within-Subjects Effects table.

Figure E.58 – Mixed-design Mauchly's test of sphericity for flight path angle gap.

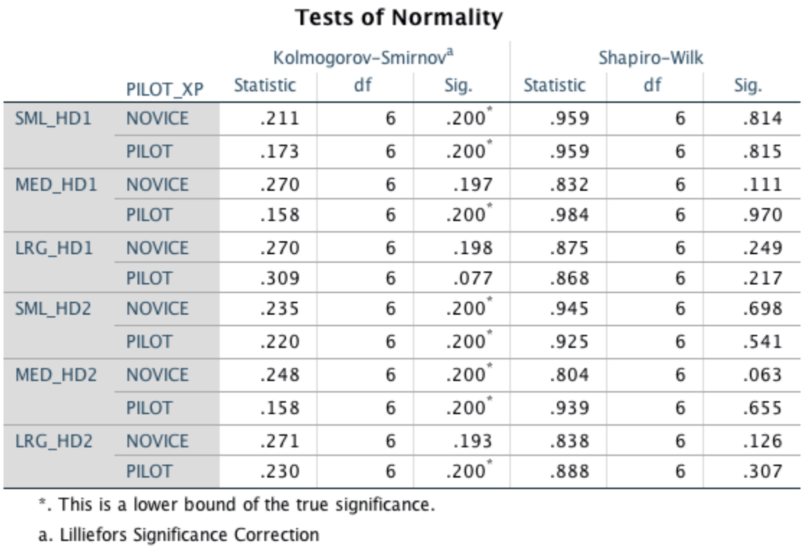

Tests of Normality

	PILOT_XP	Kolmogorov-Smirnov[a] Statistic	df	Sig.	Shapiro-Wilk Statistic	df	Sig.
SML_HD1	NOVICE	.211	6	.200*	.959	6	.814
	PILOT	.173	6	.200*	.959	6	.815
MED_HD1	NOVICE	.270	6	.197	.832	6	.111
	PILOT	.158	6	.200*	.984	6	.970
LRG_HD1	NOVICE	.270	6	.198	.875	6	.249
	PILOT	.309	6	.077	.868	6	.217
SML_HD2	NOVICE	.235	6	.200*	.945	6	.698
	PILOT	.220	6	.200*	.925	6	.541
MED_HD2	NOVICE	.248	6	.200*	.804	6	.063
	PILOT	.158	6	.200*	.939	6	.655
LRG_HD2	NOVICE	.271	6	.193	.838	6	.126
	PILOT	.230	6	.200*	.888	6	.307

*. This is a lower bound of the true significance.

a. Lilliefors Significance Correction

Figure E.59 – Mixed-design normality tests for flight path angle gap.

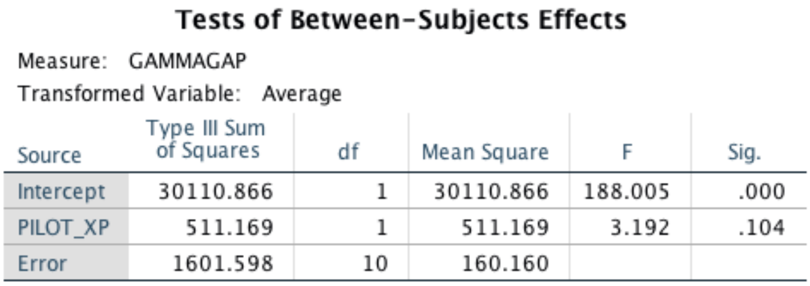

Tests of Between-Subjects Effects

Measure: GAMMAGAP
Transformed Variable: Average

Source	Type III Sum of Squares	df	Mean Square	F	Sig.
Intercept	30110.866	1	30110.866	188.005	.000
PILOT_XP	511.169	1	511.169	3.192	.104
Error	1601.598	10	160.160		

Figure E.60 – Mixed-design ANOVA for flight path angle gap.

Within-Subjects ANOVA

A box plot of the Experience-lumped γ_{gap} is displayed in **??**. Mauchly's test could not reject the assumption of sphericity for Grid and for the Grid × Dynamics interaction $\chi^2(2) = 4.016$, $p = .134$ and $\chi^2(2) = 1.539$, $p = .463$, respectively. Normality was assumed even though it was rejected for one repeated measure by a Shapiro-Wilk test.

ANOVA indicated a significant main effect of both Grid and Dynamics on γ_{gap}. Grid was found to have a significant main effect on γ_{gap}, increasing the grid cells from small to medium elicited a mean value decrease from 20.82(5.75) deg to 17.19(6.50) (p = .054), while further increasing to the large grid cells increased mean γ_{gap} to 23.33(8.29) deg (p = .012). Switching Dynamics from 1 to 2 increased mean γ_{gap} from 18.50(6.23) deg to 22.40(7.47) deg, p = .006. No interaction effect was found for Grid × Dynamics.

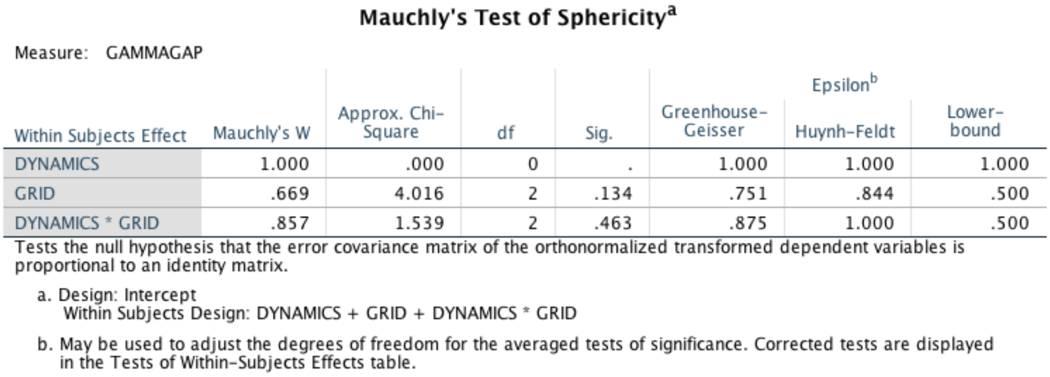

Mauchly's Test of Sphericity[a]

Measure: GAMMAGAP

Within Subjects Effect	Mauchly's W	Approx. Chi-Square	df	Sig.	Epsilon[b] Greenhouse-Geisser	Epsilon[b] Huynh-Feldt	Epsilon[b] Lower-bound
DYNAMICS	1.000	.000	0	.	1.000	1.000	1.000
GRID	.669	4.016	2	.134	.751	.844	.500
DYNAMICS * GRID	.857	1.539	2	.463	.875	1.000	.500

Tests the null hypothesis that the error covariance matrix of the orthonormalized transformed dependent variables is proportional to an identity matrix.

a. Design: Intercept
Within Subjects Design: DYNAMICS + GRID + DYNAMICS * GRID

b. May be used to adjust the degrees of freedom for the averaged tests of significance. Corrected tests are displayed in the Tests of Within-Subjects Effects table.

Figure E.61 – Mauchly's test of sphericity for within-subjects flight path angle gap.

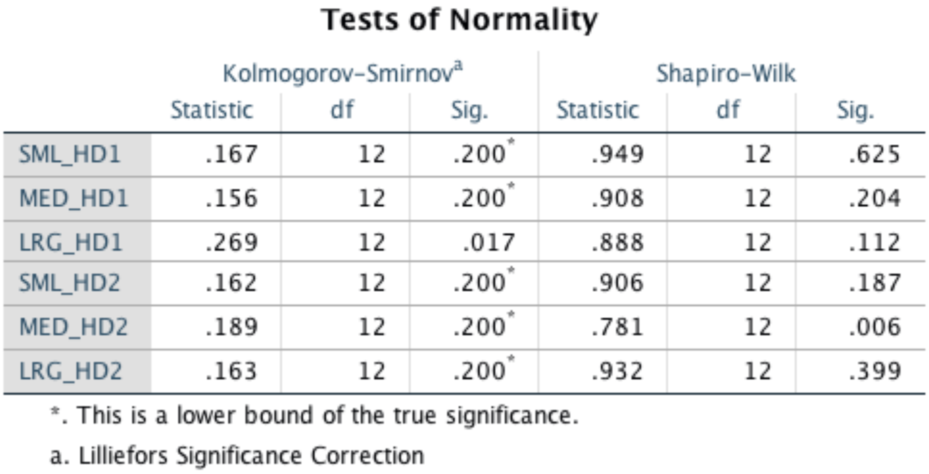

Tests of Normality

	Kolmogorov-Smirnov[a] Statistic	Kolmogorov-Smirnov[a] df	Kolmogorov-Smirnov[a] Sig.	Shapiro-Wilk Statistic	Shapiro-Wilk df	Shapiro-Wilk Sig.
SML_HD1	.167	12	.200*	.949	12	.625
MED_HD1	.156	12	.200*	.908	12	.204
LRG_HD1	.269	12	.017	.888	12	.112
SML_HD2	.162	12	.200*	.906	12	.187
MED_HD2	.189	12	.200*	.781	12	.006
LRG_HD2	.163	12	.200*	.932	12	.399

*. This is a lower bound of the true significance.

a. Lilliefors Significance Correction

Figure E.62 – Normality tests for within-subjects flight path angle gap.

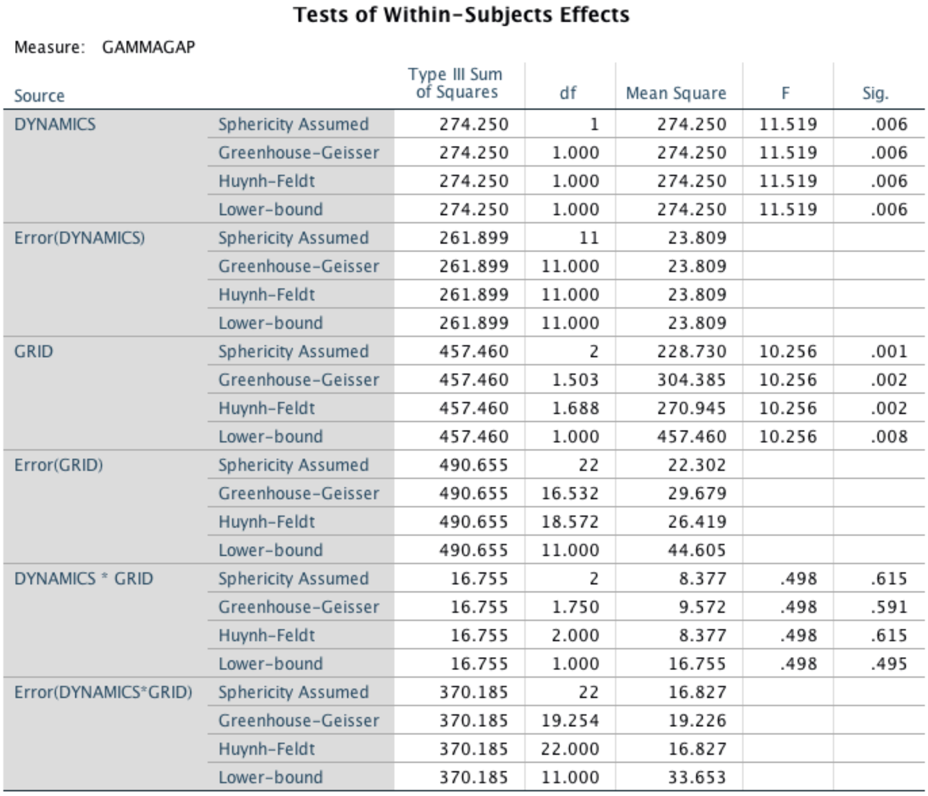

Tests of Within-Subjects Effects

Measure: GAMMAGAP

Source		Type III Sum of Squares	df	Mean Square	F	Sig.
DYNAMICS	Sphericity Assumed	274.250	1	274.250	11.519	.006
	Greenhouse-Geisser	274.250	1.000	274.250	11.519	.006
	Huynh-Feldt	274.250	1.000	274.250	11.519	.006
	Lower-bound	274.250	1.000	274.250	11.519	.006
Error(DYNAMICS)	Sphericity Assumed	261.899	11	23.809		
	Greenhouse-Geisser	261.899	11.000	23.809		
	Huynh-Feldt	261.899	11.000	23.809		
	Lower-bound	261.899	11.000	23.809		
GRID	Sphericity Assumed	457.460	2	228.730	10.256	.001
	Greenhouse-Geisser	457.460	1.503	304.385	10.256	.002
	Huynh-Feldt	457.460	1.688	270.945	10.256	.002
	Lower-bound	457.460	1.000	457.460	10.256	.008
Error(GRID)	Sphericity Assumed	490.655	22	22.302		
	Greenhouse-Geisser	490.655	16.532	29.679		
	Huynh-Feldt	490.655	18.572	26.419		
	Lower-bound	490.655	11.000	44.605		
DYNAMICS * GRID	Sphericity Assumed	16.755	2	8.377	.498	.615
	Greenhouse-Geisser	16.755	1.750	9.572	.498	.591
	Huynh-Feldt	16.755	2.000	8.377	.498	.615
	Lower-bound	16.755	1.000	16.755	.498	.495
Error(DYNAMICS*GRID)	Sphericity Assumed	370.185	22	16.827		
	Greenhouse-Geisser	370.185	19.254	19.226		
	Huynh-Feldt	370.185	22.000	16.827		
	Lower-bound	370.185	11.000	33.653		

Figure E.63 – ANOVA for within-subjects flight path angle gap.

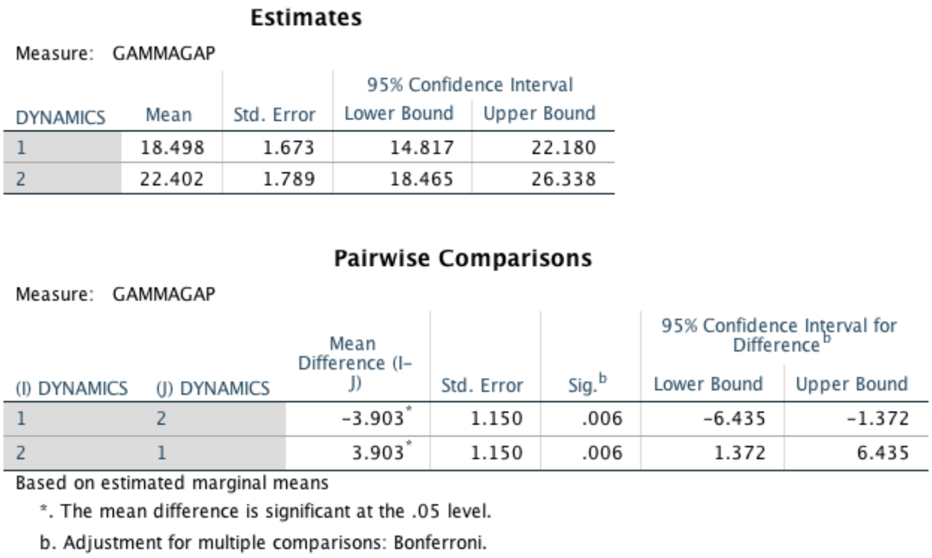

Estimates

Measure: GAMMAGAP

DYNAMICS	Mean	Std. Error	95% Confidence Interval Lower Bound	95% Confidence Interval Upper Bound
1	18.498	1.673	14.817	22.180
2	22.402	1.789	18.465	26.338

Pairwise Comparisons

Measure: GAMMAGAP

(I) DYNAMICS	(J) DYNAMICS	Mean Difference (I-J)	Std. Error	Sig.^{b}	95% Confidence Interval for Difference^b Lower Bound	95% Confidence Interval for Difference^b Upper Bound
1	2	-3.903*	1.150	.006	-6.435	-1.372
2	1	3.903*	1.150	.006	1.372	6.435

Based on estimated marginal means

*. The mean difference is significant at the .05 level.

b. Adjustment for multiple comparisons: Bonferroni.

Figure E.64 – Estimated marginal means and pairwise comparisons for Grid.

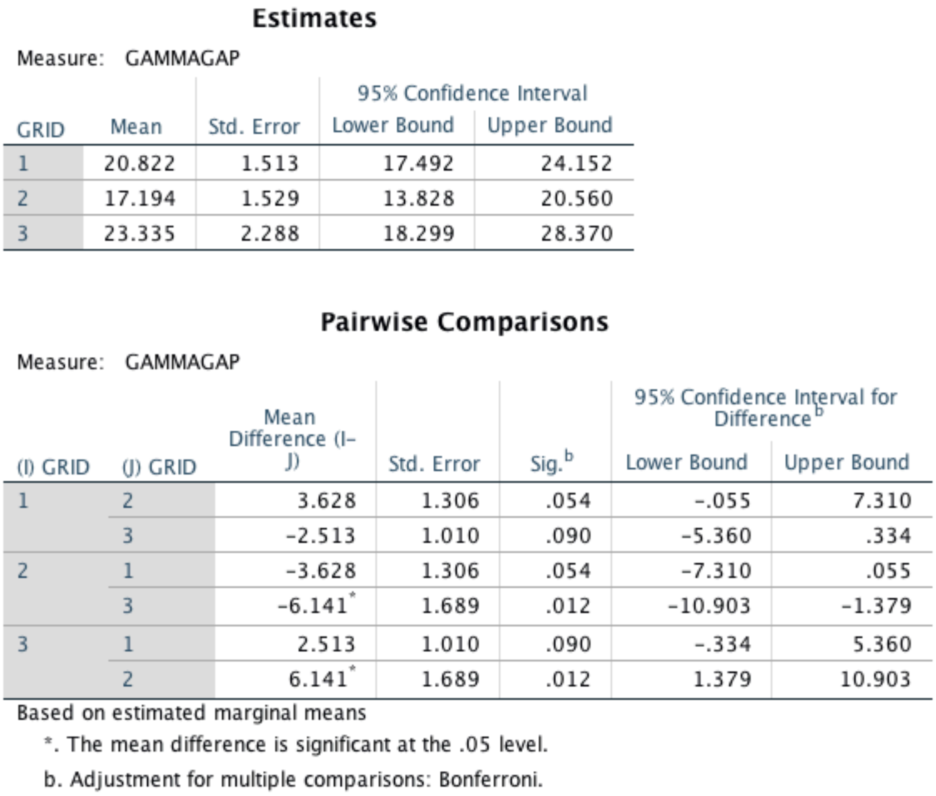

Estimates

Measure: GAMMAGAP

GRID	Mean	Std. Error	95% Confidence Interval Lower Bound	95% Confidence Interval Upper Bound
1	20.822	1.513	17.492	24.152
2	17.194	1.529	13.828	20.560
3	23.335	2.288	18.299	28.370

Pairwise Comparisons

Measure: GAMMAGAP

(I) GRID	(J) GRID	Mean Difference (I–J)	Std. Error	Sig.[b]	95% Confidence Interval for Difference[b] Lower Bound	95% Confidence Interval for Difference[b] Upper Bound
1	2	3.628	1.306	.054	-.055	7.310
	3	-2.513	1.010	.090	-5.360	.334
2	1	-3.628	1.306	.054	-7.310	.055
	3	-6.141*	1.689	.012	-10.903	-1.379
3	1	2.513	1.010	.090	-.334	5.360
	2	6.141*	1.689	.012	1.379	10.903

Based on estimated marginal means

*. The mean difference is significant at the .05 level.

b. Adjustment for multiple comparisons: Bonferroni.

Figure E.65 – Estimated marginal means and pairwise comparisons for Dynamics.

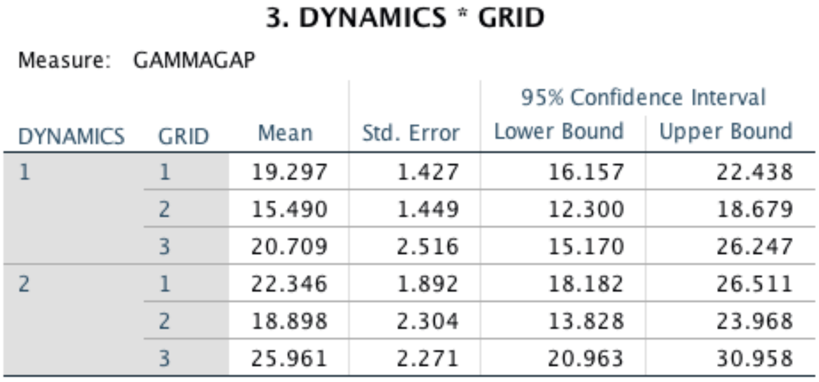

3. DYNAMICS * GRID

Measure: GAMMAGAP

DYNAMICS	GRID	Mean	Std. Error	95% Confidence Interval Lower Bound	95% Confidence Interval Upper Bound
1	1	19.297	1.427	16.157	22.438
	2	15.490	1.449	12.300	18.679
	3	20.709	2.516	15.170	26.247
2	1	22.346	1.892	18.182	26.511
	2	18.898	2.304	13.828	23.968
	3	25.961	2.271	20.963	30.958

Figure E.66 – Estimated marginal means of Grid - Dynamics interaction.

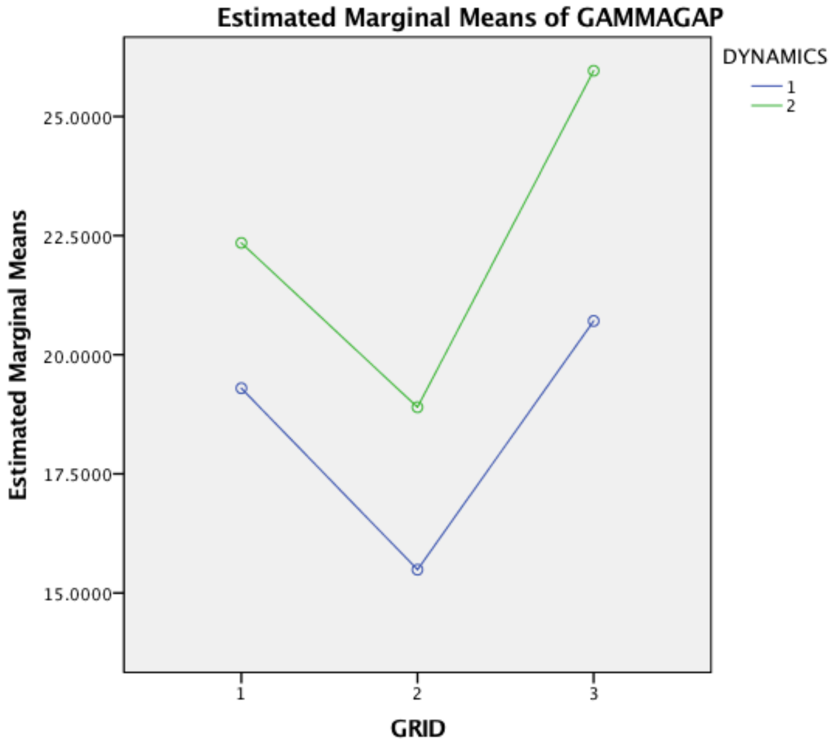

Figure E.67 – Profile plot for within-subjects ANOVA of flight path angle gap.

E.7. Coupling constant

Between-Subjects ANOVA

Experience was not a significant factor for the coupling constant *k*. The assumption of sphericity had not been violated for Grid according to Mauchly's test, $\chi^2(2) = 0.371$, $p = .831$. The assumption of homogeneity of variance could not be rejected by Levene's test. The null hypothesis that the *k* data came from a normally-distributed population could not be rejected by Shapiro-Wilk's test. Mixed ANOVA did not reject the null hypothesis that the means for *k* are the same for both Experience levels, so ANOVA was done on the Experience-lumped *k* data.

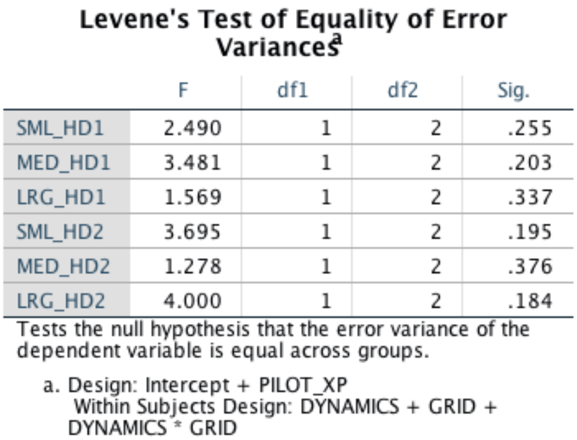
Levene's Test of Equality of Error Variances[a]

	F	df1	df2	Sig.
SML_HD1	2.490	1	2	.255
MED_HD1	3.481	1	2	.203
LRG_HD1	1.569	1	2	.337
SML_HD2	3.695	1	2	.195
MED_HD2	1.278	1	2	.376
LRG_HD2	4.000	1	2	.184

Tests the null hypothesis that the error variance of the dependent variable is equal across groups.

a. Design: Intercept + PILOT_XP
Within Subjects Design: DYNAMICS + GRID + DYNAMICS * GRID

Figure E.68 – Mixed-design Levene'e test of homogeneity of variance for coupling constant.

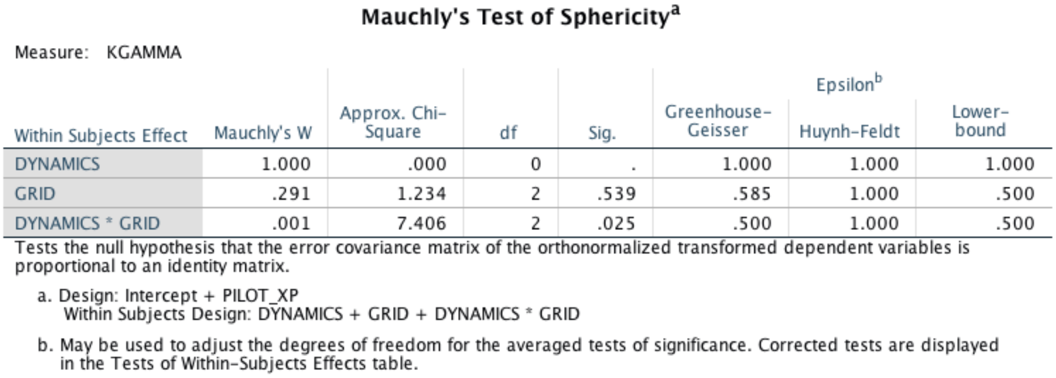

Mauchly's Test of Sphericity[a]

Measure: KGAMMA

Within Subjects Effect	Mauchly's W	Approx. Chi-Square	df	Sig.	Epsilon[b] Greenhouse-Geisser	 Huynh-Feldt	 Lower-bound
DYNAMICS	1.000	.000	0	.	1.000	1.000	1.000
GRID	.291	1.234	2	.539	.585	1.000	.500
DYNAMICS * GRID	.001	7.406	2	.025	.500	1.000	.500

Tests the null hypothesis that the error covariance matrix of the orthonormalized transformed dependent variables is proportional to an identity matrix.

a. Design: Intercept + PILOT_XP
Within Subjects Design: DYNAMICS + GRID + DYNAMICS * GRID

b. May be used to adjust the degrees of freedom for the averaged tests of significance. Corrected tests are displayed in the Tests of Within-Subjects Effects table.

Figure E.69 – Mixed-design Mauchly's test of sphericity for coupling constant.

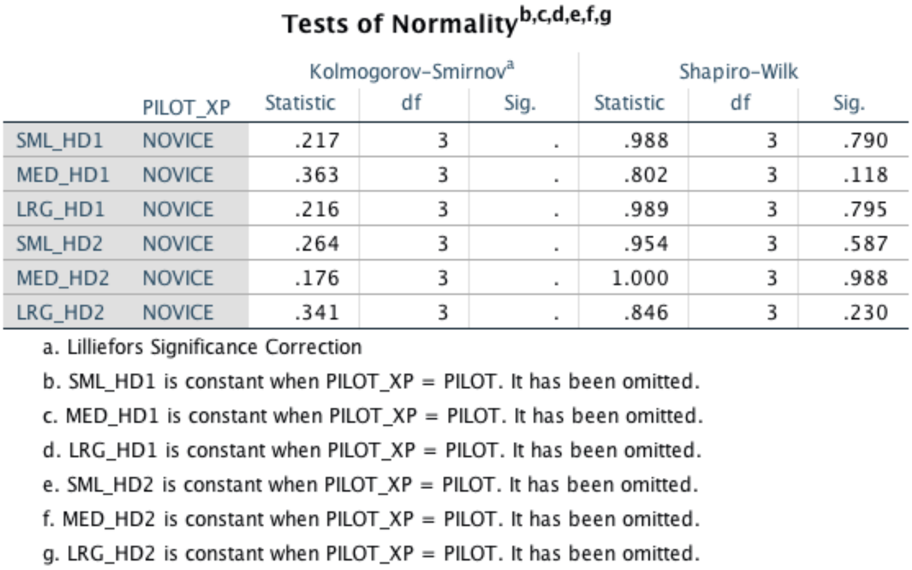

Tests of Normality[b,c,d,e,f,g]

	PILOT_XP	Kolmogorov-Smirnov[a] Statistic	 df	 Sig.	Shapiro-Wilk Statistic	 df	 Sig.
SML_HD1	NOVICE	.217	3	.	.988	3	.790
MED_HD1	NOVICE	.363	3	.	.802	3	.118
LRG_HD1	NOVICE	.216	3	.	.989	3	.795
SML_HD2	NOVICE	.264	3	.	.954	3	.587
MED_HD2	NOVICE	.176	3	.	1.000	3	.988
LRG_HD2	NOVICE	.341	3	.	.846	3	.230

a. Lilliefors Significance Correction

b. SML_HD1 is constant when PILOT_XP = PILOT. It has been omitted.

c. MED_HD1 is constant when PILOT_XP = PILOT. It has been omitted.

d. LRG_HD1 is constant when PILOT_XP = PILOT. It has been omitted.

e. SML_HD2 is constant when PILOT_XP = PILOT. It has been omitted.

f. MED_HD2 is constant when PILOT_XP = PILOT. It has been omitted.

g. LRG_HD2 is constant when PILOT_XP = PILOT. It has been omitted.

Figure E.70 – Mixed-design normality tests for coupling constant.

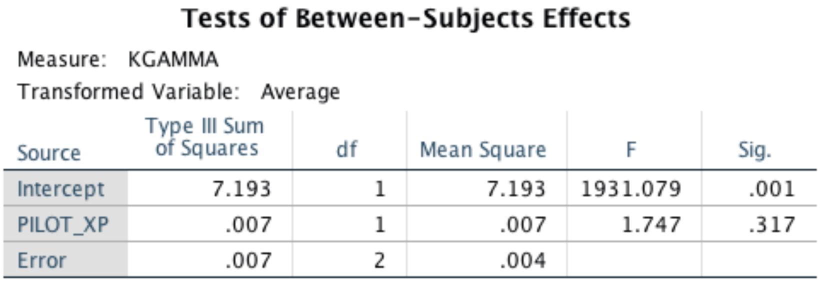

Tests of Between-Subjects Effects

Measure: KGAMMA

Transformed Variable: Average

Source	Type III Sum of Squares	df	Mean Square	F	Sig.
Intercept	7.193	1	7.193	1931.079	.001
PILOT_XP	.007	1	.007	1.747	.317
Error	.007	2	.004		

Figure E.71 – Mixed-design ANOVA for coupling constant.

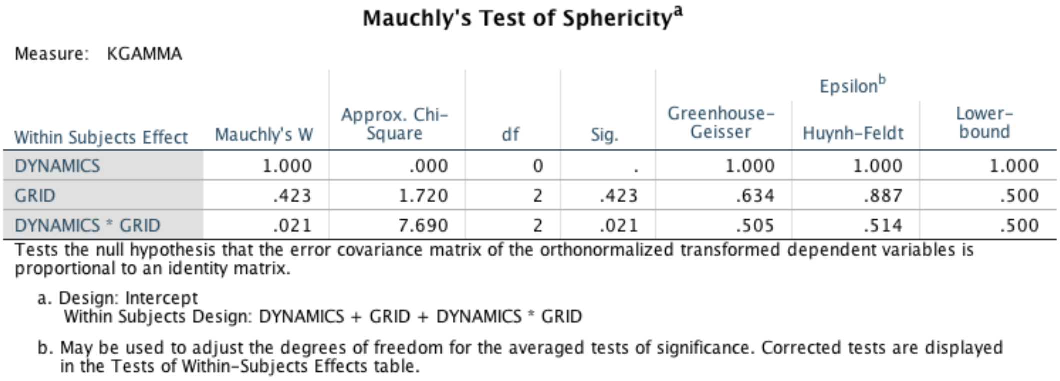

Mauchly's Test of Sphericity[a]

Measure: KGAMMA

					Epsilon[b]		
Within Subjects Effect	Mauchly's W	Approx. Chi-Square	df	Sig.	Greenhouse-Geisser	Huynh-Feldt	Lower-bound
DYNAMICS	1.000	.000	0	.	1.000	1.000	1.000
GRID	.423	1.720	2	.423	.634	.887	.500
DYNAMICS * GRID	.021	7.690	2	.021	.505	.514	.500

Tests the null hypothesis that the error covariance matrix of the orthonormalized transformed dependent variables is proportional to an identity matrix.

a. Design: Intercept
Within Subjects Design: DYNAMICS + GRID + DYNAMICS * GRID

b. May be used to adjust the degrees of freedom for the averaged tests of significance. Corrected tests are displayed in the Tests of Within-Subjects Effects table.

Figure E.72 – Mauchly's test of sphericity for within-subjects coupling constant.

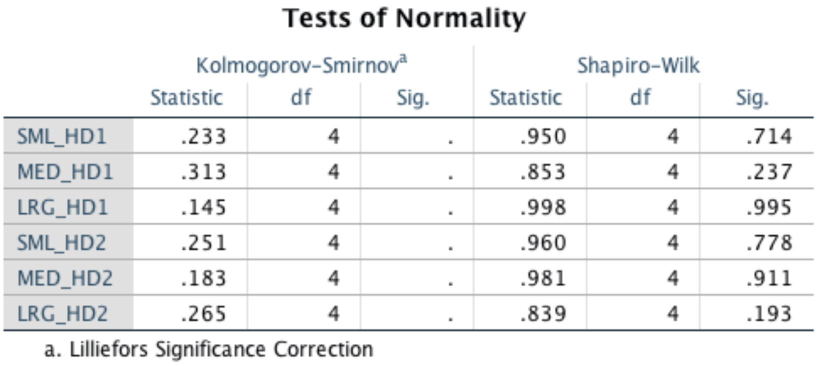

Tests of Normality

	Kolmogorov-Smirnov[a]			Shapiro-Wilk		
	Statistic	df	Sig.	Statistic	df	Sig.
SML_HD1	.233	4	.	.950	4	.714
MED_HD1	.313	4	.	.853	4	.237
LRG_HD1	.145	4	.	.998	4	.995
SML_HD2	.251	4	.	.960	4	.778
MED_HD2	.183	4	.	.981	4	.911
LRG_HD2	.265	4	.	.839	4	.193

a. Lilliefors Significance Correction

Figure E.73 – Normality tests for within-subjects coupling constant.

Within-Subjects ANOVA

A box plot of the Experience-lumped *k* is displayed in **??**. Mauchly's test could not reject the assumption of sphericity for Grid and for the Grid × Dynamics interaction $\chi^2(2) = 1.243$, $p = .537$ and $\chi^2(2) = 2.775$, $p = .250$, respectively. The assumption of normality could not be rejected for one repeated measure by a Shapiro-Wilk test. ANOVA indicated neither a significant main effect of Dynamics or Grid on *k*, nor a significant interaction effect of Grid × Dynamics.

0

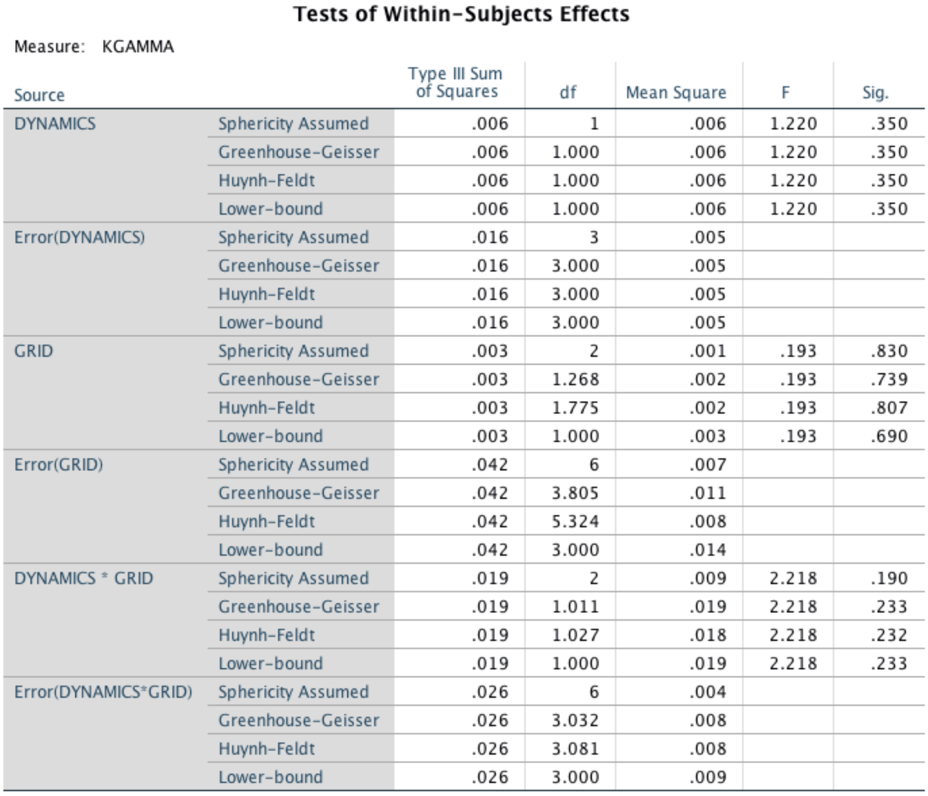

Tests of Within-Subjects Effects

Measure: KGAMMA

Source		Type III Sum of Squares	df	Mean Square	F	Sig.
DYNAMICS	Sphericity Assumed	.006	1	.006	1.220	.350
	Greenhouse-Geisser	.006	1.000	.006	1.220	.350
	Huynh-Feldt	.006	1.000	.006	1.220	.350
	Lower-bound	.006	1.000	.006	1.220	.350
Error(DYNAMICS)	Sphericity Assumed	.016	3	.005		
	Greenhouse-Geisser	.016	3.000	.005		
	Huynh-Feldt	.016	3.000	.005		
	Lower-bound	.016	3.000	.005		
GRID	Sphericity Assumed	.003	2	.001	.193	.830
	Greenhouse-Geisser	.003	1.268	.002	.193	.739
	Huynh-Feldt	.003	1.775	.002	.193	.807
	Lower-bound	.003	1.000	.003	.193	.690
Error(GRID)	Sphericity Assumed	.042	6	.007		
	Greenhouse-Geisser	.042	3.805	.011		
	Huynh-Feldt	.042	5.324	.008		
	Lower-bound	.042	3.000	.014		
DYNAMICS * GRID	Sphericity Assumed	.019	2	.009	2.218	.190
	Greenhouse-Geisser	.019	1.011	.019	2.218	.233
	Huynh-Feldt	.019	1.027	.018	2.218	.232
	Lower-bound	.019	1.000	.019	2.218	.233
Error(DYNAMICS*GRID)	Sphericity Assumed	.026	6	.004		
	Greenhouse-Geisser	.026	3.032	.008		
	Huynh-Feldt	.026	3.081	.008		
	Lower-bound	.026	3.000	.009		

Figure E.74 – Within-subjects ANOVA of coupling constant.

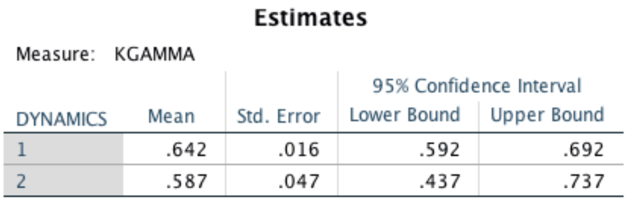

Estimates

Measure: KGAMMA

DYNAMICS	Mean	Std. Error	95% Confidence Interval Lower Bound	95% Confidence Interval Upper Bound
1	.642	.016	.592	.692
2	.587	.047	.437	.737

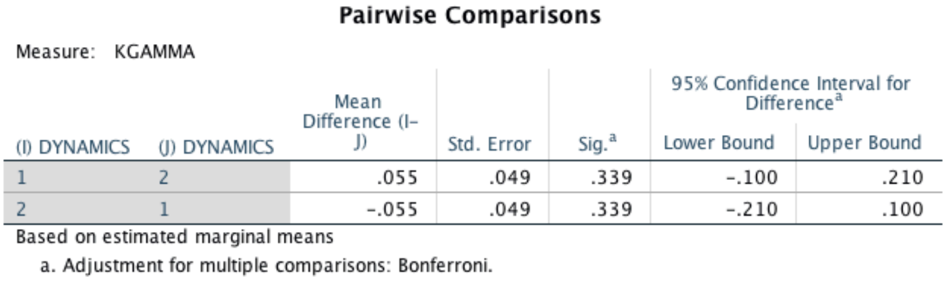

Pairwise Comparisons

Measure: KGAMMA

(I) DYNAMICS	(J) DYNAMICS	Mean Difference (I-J)	Std. Error	Sig.[a]	95% Confidence Interval for Difference[a] Lower Bound	95% Confidence Interval for Difference[a] Upper Bound
1	2	.055	.049	.339	-.100	.210
2	1	-.055	.049	.339	-.210	.100

Based on estimated marginal means

a. Adjustment for multiple comparisons: Bonferroni.

Figure E.75 – Estimated marginal means and pairwise comparisons for Grid.

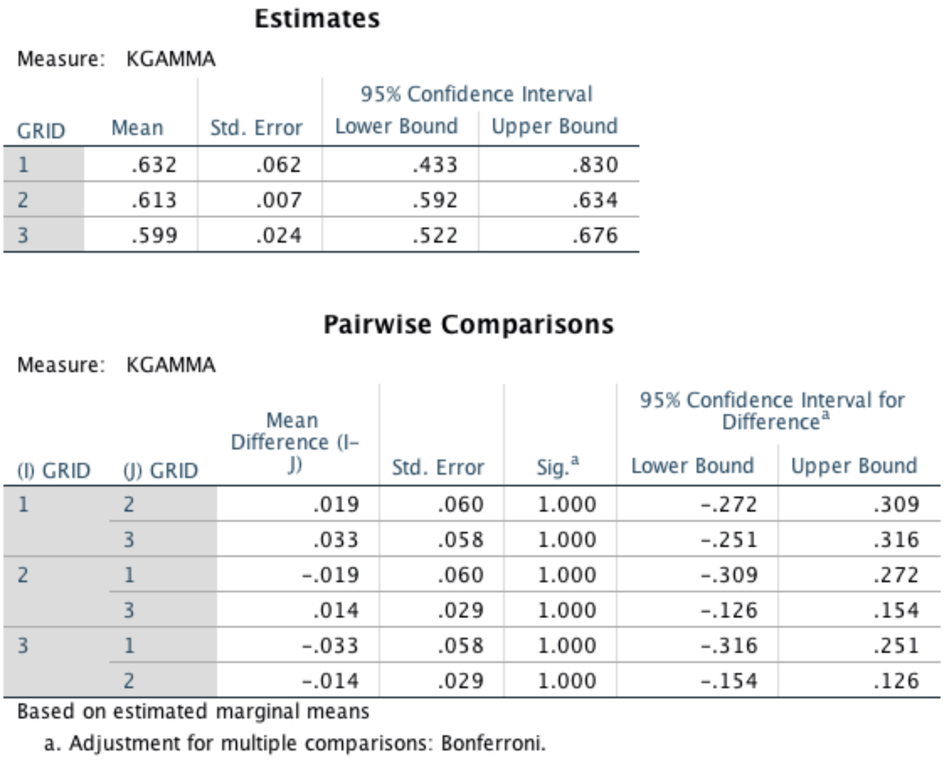

Estimates

Measure: KGAMMA

GRID	Mean	Std. Error	95% Confidence Interval Lower Bound	95% Confidence Interval Upper Bound
1	.632	.062	.433	.830
2	.613	.007	.592	.634
3	.599	.024	.522	.676

Pairwise Comparisons

Measure: KGAMMA

(I) GRID	(J) GRID	Mean Difference (I–J)	Std. Error	Sig.[a]	95% Confidence Interval for Difference[a] Lower Bound	95% Confidence Interval for Difference[a] Upper Bound
1	2	.019	.060	1.000	-.272	.309
	3	.033	.058	1.000	-.251	.316
2	1	-.019	.060	1.000	-.309	.272
	3	.014	.029	1.000	-.126	.154
3	1	-.033	.058	1.000	-.316	.251
	2	-.014	.029	1.000	-.154	.126

Based on estimated marginal means

a. Adjustment for multiple comparisons: Bonferroni.

Figure E.76 – Estimated marginal means and pairwise comparisons for Dynamics.

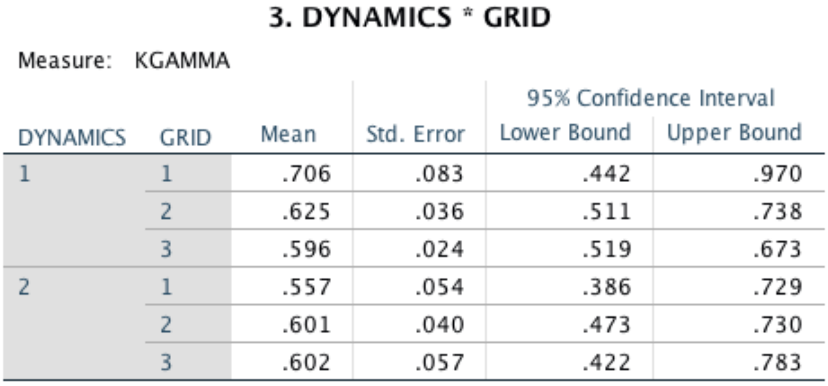

3. DYNAMICS * GRID

Measure: KGAMMA

DYNAMICS	GRID	Mean	Std. Error	95% Confidence Interval Lower Bound	95% Confidence Interval Upper Bound
1	1	.706	.083	.442	.970
	2	.625	.036	.511	.738
	3	.596	.024	.519	.673
2	1	.557	.054	.386	.729
	2	.601	.040	.473	.730
	3	.602	.057	.422	.783

Figure E.77 – Estimated marginal means of Grid - Dynamics interaction.

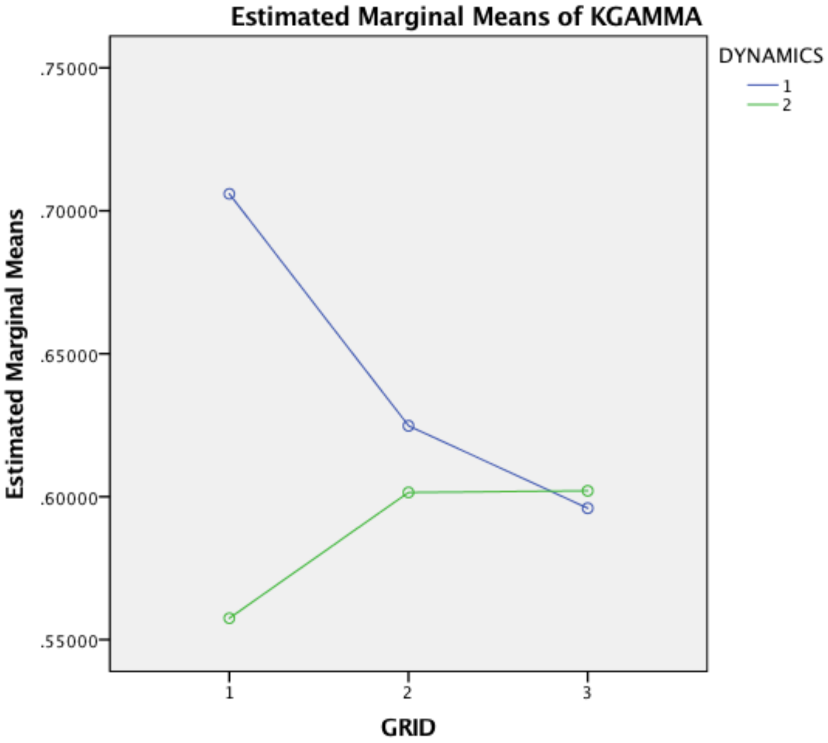

Figure E.78 – Profile plot for within-subjects ANOVA of coupling constant.

F

Tau Motion Analysis

This appendix serves as an extension to the research paper. It contains a full description of the tau motion analysis applied to the experimental data. First the data selection of the pull up manoeuvre is explained in Section F.1, followed by a description of the method used to fit the constant acceleration motion guide in Section F.2. Finally, the procedure to rate the quality of the fit is explained in Section F.3.

F.1. Manoeuvre selection

A first step of the analysis is to select the start and end of the manoeuvre within the full run. This begins with plotting control input, vertical position, flight path angle and flight path angle rate against time, as shown in Figure F.1. The control input and vertical position signals indicate the approximate instant the climb was initiated at. The time axes of both the flight path angle and flight path angle rate plots are then set around that instant to determine the manoeuvre start.

In theory, the start of the manoeuvre is defined as the instant at which the pilot starts applying positive collective control input that sets the aircraft into a climb. At that instant the flight path angle rate crosses zero from negative to positive. Selecting the manoeuvre start accordingly turns out to be impractical as a the control signal is almost never zero. Moreover, fixed threshold values on the collective control signal or the flight path angle rate are unreliable due to individual differences in control style. Therefore the following guidelines are used:

- Vertical flight position starts increasing with the intention of flying over the hill.
- Collective control input is positive and increasing.
- Flight path angle is positive.
- Flight path angle rate is positive after a zero-crossing.

The manoeuvre ends when the pilot reaches the target flight path angle. It is the moment, directly after the manoeuvre start, at which the flight path angle rate crosses zero to become negative. In practice, the ending flight path angle rate has to be strictly positive to prevent the time to contact to overshoot zero and become negative. Thus the last positive data point before crossing zero flight angle rate is automatically selected.

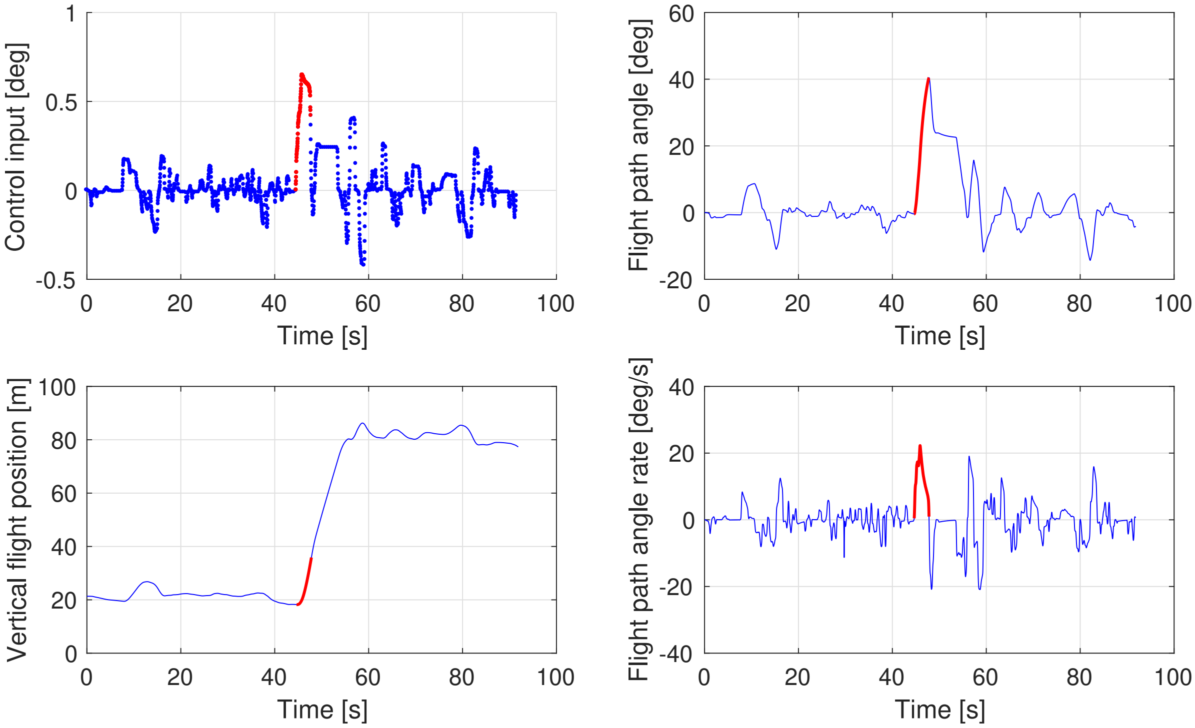

Figure F.1 – Control input, vertical position, flight path angle and flight path angle rate are plotted against time. The selected maneuver is displayed in the bold, red curve.

A cubic smoothing spline of the flight path angle signal is constructed using Matlab's csaps function using a smoothing parameter of $p = 0.995$. This helps to avoid numeric problems when differentiating the digital signal. The function fnder is then used to set up the cubic smoothing spline of the first and second derivatives of the flight path angle. When the final slope angle of the manoeuvre is captured, the first derivative of the flight path angle crosses zero at a negative slope. Therefore, the manoeuvre end is selected as the first time instant after the start that has zero flight path angle rate and negative second derivative of flight path angle:

$$\frac{d\gamma(t_f)}{dt} = 0 \ , \quad \frac{d^2\gamma(t_f)}{d^2t} < 0 \tag{F.1}$$

With the starting instant of the tau manoeuvre t_0 and its end t_f, the manoeuvre time vector t_m is simply defined by Equation (F.2).

$$t_m = \{t_0 \leq t \leq t_f\} \tag{F.2}$$

The manoeuvre duration T is calculated using Equation (F.3):

$$T = t_f - t_0 \tag{F.3}$$

The instantaneous flight path error γ_a, also called gamma to go, is defined as the deviation from the goal flight path angle $\gamma_f = \gamma(t_f)$⍰ as in Equation (F.4).

$$\gamma_a = \gamma - \gamma_f \tag{F.4}$$

The angular motion gap γ_{gap} is calculated as the difference in flight path angle between the manoeuvre start and end, as shown by Equation (F.5).

$$\gamma_{\text{gap}} = \gamma_f - \gamma_0 \tag{F.5}$$

After selecting the start and end of the tau manoeuvre, an overview of this selected part of data is made to visualize the run context to identify possibly uncommon characteristics. This overview includes a 3D representation of the run, as well as the eye-height distance and the time-to-contact as functions of longitudinal position, as shown in Figure F.2.

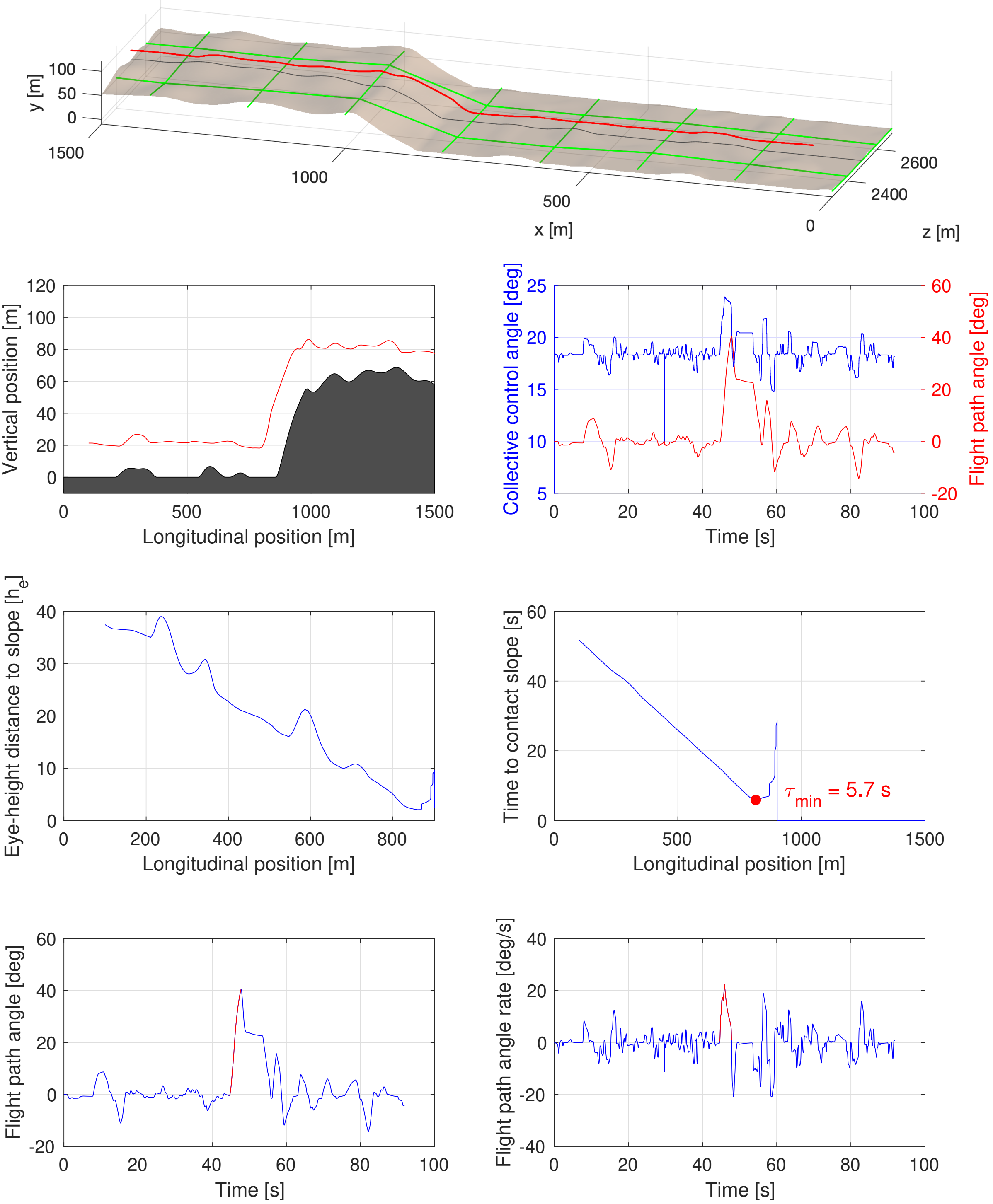

Figure F.2 – Overview of various run data used during the analysis

F.2. Fitting the tau guide

Everything is now set up for the actual tau analysis, which consists of finding a least-squares fit of the constant acceleration tau guide τ_g, linearly coupled by the coupling constant k, to the tau motion, as in Equation (F.6).

$$\tau_\gamma = k\,\tau_g\,, \quad 0 < k < 1 \tag{F.6}$$

From Equation (F.4) it is inferred that the instantaneous flight path error rate $\dot{\gamma}_a$ equals the flight path angle rate because γ_f is constant. The tau of the flight path angle error is calculated using Equation (F.7).

$$\tau_\gamma = \frac{\gamma_a}{\dot{\gamma}_a} \tag{F.7}$$

The manoeuvre-scaled time vector $\bar{t}$ is set up by normalizing the manoeuvre time vector t_m by means of the manoeuvre start t_0 and duration T as in Equation (F.8):

$$\bar{t} = \frac{t_m - t_0}{T} \tag{F.8}$$

The constant acceleration tau guide for the manoeuvre τ_g is calculated using Equation (F.9):

$$\tau_g = -\frac{T}{2}\frac{1}{\bar{t}} - \bar{t}\boxed{?} \tag{F.9}$$

Practically speaking, fitting the tau guide to the tau manoeuvre is not as straightforward as finding the value for the coupling constant k for which the constant acceleration tau guide τ_g has the highest correlation with τ_γ. In tau theory a perceived motion variable is steered towards a target state. While moving closer to the goal state, the control coordination becomes increasingly critical. The strategy used to guide the controlled variable to its target is more expressed at the end of the manoeuvre than at the beginning portion. The tau guide is therefore fitted in a backwards direction from the manoeuvre end towards the start, trying to include as big a part of the manoeuvre as possible. So, fitting the linearly coupled tau guide to the manoeuvre flown boils down to finding the value of k and the largest possible number of data points N_f used in the fit for which the tau guide fit yields a high possible coefficient of determination R^2.

Flight path angle and its rate Figure F.3 presents the various steps of the tau analysis. In the top left corner the flight path angle and flight path angle rate are shown as functions of normalized manoeuvre time. As the flight path angle rate quantifies the variation of the motion variable the higher frequency content of the motion signal becomes more visible.

Tau and tau guide Applying Equation (F.7) yields tau, displayed as a function of normalized manoeuvre time in the top right corner and as a function of the guide time to contact in the bottom left corner of Figure F.3. The tau curve features the same high-variation signal content as the gamma rate. There's also a decreasing tau differential between adjacent data points on the graph towards the start of the manoeuvre, further extending to lower values of tau. This is caused by the gamma rate tending to zero while the gamma gap is stable at its starting value.

Coupling constant and correlation Finally, in the bottom right corner the evolutions of R^2 and k are shown as a function of N_f. This is the main plot used to determine the length of the recorded run the tau guide is fitted to. The coupling constant k and resulting R^2 are calculated for each fraction of the manoeuvre, moving back from the last two data points towards all data points.

Picking the manoeuvre length used in the fit is not as straightforward as selecting the maximum value of N_f that yields a sufficient R^2. The minimum R^2 value is set at 0.97 since this condition provides satisfactory correlation with the tau guide while remaining attainable throughout almost all runs. As can be seen in the last plot in Figure F.3, the coefficient of determination meets the 0.97 threshold during the last third of the run and also for $N_f = 314$. This occurs for virtually every run because the data points with higher tau values at the start of the manoeuvre have a larger impact on R^2 then those at the end.

The objectives of both a high R^2 and N_f could be easily met by fitting the data points to (almost) the entire manoeuvre, neglecting the end of the motion where the control strategy tends to be most expressed in order to reach the target flight path angle. Rather, the N_f was chosen as the last data point before R^2 drops below 0.97 and only recovers when nearly fitting the whole manoeuvre.

To summarize, these are the criteria used:

- Coupling constant k from least-squares regression, not exceeding unity: $0 < k < 1$.
- Coefficient of determination $R^2 > 0.97$.
- Moving backwards from the end of the manoeuvre, N_f is selected as the last value before R^2 drops below its threshold.
- N_f values close to the maximum value that yield satisfactory R^2 are disregarded.

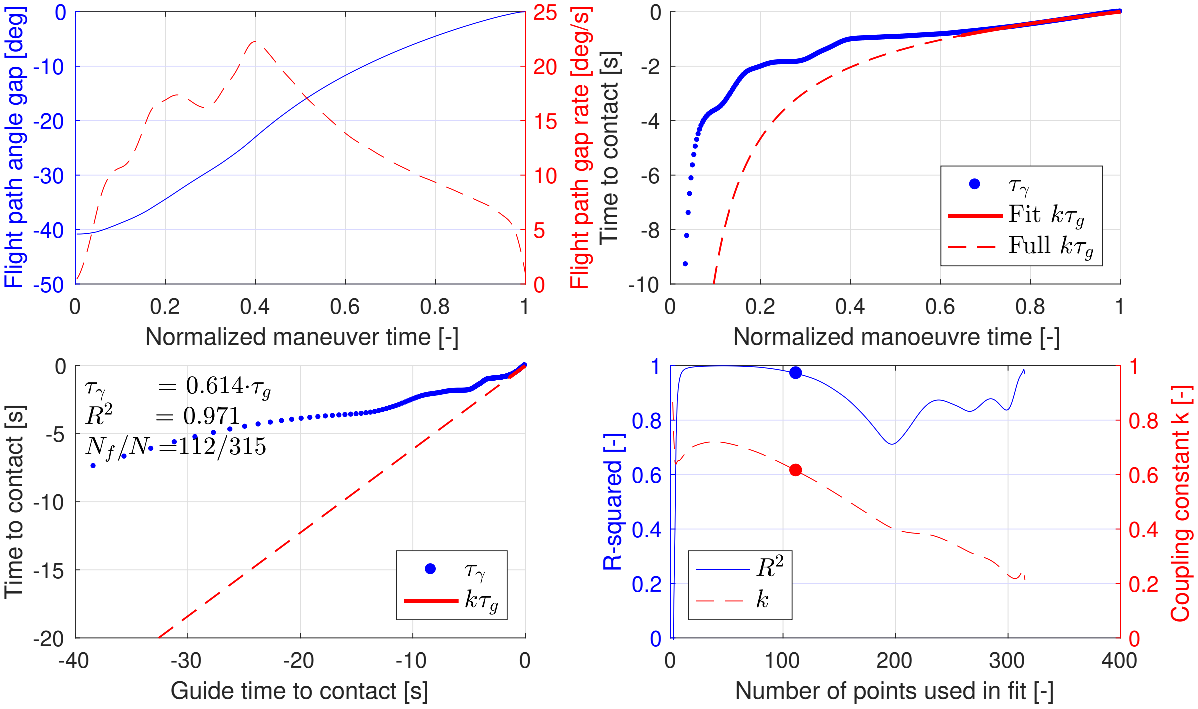

Figure F.3 – Overview of plots used for the tau analysis, including flight path angle and its rate as a function of manoeuvre time, time to contact as a function of manoeuvre time and as a function of the time to contact of the motion guide, and the correlation.

F.3. Rating the fit

After finding no significant effects of the independent variables on the dependent measures related to the tau analysis, the statistical analysis has been applied to a subset of the data. The selection of the subset is made by subjectively rating the fitted tau guide to the last half of the manoeuvre from 0 to 5 with the following rating descriptions:

Rating criteria

0. Does not meet fitting conditions
1. Barely describes last half of manoeuvre
2. Slightly good
3. Moderately good
4. Good
5. Very good

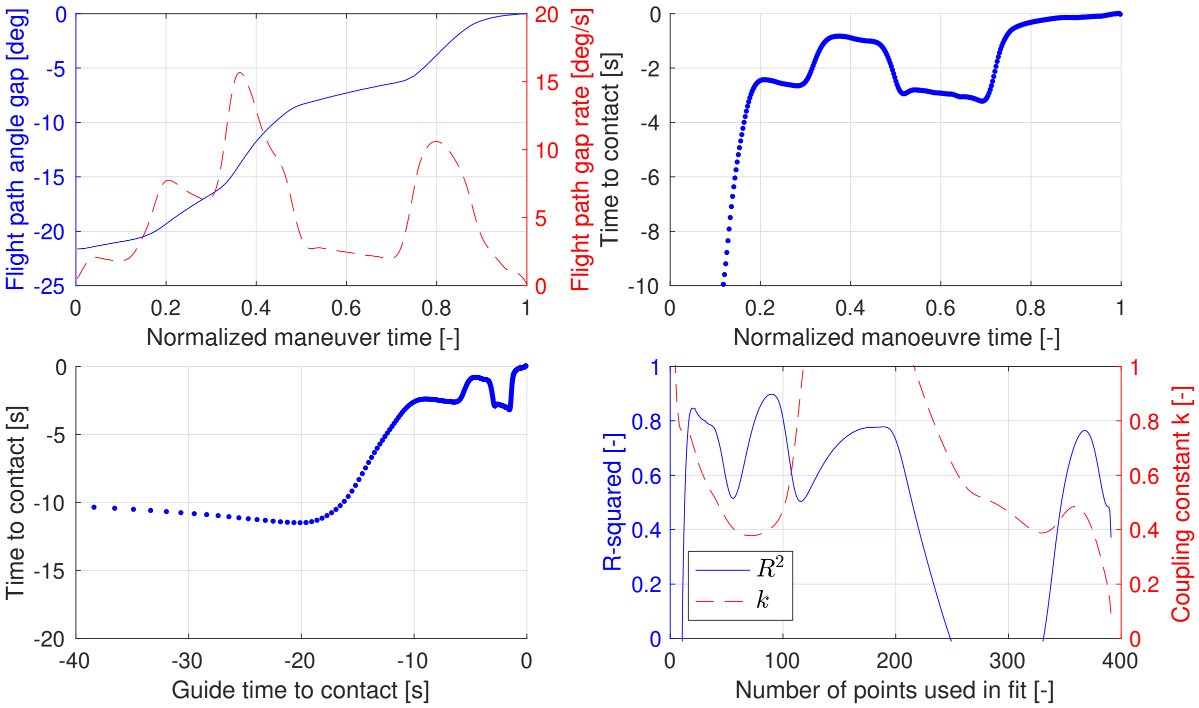

Figure F.4 – Run rated 0 since the tau guide could not be fitted.

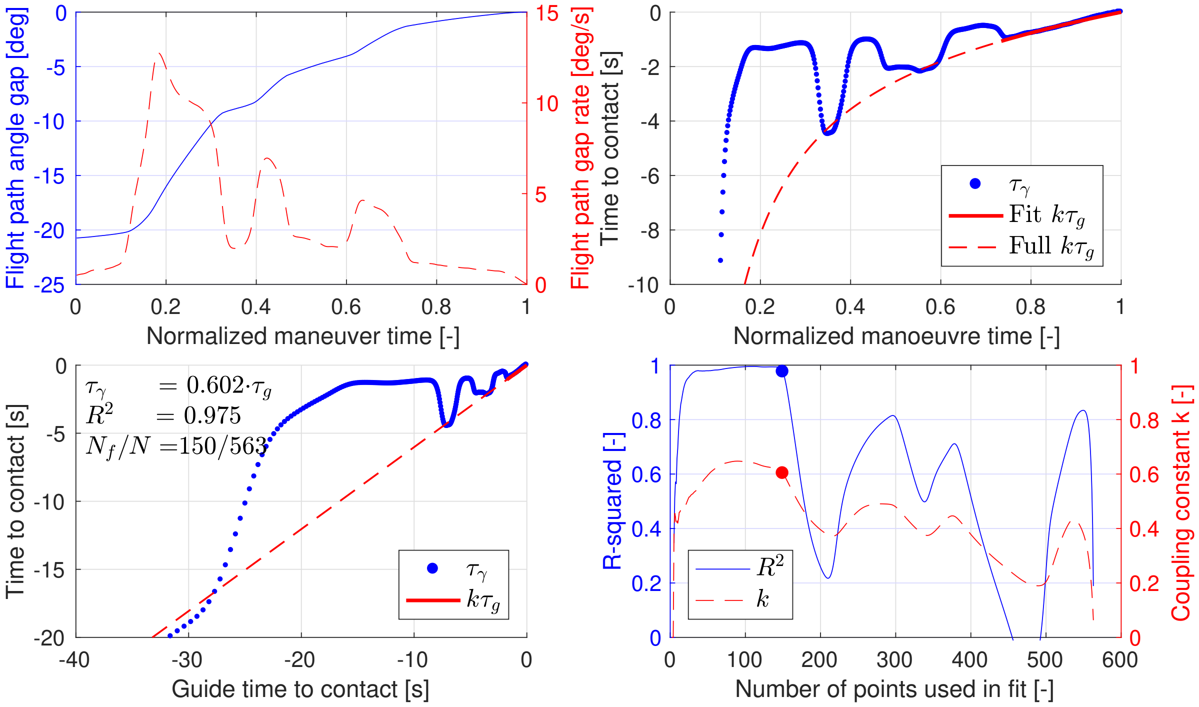

Figure F.5 – Run rated 1 since last half of manoeuvre is barely described by the tau guide.

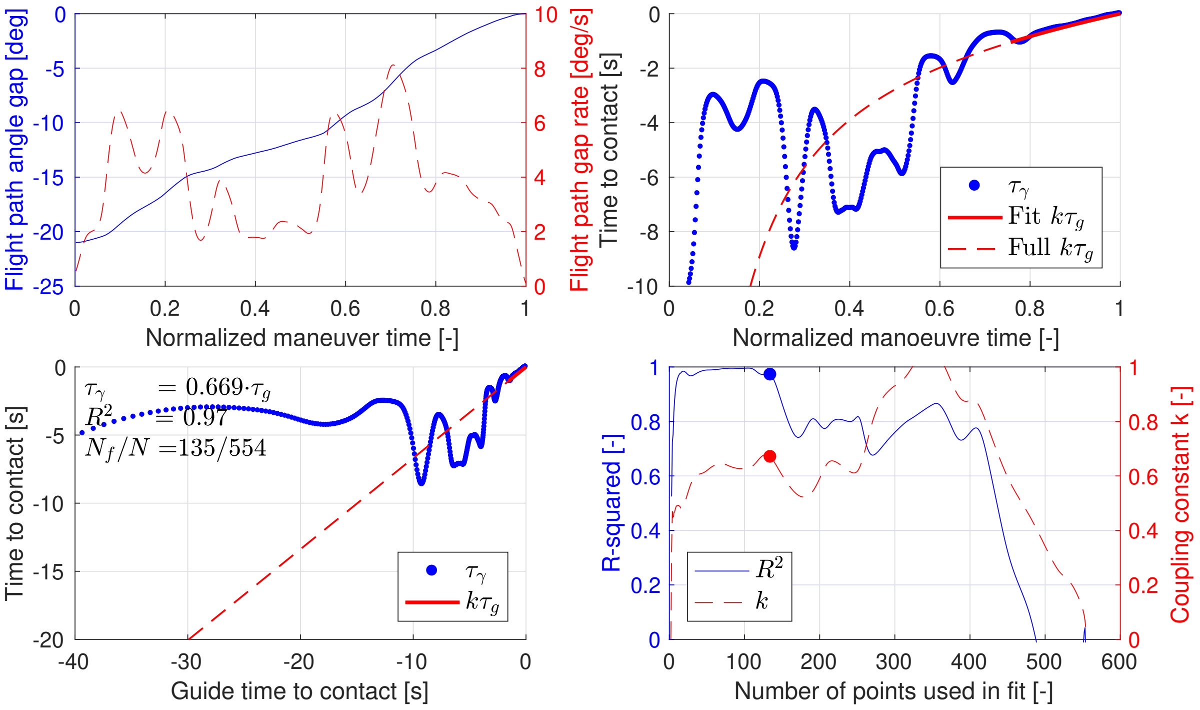

Figure F.6 – Run rated 2 since the tau guide could not be fitted.

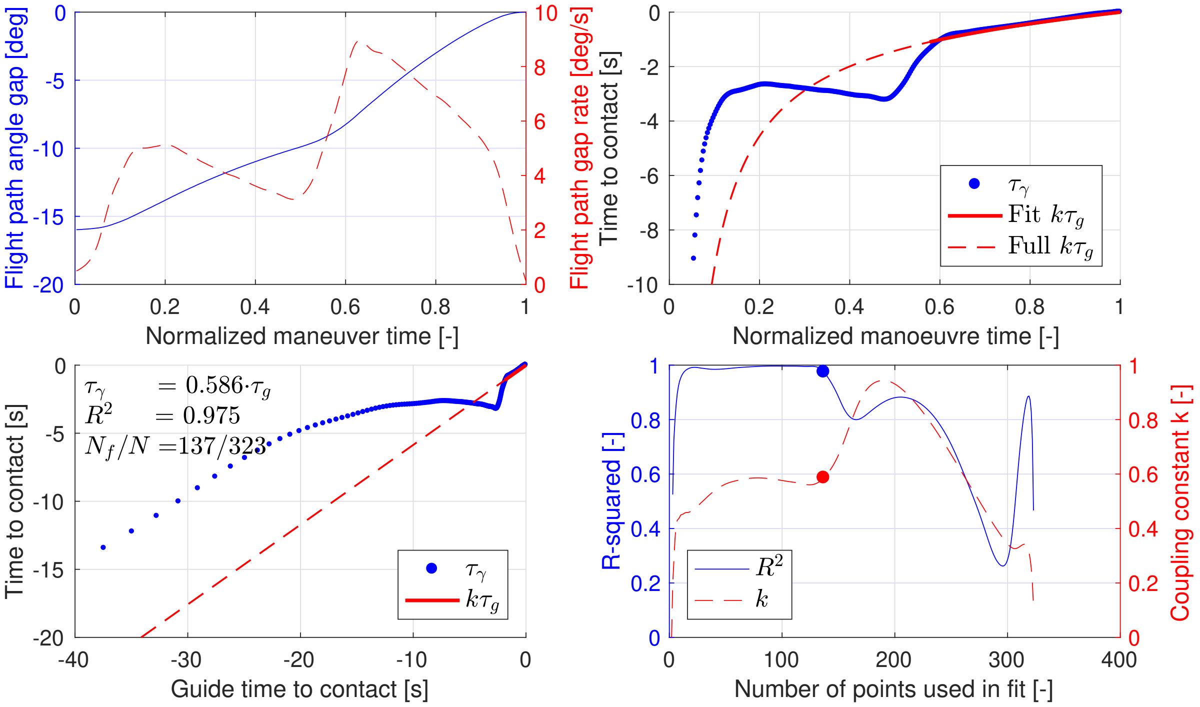

Figure F.7 – Run rated 3 since the tau guide could not be fitted.

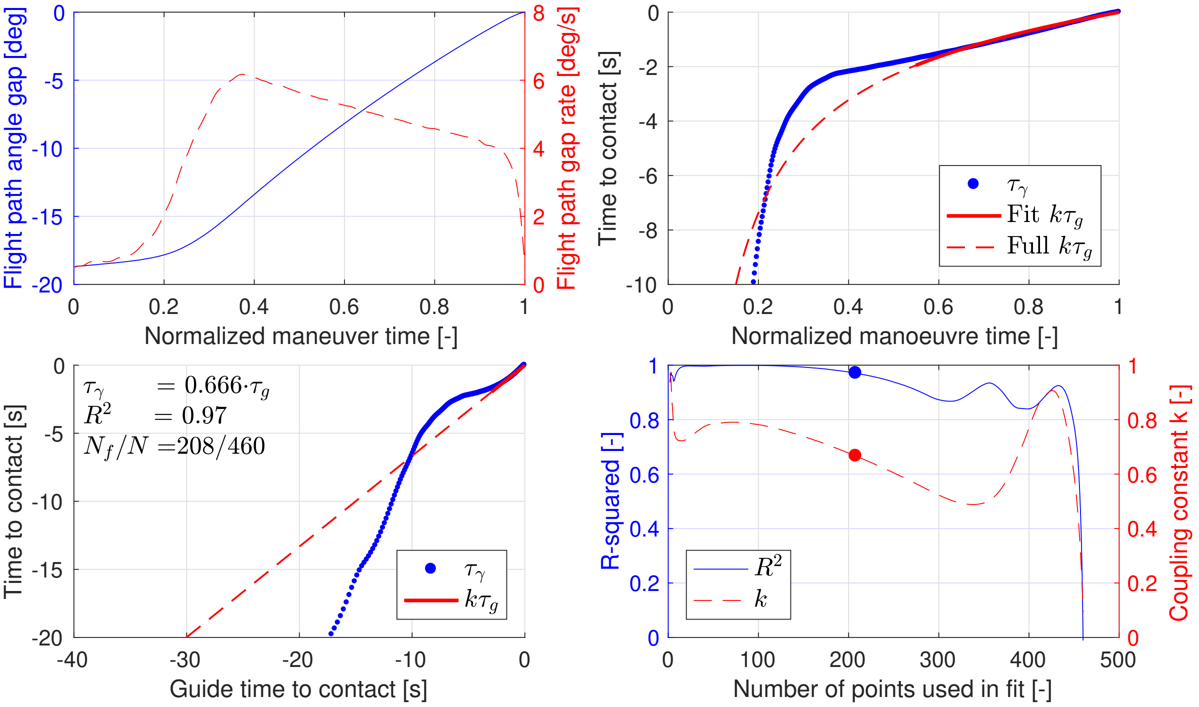

Figure F.8 – Run rated 4 since the tau guide could not be fitted.

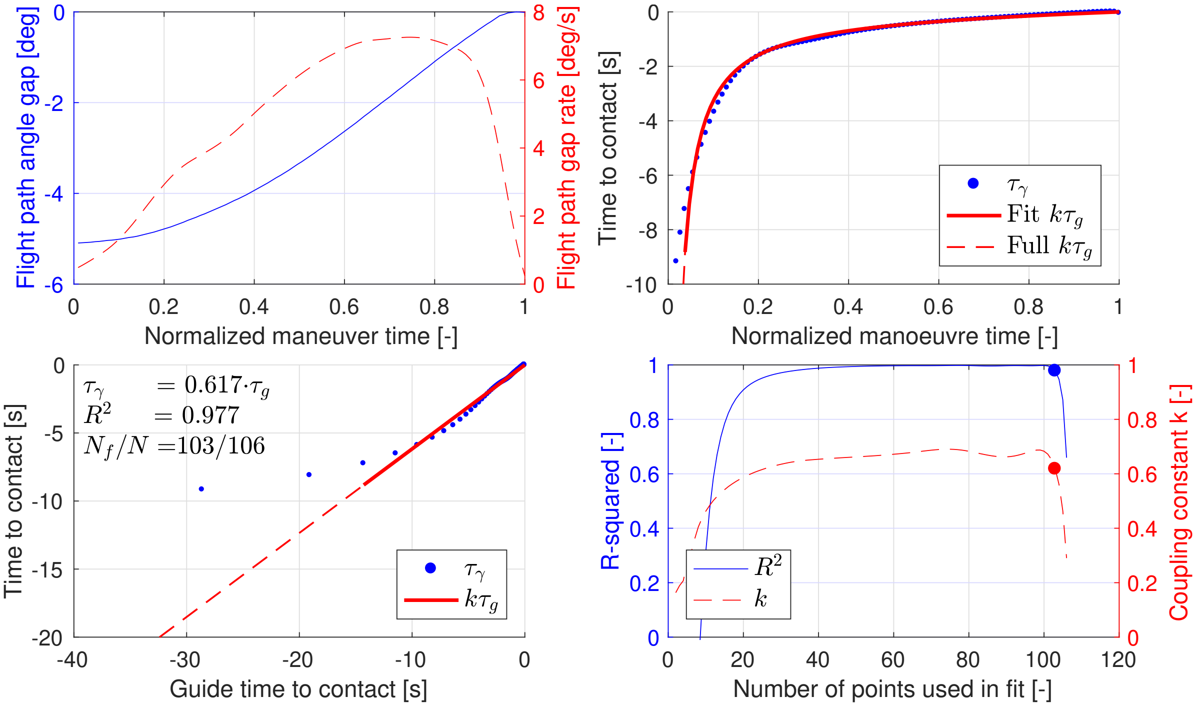

Figure F.9 – Run rated 5 since the tau guide could not be fitted.

G

Optical variables analysis

This appendix describes optical variable analysis that's been applied to the experiment scene. The analysis focuses on the effects of the terrain grid geometry on the splay and density angle and their rates. Scrutiny of these interactions may help explain some experimental results.

To study the effects of the terrain grid geometry on the optical variables some neutral data is needed, so that any potential influences of the pilots are excluded. To that end, a point-mass simulation is performed for each of the three starting positions in the experiment scene such that the vehicle constantly maintains the nominal height of 70 ft above terrain.

Section G.1 describes the analysis of the total depression angle rate from this nominal height simulation after which the analysis of the splay rate is discussed in Section G.2.

G.1. Total depression angle rate

The depression angle is defined as the angular position from the observer to a texture element parallel to the horizon, scaled by the observer height. As the terrain height in the experiment scene varies in the direction perpendicular to the direction of flight, the depression lines are slightly slanted. So, the grid height is averaged between two adjacent grid points to calculate the depression angle in the forward line of sight. The depression angle can then be calculated for each grid line perpendicular to the direction of flight by applying Equation (G.1).

$$\delta = tan^{-1} \left(\frac{x_g}{z} \right) \tag{G.1}$$

With δ the depression angle, x_g the longitudinal distance on the ground to the texture element and z the altitude.

As the AR terrain display has multiple grid lines, each visible at a certain depression angle varying across time, the combined depression angle rate cannot directly be expressed as a single value at each instant. The depression angle rate of each edge varies from naught when the edge is at the horizon to a maximum value when the edge is passing underneath the observer. If the depression angle rate of each edge visible in the forward field of view is summed, we get a total depression angle rate Δ as defined by Equation (G.2):

$$\Delta = \Sigma \begin{cases} \dot{\delta}, & \text{if } x_g \geq 0 \\ 0 & \text{if } x_g < 0. \end{cases} \tag{G.2}$$

Total depression rate for all three runs and for the different grid cell sizes is plotted against time in Figure G.1. The passing of the edges is clearly reflected in the signal. When the upcoming edge is relatively far away, total depression rate is near zero. Once the edge approaches the total depression angle rate decreases to a maximum absolute value with an increasing rate. It returns to about zero once the pilot has moved over the edge.

As the total number of edges increases as the grid cell size decreases, the total depression angle shows more peaks as the grid cell size is smaller. A smaller grid cell size will therefore provide more visual feedback, as confirmed by the total depression angle rate. Grid size does not have an effect on the absolute maximum depression angle rate, as witnessed by the coinciding edges of the small and large grid cells.

G.2. Splay rate

The optical splay angle S is the angle between a texture line that runs parallel to the direction of motion and the horizon line at the convergence point on the horizon. To calculate the splay angle in the experiment scene for the nominal height data, the average splay angle of the splay lines directly next to the pilot is calculated through Equation (G.3), where Y_g is the lateral displacement from the ground track and z the altitude. The splay rate is then simply found by differentiating the splay angle against time.

$$S = tan^{-1} \frac{Y_g}{z} \text{⍰} \tag{G.3}$$

Splay rate is plotted against time for all three runs and for the different grid cell sizes in Figure G.1. The time axis is broadly set around the moment of the climb. Comparing the different starting positions, the starting instant of the climb comes sooner as the pilot starts the experimental run closer to the hill.

Comparing the effect of the different grid cell sizes, the splay rate varies more when the grid size is smaller. In Figure G.1 it can be seen that of the three splay rate signals the small grid cell size has the most highest absolute splay ratios. When pilots see a finer terrain grid display, they observe more variation in the optical splay rate cue. Due to the lack of reference data for splay rate perception thresholds it cannot be assessed whether the differences in the splay rate signal due to the different grid cell sizes can be readily distinguished by the pilots.

To try to compare the magnitude of the splay rates between the grid cell sizes, a splay rate ratio is calculated and shown in Figure G.2. This graph does not provide additional insight.

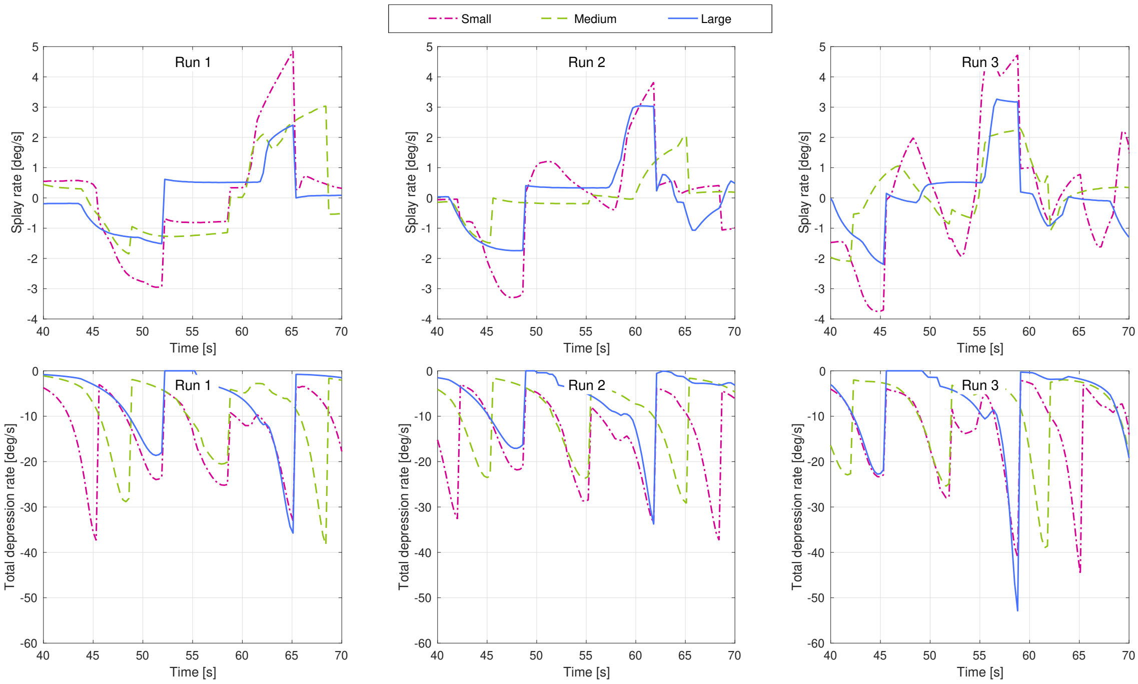

Figure G.1 – Compression and splay angle rates for nominal height across grid cell sizes and and starting positions (run 1 to 3)

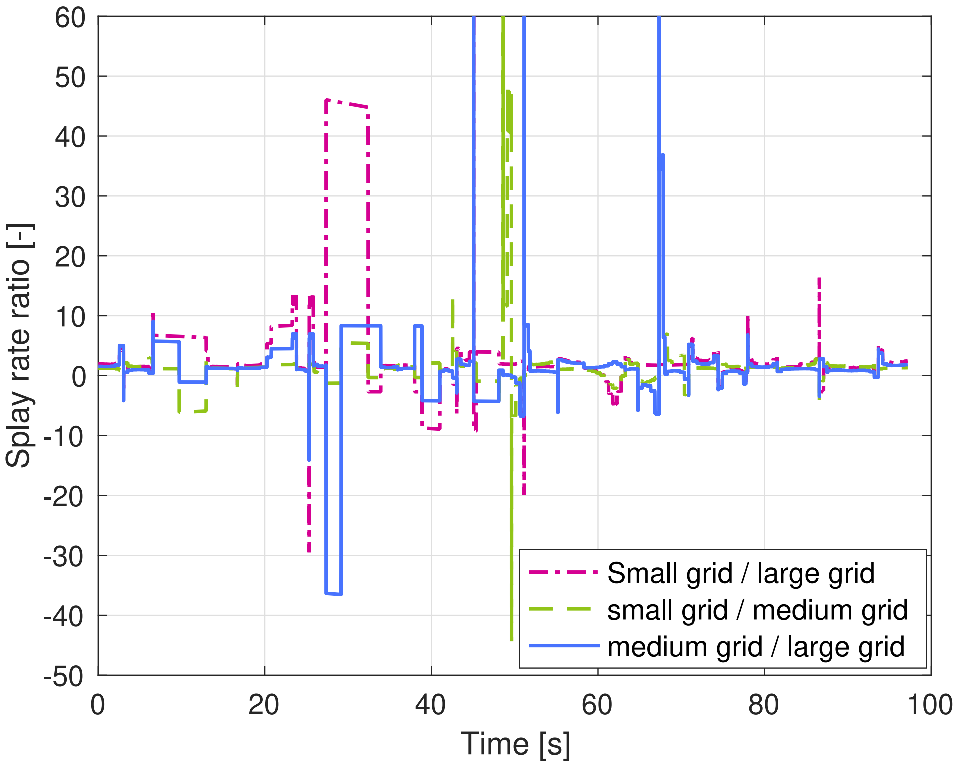

Figure G.2 – Splay rate ratios comparing splay rates between the three grid cell sizes

H

Experiment Briefing

GECO Simulator Experiment Briefing

Altitude Control in Degraded Visibility using a Terrain Visualisation Display

During Nap-of-the-Earth helicopter missions, pilots fly slightly above the treetops, following the contour of the terrain surface. This task becomes particularly challenging when the outside view is obscured by dense fog. In such conditions, a helmet-mounted display can be used to visualise the terrain through a synthetic grid. This research project aims to understand how humans use such a display.

1 Objectives

The aim of this experiment is to investigate how a synthetic terrain grid shown on a helmet-mounted display can help pilots control altitude in degraded visual conditions. On the one hand, it is known that a terrain grid increases the situation awareness of the pilot. On the other hand, it is unclear how such a grid affects the pilot control behaviour and how it can be used for different helicopter types. The current experiment intends to help understand these factors.

Figure 1. GECO Simulator

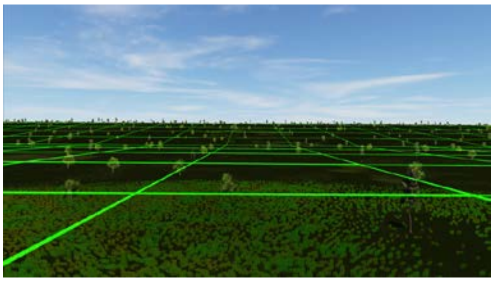

Figure 2. Terrain Grid

2 Control Task

The control task in this experiment is to maintain altitude of a helicopter flying at 70ft above the ground. Cockpit instruments are disabled, so the outside visual scene provides all usable altitude information. As the pilot, you will fly through dense fog while using a simulated head-mounted display that shows a terrain grid overlaid over the outside visual scene. The helicopter automatically maintains airspeed, power and a forward flight path. The attitude is also fixed, so the nose of the aircraft will not pitch up or down. Your objective is to fly as accurately as possible at 70ft above the ground, while following the contour of the terrain.

Depending on the experimental condition, you will control helicopter one or helicopter two. The difference between the two helicopter types is how they tend to react to control input. Moreover, the terrain grid will vary in grid cell size, providing different amount of visual detail.

3 Experimental Apparatus

In this experiment, the Generic Cockpit (GECO) Simulator will be used, shown in Fig. 1. You will be seated in the right seat of the simulator cockpit, and use the sidestick to your right to provide the control input by moving the stick forward and backward. The task is shown on the outside visual display, visible through the cockpit windows. Helicopter sound will be played to help focus on the task. The simulator does not provide motion cues.

4 Experimental Conditions

The conditions to be tested include two helicopter types and three terrain grid cell sizes. The helicopter types are a helicopter one and a helicopter two. The terrain grid visualisation, shown in Fig. 2, will vary in three steps: small, medium and large. This yields a total of six experimental conditions that will be presented in random order.

5 Experimental Procedure

The experiment consists of two phases: a training phase and a measurement phase. The training phase allows you to get used to controlling both helicopters. During training, symbols will be shown at the outmost edges of the visual field to indicate whether you are flying at the intended altitude, or whether you are too high or too low. These symbols, shown in Fig. 3, provide the necessary information without distracting from the forward view. First you will get to practise in good visibility. Then you will practice flying in the fog conditions that will be used during the measurement phase.

During the training phase, the experimenter will track your performance and report the root mean square error as an indication of your performance. The lower the score, the better your performance is. During the measurement phase, three runs will be taken for each condition. Each run takes approximately three minutes. After each run you are asked to rate the mental workload you endured on a 1-7 scale, one being the lowest and 7 the highest. Breaks are given between conditions to avoid fatigue. The total experiment time is expected to be around 3 hours.

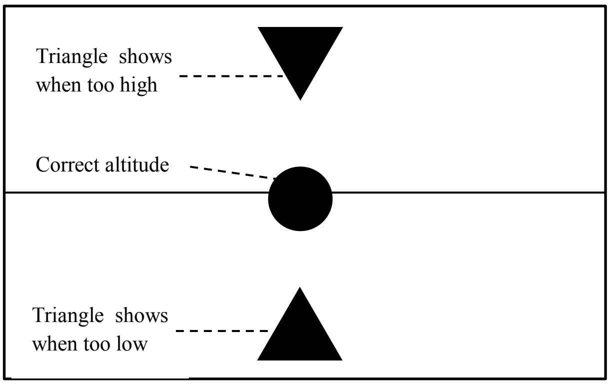

Figure 3. Altitude training symbol

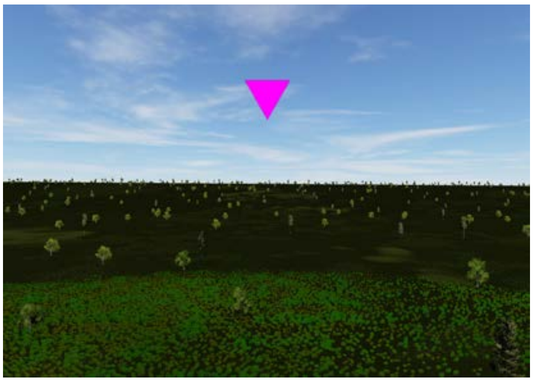

Figure 4. Training display when too high

6 Participant Rights

Your participation in this experiment is voluntary, and you can terminate it at any time, before or during the experiment. The data collected in this experiment is anonymous and confidential. The treatment and presentation of the data will be done such that only the experimenter can link the results to the participants, and all participants will remain anonymous. Your participation means that you allow the data to be published.

In order to confirm that you agree and understand all of the above, you will be asked to sign an informed consent form before you start the experiment.

Consent Form

Declaration of Consent

Experimental Evaluation of a Head-Up Display Terrain Visualization for Nap-of-the-Earth Helicopter Flight

- I hereby declare that I have read and understood the instructions handed out by the researcher.
- I am currently feeling healthy and in good condition to perform well in the tasks assigned to me during the experiment.
- I am aware of the fact that I can stop the experiment at any time without having to provide a reason.
- I hereby accept the collection of data during the experiment, as well as personal data on the information sheets filled out. The data will be collected as regulated by data collection regulations and data analysis will be conducted anonymously.

____

(Place, Date) (Signature of Participant)

____

(Place, Date) (Signature of Researcher)